

UNIVERSIDAD DE CANTABRIA

Programa de
Doctorado en Ciencia y Tecnología



Tesis Doctoral

**Plasmónica con materiales nanoestructurados
poco convencionales para aplicaciones en el UV**

PhD Thesis

**Plasmonics with unconventional nanostructured
materials for UV applications**

Realizada por

Yael Gutiérrez Vela

Dirigida por

Fernando Moreno y Francisco González

Escuela de Doctorado de la Universidad de Cantabria

Santander 2019

Never half-ass two things. Whole-ass one thing.
Ron Swanson.



Acknowledgements

Look for yourself ...

G	Q	E	F	A	D	H	U	R	T	P	A	U	R	N	S	O	N	U	H
J	A	S	D	V	R	S	A	G	N	A	N	D	R	E	A	D	A	F	T
P	X	V	C	A	D	G	R	H	J	C	V	H	M	B	S	U	T	N	G
J	C	X	F	E	R	N	A	N	D	O	N	A	I	F	I	D	Z	T	A
S	O	V	B	A	E	E	V	U	M	A	X	U	D	E	L	E	S	F	J
S	A	S	Ñ	H	A	H	H	C	A	L	E	J	A	D	V	G	A	O	U
T	E	V	E	N	D	A	S	E	R	J	M	U	N	C	I	M	R	Y	L
L	I	X	A	M	C	H	I	C	T	U	F	E	N	J	A	V	I	E	R
O	V	A	H	L	A	H	G	Ñ	A	R	O	L	Ñ	R	Y	D	T	B	D
S	A	M	F	R	E	N	E	R	H	T	O	F	I	E	I	B	A	R	L
O	V	A	S	V	G	R	U	M	B	L	X	A	B	O	U	J	L	G	B
S	A	F	C	E	R	G	I	E	A	J	O	R	C	A	B	E	Y	L	U
A	J	E	V	I	F	D	L	A	L	G	B	J	L	H	E	N	R	Y	J
S	Z	D	I	E	G	O	W	F	A	M	I	L	I	A	O	F	J	S	Ñ
G	M	A	N	O	L	O	B	Ñ	R	R	H	R	J	I	R	P	L	I	J
A	C	V	W	T	H	G	C	P	A	B	L	O	R	O	L	E	O	D	R
L	J	I	L	U	A	L	D	M	F	O	N	S	O	J	R	D	B	O	K
D	A	D	F	Z	C	X	E	R	A	K	U	Y	S	H	F	R	D	Y	O
Z	L	T	H	A	S	E	M	N	B	E	W	M	U	T	S	R	Y	B	S
O	J	G	A	L	B	E	R	T	O	V	M	O	Y	U	I	H	A	S	I

Abstract

There is a growing interest in extending plasmonics into the UV range due to the new challenges arising in fields such as biosensing, chemistry or spectroscopy. Because common plasmonic materials employed in the visible range (i.e., Au and Ag) present interband transitions above 3 eV, their use in UV plasmonics is inhibited. Therefore, there is an ongoing quest for materials, both metal and high refractive index dielectrics, for plasmonic applications in the UV.

Concerning metals, recent studies have presented Mg, Ga and Rh as promising candidates. The work in this dissertation will tackle some of the current problems when applying these metals in real applications. Both Ga and Mg nanoparticles form an oxide shell when exposed to air that critically affect their plasmonic response and hinder their use in certain applications like surface-enhanced spectroscopies or photocatalysis. The oxidation effect is studied thoroughly, not only in these two materials, but also on Al, which also has been presented as a good candidate for UV plasmonics. More in detailed is studied the role of a MgO layer in the H uptake of Mg nanoparticles. This study is of relevance due to the potential role of Mg nanoparticles in the hydrogen-based economy. However, oxidation is not the only surface transformation occurring on the surface of Mg nanoparticles. Here, we report the tarnishing of Mg, a phenomenon already known to occur on Ag surfaces. Gallium nanostructures, whose oxidation process is stopped after the growth of a ≈ 1 nm oxide shell, have been presented as building blocks for plasmonic phase-change devices. It presents a wide polymorphism with at least five solid phases at atmospheric pressure, plus several others at high-pressure. The design of this type of devices has been severely hampered by the lack of information on the dielectric constant of the different Ga polymorphs. In this work, it is presented a comprehensive analysis of the interdependence of the crystal structure, band structure, and dielectric function of some of the different Ga-phases. Conversely to Mg and Ga, Rh do not oxidize. This property along with its inherent catalytic properties and UV plasmonic response, make it an adequate material for photocatalytic applications. In fact, recently it was reported the role of Rh nanocubes in the CO₂ catalyzation. In this PhD thesis, it is presented an optimization of these nanostructures' geometry attending to their ability to produce hot-spots and surface charge distributions.

The applicability of high refractive index dielectric materials for plasmonics in the UV range still remains a challenge. In part due to the lack of materials with loss-less behavior above 3 eV with, at the same time, a refractive index high enough to produce the so-called Mie resonances (i.e., the analog in dielectrics to the localize surface plasmon resonances in metals). In this dissertation it is performed a systematic quest

for materials that fulfill these conditions along with an analysis of their applicability to UV light guiding and surface-enhanced spectroscopies.

Resumen

Existe un creciente interés en extender el campo de la plasmónica al ultravioleta debido a los nuevos retos que han surgido en campos como el biosensado, la química o la espectroscopía. Dado que los metales usados comúnmente en plasmónica en el rango visible (Au y Ag) presentan transiciones interbanda por encima de los 3 eV, su uso queda inhabilitado en el UV. Por lo tanto, existe una constante búsqueda de materiales, tanto metálicos como dieléctricos de alto índice de refracción, para aplicaciones plasmónicas en este rango espectral.

En lo que se refiere a metales, estudios recientes han presentado al Mg, Ga y Rh como candidatos muy prometedores. En esta tesis abordamos algunos de los problemas que surgen al utilizar estos metales en situaciones reales. Tanto el Ga como el Mg se oxidan cuando son puestos en contacto con el aire. La capa de óxido que se forma tiene un efecto crítico en su respuesta plasmónica, afectando a su uso en algunas aplicaciones como la fotocatalisis o la espectroscopía ensalzada por superficie. El efecto del óxido es estudiado en profundidad, no solo para el Mg y el Ga, sino que también para el Al, otro metal con buena respuesta plasmónica en el UV. Más en detalle es estudiado el papel que juega la capa de MgO en la adsorción de H en nanopartículas de Mg. La relevancia de este estudio proviene del potencial uso de nanopartículas de Mg en la emergente economía del hidrógeno. Sin embargo, la oxidación no es la única transformación que ocurre en la superficie de las nanopartículas de Mg. En este trabajo demostramos que en dicha superficie puede producirse además un efecto de *tarnishing*, un fenómeno similar al que ocurre en superficies de Ag. Las nanoestructuras de Ga, cuya oxidación produce una capa de óxido de aproximadamente 1 nm, se han presentado como base para la construcción de dispositivos de “fase variable”. El Ga presenta un amplio polimorfismo, con cinco posibles fases a presión atmosférica, más otras tantas a altas presiones. El diseño de estos dispositivos de “fase variable” se ha visto obstaculizado por la falta de información acerca de las constantes ópticas de algunas de estas fases. En este trabajo se presenta un análisis de la interdependencia entre la estructuras cristalina, estructura electrónica y propiedades ópticas de diferentes fases del Ga. Al contrario de lo que ocurre con el Mg y el Ga, el Rh no se oxida. Esta propiedad, junto con sus inherentes propiedades catalíticas y su buena respuesta plasmónica en el UV, hacen que el Rh sea un metal adecuado para aplicaciones en fotocatalisis. De hecho, muy recientemente, se ha descubierto el papel que pueden jugar nanocubos de Rh en la catalización del CO₂. En esta tesis, se realiza una optimización de estas nanoestructuras para su uso en fotocatalisis en función de su habilidad para producir hot-spots y la distribución de su densidad superficial de carga.

La aplicación de materiales dieléctricos de alto índice de refracción en plasmónica en el UV es aún un reto. Esto se debe a la falta de materiales que no presenten pérdidas por encima de 3 eV y que al mismo tiempo presenten un índice de refracción lo suficientemente alto para producir resonancias de Mie (el análogo en dieléctricos a las resonancias plasmónicas localizadas en metales). En esta tesis se ha realizado una búsqueda sistemática de materiales que cumplan estas condiciones analizando además su aplicabilidad al guiado de luz y a las espectroscopías ensalzadas por superficie en el UV.

Table of contents

List of Publications	xv
List of figures	xxvii
List of tables	xxix
List of Acronyms and Abbreviations	xxxix
1 Introduction	1
1.1 Motivation	1
1.2 Interdisciplinarity	5
1.3 Objectives	7
1.4 Thesis Overview	7
2 Light and Matter	9
2.1 Maxwell's equations	10
2.2 Plane Waves	12
2.2.1 Reflection and Transmission: Fresnel Equations	14
2.3 Absorption, Scattering and Extinction	15
2.3.1 Cross-Sections and Efficiency Factors	16
2.4 Scattering by a Sphere: Mie's Theory	17
2.4.1 General Formulation	17
2.4.2 Localized Surface Plasmons in the Quasi-Static Approximation	21
2.4.3 Plasmon Dynamics and Hot Electron Generation	23
2.4.4 Scattering by Dielectric Nanoparticles	24
2.5 Scattering by Particles with Arbitrary Shape	27
2.5.1 Discrete Dipole Approximation (DDA)	27
2.5.2 Finite Element Method (FEM)	27
2.5.3 Finite-Difference Time-Domain (FDTD)	28

3	Dielectric Function: Classic, Quantum and Experimental Approaches	31
3.1	Classical Theories	31
3.1.1	Lorentz Oscillator	32
3.1.2	Drude Model	35
3.2	Quantum Approach: General Hamiltonian	37
3.2.1	Density Functional Theory	39
3.2.2	Calculation of the Dielectric Function: First-order time-dependent perturbation theory	41
3.3	Ellipsometry: Measuring the Dielectric Function	42
I	Dielectric Function Calculation in Novel Materials	45
4	Dielectric Function of Gallium Polymorphs	47
4.1	Methods	49
4.1.1	Computational Details	49
4.1.2	Optical Response	51
4.1.3	Electromagnetic Simulations	52
4.1.4	Ga layers formation and analysis	52
4.2	Results	53
4.2.1	Crystal and electronic structure of the Ga phases	53
4.2.2	Implications of Ga phases in plasmonic nanostructures	60
4.3	Conclusions	66
5	Dielectric Function of High-Pressure Gallium Phases	67
5.1	Methods	68
5.1.1	Computational Details and Optical Response	68
5.1.2	Reflectance Calculations	68
5.2	Results	69
5.2.1	Crystal and Electronic Structures	69
5.2.2	Plasmonic Behavior	72
5.3	Conclusions	76
II	Novel Plasmonics Systems for UV and Photocatalysis	77
6	Experimental Methods	79
6.1	Raman and Fourier Transform Infrared Spectroscopy	79

6.2	X-Ray Photoelectron Spectroscopy	80
6.3	Spectroscopic Ellipsometry	81
7	UV plasmonics: State of the Art	83
7.1	State of the Art	83
7.2	High Oxidation Tendency: Aluminum and Magnesium	85
7.2.1	Aluminum	85
7.2.2	Magnesium	87
7.3	Low Oxidation Tendency: Gallium and Rhodium	88
7.3.1	Gallium	88
7.3.2	Rhodium	89
7.4	Comparison of the Plasmonic Response of Simple Geometries	90
7.5	Conclusions	94
8	Oxide Effects on Al, Ga and Mg Nanoparticles	97
8.1	System Geometry and Numerical Methods	98
8.2	Results and Discussion	100
8.2.1	Comparative Study in the Far-Field: Influence of NP Shapes	100
8.2.2	Near-Field Enhancement	103
8.2.3	Influence of the Oxidation on Plasmonic Performance	106
8.3	Conclusions	108
9	The Tarnishing of Mg/MgO Nanoparticles	109
9.1	Methods	111
9.1.1	Sample Fabrication	111
9.1.2	Sample Characterization	111
9.1.3	Hydrogen Plasma Treatment	111
9.1.4	Electromagnetic simulations	111
9.2	Results	112
9.3	Conclusions	123
10	Optical Monitoring the Interacion of H with Mg/MgO Films and Nanoparticles	125
10.1	Methods	127
10.1.1	Sample Fabrication	127
10.1.2	Hydrogenation and Sample Characterization	127
10.1.3	Electromagnetic Simulations	128
10.2	Results	128

10.2.1 Mg Films	128
10.2.2 Mg Nanoparticles	131
10.3 Conclusions	135
11 Rh Nanocubes in Photocatalysis Applications	137
11.1 System Geometry and Methods	138
11.2 Results and Discussion	140
11.2.1 Comparison of Ag and Rh in Simple Geometries.	140
11.2.2 Rh Nanocubes: Perfect Shape	142
11.2.3 Rh Nanocubes: Effect of a Deformation	143
11.2.4 Rh Nanocubes: Effect of a Dielectric Substrate	148
11.3 Conclusions	151
12 The search for High Refractive Index materials in the UV	153
12.1 Methods	155
12.1.1 Mie theory	155
12.1.2 Temperature Calculations	157
12.2 Materials	157
12.3 Results	159
12.3.1 Near-Field Enhancement	159
12.3.2 Directionality Properties: The Full-Forward Condition	161
12.3.3 Interaction Effects	163
12.4 Conclusions	165
13 Conclusions and Future Work	167
13.1 Conclusions	167
13.1.1 Dielectric function of Ga polymorphs	167
13.1.2 Dielectric function of high-pressure Ga phases	168
13.1.3 Oxide effects on Al, Ga and Mg nanoparticles	168
13.1.4 The Tarnishing of Mg/MgO Nanoparticles	169
13.1.5 Interaction of H with Mg/MgO nanoparticles and films	169
13.1.6 Rh nanocubes in photocatalysis applications	169
13.1.7 High refractive index dielectric materials in the UV	170
13.2 Future Work	170
References	175

List of Publications

Some ideas and figures have appeared previously in the following publications:

- Y. Gutierrez, D. Ortiz, J. M. Sanz, J. M. Saiz, F. González, H. O. Everitt, and F. Moreno, “How an oxide shell affects the ultraviolet plasmonic behavior of Ga, Mg, and Al nanostructures,” *Opt. Express* 24, 20621 (2016).
- X. Zhang, P. Li, A. Barreda, Y. Gutierrez, F. González, F. Moreno, H. O. Everitt, and J. Liu, “Size-tunable rhodium nanostructures for wavelength-tunable ultraviolet plasmonics,” *Nanoscale Horiz.* 1, 75–80 (2016).
- Y. Gutiérrez, D. Ortiz, J. Saiz, F. González, H. Everitt, and F. Moreno, “The UV Plasmonic Behavior of Distorted Rhodium Nanocubes,” *Nanomaterials* 7, 425 (2017).
- X. Zhang, X. Li, M. E. Reish, D. Zhang, N. Q. Su, Y. Gutiérrez, F. Moreno, W. Yang, H. O. Everitt, and J. Liu, “Plasmon-Enhanced Catalysis: Distinguishing Thermal and Nonthermal Effects,” *Nano Lett.* 18, 1714–1723 (2018).
- Y. Gutiérrez, R. Alcaraz, D. Osa, D. Ortiz, J. M. Saiz, F. González, and F. Moreno, “Plasmonics in the Ultraviolet with Aluminum, Gallium, Magnesium and Rhodium,” *Appl. Sci.* 8, 64 (2018).
- Y. Gutiérrez, D. Ortiz, J. Saiz, F. González, P. Albella, and F. Moreno, “The Quest for Low Loss High Refractive Index Dielectric Materials for UV Photonic Applications,” *Appl. Sci.* 8, 2065 (2018).
- Y. Gutiérrez, M. M. Giangregorio, F. Palumbo, A. S. Brown, F. Moreno and M. Losurdo, “Optically Addressing Interaction of Mg/MgO Plasmonic Systems with Hydrogen,” *Opt. Express* 2019, 27 (4), A197–A205 (2019).

- Y. Gutiérrez, M. Losurdo, P. García-Fernández, M. Sainz de la Maza, F. González, A. S. Brown, H: O. Everitt, J. Junquera, F. Moreno, “Gallium Polymorphs: Phase-Dependent Plasmonics,”. *Adv. Opt. Mater.* (2019)
- Y. Gutiérrez, M. Losurdo, P. García-Fernández, M. Sainz de la Maza, F. González, A. S. Brown, H: O. Everitt, J. Junquera, F. Moreno, “Dielectric Function and Plasmonic Behavior of Ga(II) and Ga(III)”. Under Consideration in *Opt. Mater. Express*.
- Y. Gutiérrez, M. M. Giangregorio, F. Palumbo, F. González, A. S. Brown, F. Moreno and M. Losurdo, “All that Glitters is not MgO: Novel Insight into Reactivity of Plasmonic Mg Nanoparticles and their Benefit for Air Remediation”. Under Consideration in *RSC Adv*.

Other publications:

- A. J. Yuffa, Y. Gutiérrez, J. M. Sanz, R. Alcaraz de la Osa, J. M. Saiz, F. González, F. Moreno, and G. Videen, "Frequency shift between near- and far-field scattering resonances in dielectric particles," *J. Opt. Soc. Am. A* 32, 1638 (2015).
- A. J. Yuffa, Y. Gutiérrez, J. M. Sanz, R. Alcaraz de la Osa, J. M. Saiz, F. González, F. Moreno, and G. Videen, “Near- and far-field scattering resonance frequency shift in dielectric and perfect electric conducting cylinders,” *J. Opt. Soc. Am. A* 33, 391 (2016).
- Á. I. Barreda, Y. Gutiérrez, J. M. Sanz, F. González, and F. Moreno, “Polarimetric response of magnetodielectric core-shell nanoparticles: an analysis of scattering directionality and sensing,” *Nanotechnology* 27, 234002 (2016).
- Á. I. Barreda, Y. Gutiérrez, J. M. Sanz, F. González, and F. Moreno, “Light guiding and switching using eccentric core-shell geometries,” *Sci. Rep.* 7, 11189 (2017).
- Á. I. Barreda, Y. Gutiérrez, R. Alcaraz de la Osa, F. González, and F. Moreno, “Optimizing shape characteristics of High Refractive Index particles to improve forward scattering,” Just Accepted in *J. Quant. Spectrosc. Radiat. Transf.*

List of figures

1.1	Nanoparticle resonances for a range of plasmon resonances for a variety of particle morphologies made of gold and silver. Image adapted from Ref. [1].	4
1.2	Cover of Nature No. 7569.	6
2.1	A plane electromagnetic wave, with its electric \mathbf{E} and magnetic fields \mathbf{H} oscillating in directions perpendicular to each other and to the direction of propagation \mathbf{k}	13
2.2	Incident electromagnetic field \mathbf{E}^i on a planar boundary. \mathbf{E}^t and \mathbf{E}^r represent the transmitted and reflected fields. With an arrow and a dot are represented the parallel (p -waves) and perpendicular (s -waves) components of the fields with respect to the plane of incidence.	14
2.3	Extinction by a collection of particles. Adapted from Bohren and Huffman [2].	16
2.4	Schematic of a localized surface plasmon resonance (LSPR) excited in a sphere whose size $a \ll \lambda$ (dipolar regime). Coherent oscillations in the free electrons of the material may be induced by the oscillating electric field of the incident light.	21
2.5	(a) Aluminum complex dielectric function (left axis) and the corresponding absorption efficiency Q_{abs} of a 20 nm sphere embedded in air ($\epsilon_m = 1$, right axis). The horizontal black line indicates $2\epsilon_m$. With a vertical dashed line is highlighted the Fröhlich frequency ($\text{Re}(\epsilon_s) = -2\epsilon_m$). (b) Electric field enhancement around the 20 nm Al sphere illuminated with photon energy equal to the Fröhlich frequency.	23
2.6	Photoexcitation and subsequent relaxation processes following the illumination of a metallic nanoparticle with a laser pulse and characteristic time scales.	24

2.7	(a) Extinction efficiency (Q_{ext}) of a $R = 100$ nm silicon sphere (blue line). With yellow and red lines are plotted the dipolar electric (a_1) and dipolar magnetic (b_1) contribution to the extinction efficiency respectively. With dashed lines are highlighted the wavelengths at which the minimum-forward and zero-backward conditions are met. (b,c) Angle dependent scattered intensity by the same silicon sphere at the wavelengths corresponding to the minimum-forward and zero-backward condition. With red and blue arrows are indicated the polarization of the incoming electric field \mathbf{E} and wave vector \mathbf{k}	26
2.8	The function u (solid blue line) is approximated with u_h (dashed red line), which is a linear combination of linear basis functions ψ_i (solid black lines). The coefficients are denoted by u_0 through u_9	28
3.1	Schematic band diagram for a metal. In blue is indicated direct interband transition. In red, a intraband transition is highlighted.	32
3.2	Frequency dependence of ϵ_1 and ϵ_2 described by the Lorentz model. . .	34
3.3	Complex dielectric function $\epsilon = \epsilon_1 + i\epsilon_2$ of ice in the far infrared-microwave ranges [3]. With a dashed line are highlighted two of the characteristic frequencies.	34
3.4	Frequency dependence of ϵ_1 and ϵ_2 in a free-electron Drude model at visible and ultraviolet frequencies.	36
3.5	Fitting of the experimental dielectric function ($\epsilon = \epsilon_1 + i\epsilon_2$) of liquid Gallium (red line) [4] to a Drude model (blue dots).	37
3.6	Components of a conventional spectroscopic ellipsometer: a white light source illuminates the sample through a polarizer at an incident angle ϕ_0 . Upon reflection the polarization of the light changes and it is analyzed by another polarizer (analyzer). Finally, the light is collected by a detector.	43
4.1	Phase diagram of bulk Ga from Ref. [5] (right panel) and for Ga NPs (left panel), as summarized from data reported in various sources [4, 6, 7], showing the phases expected at the various temperatures.	48
4.2	(a) Density of states (DOS), (b) complex dielectric function and (c) structure of the unit cell of α -Ga, β -Ga, γ -Ga and δ -Ga.	54

- 4.3 Band diagram of (top) α - and (bottom) β - Ga. With arrows are indicated the interband transitions appearing in the complex dielectric function of α - and β -Ga at 1.18 (red arrows) and 2.18 eV (blue arrows), and 1.88 eV (blue arrows), respectively. With a color code is represented the intensity of the transition based on the evaluation of the optical matrix element $M_{cv\mathbf{k}}$ 57
- 4.4 (a) Comparison of measured complex dielectric function of Ga reported by several authors [8–10] and the calculated dielectric function of α -Ga (blue curve) and β -Ga (red curve) for which continuous lines correspond to the real part of the dielectric function and dot-dashed lines correspond to its imaginary part. Ellipsometric measurements of the pseudo-dielectric function (solid lines) of samples with (b) α -Ga/ β -Ga and (c) α -Ga/ γ -Ga content at a 70° angle of incidence for two sample locations (red and blue curves). The dashed lines represent the Bruggeman effective dielectric functions obtained through the mixture of the corresponding theoretical dielectric functions, for which the parameter f_α represents the volume fraction of α -Ga in the sample. 59
- 4.5 (a) Q_{SPP} and (b) Q_{LSP} spectra for each of the analyzed phases for a Ga NP. 61
- 4.6 Reflectance spectra (R) of α -Ga/ β -Ga (a, b) and α -Ga/ γ -Ga (c, d) thin films on a sapphire substrate (refractive index $n=1.78$). The dielectric function considered in each case is calculated through the Bruggeman effective medium approximation, with the α -phase filling fraction f_α indicated in the legend. The thin films have thicknesses of $h = 20$ (a, c) and 150 nm (b, d) and are illuminated at normal incidence (AOI = 0°). 62
- 4.7 (a) Absorption cross-section (C_{abs}) of spherical NPs with radius $R = 10$ nm made of the different Ga-phases. (b,c) C_{abs} of nanorods of length $L = 250$ nm and radius $R = 10$ nm made of the different Ga-phases: (b) nanorod illuminated along its symmetry axis, and (c) nanorod illuminated perpendicular to it with a polarization angle 45° . The insets indicate the propagating direction of the illuminating beam (\mathbf{k}) and its polarization (\mathbf{E}). (c) Near-field ($\log_{10}(|\mathbf{E}|^2)$) color maps of the nanorods made of each Ga-phase, excited at their low energy (longitudinal) mode. 63

4.8	Absorption cross-section (C_{abs} , blue curve) and near-field enhancement ($\langle \mathbf{E} ^2 \rangle$, red curve) averaged over the surface of a $R = 60$ nm (a) α -Ga, (b) β -Ga, (c) γ -Ga, and (d) δ -Ga hemispherical NP on a sapphire substrate. Near-field distribution ($\log_{10}(\mathbf{E} ^2)$) of the (e) low and (f) high energy modes. The top panels show the plane containing the wave (\mathbf{k}) and electric field vector (\mathbf{E}). The bottom panels present $\log_{10}(\mathbf{E} ^2)$ in a plane lifted $h = 45$ nm above the substrate, near where most adsorbates will attach. Although the near-field maps correspond to δ -Ga, the near-field distribution is the same for all phases.	65
5.1	(a) Phase diagram of bulk Ga adapted from Ref. [5] and (b) extended pressure temperature phase diagram adapted from Ref. [11].	67
5.2	(a,d) Structure of the unit cell, (b,e) density of states DOS and (c,f) complex dielectric function ($\epsilon = \epsilon_1 + i\epsilon_2$) of Ga(II) (left) and Ga(III) (right)	69
5.3	Band diagram of Ga(III). The arrows indicated the interband transitions appearing in its complex dielectric function at 1.44 eV. With a color code in the arrows is indicated the intensity of the transition based on the evaluation of $M_{cv\mathbf{k}}$	71
5.4	(a) Imaginary and (b) real part of the effective dielectric function ($\epsilon = \epsilon_1 + i\epsilon_2$) of a mixture of Ga(II) and β -Ga obtained using Bruggeman effective medium approximation with different Ga(II) filling fractions $f_{\text{Ga(II)}}$ (dashed lines). With red and blue solid lines are represented the dielectric function of Ga(II) and β -Ga respectively.	72
5.5	Faraday number and Fröhlich frequency of the different Ga-phases. . .	73
5.6	Absorption cross-section (C_{abs} , blue line) and near-field enhancement averaged $\langle \mathbf{E} ^2 \rangle$ red line) over the surface of (a) Ga(II) and (b) Ga(III) $R = 60$ nm hemispherical NPs on an infinite sapphire substrate embedded in air. Respective near-field distributions ($\log_{10}(\mathbf{E} ^2)$) of their (c, e) low and (d, f) high energy modes. Red and blue arrows indicate the electric field (\mathbf{E}) and wave vectors (\mathbf{k}), respectively.	74
5.7	(a) Reflectance spectra at normal incidence of a layer $h = 150$ nm thick made of the different Ga-phases on a sapphire substrate. (b) Reflectance spectrum at normal incidence of a layer $h = 150$ nm thick made of a mixture of β -Ga and Ga(II) on a sapphire substrate with different Ga(II) filling fractions $f_{\text{Ga(II)}}$	75

-
- 6.1 (a) the C_{abs} spectrum calculated for a 52 nm radius Ga hemisphere on a Al_2O_3 substrate and (b) the $\langle\epsilon_i\rangle$ spectrum measured on a sample of Ga hemispheres deposited on a Al_2O_3 substrate whose mean radius $\langle R \rangle$ has been estimated to be 55 nm attending to the AFM measurements. 82
- 7.1 Faraday number (Fa) for different metals. The blue dot represents the resonant energy (Fröhlich frequency, frequency at which $Re(\epsilon) = -2$ [12]) and the shadowed region the exciting photon energies above 3 eV. The blue solid line represents the range of energies studied in each case (this depends on the optical constants available in the literature [13–15, 4]). 85
- 7.2 Real (solid line) and imaginary (dashed line) parts of the complex dielectric function ($\epsilon = \epsilon_r + i\epsilon_i$) of Al, Mg, Ga, Rh (left) and their corresponding oxides (right) as a function of the photon energy of the incident beam. The values of the complex dielectric functions have been taken from different sources from the literature [16, 13, 4]. 91
- 7.3 Spectral enhancement of the local intensity averaged over the NP surface $\langle|E|^2\rangle$ (left column) and the absorption cross-section C_{abs} for equivalent tripod stars ($l = 10$ nm; $w = h = 5$ nm), cubes ($L = 8.1139$ nm) and spheres ($R = 5.0335$ nm) composed of Al + Al_2O_3 , Mg + MgO, Ga + Ga_2O_3 and Rh, illuminated under normal incidence. 92
- 7.4 $|E|^2$ maps (logarithmic scale) at $E = 3.82$ eV ($\lambda = 325$ nm, HeCd laser) for Rh (top row) and Ga + Ga_2O_3 (bottom row) tripod stars ($l = 10$ nm; $w = h = 5$ nm), cubes ($L = 8.1139$ nm) and spheres ($R = 5.0335$ nm). 93
- 8.1 The two analyzed scattering geometries: a) Isolated spherical geometry, b) Hemispherical geometry on a dielectric substrate. ($R = 40$ nm, R_{core} will range from 20 nm to 40 nm). 99
- 8.2 Real (solid line) and imaginary (dashed line) part of the dielectric function for (a) Al, Mg, and Ga and (b) their corresponding oxides. . . 100

- 8.3 (a) Absorption efficiency, Q_{abs} , of a core-shell spherical (left column) and a hemispherical NP (right column), for Mg/MgO (first row), Al/Al₂O₃ (second row) and Ga/Ga₂O₃ (third row). The particle total radius is $R = 40$ nm while the core radius varies from $R_{core} = 20$ to 40 nm. (b) 2D color map of the normalized absorption efficiency as a function of the wavelength and the core radius R_{core} for Mg/MgO (first row), Al/Al₂O₃ (second row) and Ga/Ga₂O₃ (third row) spherical (right column) and hemispherical on substrate NPs (right column). 102
- 8.4 Local electric field distribution for an isolated core-shell spherical and hemispherical nanoparticle for each metal, with $R = 40$ nm, $R_{core} = 30$ nm, and a 10 nm thick oxide shell. The illuminating wavelength in each case corresponds to the one that makes Q_{abs} maximum. 104
- 8.5 Evolution of $\langle |\mathbf{E}_{core}|^2 \rangle / \langle |\mathbf{E}_{shell}|^2 \rangle$ for each metal as a function of the metallic core size for a spherical and hemispherical nanoparticle of radius 40 nm at the wavelength at which $\langle |\mathbf{E}_{shell}|^2 \rangle$ takes its maximum in the electric dipolar resonance. 105
- 8.6 Evolution of the peak value (top) and location (bottom) for the Q_{abs} (circles) and the $\langle |\mathbf{E}|^2 \rangle$ (squares) for spherical (red) and hemispherical (blue) nanoparticles of Mg/MgO, Al/Al₂O₃ and Ga/Ga₂O₃. 107
- 9.1 (a,c) Real time evolution of the imaginary part of the pseudodielectric function ($\langle \epsilon \rangle = \langle \epsilon_r \rangle + \langle \epsilon_i \rangle$) for Mg NPs grown on Al₂O₃; (a) shorter Mg deposition time corresponding to smaller NPs, and (c) larger Mg deposition time corresponding to higher density and larger NPs as well as aggregates of NPs. (b,d) Mg NPs LSPR quenching due to air exposure. (e) Scheme of the geometry in which electromagnetic simulations have been performed: Mg/MgO core-shell spherical NP of total radius $R = 50$ nm. (f) 2D color map of the spectral absorption efficiency (Q_{abs}) of a Mg/MgO core-shell as a function of the MgO shell thickness. 113
- 9.2 AFM topography of Mg NPs of different R_{p-v} (value is indicated) soon after the deposition and after air exposure. Different scan size images after air exposure are reported to better show the different shape of those crystals. The phase images of both samples after air exposure, indicating the different chemical nature of those crystals are also reported. Larger size optical microscopy images are also shown to put in evidence the distribution of those different shape microcrystals. 114

- 9.3 (a) Raman spectra taken on the crystal (blue line, blue circle in the inset) and on the Al_2O_3 substrate (red line, red circle in the inset). With red, yellow and blue arrows are indicated those peaks assigned to Al_2O_3 , MgSO_4 and MgFAl_2 . (b) FTIR absorbance spectra. In yellow is shadowed ν^3 band of SO_4 in MgSO_4 . (c) XPS spectra of the F1s, O1s, MgSO_4 and Mg2p photoelectron core level. As an inset in the F1s spectra is indicated the possible Mg-F-O arrangement. 116
- 9.4 (a) Oxygen, (O), fluorine (F), and sulfur (S), to Mg ratios measured by XPS for the two representative samples in Fig. 9.2; (red and blue colours refer to samples (a) and (b)). (b) Mean peak-to-valley distance (R_{p-v}) values measured through AFM in both samples after deposition as function of the sampled area. 117
- 9.5 (a) *In-situ* ellipsometry monitoring at 2.75 eV of the real (blue line) and imaginary part (red line) during the H_2 plasma exposure. (b) Experimental real (blue line) and imaginary (red lines) parts of pseudodielectric function of a sample of oxidized Mg NPs before (solid line) and after (dashed line) hydrogenation. (c) Micrography of the surface of the sample before and after the hydrogenation process. (d) XPS survey spectra of the sample before (top) and after (bottom) the hydrogenation process. 118
- 9.6 (a) Scheme of the geometry in which the electromagnetic simulations have been performed: Mg/MgO core shell of total radius $R = 50$ nm and core radius R_c . The MgO shell is converted progressively into $\text{MgSO}_4/\text{MgF}_2$ until it is completely consumed (100% $\text{MgSO}_4/\text{MgF}_2$ shell). (b) Near-field $|\mathbf{E}|$ map for Mg/MgO/MgF₂ multilayered sphere with $R_c = 5$ and 25 nm and MgF₂ shell thickness of 5 nm. With arrows are indicated incident electric field \mathbf{E} polarization (red) and propagation direction $|\mathbf{k}|$ (yellow). (c,d) Spectral shift ($\Delta\lambda$) of the LSP dipolar resonance as the MgO shell is converted to $\text{MgSO}_4/\text{MgF}_2$ with respect to the spectral position of the 100% MgO shell. This calculation has been performed for different values of R_c while keeping the total radius fixed to $R = 50$ nm. 120

- 9.7 (a) Scheme of the geometry in which the colorimetric simulations have been performed: multilayer system constituted by an infinite Al_2O_3 substrate, a Mg layer of thickness h , a layer of MgO which is converted in $\text{MgSO}_4/\text{MgF}_2$ and air as surrounding medium. The total thickness of the Mg and MgO layers have been fixed to 50 nm. (b-d) Color coordinates in $L^*a^*b^*$ space of Mg thin films with thickness (b) $h = 5$ nm, (c) and $h = 10$ nm and (d) $h = 20$ nm covered by MgO layer converted progressively into MgF_2 and MgSO_4 . The color of each dot corresponds to the color of the film. (e,f) Color difference ΔE between the 100% MgO layer and the progressive conversion into (e) MgSO_4 and (f) MgF_2 122
- 10.1 Complex dielectric function ($\epsilon = \epsilon_r + i\epsilon_i$) of (a) Mg [13] and (b) MgO [13] and $\alpha\text{-MgH}_2$ [17]. (c) Experimental complex pseudodielectric function ($\langle\epsilon\rangle = \langle\epsilon_r\rangle + i\langle\epsilon_i\rangle$) of a layer of Mg before (blue line) and after exposure (yellow line) to a H_2 plasma. As a reference, the dielectric function of Mg (red line) from Ref. [13] is also plotted (d) *In-situ* ellipsometry monitoring at 2 eV of the real (blue line) and imaginary part (red line) of the pseudodielectric function during the H_2 plasma exposure. Reflectance color map as a function of the photon energy and the (e) Mg and (f,g) MgH_2 layer thickness under normal incidence. The multilayer configuration in each case is presented underneath. 129
- 10.2 (a) Real time evolution of the imaginary part of the pseudodielectric function ($\langle\epsilon\rangle = \langle\epsilon_r\rangle + i\langle\epsilon_i\rangle$) for Mg NPs grown on Al_2O_3 . With arrows are indicated the evolution in time of the two LSPRs. As inset are shown AFM images of the samples under study. (b) Mg LSPR damping by air exposure and oxidation. (c) *In-situ* ellipsometry monitoring at 3 eV of the real (blue line) and imaginary part (red line) during the H_2 plasma exposure at different temperatures. (d) Experimental pseudodielectric function of a sample of oxidized Mg NPs before and after hydrogenation, and its evolution after air exposure. Absorption efficiency color map as a function of the photon energy and the (e) Mg and (f,g) MgH_2 shell thickness. The core-shell configuration in each case is presented underneath. The NPs are placed in a medium with refractive index $n_{med} = 1.5$ to take into account the effect of the substrate and the rest of the NPs in the sample. 133

10.3	(a) XPS spectra of the MgKLL Auger line, and of the Mg2s and O1s photoelectron core level of the Mg NPs sample before and after hydrogenation, both after air exposure for 5h. (b) Raman spectra of Mg nanoparticles before and after H ₂ plasma exposure.	134
10.4	Scheme of the heterolytic -Mg(H)-O(H)- chemisorption of hydrogen on MgO surfaces.	135
11.1	Diagram of a nanocube. It is illuminated by a monochromatic plane wave propagating (\vec{k}) along the Z-axis with either P- or S-polarization.	139
11.2	Real (solid line) and imaginary (dashed line) parts of the complex relative permittivity (ϵ) of Ag (blue), Ag ₂ O (yellow) and Rh (red) as a function of the photon energy of the incident beam.	140
11.3	Absorption cross-section (C_{abs}) (left column) and spectral electric field intensity ($\langle \mathbf{E} ^2 \rangle$) averaged over the NP's closed surface (right column) for spheres ($R = 18.6$ nm), disks ($R = h = 20.5$ nm), and cubes ($L = 30$ nm) composed of Rh (red) or Ag (blue) illuminated under normal incidence, and embedded either in air.	141
11.4	UV-Vis normalized extinction spectra (a) experimental and (b) theoretical of monodisperse Rh nanocubes embedded in ethanol with their corresponding TEM images. The average sizes are: (i) 15, (ii) 21, (iii) 27, (iv) 39, (v) 47 and (vi) 59 nm respectively. The scale bars of the inset images are 20 nm.	142
11.5	Relationship of size and LSPR energies from experimental measurements (red circles) and numerical simulations (blue circles) of Rh NCs in ethanol. The blue line is a linear fitting of the simulated results.	143
11.6	(a) Absorption cross-sections (C_{abs}) of edge length $L = 30$ nm Rh NCs with rounded edges and corners with a curvature radii R_c varying from 0 (perfect cube) to 15 nm (perfect sphere). (b) Local field enhancement ($ \mathbf{E} ^2$) averaged over the corners and edges (where charge is most concentrated) of the NC with different R_c . (c) Local field enhancement in logarithmic scale ($ \mathbf{E} ^2$) over the surface of the different NCs when illuminated with the corresponding resonant wavelength.	144
11.7	Absorption cross-sections (C_{abs}) spectra of (a) cubes with $R_c = 5$ nm with the same volume as those with $L = 30$ nm and R_c indicated by the legend and (b) cubes with the same volume as a cube with $L = 30$ nm and $R_c = 5$ nm, but with a R_c given by the legend.	145

11.8	(a) Surface charge distribution (σ) over Rh NCs with rounded edges and tips with a curvature radii R_c when illuminated at the resonant wavelength. The red/blue regions represent positive/negative charge densities. (b) Normalized values of σ averaged over the edges and corners, and (c) over the flat faces of the NCs.	145
11.9	(a) Absorption cross-sections (C_{abs}) of $L = 30$ nm and $R_c = 2$ nm Rh NCs as a function of concave/convex deformation parameter d indicated in the legend. (b) Local field enhancement ($ \mathbf{E} ^2$) averaged over the corners and edges of NC with different d . (c) Local field enhancement in logarithmic scale ($ \mathbf{E} ^2$) over the surface of the different NCs when illuminated at resonance.	147
11.10	(a) Surface charge distribution (σ) over concave and convex Rh NCs with $L = 30$ nm and $R_c = 2$ nm when illuminated at resonance. The red/blue regions represent positive/negative charge densities. Normalized values of σ averaged over (b) the edges and corners, and (c) over their deformed faces of the NCs.	148
11.11	(a) Absorption cross-section (C_{abs}) of a $L = 30$ nm and $R_c = 2/10$ nm (solid/dashed line) Rh NC under normal incidence with a P-polarization beam on substrates with different refractive indexes. (b) averaged over the corners and edges in the bottom (contact with the substrate, blue line) and top (red line) faces of the cube on a glass ($n = 1.5$) and sapphire ($n = 1.78$) substrates. (c) Logarithmic scale near-field maps for $R_c = 2/10$ nm Rh NC (top/bottom) on sapphire substrate ($n = 1.78$) at $E = 4.4/5.6$ eV and $E = 6.4/7.2$ eV.	149
11.12	(a) Absorption cross-section (C_{abs}) of a $L = 30$ nm and $R_c = 2$ nm Rh (dashed line) and Ag (solid line) NC under normal incidence with a P-polarization beam on substrates with different refractive indices. The shadowed region corresponds to the UV range. (b) Absorption cross-section (C_{abs}) for $L = 5$ nm Rh and Ag (with 1 nm Ag_2O shell). The vertical lines indicate two commercial wavelengths (460 nm (2.7 eV) and 365 nm (3.4 eV), respectively).	151

- 12.1 Real (solid line) and imaginary (dashed line) parts of the dielectric function ($\epsilon = \epsilon_1 + i\epsilon_2$) of (a) AlP [18], (b) AlAs [19], (c) AlN [20], (d) diamond, (e) CeO₂ [21], (f) TiO₂ [22], (g) Al, (h) Rh [13] and (i) the HRI taken as a reference: Si (blue), GaAs (yellow) and Ge (red)[13]. The region in which $\epsilon_2 < 1$ and $\epsilon_1 > 4$ is shadowed in grey. In the case of the reference materials (Si, Al and Rh) the shadowed region indicates the UV spectral range. 159
- 12.2 Near-field enhancement averaged over the surface $\langle |\mathbf{E}|/|\mathbf{E}_0| \rangle$ of spheres with radius R (between 30 and 90 nm). A white dashed line represents the energy where $\epsilon_2 = 1$, and a white solid line indicates the energy where we consider the UV regime starts, 3 eV. 160
- 12.3 (a) Photon energies where the zero-backward condition holds (E_{ZB}), (b) scattering efficiency Q_{sca} at the photon energy of the zero-backward condition, (c) forward to backward intensity ratio I_{Fwd}/I_{Bck} at the zero-backward condition and (d) zero backward efficiency, Q_{ZB} , for spheres of radius R (between 30 and 90 nm) made of different materials. 162
- 12.4 Electric field enhancement $|\mathbf{E}|/|\mathbf{E}_0|$ (blue line, left axis) and temperature difference with respect to ambient temperature ΔT (red line, right axis) at the center of the gap of (a) Al/Al₂O₃, (b) TiO₂ and (c) diamond dimers. The analyzed dimer configuration is shown as inset in (a): a dimer of spheres of $R = 70$ nm with gap = 10 (dashed line) and 20 nm (solid line), illuminated with a plane wave linearly polarized along the dimer axis. 164
- 12.5 Near field $|\mathbf{E}|/|\mathbf{E}_0|$ (top row) and temperature difference ΔT (bottom row) maps for a diamond and Al/Al₂O₃ dimers with gap = 20 nm. Both dimers are illuminated at resonance (photon energy indicated as a inset), with a p -polarized beam \mathbf{E} and wave vector \mathbf{k} . E_{photon} corresponds to the photon energy of the illuminating beam. The chosen values of E_{photon} are those that produce the maximum near-field enhancement at the center of the gap. 165

List of tables

4.1	Reference configuration, cutoff radii and matching radius between the full core charge and the partial core charge for the pseudopotentials used in the study.	50
4.2	Soft-confinement pseudopotential parameters.	50
4.3	Measured d -spacings for Ga samples and d -spacings from ICSD database.	53
4.4	Lattice constants and structural parameters of α -Ga, β -Ga, γ -Ga and δ -Ga.	55
4.5	R -square coefficient of determination for fitting the experimental values with the imaginary part of the dielectric constant of α -Ga/ β -Ga (sample Ga#1) and α -Ga/ γ -Ga (sample Ga#2) to those calculated through Brueggemann EMT using a filling fraction of the α -phase f_α . These fittings are shown in Figs. 4.4(b,c) in the main text.	60
4.6	R -square coefficient of determination for fitting the experimental values with the imaginary part of the dielectric constant of sample Ga#1 and sample Ga#2 with those calculated through a weighted average of α -Ga and l -Ga using a filling fraction of the α -phase f_α . This methodology is used in Ref. [23] to model the dielectric function of solid Ga	60
5.1	Theoretical lattice constants, structural parameters and atomic coordinates of Ga(II) and Ga(III). Some experimental values are added for reference.	70
5.2	Reflectance at normal incidence of a layer $h = 150$ nm thick made of the different Ga-phases on a sapphire substrate at 1 and 6 eV.	76
7.1	Percentage of metal content in each of the studied nanoparticles.	92
12.1	Photon energy at which $\epsilon_2 < 1$ for each of the selected materials.	158

List of Acronyms and Abbreviations

AFM	Atomic Force Microscopy
FEM	Finite Elements Method
FDTD	Finite-Difference Time-Domain
FTIR	Fourier Transform Infrared Spectroscopy
HRID	High Refractive Index Dielectric
LSP	Localized Surface Plasmon
LSPR	Localized Surface Plasmon Resonance
NC	Nanocube
NIR	Near Infrared
NP	Nanoparticle
SE	Spectroscopic Ellipsometry
SERS	Surface-Enhanced Raman Spectroscopy
SPP	Surface Plasmon Polariton
UV	Ultraviolet
VIS	Visible
XPS	X-Ray Photoelectron Spectroscopy

Chapter 1

Introduction

1.1 Motivation

One of the biggest challenges faced by today's society is to overcome the irreversible risks and consequences of climate change. According to data provided by NASA [24], CO₂ levels in Earth's atmosphere are the highest of the last 650 years, 16 out of the 17 warmest years on records have occurred since 2001 and the sea level has increased 178 mm in the last 100 years. These are only some of the shocking facts that NASA offers in their official website. Since the beginning of the industrial revolution, green house effect gases like carbon dioxide, CO₂, methane, CH₄, or nitrous oxide, N₂O have been released with hardly any regulation. If humanity does not push forward to remedy this situation, Earth's temperature and sea level will keep rising, the Arctic will disappear, droughts will be more frequent, and the precipitation patterns will change.

The solution to these problems goes through the development of cleaner energies and more efficient industrial processes. From this starting point arises the field of photocatalysis, which proposes a mechanism in which chemical reactions are assisted by light, like for example, that coming from the sun [25, 26]. By exciting with low-intensity sunlight photons the localized surface plasmons (LSPRs) in metallic nanoparticles (NPs), e.g., NPs made of rhodium, magnesium or gallium, it is possible to drive commercially important catalytic reactions efficiently. This is the basis of plasmonic assisted photocatalysis or plasmonic photocatalysis. This field is presented as an alternative to thermal catalysis, in which high temperatures and pressures are needed, leading to a very low efficiency due to the significant energy input required to run chemical reactions that are inherently exothermic [27, 28].

Two of the main challenges that the field of photocatalysis faces in order to overcome the effects of climate change are: the CO₂ catalyzation and assisting the so-called hydrogen economy.

Carbon dioxide, CO₂, is one of the most abundant greenhouse gases. It is released through human activities, such as burning fossil fuels and deforestation, as well as by natural processes, like volcanic eruptions. The CO₂ in the atmosphere has risen from 278 ppm at the beginning of the industrial revolution to >400 ppm today [24]. Rising atmospheric CO₂ concentrations can be reduced by reacting ambient CO₂ with renewably generated hydrogen, H₂. However, product selectivity is essential to ensure production of hydrocarbons such as methane, CH₄, instead of the kinetically preferred product carbon monoxide, CO. Very recently, Rhodium, Rh, NPs have been demonstrated to be photocatalytic. They simultaneously lower activation energies and exhibit strong product photo-selectivity. CO₂ hydrogenation on Rh at atmospheric pressure proceeds through two competing pathways: CO₂ methanation (CO₂ + 4H₂ → CH₄ + 2H₂O) and reverse water gas shift (CO₂ + H₂ → CO + H₂O). It has been demonstrated that illumination of the Rh nanoparticles not only reduced activation energies for CO₂ hydrogenation ≈ 35% below thermal activation energies, it also produces a strong selectivity towards CH₄ over CO [27]. Therefore, the design and optimization of Rh nanostructures to assist this photocatalytic process can have a real impact on the reduction of atmospheric CO₂ levels.

Plasmonic photocatalysts and plasmonic nanostructures has also been presented as a key piece for the looming hydrogen economy [29, 30]. This concept is based in the efficient generation of H, its purification, storage, distribution and usage in reduction of fossil fuels. Indeed, H would be an ideal synthetic fuel because it is light-weighted, highly abundant and its oxidation produces water [29, 31]. Metallic NPs can assist three of the processes involved in the hydrogen economy:

- Hydrogen production: although H is the most abundant element in Earth, it does not exist in its pure form [31]. It has to be separated from other chemical compounds such as water or hydrocarbons, or dissociated from H₂ molecules. Plasmonic photocatalysis has been presented as a very promising tool for driving chemical reactions that allow the separation of H from other compounds [32–34]. For instance, several nanostructures have been reported for H production through the water splitting reaction (2H₂O → 2H₂ + O₂) [34] or H₂ dissociation [32, 33].
- Hydrogen sensing: in the recent years, Pd and Au NP based optical H sensors have been reported in the literature [29, 35, 36, 35]. These NPs are capable of

incorporating H in their crystal lattice while modifying their electronic structure [37]. These modifications lead to changes of the optical properties that can be monitored through the spectral shifts of their LSPRs. In this way, the H content in the nanoparticle can be correlated with the spectral shift of its LSPRs [35, 36].

- Hydrogen storage: as H is incorporated in the NPs, not only they become sensors but also reservoirs [29, 30]. The H storage in the crystal lattice can be freed under some specific experimental conditions. Metal hydrides have been recognized as safe and efficient ways for advancing in the solution of the hydrogen storage problem [30].

In this context and recently, a lot of attention has been paid to magnesium (Mg). Magnesium has been subjected to extensive investigation due to their potential role in the hydrogen-based economy. Mg itself is an abundant low-cost material, and its hydride, MgH_2 , has relatively high storage capacity, i.e., MgH_2 is able to absorb up to 7.6 wt % of hydrogen gas. However, there are critical drawbacks that limit its actual use in the looming hydrogen technology: (i) its hydrogen desorption temperature (higher than 300°C), (ii) sluggish kinetics of the hydrogen adsorption/desorption processes, mainly, due to the low diffusion rate of H into MgH_2 , (iii) low activity in the dissociation of H_2 , and (iv) the formation of an $\text{MgO}/\text{Mg}(\text{OH})_2$ overlayer when exposed to ambient conditions that inhibit the dissociation of H_2 and the diffusion of H into the bulk [38, 39]. It has demonstrated that these problems can be overcome by alloying or doping Mg with other metals [30]. For example, it has been demonstrated that alloying Mg with gallium, Ga, improves Mg storage capacity [40].

Addressing and predicting the behavior of plasmonic nanosystems for photocatalytic applications requires of new materials whose optical constants can not be directly assessed through experimental techniques. The performance of computers has dramatically increased in the last years, both by improvements in the transistor technology and by the creation of large clusters of computing units that allow simulating massive systems. As a benefit of this evolution, it has become possible to calculate from first-principles methods the optical properties of materials computationally with the structural information of the material's lattice and electronic properties as starting points. In this dissertation, we tackle the problem of Ga polymorphs. Gallium is material of wide interest not only for its capability of improving the H storage capacity of Mg nanosystems. It is also non-toxic, biocompatible, flexible, stretchable, and deformable metal at room temperature with low viscosity and excellent thermal and electrical conductivities [41, 42]. Its plasmonic response has been demonstrated to span

from the near-infrared to the UV [43]. These properties have already been exploited in chemical sensing (using UV surface enhanced Raman spectroscopy)[44], molecular sensing [45] or delivery of cancer therapy drugs (using transformable liquid-metal nanospheres composed of a liquid-phase gallium core and a thiolated polymeric solid shell) [41].

It has been demonstrated that Ga can exist in different forms depending on the size of the nanosystem, the temperature and pressure [5, 7]. In the literature it has been reported the existence of α -, β -, γ and δ -Ga phases at atmospheric pressure, each of it with a different dielectric function that allow a wide variety of phase-change plasmonic systems [46–48] whose accurate electromagnetic modeling has been hampered by the lack of information about the dielectric profiles of each phase. Experimentally, isolating each phase for measuring its optical constants is not feasible. Therefore, first-principles calculations is a tool that allows the complete optical characterization of each of the Ga phases.

The plasmonic UV response of Rh, Mg and Ga not only can be useful for photocatalytic applications. Other areas of research, like biosensing, can also take advantage of the UV plasmonic response of these materials[12, 49]. However, until very recently, most of the plasmonic studies have been performed in the visible and near-infrared using silver and gold nanostructures [1], as seen in Fig. 1.1.

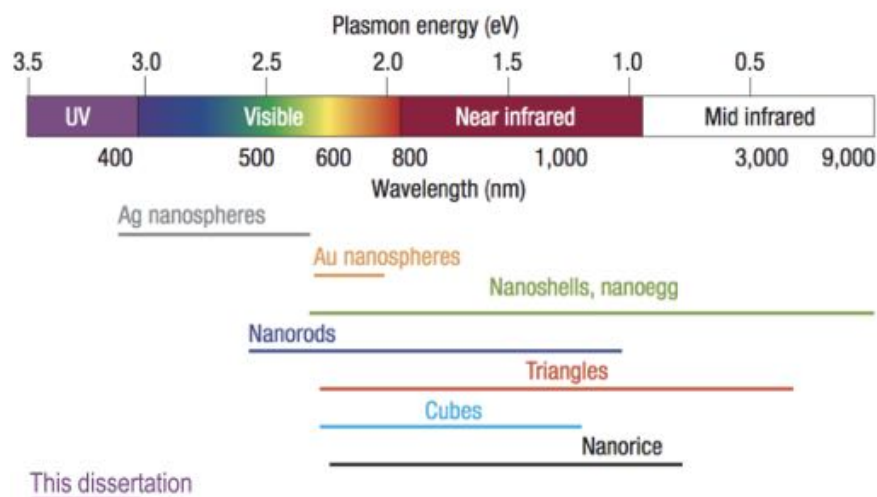


Figure. 1.1 Nanoparticle resonances for a range of plasmon resonances for a variety of particle morphologies made of gold and silver. Image adapted from Ref. [1].

Therefore, extending nanoplasmonics to the UV range has become a topic of interest due to the new challenges arising in specific areas. As aforementioned, not only photocatalysis can benefit from UV plasmonics. Biosensing is another area that can take advantage from the development of UV plasmonics. For instance, many biological compounds, such as nucleotide bases, nucleic acids or aromatic amino acids in cells, have absorption bands in the UV (below $\lambda = 300$ nm) [50]. By using hot spots excited by LSPRs in the UV, it is possible to improve surface-enhanced spectroscopy techniques (surface-enhanced Raman spectroscopy, SERS, tip-enhanced Raman spectroscopy, TERS, etc.) that ease the detection and recognition of these kinds of biomolecules [51–53]. Bioimaging techniques can also be improved through UV plasmonics. The optical resolution, i.e. the ability of an imaging system to resolve detail in a image, is ultimately limited by the diffraction limit. This limit, in turn, is proportional to the illuminating wavelength. Since UV light has a shorter wavelength than visible light, it allows reaching a higher imaging resolution than conventional optical devices.

A field that has not yet been opened in UV plasmonics is that related to high refractive index, HRI, dielectric materials. This field has experienced a huge development in the last decade for applications in the visible and near infrared [54]. Although, in general, metallic NPs exhibit good plasmonic performance their intrinsic Joule losses limit their use for some applications [55, 56]. To overcome this problem, a lot of attention has been paid to dielectric nanostructures made of HRI materials. HRI dielectric NPs show the “ability” of enhancing the electromagnetic field, just like metallic NPs, but with no localized heating [55, 56]. Moreover, these NPs manifest interesting scattering directionality properties: scattered radiation from a single HRI dielectric spherical nanoparticle can be concentrated either in the backward or forward scattering regions [57, 58]. Many semiconductor such as silicon, Si, or germanium, Ge, have been reported to have HRI properties in the visible and near infrared [59]. However, finding materials with HRI behavior in the UV remains a challenge.

1.2 Interdisciplinarity

In September 2015, Nature published an article entitled “Why interdisciplinary research matters” [60]. In it, it is claimed that to solve the biggest challenges facing society, scientists and social scientists must work together.

Theodore Brown, former vice-chancellor for research at the University of Illinois at Urbana–Champaign, back in 1983, put together a proposal to build an institute for interdisciplinary research. Brown argued that it would allow faculty members to

tackle bigger scientific and societal questions than they normally could. Since then, the interdisciplinary model has spread around the world, countering the trend towards specialization that had dominated science since the Second World War. As he said: “The problems challenging us today, the ones really worth working on, are complex, require sophisticated equipment and intellectual tools, and just don’t yield to a narrow approach” [61].

Taking this in mind, this dissertation has been conceived as an interdisciplinary work with the intention of merging together elements of chemistry, electromagnetism and solid state physics to tackle problems in photocatalysis and UV plasmonics.



Figure. 1.2 Cover of Nature No. 7569.

1.3 Objectives

The objective of the current dissertation is to explore the UV plasmonic response of nanostructured systems made of unconventional materials and their role in photocatalysis. In order to accomplish such an ambitious task, the following objectives have to be fulfilled:

- Being able of calculating the dielectric function of arbitrary materials using first-principles calculations, specifically that of the different Ga polymorphs.
- Develop a methodology that merge chemical characterization, spectroscopic ellipsometry and optical modeling to study the interaction of H with nanostructured systems, in this case made of Mg.
- Study the main processes that nanoparticles made of the most extended materials used in UV plasmonics go through when exposed to ambient conditions.
- Model the plasmonic response of Rh nanostructures used in real photocatalytic processes.
- Establish a series of materials that, as Si or Ge in the visible and near-infrared, have high refractive index behavior in the UV.

1.4 Thesis Overview

Throughout this dissertation we have adhered to the following outline:

- A part dedicated to the theoretical foundations on which this dissertation is based, divided in two chapters:
 - A theoretical introduction about the interaction of light with matter, including a summary of the most widely used numerical methods to model this interaction.
 - An overview on the dielectric function of materials from classical to quantum theories, and experimental approaches.
- A part focused in the calculation of the dielectric function of novel materials divided in two chapters:
 - The calculation of the dielectric function of the different Ga polymorphs at atmospheric and high pressure.

- A part devoted to the electromagnetic simulations and experiments on plasmonic nanostructured systems in photocatalysis and UV applications. This part is divided in several chapters that include the following topics:
 - An overview on the experimental techniques used through this dissertation.
 - A review on the state-of-the-art of UV plasmonics.
 - An study on the effect of a growing oxide shell and tarnishing in NPs made of the most extended metals used for UV plasmonic applications.
 - An study of the interaction of H with Mg NPs.
 - An study on the plasmonic response of Rh nanocubes for photocatalysis applications.
 - A quest for materials with high refractive index behavior in the UV.
- In the final section, a summary of the main conclusions as well as some future perspectives are presented.

Chapter 2

Light and Matter

Scattering is a cornerstone concept that arises when dealing with the light-matter interaction. It involves phenomena in which the energy of light is redistributed in different directions after its interaction with matter. Scattering, together with its counterpart, absorption, are responsible with everyday phenomena such as the blue of the sky or the rainbow.

The study of the scattering phenomena at the nanoscale has led to discoveries of great impact such as the Localized Surface Plasmons (LSPs). LSPs are non-propagating excitations of the conduction electrons of metallic nanostructures coupled to an illuminating electromagnetic field. Under certain conditions, LSPs are able to intensify and confine the electromagnetic field around the nanoparticle in a dimension smaller than the wavelength of the incoming field. This phenomenon has found to be exploited in many areas of research that range from medicine, energy technologies, photochemistry, spectroscopy among others [62, 63].

Before analyzing the phenomenon of scattering at the nanoscale, it is necessary to set the equations that rule the propagation of light and its interaction with matter at the macroscopic level. For that reason, this chapter begins reviewing Maxwell's equations, which provide the physical and mathematical apparatus necessary to model these phenomena. Section 2.2 is devoted to a particular solution of Maxwell's equations: the plane waves. Section 2.3 is dedicated to the concepts of absorption, scattering and extinction, and how they can be quantified in systems composed of a collection or individual particles. Section 2.4 shows the exact solution of the problem *light scattering by a sphere* developed by Mie in 1908. Finally, section 2.5 is intended to give a short overview about state-of-the-art methods widely employed to solve the scattering problem by structures of arbitrary shape.

2.1 Maxwell's equations

Maxwell's equations govern the propagation and interaction of light with matter [64, 65]. In their differential form, they can be expressed as

$$\nabla \cdot \mathbf{D} = \rho \quad (2.1)$$

$$\nabla \times \mathbf{E} + \frac{\partial \mathbf{B}}{\partial t} = 0 \quad (2.2)$$

$$\nabla \cdot \mathbf{B} = 0 \quad (2.3)$$

$$\nabla \times \mathbf{H} - \frac{\partial \mathbf{D}}{\partial t} = \mathbf{J} \quad (2.4)$$

where \mathbf{E} is the electric field, \mathbf{D} the dielectric displacement, \mathbf{H} the magnetic field and \mathbf{B} is the magnetic induction. Both the charge density ρ and the current density \mathbf{J} are associated with the “free” charges.

The electric displacement \mathbf{D} and the magnetic induction \mathbf{B} represents how the medium reacts to the propagating electromagnetic field given by \mathbf{E} and \mathbf{H} . These magnitudes are related through

$$\mathbf{D} = \epsilon_0 \mathbf{E} + \mathbf{P} \quad (2.5)$$

$$\mathbf{H} = \frac{\mathbf{B}}{\mu_0} - \mathbf{M} \quad (2.6)$$

where \mathbf{P} and \mathbf{M} are the electric polarization and magnetization respectively. \mathbf{P} represents the average electric dipole moment per unit of volume and ϵ_0 is the permittivity of the free space. In analogy, \mathbf{M} represents the average magnetic dipole moment per unit of volume and μ_0 is the permeability of the free space.

However, eq. (2.1)-(2.6) are not enough to obtain a unique solution for the electric and magnetic fields from a given distribution of charges and currents. It is necessary to introduce the so-called constitutive relations. They contain the properties of the medium in which the electromagnetic field is propagating.

$$\mathbf{P} = \epsilon_0 \chi_e \mathbf{E} \quad (2.7)$$

$$\mathbf{J} = \sigma \mathbf{E} \quad (2.8)$$

$$\mathbf{M} = \chi_m \mathbf{H} \quad (2.9)$$

where χ_e and χ_m are the electric and magnetic susceptibility and σ is the conductivity. Equations (2.5) and (2.7) yield

$$\mathbf{D} = \epsilon \mathbf{E} \quad (2.10)$$

$$\mathbf{B} = \mu \mathbf{H} \quad (2.11)$$

being $\epsilon = (1 + \chi_e)\epsilon_0$ and $\mu = (1 + \chi_m)\mu_0$. ϵ is known as the relative permittivity of the medium, and it determines its response to the excitation by a electromagnetic field. This magnitude is in general represented by 2^{nd} rank tensor. However, for linear response and isotropic media can be expressed as an scalar magnitude. For now on, we will refer to the relative permittivity of the medium as the *dielectric function*. The parameter μ is the magnetic permeability and it is unity for non magnetic materials. The dielectric function and magnetic permeability describe the response of a material to an applied electric and magnetic fields respectively.

The electromagnetic field is required to satisfy the Maxwell equations at points where the permittivity and the permeability are continuous. However, as one crosses the boundary from one medium to another (e.g. from a particle to its surrounding medium or vice versa) there is, in general, a sudden change in these properties. This change occurs over a transition region with thickness of atomic dimensions. At such boundary, it is necessary to apply the following boundary conditions, which are in turn derived from the integral equivalents of the Maxwell's equations,

$$[\mathbf{E}_2(\mathbf{r}_0) - \mathbf{E}_1(\mathbf{r}_0)] \times \hat{\mathbf{n}} = 0 \quad (2.12)$$

$$[\mathbf{H}_2(\mathbf{r}_0) - \mathbf{H}_1(\mathbf{r}_0)] \times \hat{\mathbf{n}} = \mathbf{j}_s \quad (2.13)$$

$$[\mathbf{D}_2(\mathbf{r}_0) - \mathbf{D}_1(\mathbf{r}_0)] \cdot \hat{\mathbf{n}} = \sigma_s \quad (2.14)$$

$$[\mathbf{B}_2(\mathbf{r}_0) - \mathbf{B}_1(\mathbf{r}_0)] \cdot \hat{\mathbf{n}} = 0 \quad (2.15)$$

where the subscripts 2 and 1 represent the regions around and inside the particle. \mathbf{r}_0 is a point in the particle's surface and $\hat{\mathbf{n}}$ is the outward unitary vector directed normal to it. The *tangential component* of the \mathbf{E} is required to be continuous along a boundary separating media with different properties. The tangential component of \mathbf{H} is also continuous if there is no surface current \mathbf{j}_s . The *normal component* of the \mathbf{D} is continuous along the boundary separating two media if there is no surface charge density σ_s . In the case of the normal component of \mathbf{B} , it is required to be continuous across the boundary.

2.2 Plane Waves

The interaction of light with a non-charged ($\rho = \mathbf{J} = 0$) isotropic medium allow us to simplify eq. (2.1)-(2.6) [65]. Thus,

$$\nabla \cdot \mathbf{E} = 0 \quad (2.16)$$

$$\nabla \times \mathbf{E} + \mu \frac{\partial \mathbf{H}}{\partial t} = 0 \quad (2.17)$$

$$\nabla \cdot \mathbf{H} = 0 \quad (2.18)$$

$$\nabla \times \mathbf{H} - \epsilon \frac{\partial \mathbf{E}}{\partial t} = \sigma \mathbf{E} \quad (2.19)$$

Using the vector identity

$$\nabla \times (\nabla \times \mathbf{E}) = \nabla(\nabla \cdot \mathbf{E}) - \nabla^2 \mathbf{E} \quad (2.20)$$

we obtain the wave equation for a electric field plane wave propagating in an energy absorbing medium,

$$\nabla^2 \mathbf{E} = \epsilon \mu \frac{\partial^2 \mathbf{E}}{\partial t^2} + \sigma \mu \frac{\partial \mathbf{E}}{\partial t} \quad (2.21)$$

We will refer to the conductivity σ as *optical conductivity*. This is because the energy absorption with which we are concerned is that arising from electronic transitions accompanying photon absorption. A similar wave equation is obtained for the magnetic field \mathbf{H} .

The plane wave is a possible solution of eq. (2.21). This type of wave is characterized for having wave-fronts (surfaces of constant phase) and constant amplitude that are infinite parallel planes defined by a wave vector \mathbf{k} . The wave vector points in the direction of propagation. The plane waves are suitable for describing light coming from a distant source. In addition, every electromagnetic field can be expressed as a sum of plane waves.

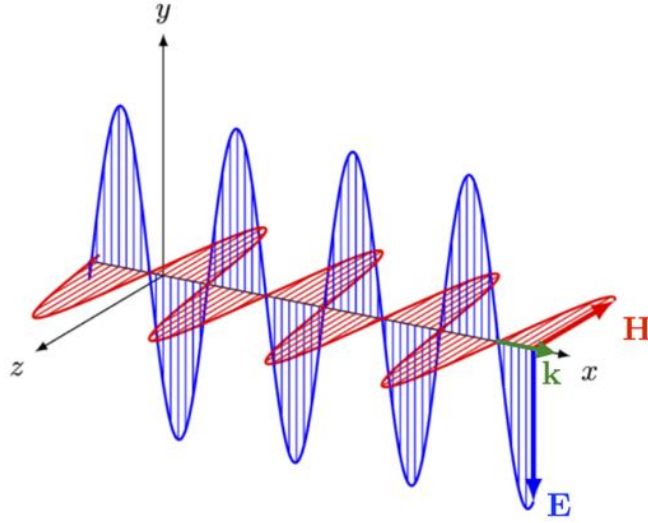


Figure. 2.1 A plane electromagnetic wave, with its electric \mathbf{E} and magnetic fields \mathbf{H} oscillating in directions perpendicular to each other and to the direction of propagation \mathbf{k} .

A monochromatic electromagnetic field expressed as plane waves propagating in an isotropic medium can be expressed as

$$\mathbf{E} = \mathbf{E}_0 \exp i(\mathbf{k} \cdot \mathbf{r} - \omega t) \quad (2.22)$$

$$\mathbf{H} = \mathbf{H}_0 \exp i(\mathbf{k} \cdot \mathbf{r} - \omega t) \quad (2.23)$$

where \mathbf{E}_0 and \mathbf{H}_0 are the amplitudes of the electric and magnetic fields. They are perpendicular to each other, and perpendicular to the direction of propagation \mathbf{k} (transverse waves). ω is the angular frequency of the electromagnetic field. The electric field modulus is $c = 1/\sqrt{\epsilon_0\mu_0}$ times higher than that of the magnetic field. Therefore, for now on, we will restrict our analysis to the electric field.

By introducing eq. (2.22) into (2.21) it is obtained that

$$\mathbf{k}^2 = \mu\omega^2 \left(\epsilon + i\frac{\sigma}{\omega} \right) \quad (2.24)$$

Now, we define a complex refractive index N such that

$$\mathbf{k} = \frac{\omega}{c} N \hat{\mathbf{n}} = \frac{\omega}{c} (n + ik) \hat{\mathbf{n}} \quad (2.25)$$

where n is the refractive index, k is the extinction coefficient and $\hat{\mathbf{n}}$ an unitary vector pointing in the propagation direction. Now, it is possible to rewrite eq. (2.22) as

$$\mathbf{E} = \mathbf{E}_0 \exp\left(-k\frac{\omega}{c}(\hat{\mathbf{n}} \cdot \mathbf{r})\right) \exp\left(i\left(n\frac{\omega}{c}(\hat{\mathbf{n}} \cdot \mathbf{r}) - \omega t\right)\right) \quad (2.26)$$

The first exponential describes the attenuation of wave amplitude with distance. The second exponential factor describes the propagation of plane wave with phase velocity c/n .

The expressions for ϵ and σ can be obtained in terms of n and k . Thus,

$$\epsilon = \frac{(n^2 - k^2)}{\mu} \quad \frac{\sigma}{\omega} = \frac{2nk}{\mu} \quad (2.27)$$

We define the complex dielectric function ϵ as $\epsilon = \epsilon_1 + i\epsilon_2 = N/\mu$. Thus,

$$\epsilon_1 = \frac{(n^2 - k^2)}{\mu} \quad \epsilon_2 = \frac{2nk}{\mu} = \frac{\sigma}{\omega} \quad (2.28)$$

2.2.1 Reflection and Transmission: Fresnel Equations

Transmission and reflection of plane waves at a boundary between two media are governed by the Fresnel equations [64]. Let's consider a plane wave incident on the boundary between two media. This apparently simple situation, is the basis of very advanced methods (e.g., ellipsometry techniques) for measuring the dielectric function of materials.

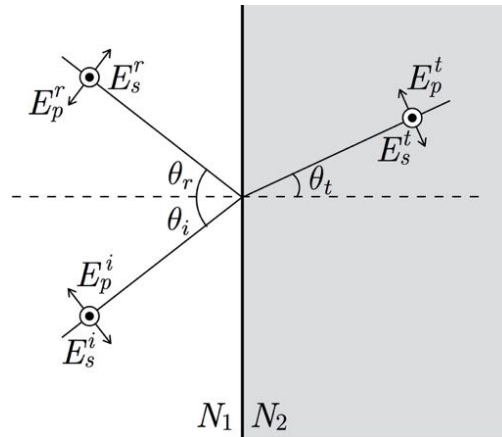


Figure. 2.2 Incident electromagnetic field \mathbf{E}^i on a planar boundary. \mathbf{E}^t and \mathbf{E}^r represent the transmitted and reflected fields. With an arrow and a dot are represented the parallel (p -waves) and perpendicular (s -waves) components of the fields with respect to the plane of incidence.

Let's consider a plane wave propagating through a non-absorbing medium with refractive index $N_1 = n_1$ incident on another medium, whose refractive index is $N_2 = n_2 + ik_2$, at an angle θ_i . The boundary between both media is planar (see Fig. 2.2). The incident, reflected and transmitted fields are denoted \mathbf{E}^i , \mathbf{E}^r and \mathbf{E}^t respectively. θ_r is the reflection angle, and fulfills $\theta_i = \theta_r$. For the refraction angle, it can be considered the following relation (i.e., Snell's law),

$$\sin \theta_t = \frac{\sin \theta_i}{m} \quad (2.29)$$

where m is the relative refractive index between media, $m = \frac{N_2}{N_1}$.

Two different polarization states are considered: one parallel (p -wave) and another perpendicular (s -wave) to the plane of incidence. This plane contains the boundary normal and the propagation's direction. The distinction between s - and p -polarizations arises from the different boundary conditions for the perpendicular and tangential components of the electromagnetic field at the interface. The Fresnel coefficients for reflection (r) and transmission (t) for each polarization state is given by

$$r_p = \frac{E_p^r}{E_p^i} = \frac{\cos \theta_t - m \cos \theta_i}{\cos \theta_t + m \cos \theta_i} \quad t_p = \frac{E_p^t}{E_p^i} = \frac{2 \cos \theta_i}{\cos \theta_t + m \cos \theta_i} \quad (2.30)$$

$$r_s = \frac{E_s^r}{E_s^i} = \frac{\cos \theta_i - m \cos \theta_t}{\cos \theta_i + m \cos \theta_t} \quad t_s = \frac{E_s^t}{E_s^i} = \frac{2 \cos \theta_i}{\cos \theta_i + m \cos \theta_t} \quad (2.31)$$

The total reflectance R and transmittance T , or their s -/ p - components, can be easily obtained from the Fresnel coefficient through the following relations,

$$R_p = |r_p|^2, \quad R_s = |r_s|^2, \quad R = \frac{1}{2}(R_p + R_s) \quad (2.32)$$

$$T_p = |t_p|^2, \quad T_s = |t_s|^2, \quad T = \frac{1}{2}(T_p + T_s) \quad (2.33)$$

The reflectance R is defined as the ratio of the reflected irradiance to the incident one. Analogously, the transmittance T is the ratio of the transmitted irradiance to the incident one.

2.3 Absorption, Scattering and Extinction

Let's consider a single or a collection of particles placed in a homogeneous non absorbing medium [2]. The system is illuminated by a collimated monochromatic beam with no change in its intensity and polarization state (see Fig. 2.3). The rate at which

electromagnetic energy is received by a detector D aligned with the incident radiation from the particles is denoted by I . If the particles are removed, the power received by the detector is I_0 , where $I_0 > I$. The difference between $I_0 - I$ is due to absorption (i.e., transformation of the electromagnetic energy into other forms like heat) and scattering (i.e., diffusion of the electromagnetic radiation in other directions) by the particles. These two phenomena constitute what is known as extinction (extinction = absorption + scattering). The extinction is dependent on properties of both the material (size, shape, orientation, material, ...) of the particles and the illuminating beam (polarization state and wavelength).

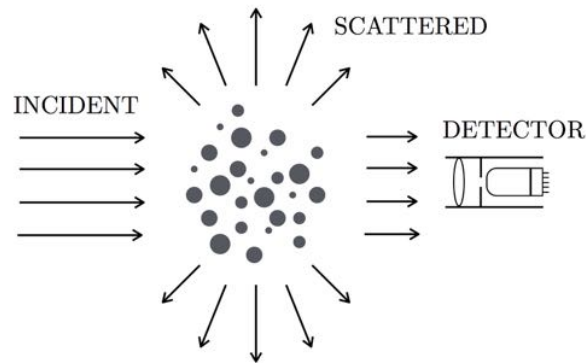


Figure. 2.3 Extinction by a collection of particles. Adapted from Bohren and Huffman [2].

2.3.1 Cross-Sections and Efficiency Factors

Cross-sections and efficiencies are two magnitudes widely used to describe the scattering and absorption characteristics of a particle or a collection of them [2]. To define the concept of cross-section let's consider a light beam incident on a particle embedded in a non absorbing medium. Part of the radiant power incident on the particle will be scattered in all directions, while the rest will go through it. The ratio of the total radiant power scattered by a particle in all directions, W_{sca} , to the radiant power incident on it, I_0 , is denoted the scattering cross section C_{sca} .

$$C_{sca} = \frac{W_{sca}}{I_0} \quad (2.34)$$

Similarly, the absorption cross-section, C_{abs} , can be defined as the ratio of the total radiant power absorbed by a particle, W_{abs} , to the radiant power incident on it, I_0 ,

$$C_{abs} = \frac{W_{abs}}{I_0} \quad (2.35)$$

Since the extinction cross-section, C_{ext} , represents the amount of radiant power removed from the incident beam, and taking into account eq. (2.34) and (2.35), C_{ext} can be expressed as

$$C_{ext} = \frac{W_{sca} + W_{abs}}{I_0} = C_{sca} + C_{abs} \quad (2.36)$$

It is worth mentioning that this cross-section is not equal to the geometrical one. Both of them are related through the efficiency factors, normally denoted by Q . The scattering, absorption and extinction efficiencies are the ratios of their respective cross-sections to the geometrical cross-section of the particle, e.g., in the case of the sphere πa^2 , being a its radius.

2.4 Scattering by a Sphere: Mie's Theory

2.4.1 General Formulation

Mie's Theory [2] provides a way to calculate analytically the field scattered and absorbed by spheres of arbitrary radius, a , and refractive index, N . By expanding the incident electromagnetic wave into spherical harmonics, Gustav Mie was able to solve the Maxwell equations for this kind of geometry taking into account the boundary condition between the sphere and the medium that surrounds it.

The solutions of the absorbed and scattered fields are developed into vector spherical harmonics. Both solutions depend on different coefficients which are called Mie coefficients. On the one hand, there are the scattering coefficients which are usually denoted as a_n and b_n . On the other hand, there are the coefficients related to the field inside the sphere, c_n and d_n .

For a linear, homogeneous and isotropic medium, the electromagnetic field must satisfy the Helmholtz equation

$$\nabla^2 \mathbf{E} + k^2 \mathbf{E} = 0 \quad \nabla^2 \mathbf{H} + k^2 \mathbf{H} = 0 \quad (2.37)$$

where \mathbf{E} and \mathbf{H} are the electric and magnetic fields and $k = \frac{2\pi n}{\lambda}$, being n the refractive index of the medium, and λ the wavelength of the electromagnetic field.

If the electromagnetic field travels through a free charge medium, the divergence of the electric and the magnetic field is zero

$$\nabla \cdot \mathbf{E} = 0 \quad \nabla \cdot \mathbf{H} = 0 \quad (2.38)$$

and the relation between the electric and magnetic field is given by

$$\nabla \times \mathbf{E} = i\omega\mu\mathbf{H} \quad \nabla \times \mathbf{H} = i\omega\epsilon\mathbf{E} \quad (2.39)$$

where i is the imaginary unit, ω the angular frequency of the electromagnetic field, μ the magnetic permeability of the medium, and ϵ the electric permittivity of the medium.

In order to solve the Helmholtz equation it is convenient to define a new function, \mathbf{M} , as

$$\mathbf{M} = \nabla \times (\mathbf{c}\psi) \quad (2.40)$$

where \mathbf{c} is a constant vector and ψ an scalar function. The divergence of the function \mathbf{M} is zero.

Taking into account the relation between the electric and magnetic fields, it is possible to generate another divergence free function from \mathbf{M} that fulfill the Helmholtz equation

$$\mathbf{N} = \frac{\nabla \times \mathbf{M}}{k} \quad (2.41)$$

This pair of functions, \mathbf{M} and \mathbf{N} , are known as the vector harmonics. By means of this functions, the initial problem of solving a vectorial differential equation (i.e., Helmholtz equation) has been simplified to an easier one: finding the solution to a scalar differential equation

$$\nabla^2\psi + k^2\psi = 0 \quad (2.42)$$

Because this theory is going to be applied to spheres, the correct set of coordinates to solve the problem are the spherical coordinates. So the scalar function chosen to generate the vector harmonics must satisfy the wave equation in spherical coordinates. In order to solve this equation, it is necessary to apply the separation of variables

method. So the solutions that are being sought, have this form

$$\psi(r, \theta, \phi) = R(r)\Theta(\theta)\Phi(\phi) \quad (2.43)$$

As a result, the solutions obtained are

$$\psi_{omn} = \cos(m\phi)P_n^m(\cos\theta)z_n(kr) \quad \psi_{emn} = \sin(m\phi)P_n^m(\cos\theta)z_n(kr) \quad (2.44)$$

where m is an integer, P_n^m are the associated Legendre functions of first kind, of degree n and order m , where $n = m, m+1 \dots$ and z_n represents the spherical Bessel functions. The subscripts o and e indicates either the function has a positive (even) or negative (odd) parity.

By introducing these into (2.40) and (2.41) the formulas of the vector spherical harmonics, $\mathbf{M}_{o1n}^{(1)}$, $\mathbf{M}_{e1n}^{(1)}$, $\mathbf{N}_{o1n}^{(1)}$, $\mathbf{N}_{e1n}^{(1)}$, are obtained. This peculiar functions give the normal modes of a spherical particle.

So let a linearly polarized plane wave of wavelength λ be incident on a spherical particle of radius a in the vacuum ($\epsilon_m = 1$). The electric permittivity of the particle is ϵ and its magnetic permeability is μ . In a laboratory coordinate system, the incident electric and magnetic fields are given by

$$\mathbf{E}_i = E_0 \exp(i\mathbf{k} \cdot \mathbf{r}) \mathbf{e}_x \quad \mathbf{H}_i = H_0 \exp(i\mathbf{k} \cdot \mathbf{r}) \mathbf{e}_y \quad (2.45)$$

The expansion of these incident fields into vector spherical harmonics can be expressed as

$$\mathbf{E}_i = E_0 \sum_{n=1}^{\infty} i^n \frac{2n+1}{n(n+1)} (\mathbf{M}_{o1n}^{(1)} - i\mathbf{N}_{e1n}^{(1)}) \quad (2.46)$$

$$\mathbf{H}_i = -\frac{k}{\omega\mu} E_0 \sum_{n=1}^{\infty} i^n \frac{2n+1}{n(n+1)} (\mathbf{M}_{e1n}^{(1)} - i\mathbf{N}_{o1n}^{(1)}) \quad (2.47)$$

where ω is the angular frequency of the field, μ the magnetic permeability of the medium and the super index (1) indicates that the spherical Bessel function of first kind, $j_n(kr)$, should be used for the calculus of the vector spherical harmonics.

Therefore, the scattered field is

$$\mathbf{E}_s = E_0 \sum_{n=1}^{\infty} i^n \frac{2n+1}{n(n+1)} (ia_n \mathbf{N}_{e1n}^{(3)} - b_n \mathbf{M}_{o1n}^{(3)}) \quad (2.48)$$

$$\mathbf{H}_s = -\frac{k}{\omega\mu} E_0 \sum_{n=1}^{\infty} i^n \frac{2n+1}{n(n+1)} (ib_n \mathbf{N}_{o1n}^{(3)} + a_n \mathbf{M}_{e1n}^{(3)}) \quad (2.49)$$

where the super index (3) indicates that the spherical Hankel function, $h_n^{(1)}$, may be used for the calculus of the vector spherical harmonics of these expansions.

The scattering coefficients, a_n and b_n , can be expressed as a function of the Ricatti-Bessel functions

$$\phi_n(\rho) = \rho j_n(\rho) \quad \zeta_n(\rho) = \rho h_n^{(1)}(\rho) \quad (2.50)$$

For a non magnetic medium the expressions of the scattering coefficients are

$$a_n = \frac{m\psi_n(mx)\psi_n'(x) - \psi_n(x)\psi_n'(mx)}{m\psi_n(mx)\zeta_n'(x) - \zeta_n(x)\psi_n'(mx)} \quad (2.51)$$

$$b_n = \frac{\psi_n(mx)\psi_n'(x) - m\psi_n(x)\psi_n'(mx)}{\psi_n(mx)\zeta_n'(x) - m\zeta_n(x)\psi_n'(mx)} \quad (2.52)$$

where x is the size parameter and m is the relative refractive index defined by

$$x = \frac{2\pi a}{\lambda} \quad m = \frac{N_{sphere}}{N_{medium}} \quad (2.53)$$

In addition, the expansion in terms of the Mie scattering coefficients gives us a multipolar expansion of the field. The a_n coefficients represent the electric multipolar contribution whereas the b_n coefficients represent the magnetic multipolar contribution to the scattered field. The subindex n indicates which multipole we are considering. For example, $n = 1$ represents the dipole term, $n = 2$ the quadrupole terms and so on. By evaluating them as function of the wavelength it is easy to know for which wavelengths the resonances are produced. For example, the wavelength that makes a_1 maximum is the one at which the electric dipole resonance is produced.

The scattering and extinction cross-sections of a sphere can be expressed in terms of the Mie scattering coefficients as

$$Q_{ext} = \frac{2}{x^2} \sum_{n=1}^{\infty} (2n+1) \text{Re}(a_n + b_n) \quad (2.54)$$

$$Q_{sca} = \frac{2}{x^2} \sum_{n=1}^{\infty} (2n+1)(|a_n|^2 + |b_n|^2) \quad (2.55)$$

Due to energy conservation, the extinguished radiation may be equal to the sum of the scattered and absorbed radiation. As a result of this, it is possible to give an expression for the absorption efficiency, Q_{abs} .

$$Q_{abs} = Q_{ext} - Q_{sca} \quad (2.56)$$

2.4.2 Localized Surface Plasmons in the Quasi-Static Approximation

Mie theory has no restriction in the size of the sphere. However, an interesting phenomenon appears when dealing with metallic nanoparticles whose size is smaller to the illuminating wavelength: *Localized Surface Plasmons Resonances (LSPRs)*. LSPRs are non-propagating excitations of the conduction electrons of metallic nanostructures coupled to the electromagnetic field [66].

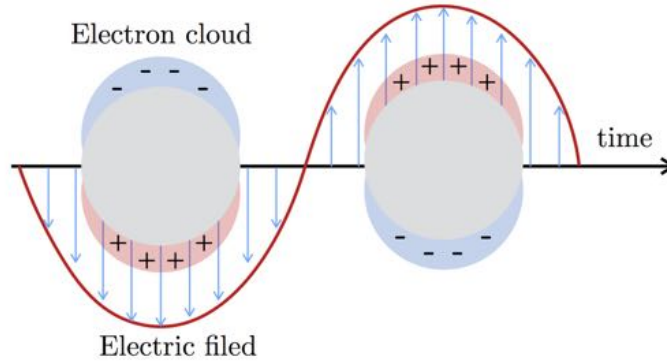


Figure. 2.4 Schematic of a localized surface plasmon resonance (LSPR) excited in a sphere whose size $a \ll \lambda$ (dipolar regime). Coherent oscillations in the free electrons of the material may be induced by the oscillating electric field of the incident light.

In order to have a deeper insight into this phenomenon we will consider the case of a metallic sphere whose size is much smaller than the illuminating wavelength ($Nx \ll 1$, dipolar regime). Under this condition we can assume Mie theory under the quasi-static approximation i.e., the phase of the harmonically oscillating electromagnetic field is practically constant over the particle volume, so one can solve the problem by assuming an electrostatic field acting on the particle [2, 66].

Under this approximation, the electric field outside the sphere given by eq. (2.48), is reduced to the superposition of the applied field and the field of an ideal dipole at the origin with a dipolar moment \mathbf{p}

$$\mathbf{p} = 4\pi\epsilon_m a^3 \frac{\epsilon_s - \epsilon_m}{\epsilon_s + 2\epsilon_m} \mathbf{E}_0 \quad (2.57)$$

where ϵ_m and ϵ_s are the dielectric function of the surrounding medium and sphere. Therefore, the applied field induces a dipole moment proportional to the field. The polarizability α of the sphere is defined as

$$\mathbf{p} = \epsilon_m \alpha \mathbf{E}_0 \quad (2.58)$$

$$\alpha = 4\pi a^3 \frac{\epsilon_s - \epsilon_m}{\epsilon_s + 2\epsilon_m} \quad (2.59)$$

The polarizability value shows a resonant enhancement under the condition that $|\epsilon_s + 2\epsilon_m| = 0$, which for the case of small value of $\text{Im}(\epsilon_s)$ around the resonance simplifies to

$$\text{Re}(\epsilon_s) = -2\epsilon_m \quad (2.60)$$

Note that fulfilling this condition requires a value of $\text{Re}(\epsilon_s) < 0$, that is characteristic of metals. This relationship is called the Fröhlich condition. It is associated with the dipolar localized surface plasmon excitation of the metal nanoparticle and produces an enhancement of the electric field outside the sphere.

In the quasi-static approximation the absorption and scattering efficiencies may be written as

$$Q_{abs} = 4x \text{Im}\left(\frac{\epsilon_s - \epsilon_m}{\epsilon_s + 2\epsilon_m}\right) \quad (2.61)$$

$$Q_{sca} = \frac{8}{3} x^4 \left| \frac{\epsilon_s - \epsilon_m}{\epsilon_s + 2\epsilon_m} \right|^2 \quad (2.62)$$

Under the Fröhlich condition (see eq. (2.60)) Q_{abs} and Q_{sca} also present a resonant enhancement. Therefore, peaks appearing in the spectra of these magnitudes are indicators of the presence of LSPRs.

As an example, Fig. 2.5(a) shows the spectral behavior of the complex dielectric function of aluminum along with the absorption efficiency of a 20 nm aluminum sphere. With a vertical dashed line is indicated the Fröhlich frequency. At this photon energy

the condition $\text{Re}(\epsilon_s) = -2\epsilon_m$ is fulfilled. The Q_{abs} spectrum shows a peak with its maximum at the Fröhlich frequency. The electric field outside the sphere at this photon energy shows an enhancement of a factor ten with respect to the intensity of the illuminating field (see Fig. 2.5(b)). It can be seen how the enhanced field is confined near the surface of the particle. These regions are called *hot-spots*.

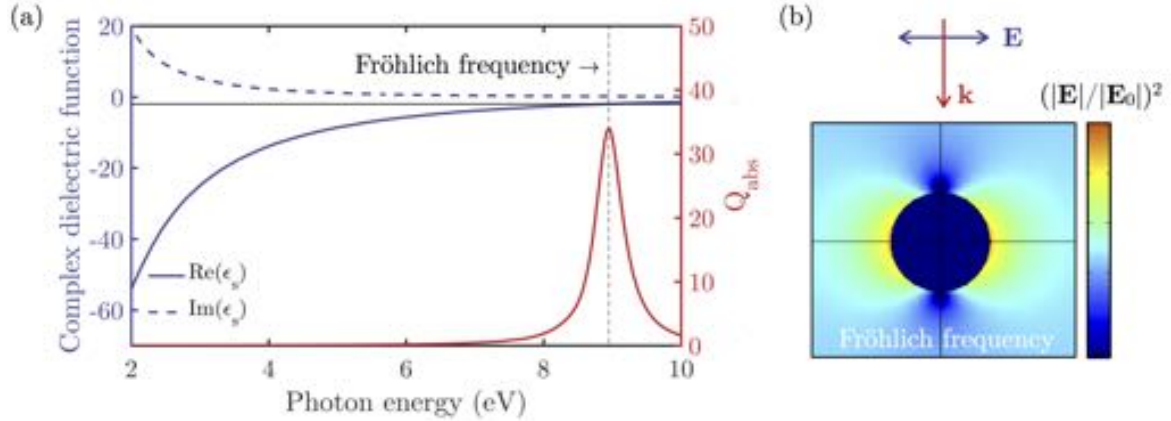


Figure. 2.5 (a) Aluminum complex dielectric function (left axis) and the corresponding absorption efficiency Q_{abs} of a 20 nm sphere embedded in air ($\epsilon_m = 1$, right axis). The horizontal black line indicates $2\epsilon_m$. With a vertical dashed line is highlighted the Fröhlich frequency ($\text{Re}(\epsilon_s) = -2\epsilon_m$). (b) Electric field enhancement around the 20 nm Al sphere illuminated with photon energy equal to the Fröhlich frequency.

2.4.3 Plasmon Dynamics and Hot Electron Generation

Light absorption by metallic nanostructures triggers a series of complex processes that can have as an outcome the generation of energetic charge-carriers known in the literature as *hot electrons*. The elevated electric field appearing in the surface of metallic NPs when illuminated under resonance enhances the generation of this energetic charge-carriers (hot electrons) that, in turn, can induce photochemical transformations among other phenomena through a charge-transfer mechanism or by localized heating.

Indeed, in metallic nanoparticles, light absorption is enhanced by the excitation of LSPRs which, in general, increases the generation of hot electrons. The dynamics of excitation and further relaxation of this type of NPs is illustrated in Fig. 2.6 [67, 68]:

- a. The first step is the LSP excitation in the nanoparticle. At the moment prior to the plasmon excitation the electrons follow a Fermi-Dirac distribution at the thermal temperature of the system.

- b. Plasmon resonances can be damped radiatively by emission of a photon or non-radiatively through the creation of electron-hole pairs via Landau damping. Landau damping is pure quantum mechanical process that consists in the transfer of a plasmon quantum into a electron-hole pair. The time scale of this phenomenon is 1-100 fs. This process produces an athermal electron distribution.
- c. The hot electrons produced by the plasmon decay will redistribute their energy among lower energy electrons via electron-electron scattering processes. The time scale of the carrier relaxation is of a several hundred of femtoseconds. This process leads to a Fermi-Dirac electron distribution characterized by a large effective electron temperature.
- d. In the final step heat is transferred to the surroundings of the nanoparticle. Depending on the material, particle size and thermal conduction of the surroundings, this process can take from 100 ps to 10 ns. During this step, the electron distribution start to thermalize to the temperature of the system.

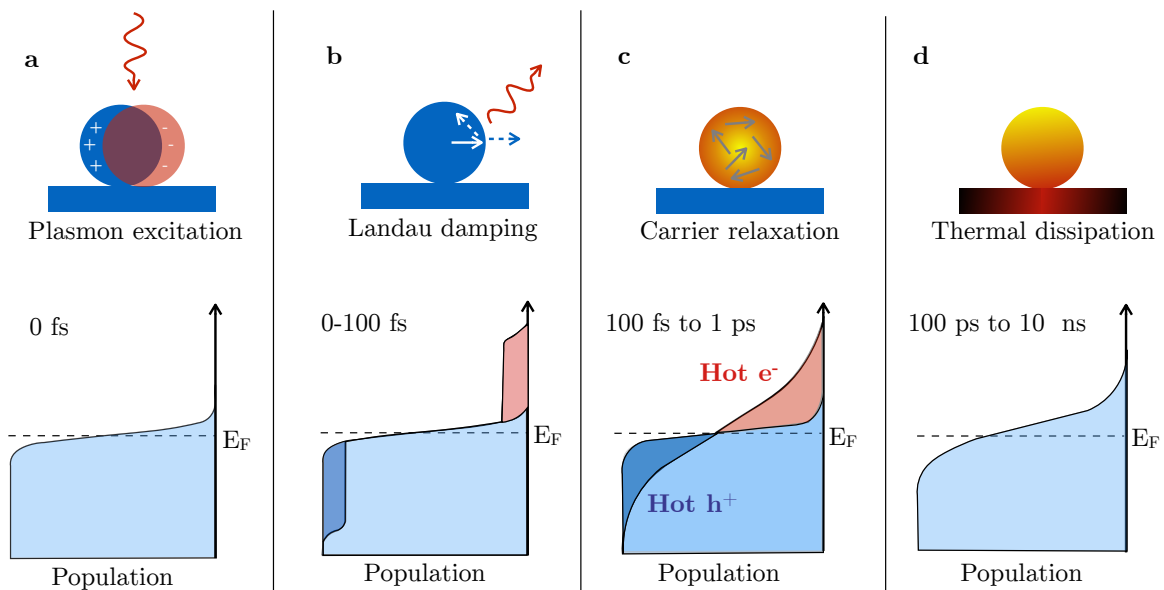


Figure. 2.6 Photoexcitation and subsequent relaxation processes following the illumination of a metallic nanoparticle with a laser pulse and characteristic time scales.

2.4.4 Scattering by Dielectric Nanoparticles

Localized surface plasmons are a characteristic phenomenon of metallic nanoparticles that enhances and confines the illuminating electromagnetic field in the vicinity of

the NPs due to the presence of free electrons. However, a similar effect can be observed in dielectric nanostructures. Whereas in metals localized surface plasmons are created by the oscillation of the conduction electrons, in the case of dielectrics, the incident electromagnetic field creates displacement currents of the bound electrons in the material that, under specific conditions, can also enhance the near-field creating *hot-spots*.

Of special interest are those dielectrics with low-losses ($k \approx 0$) and high refractive index ($n > 2$, being the complex refractive index $N = n + ik$). Dielectric materials that fulfill these two characteristic are known in the literature as High Refractive Index Dielectric (HRID) materials. We can categorize as HRID common semiconductors such as silicon (Si), germanium (Ge) or gallium arsenide (GaAs) in the near-infrared spectral range [69]. Although, gallium phosphide (GaP) have HRID character in the visible, extending these properties to the UV remains a challenge.

In HRID NPs, unlike in the case of metals where mainly electric modes are excited (a_n coefficients in Mie expansion), it is possible to excite both dipolar electric and magnetic modes (a_1 and b_1 coefficients in Mie expansion). The possibility of exciting simultaneously the dipolar electric and dipolar magnetic response of the nanoparticles opens the chance of meeting the so-called Kerker conditions [58, 57]. In 1980's, Kerker and co-workers analytically obtained that light scattering of dipole-like particles can be suppressed in either the forward or the backward direction by interaction of their electric and magnetic resonances [70]. When the scattered field from the electric dipolar and magnetic dipolar responses of the nanoparticle oscillate in phase (condition met when $a_1 = b_1$) it is produced the Zero-Backward condition. Under this condition the intensity scattered in the backward direction is completely suppressed. Conversely, when the scattered field from the electric dipolar and magnetic dipolar responses of the nanoparticle oscillate out-of-phase (condition met when $a_1 = -b_1$) it is produced the Minimum-Forward condition. Under this condition the intensity scattered in the forward direction is minimized. At the Minimum-Forward condition, it is impossible the complete suppression of the scattered intensity in the forward direction due to the violation of the extinction theorem -also known as the Ewald-Oseen extinction theorem [2].

As an example, Fig. 2.7(a) shows the extinction efficiency (Q_{ext}) of a $R = 100$ nm silicon sphere in the 500 - 1100 nm spectral range. At these wavelengths the complex refractive index of Si takes a constant value of $m \approx 4$. With yellow and red lines are plotted the dipolar electric (a_1) and dipolar magnetic (b_1) contribution to the extinction efficiency respectively. With vertical dashed lines are indicated the

wavelengths at which the minimum-forward and zero-backward conditions are met. Figures 2.7(b,c) plots the scattering diagrams (angle dependent scattered intensity) at the minimum-forward and zero-backward conditions. With red and blue arrows are indicated the polarization of the incoming electric field \mathbf{E} and wave vector \mathbf{k} . It can be how at the zero-backward condition the scattered intensity in the backward direction (180°) is suppressed.

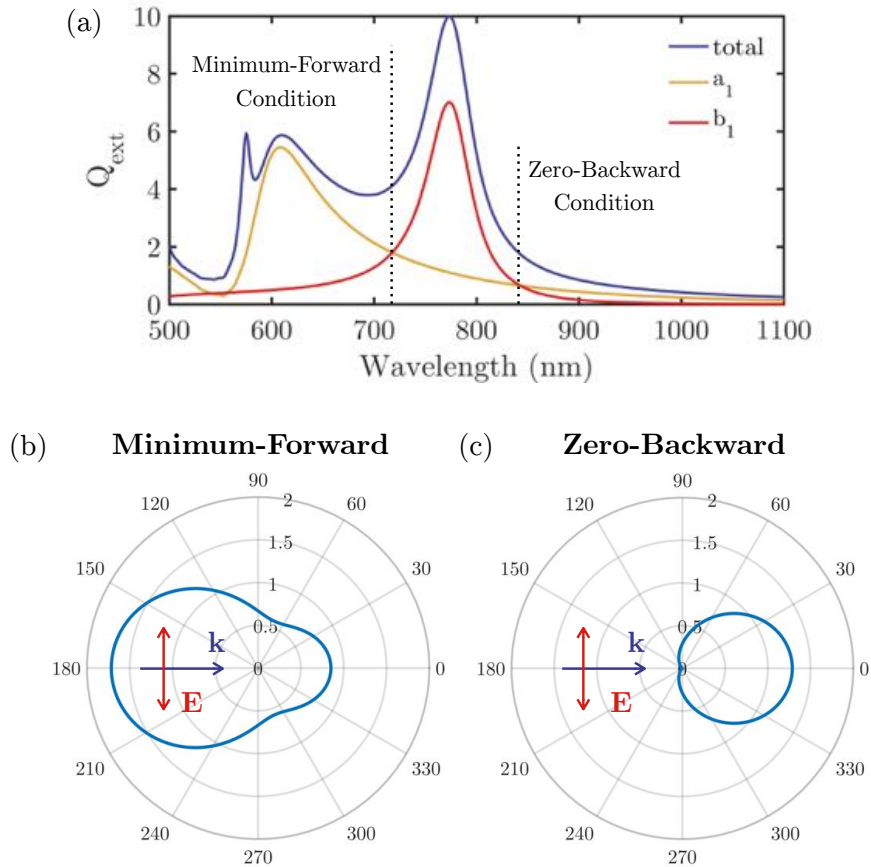


Figure. 2.7 (a) Extinction efficiency (Q_{ext}) of a $R = 100$ nm silicon sphere (blue line). With yellow and red lines are plotted the dipolar electric (a_1) and dipolar magnetic (b_1) contribution to the extinction efficiency respectively. With dashed lines are highlighted the wavelengths at which the minimum-forward and zero-backward conditions are met. (b,c) Angle dependent scattered intensity by the same silicon sphere at the wavelengths corresponding to the minimum-forward and zero-backward condition. With red and blue arrows are indicated the polarization of the incoming electric field \mathbf{E} and wave vector \mathbf{k} .

2.5 Scattering by Particles with Arbitrary Shape

Although the scattering problem for an isolated sphere can be solved analytically, the problem for more complex structures needs to be solved numerically. This includes particles with arbitrary shapes, collections of interacting particles or their interaction with substrates.

Here we present three of the most common numerical methods to solve scattering problems of complex geometries. These methods have been used to obtain the results presented in this dissertation.

2.5.1 Discrete Dipole Approximation (DDA)

The Discrete Dipole Approximation for computing scattering and absorption by particles was originally developed by Purcell and Pennypaker [71] and optimized by Draine and Flatau [72] to calculate the scattered electromagnetic field by isolated particles. In the DDA method, the scattering system is discretized and represented by an array of N point dipoles, with the spacing between dipoles small compared to the wavelength. Each dipole j is characterized by a polarizability α_j such that $\mathbf{p}_j = \alpha_j \mathbf{E}_j$, where \mathbf{p}_j is the instantaneous dipole moment and \mathbf{E}_j is the total instantaneous electric field at position j due to the incident field on the dipole, \mathbf{E}_j^{inc} , plus the effect of the other $N - 1$ dipoles

$$\mathbf{E}_j = \mathbf{E}_j^{inc} - \sum_{k \neq j} A_{jk} \mathbf{p}_k \quad (2.63)$$

where $A_{jk} \mathbf{p}_k$ is the electric field at the j^{th} dipole resulting from the k^{th} oscillating dipole.

2.5.2 Finite Element Method (FEM)

The finite element method allows to find an approximate solution to partial differential equations (PDEs) (e.g., Maxwell's equations) for systems in which they can not be analytically solved [73].

Let's consider the function u to be the dependent variable in a PDE (e.g., electric field). This function can be approximated by a function u_h defined by a linear combinations of basis functions.

$$u \approx u_h \quad u_h = \sum_i u_i \psi_i \quad (2.64)$$

where ψ_i denotes the basis functions and u_i are the coefficients of the functions that approximate u with u_h . The following figure illustrates this principle for a 1D problem. In this case, u could be the electric field along the length (z) of rod in a constant electrostatic field. The linear basis functions ψ_i have a value of 1 at their respective node and 0 otherwise. In this example are 10 nodes.

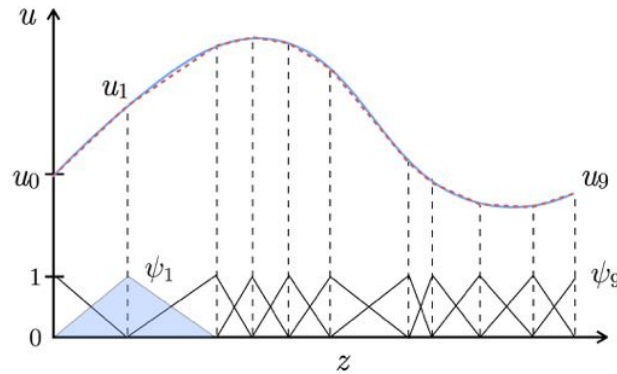


Figure. 2.8 The function u (solid blue line) is approximated with u_h (dashed red line), which is a linear combination of linear basis functions ψ_i (solid black lines). The coefficients are denoted by u_0 through u_9 .

An advantage that presents this method is that the discretization does not need to be uniform. It allows a great freedom when choosing the size of the elements used to discretize the space and the basis functions. For example, in Figure 2.8 the smaller elements are used to describe those region where the gradient of u is higher. Also, the theory provides useful error estimates, or bounds for the error, when the numerical model equations are solved on a computer.

2.5.3 Finite-Difference Time-Domain (FDTD)

The Finite-Difference Time-Domain (FDTD) method is a method for solving Maxwell's equations in complex geometries. The FDTD method solves these equations on a discrete spatial and temporal grid. The basic element of distretization is the *Yee cell* [74].

By looking at Maxwell's equation in their differential form (see section 2.1), it can be observed that the change in the electric field \mathbf{E} in time (the time derivative) is dependent on the change in the magnetic field \mathbf{H} across space (the curl). At any time in space, the updated value of the \mathbf{E} -field in time is dependent on the stored value of the \mathbf{E} -field and the curl of the local distribution of the \mathbf{H} -field in space. Conversely,

the \mathbf{H} -field is dependent on the stored value of the \mathbf{H} -field and the curl of the local distribution of the \mathbf{E} -field in space [75].

The method acts in a leapfrog manner: the \mathbf{E} -field vector components in a volume of space are solved at a given instant in time. Then the \mathbf{H} -field vector components in the same spatial volume are solved at the next instant in time. This process is repeated over and over again until convergence of the solution is achieved.

Chapter 3

Dielectric Function: Classic, Quantum and Experimental Approaches

To properly model the optical response of nanostructures, it is necessary to have their optical properties perfectly characterized. Therefore, the following chapter is intended to give a short account on the optical properties of materials. In section 3.1, classical theories such as the Lorentz model for insulators and the Drude model for metals are reviewed. Section 3.2 is dedicated to the fundamentals for the quantum computation of the dielectric function through Density Functional Theory (DFT). Finally, section 3.3 includes a brief review of ellipsometry as an experimental technique to measure the dielectric function of materials.

3.1 Classical Theories

The dielectric function describes the response of a material to an applied electric field. Classical theories used to model the dielectric function of real materials can help to qualitatively identify the physical phenomena arising from their electronic structure. In this section, we will give a brief overview of the Lorentz and Drude models for insulators and metals respectively. In general, real materials exhibit aspects arising from both models.

On the one hand, Drude model describe intraband transitions. These correspond to optical excitation of an electron in a state below the Fermi energy E_F to another one above E_F , but within the same band (see red arrow in Fig. 3.1). Intraband transitions

can only occur in metals since insulators do not have partially filled bands that would allow this type of optical excitation. On the other hand, Lorentz model describe direct interband transitions. They correspond to optical excitation of an electron to another band with no change in its momentum \mathbf{k} (see blue arrow in Fig. 3.1) [2, 65].

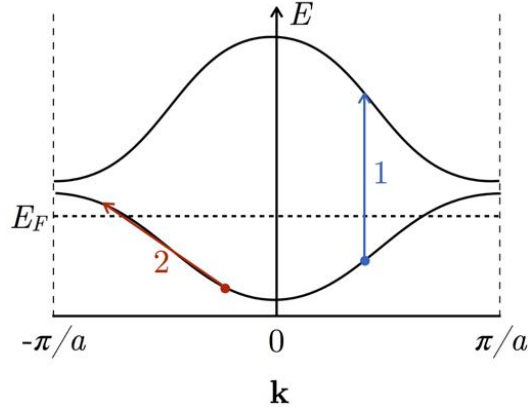


Figure. 3.1 Schematic band diagram for a metal. In blue is indicated direct interband transition. In red, a intraband transition is highlighted.

3.1.1 Lorentz Oscillator

The Lorentz model is applicable materials with interband transitions. Its quantum mechanical analog includes all direct interband transitions [65, 2]: all transitions for which the final state of the electron lies in another band with no change in the \mathbf{k} -vector in the reduced scheme (i.e., vertical transitions between bands in the band diagram).

Let's consider an atom with an electron bound to the nucleus in the same way as a small mass can be bound to a larger mass by a spring. The motion of the electron bound to the nucleus can be described by applying Newton's second law as

$$m \frac{d^2 \mathbf{r}}{dt^2} + m\Gamma \frac{d\mathbf{r}}{dt} + m\omega_0^2 \mathbf{r} = -e\mathbf{E}_{loc} \quad (3.1)$$

where m is the mass of the electron and e its charge. \mathbf{E}_{loc} is the local electric field acting on the electron. The term $m\Gamma \frac{d\mathbf{r}}{dt}$ represents viscous damping and provides for an energy loss mechanism. In this case, radiation damping. The term $m\omega_0^2 \mathbf{r}$ is a Hooke's law restoring force.

In the context of the classical model, we assume that the nucleus has an infinite mass and the electron does not interact with the magnetic field of the electromagnetic radiation. If we consider that the local electric field has a time-harmonic dependence

(in time it varies as $\exp(i\omega t)$), the solution to eq. (3.1) is

$$\mathbf{r}(\omega) = \frac{-e^2 \mathbf{E}_{loc}(\omega)/m}{(\omega_0^2 - \omega^2) - i\Gamma\omega} \quad (3.2)$$

and the induced dipole moment is

$$\mathbf{p}(\omega) = \frac{-e \mathbf{E}_{loc}(\omega)}{m} \frac{1}{(\omega_0^2 - \omega^2) - i\Gamma\omega} \quad (3.3)$$

Assuming the linear relation between \mathbf{p} and \mathbf{E}_{loc} , the frequency dependent polarizability $\alpha(\omega)$ can be expressed as

$$\mathbf{p}(\omega) = \alpha(\omega) \mathbf{E}_{loc}(\omega) \quad (3.4)$$

The macroscopic polarization for a system with N electrons per unit of volume is

$$\mathbf{P}(\omega) = N \langle \mathbf{p}(\omega) \rangle = N \alpha(\omega) \langle \mathbf{E}_{loc}(\omega) \rangle = \epsilon_0 \chi_e(\omega) \mathbf{E}(\omega) \quad (3.5)$$

In general, in a solid, $\langle \mathbf{E}_{loc}(\omega) \rangle \neq \mathbf{E}(\omega)$ since the average of the local field is usually an average over atomic sites. In general, some corrections need to be added. However, here, for simplicity, we will assume this identity.

Recalling the expression $\epsilon = \epsilon_0(1 + \chi_e)$ derived in the previous chapter, we can express the dielectric function as,

$$\epsilon(\omega) = \epsilon_1(\omega) + i\epsilon_2(\omega) = 1 + \frac{Ne^2}{m\epsilon_0} \frac{1}{(\omega_0^2 - \omega^2) - i\Gamma\omega} \quad (3.6)$$

being

$$\epsilon_1(\omega) = 1 + \frac{Ne^2}{m\epsilon_0} \frac{(\omega_0^2 - \omega^2)}{(\omega_0^2 - \omega^2)^2 + \Gamma^2\omega^2} \quad (3.7)$$

$$\epsilon_2(\omega) = \frac{Ne^2}{m\epsilon_0} \frac{\Gamma\omega}{(\omega_0^2 - \omega^2)^2 + \Gamma^2\omega^2} \quad (3.8)$$

The frequency dependence of ϵ_1 and ϵ_2 is shown in Fig. 3.2. ϵ_1 increases with increasing frequency except for a narrow region around ω_0 . This is called normal dispersion. However, for a region around ω_0 , ϵ_1 decreases with increasing frequency. This is called anomalous dispersion. The width of the anomalous dispersion region is Γ . For $\omega = \omega_0$, ϵ_2 presents a maximum, whereas $\epsilon_1 = 0$.

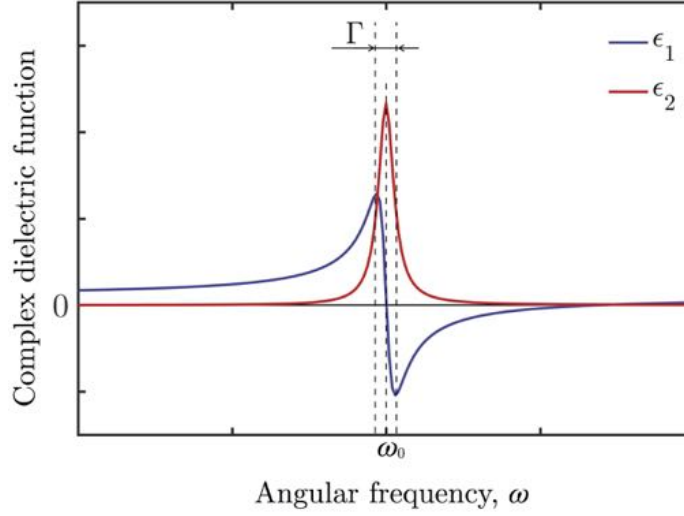


Figure. 3.2 Frequency dependence of ϵ_1 and ϵ_2 described by the Lorentz model.

In general, a optical medium will have many characteristic frequencies ω_{0j} . In that case the dielectric function is given by

$$\epsilon(\omega) = \epsilon_1(\omega) + i\epsilon_2(\omega) = 1 + \frac{Ne^2}{m\epsilon_0} \sum_j \frac{f_j}{(\omega_{0j}^2 - \omega^2) - i\Gamma_j\omega} \quad (3.9)$$

where f_j is the oscillator strength. In the quantum mechanical analog of the Lorentz model this parameter is associated with the relative probability of an atomic transition. It satisfies the rule $\sum_j f_j = 1$. As real example of a material with different characteristic frequencies ω_{0j} , Fig. 3.3 shows the complex dielectric function of ice in the far infrared-microwave ranges[3].

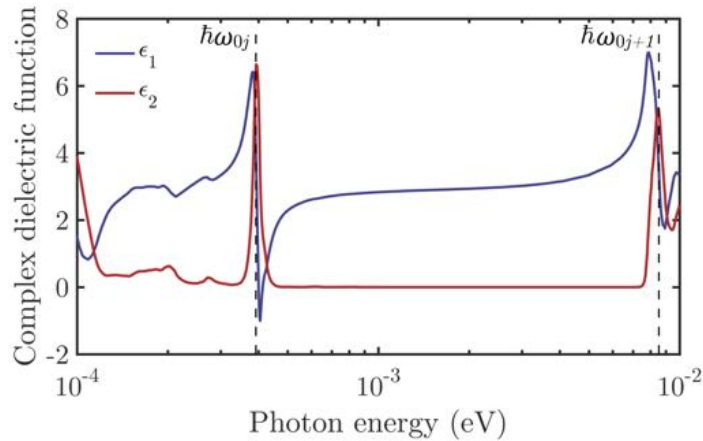


Figure. 3.3 Complex dielectric function $\epsilon = \epsilon_1 + i\epsilon_2$ of ice in the far infrared-microwave ranges [3]. With a dashed line are highlighted two of the characteristic frequencies.

3.1.2 Drude Model

The Drude model is applicable to free-electron metals. Its quantum mechanical analog includes intraband transitions: electron transitions within the same band from a state below the Fermi level to another one above it. [65, 2].

The Drude model for metals is obtained directly from the Lorentz model for insulators by simply equating the restoring force to zero. The conduction electrons of metal are not bound and they are distributed evenly throughout the metal. The field acting on the electrons is just the average field, so there is no need to make corrections to the local field.

By equating $\omega_0 = 0$ in eq. (3.7) and (3.8) we get

$$\epsilon_1(\omega) = 1 - \frac{Ne^2}{m\epsilon_0} \frac{1}{\omega^2 + \Gamma^2} \quad (3.10)$$

$$\epsilon_2(\omega) = \frac{Ne^2}{m\epsilon_0} \frac{\Gamma}{\omega(\omega^2 + \Gamma^2)} \quad (3.11)$$

The origin of the viscous damping in this free-electron model is associated with the scattering of electrons related with the electrical resistivity. We can relate the damping constant Γ to the average time between collisions τ , through $\Gamma = \tau^{-1}$.

We can define plasma frequency ω_p as

$$\omega_p^2 = \frac{Ne^2}{m\epsilon_0} \quad (3.12)$$

Therefore, we can rewrite redefine (3.10) and (3.11) in terms of the mean free path and the plasma frequency,

$$\epsilon_1(\omega) = 1 - \frac{\omega_p^2}{\omega^2 + 1/\tau^2} \quad (3.13)$$

$$\epsilon_2(\omega) = \frac{\omega_p^2}{\omega\tau(\omega^2 + 1/\tau^2)} \quad (3.14)$$

For most metals at room temperature $1/\tau$ is much smaller than ω_p ($\omega_p\tau \gg 1$). Plasma frequencies of metals are in the visible and ultraviolet: ω_p ranges from about 3 to 15 eV. Therefore, a good approximation to the Drude dielectric functions at visible

and ultraviolet frequencies is

$$\epsilon_1(\omega) \approx 1 - \frac{\omega_p^2}{\omega^2} \quad (3.15)$$

$$\epsilon_2(\omega) \approx \frac{\omega_p^2}{\omega^3\tau} \quad (3.16)$$

Fig 3.4 shows the frequency dependence of ϵ_1 and ϵ_2 in a free-electron Drude model at visible and ultraviolet frequencies ($\omega_p\tau \gg 1$). At $\omega_p = 0$ the value of ϵ_1 meets zero. For an ideal free-electron metal, the reflectivity R approaches unity below the plasma frequency. Above the plasma frequency, the metal is transparent and the reflectivity decreases rapidly with increasing frequency.

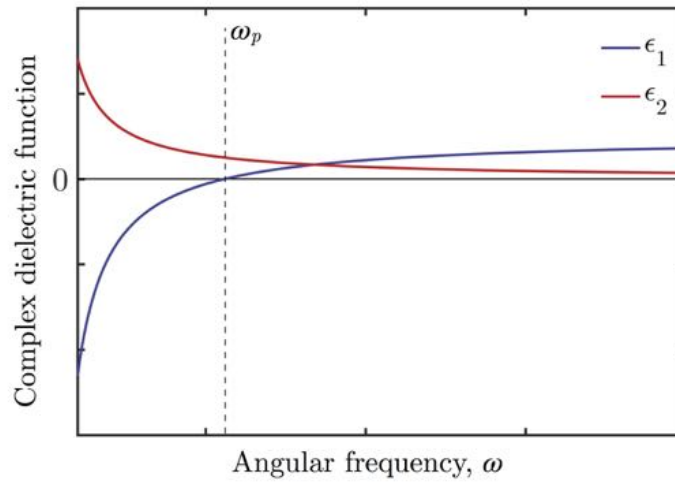


Figure. 3.4 Frequency dependence of ϵ_1 and ϵ_2 in a free-electron Drude model at visible and ultraviolet frequencies.

A metal whose optical constants have a Drude-like behaviour is Gallium in its liquid state. Ga has a melting point around room temperature, so in ambient conditions Ga is a liquid metal. Figure 3.5 shows the fitting of its dielectric function [4] to a Drude model for photon energies between 0.8 and 6 eV.

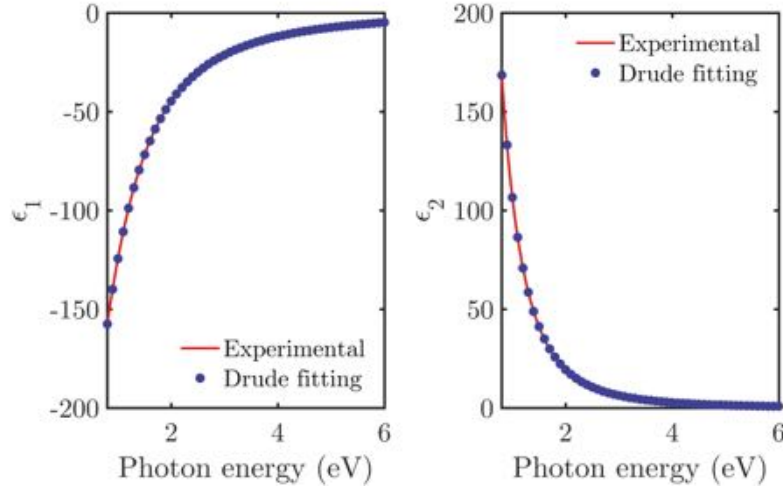


Figure. 3.5 Fitting of the experimental dielectric function ($\epsilon = \epsilon_1 + i\epsilon_2$) of liquid Gallium (red line) [4] to a Drude model (blue dots).

3.2 Quantum Approach: General Hamiltonian

The properties (including the optical ones) and structure of solids are basically dictated by the outer valence electrons of its constituent atoms. We assume that the electronic core states are atomic like in character and tightly bound to the nuclei. Therefore, core electrons plus the nuclei can be treated as single particles. It is the interaction between the valence electrons and their interaction with the ions that determines the electronic structure of the solid [76, 77].

The total Hamiltonian H_T for a system of core and valence electrons,

$$H_T = \sum_i \frac{\mathbf{p}_i^2}{2m} + \sum_n \frac{\mathbf{p}_n^2}{2M} + \frac{1}{2} \sum_{ij} \frac{e^2}{|\mathbf{r}_i - \mathbf{r}_j|} + \frac{1}{2} \sum_{nn'} \frac{Z_n Z_{n'} e^2}{|\mathbf{R}_n - \mathbf{R}_{n'}|} + \sum_{ni} V_n(\mathbf{r}_i - \mathbf{R}_n) \quad (3.17)$$

where the terms of the right-hand term in order of appearance correspond to: the kinetic energy of the valence electrons, the kinetic energy of the cores, the Coulomb interaction between electrons, the Coulomb interaction between cores and finally, the interaction between electrons and cores. For simplicity, the spin and relativistic effects are omitted.

In eq. (3.17), \mathbf{p}_i , \mathbf{r}_i , e , and m are the electron momentum, position, charge and mass. \mathbf{p}_n , \mathbf{R}_n , Z_n , and M corresponds to the core momentum, position, charge, and mass. Solving this equation for a realistic system would imply managing the order of 10^{23}

quantum numbers. For that reason, it is necessary to introduce some approximations from the start [76, 77]:

- **The Born-Oppenheimer adiabatic approximation:** the atomic cores are much heavier than the electrons. For most systems it can be assume that the electrons feel the instantaneous potential produced by the cores in their “fixed” positions. Therefore, we can decouple the movement of electrons and nuclei.

Under the Born-Oppenheimer adiabatic approximation eq. (3.17) can be rewritten as,

$$H_T = \sum_i \frac{\mathbf{p}_i^2}{2m} + \frac{1}{2} \sum_{ij} \frac{e^2}{|\mathbf{r}_i - \mathbf{r}_j|} + V_{ext}(\mathbf{r}_i) \quad (3.18)$$

- **The mean-field approximation:** it is assumed that each electron moves in the average or mean field by the cores together with all the other electrons. As a result, it is possible to introduce a position dependent, single-particle potential V_{eff} that captures the dynamic of electron interactions. This approximation accomplishes the important task of decoupling the Hamiltonian in (3.17) into a sum of one electron Hamiltonians.

Therefore, the electronic wavefunction of all the valence electrons is approximated by a product of one-electron wavefunctions,

$$\psi(\mathbf{r}_1, \mathbf{r}_2, \dots, \mathbf{r}_N) = \psi(\mathbf{r}_1)\psi(\mathbf{r}_2)\dots\psi(\mathbf{r}_N) \quad (3.19)$$

and the total energy of the system is determined by the sum of N single electron energies,

$$E = \epsilon_1 + \epsilon_2 + \dots + \epsilon_N \quad (3.20)$$

Assuming these approximations, we find that the many-electron Schrödinger equation is satisfied if N single-electron Schrodinger equations of the form

$$\left(\frac{\mathbf{p}_i^2}{2m} - V_{eff} \right) \psi(\mathbf{r}_i) = \epsilon_i \psi(\mathbf{r}_i) \quad (3.21)$$

are fulfilled.

Nowadays, density functional theory (DFT) is the most popular approach to solve the many-electron Schrödinger by reducing it to N single-electron Schrödinger equations.

3.2.1 Density Functional Theory

The many-body problem can be exactly reduced to one of solving a self-consistent-field one-particle particle using the density functional theory [76]. This theory as formulated by Hohenberg, Kohn and Sham is in principle exact in the ground state properties of a system.

The Hohenberg-Kohn Theorems

In 1964 Hohenberg and Kohn demonstrated that, for an interacting many-electron system in a static potential $V_{ext}(\mathbf{r})$, the ground-state energy E_0 can be expressed as a functional of the charge density $n(\mathbf{r})$, i.e. $E_0[n]$ [76, 77]. The ionic potential is normally taken as $V_{ext}(\mathbf{r})$.

For an interacting many-body system, the Hohenberg-Kohn theorems imply that

- The ground-state energy E_0 can be expressed as a functional of the charge density $n(\mathbf{r})$. It can be expressed as

$$E_0[n] = \int V_{ext}(\mathbf{r})n(\mathbf{r})d(\mathbf{r}) + F[n] \quad (3.22)$$

where $F[n]$ is an universal functional of the density and independent of $V_{ext}(\mathbf{r})$.

- For any particular $V_{ext}(\mathbf{r})$, $E_0[n]$ is minimum for the correct physical density $n_0(\mathbf{r})$.
- $n(\mathbf{r})$, and hence $E_0[n]$ can in principle be exactly obtained from the solution of an associated one electron-problem with an effective potential $V_{eff}(\mathbf{r})$.

If $F[n]$ was known, and by using the variational principle of quantum mechanics, the problem of determining the ground state energy and density would be quite straightforward. However, $F[n]$ is unknown.

The Kohn-Sham Equations

Kohn and Sham formulation consists in replacing the many-body problem by an auxiliary independent particle problem. Therefore, the ground state can be represented

by the ground state density of an auxiliary system of non-interacting particles [77, 76]. In this framework, Kohn and Sham presented an universal approximation for $F[n]$ in which the interaction energy is just the classical Hartree term

$$E_{Hartree}[n] = \frac{e^2}{2} \int \frac{n(\mathbf{r})n(\mathbf{r}')}{|\mathbf{r} - \mathbf{r}'|} d\mathbf{r}d\mathbf{r}' \quad (3.23)$$

And for a noninteracting system of the same density, $n(\mathbf{r})$, the kinetic energy of the system $T_s[n]$ can be obtained from the single-particle orbitals $\phi(\mathbf{r})$ as

$$T_s[n] = -\frac{\hbar}{2m} \sum_i^{occ} \int \phi_i^*(\mathbf{r}) \nabla^2 \phi_i(\mathbf{r}) d\mathbf{r} \quad (3.24)$$

where

$$n(\mathbf{r}) = \sum_i^{occ} \phi_i^*(\mathbf{r}) \phi_i(\mathbf{r}) \quad (3.25)$$

Following these definitions, Kohn-Sham were able to express eq. (3.22) as

$$E[n] = \int V_{ext}(\mathbf{r})n(\mathbf{r})d(\mathbf{r}) + T_s[n] + E_{Hartree}[n] + E_{xc}[n] \quad (3.26)$$

where $E_{xc}[n]$ is called the exchange-correlation functional. This term contains all the information about the interacting system. It contains electron-electron interactions beyond the Hartree approximation and part of the kinetic energy of the interacting electrons.

Equation (3.26) is equivalent to consider a system of N independent electrons under the effective potential $V_{eff}^{KS}(\mathbf{r}) = V_{ext}(\mathbf{r}) + V_{Hartree}(\mathbf{r}) + V_{xc}(\mathbf{r})$ in which

$$V_{Hartree}(\mathbf{r}) = e^2 \int \frac{n(\mathbf{r}')}{|\mathbf{r} - \mathbf{r}'|} d\mathbf{r}' \quad (3.27)$$

and

$$V_{xc}(\mathbf{r}) = \frac{\delta E_{xc}}{\delta n(\mathbf{r})} \quad (3.28)$$

Since E_{xc} remains unknown, approximations must be made. Two of ones that have proven to be more useful are the local density approximation (LDA) and the

generalized gradient approximation (GGA). A common approach is to write

$$E_{xc} = \int n(\mathbf{r})\epsilon_{xc}(\mathbf{r})d(\mathbf{r}) \quad (3.29)$$

where $\epsilon_{xc}(\mathbf{r})$ is the exchange correlation density. This is assumed to be function of the local density $n(\mathbf{r})$ in the LDA, or function of $n(\mathbf{r})$ and its gradient in GGA.

The Kohn-Sham equations must be solved self-consistently following these steps:

- Choosing an initial set Kohn-Sham of orbitals ϕ_i^0 .
- Calculating the corresponding electronic density $n^0(\mathbf{r}) = \sum_i |\phi_i^0(\mathbf{r})|^2$.
- Calculating the Kohn-Sham effective potential $V_{eff}^{KS}(\mathbf{r})$.
- Solving the Kohn-Sham equations $[-\frac{\hbar}{2}\nabla^2 + V_{eff}^{KS}(\mathbf{r})]\phi_j(\mathbf{r}) = \epsilon_j\phi_j(\mathbf{r})$
- Computing the electron density $n^1(\mathbf{r})$. If $n^1(\mathbf{r})$ is consistent, the ground state has been achieved. If not, $n^1(\mathbf{r})$ is mixed with $n^0(\mathbf{r})$ and used as input for another self-consistent cycle.

3.2.2 Calculation of the Dielectric Function: First-order time-dependent perturbation theory

The frequency dependent interband contribution to the optical response of a solid can be obtained using first-order time-dependent perturbation theory to calculate the dipolar transition matrix elements between occupied and unoccupied single-electron eigenstates. The imaginary part of the frequency dependent dielectric function $\epsilon(\omega) = \epsilon_1(\omega) + i\epsilon_2(\omega)$ is given by [65],

$$\epsilon_2(\omega) = \frac{2\pi}{mN} \frac{\omega_p^2}{\omega^2} \sum_{v,c} \int_{\text{BZ}} \frac{d\mathbf{k}}{(2\pi)^3} |M_{c\mathbf{v}\mathbf{k}}|^2 \delta(\epsilon_{c\mathbf{k}} - \epsilon_{v\mathbf{k}} - \hbar\omega), \quad (3.30)$$

where m is the electron mass, N is the number of electrons per unit volume, and $\omega_p^2 = 4\pi N e^2/m$ is the plasma frequency, with e being the electron charge. The single-particle electronic states $|\psi\rangle$ of energy ϵ are labeled by their crystal momentum \mathbf{k} and their valence v or conduction c band index. The sum is over connecting valence and conduction states and over all the \mathbf{k} points in the first Brillouin zone. The optical matrix element is given by $M_{c\mathbf{v}\mathbf{k}} = \langle \psi_{c\mathbf{k}} | \hat{\mathbf{e}} \cdot \mathbf{p} | \psi_{v\mathbf{k}} \rangle$, where $\hat{\mathbf{e}}$ is the polarization of the

incident light and \mathbf{p} is the momentum operator. The real part of the dielectric function $\epsilon_1(\omega)$ can be obtained from the imaginary part using the Kramers-Kronig relation.

From the calculation of imaginary part of the interband contribution to the complex dielectric function it is also possible to get an estimation of the intraband contribution (eq. (3.30)). This contribution can be described as a Drude term (eqs. (3.7) and (3.8)) dependent on the plasma frequency ω_p and the damping constant Γ of the material. Because when evaluating eq. (3.30) ω_p is computed, and by using an empirical value of Γ , it is possible to estimate the intraband term which is relevant at low photon energies.

3.3 Ellipsometry: Measuring the Dielectric Function

Spectroscopic ellipsometry (SE) is a nonperturbing optical technique based on measuring the change in polarization state of a linearly polarized light reflected from a sample surface. This technique is widely used in the ex-situ and in-situ real-time characterization of surfaces, interfaces, thin films and nanostructured materials [78, 79]. The measurables of ellipsometry are the phase change and the light amplitude change upon reflection. These two magnitudes are denoted Δ and Ψ . Both Δ and Ψ are comprised in the Fresnel coefficients reviewed in section 2.2.1 of the previous chapter. The complex reflection ρ can be written in terms of the complex Fresnel coefficients for the p - and s -polarization as

$$\rho = \frac{r_p}{r_s} = \frac{|r_p| \exp(i\delta_p)}{|r_s| \exp(i\delta_s)} = \tan \Psi \exp(i\Delta) \quad (3.31)$$

where

$$\tan \Psi = \frac{|r_p|}{|r_s|} \quad \Delta = \delta_p - \delta_s \quad (3.32)$$

The dielectric function for a simple homogeneous surface or the pseudodielectric function for a complex film covered surface (e.g. a substrate covered with hemispherical NPs), can be written in terms of the variable ρ as

$$\langle \epsilon \rangle = \sin^2 \phi_0 + \sin^2 \phi_0 \tan^2 \phi_0 \left[\frac{1 - \rho}{1 + \rho} \right]^2 \quad (3.33)$$

where ϕ_0 is the angle of incidence.

The high sensitivity of this technique arises from the fact that the measurements of both Ψ and Δ is a relative measurement of the change in polarization. State of the art ellipsometers (Ψ , Δ) technical specifications are around $\Psi \pm 0.08^\circ$ and $\Delta \pm 0.1^\circ$ taken on the spectral range visible-NIR [79].

Figure 3.6 shows an scheme of the parts of an spectroscopic ellipsometer. Conventional spectroscopic ellipsometers begin with a white light source to illuminated the sample. The incident light goes through a polarizer. When the light is reflected on the sample surface, both phase and amplitude of the light change. The phase change Δ and the amplitude change Ψ , are determined by the sample's properties (i.e. thickness, dielectric function). The change in the polarization state is analyzed by a second polarizer (analyzer). Finally, the light is detected commonly through a photomultiplier, a semiconductor photodiode or a CCD, coupled to a monochromator for a spectroscopic analysis.

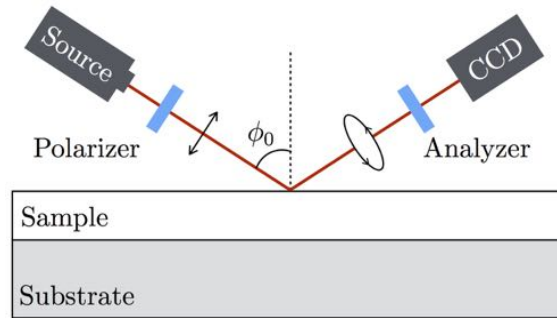


Figure. 3.6 Components of a conventional spectroscopic ellipsometer: a white light source illuminates the sample through a polarizer at an incident angle ϕ_0 . Upon reflection the polarization of the light changes and it is analyzed by another polarizer (analyzer). Finally, the light is collected by a detector.

Part I

Dielectric Function Calculation in Novel Materials

Chapter 4

Dielectric Function of Gallium Polymorphs

Gallium is most commonly known as a liquid metal with a melting temperature just above room temperature (29.7°C). It is a non-toxic, biocompatible [80], flexible, stretchable, and deformable metal at room temperature with low viscosity and excellent thermal and electrical conductivities [42]. However, gallium has several solid state phases, and these are receiving increasing interest for a number of reasons, chief among them being how its rich polymorphism [81–86] (see Fig. 4.1) enables a variety of phase-change systems [46–48]. These systems are being developed now, even though the local structure of these phases is not well understood and the local ordering of the liquid phase is still under investigation [87]. In addition, covalent bonding of Ga dimers creates an energy dip at the Fermi level with a strong absorption band around 2.3 eV [88], and the coexistence of metallic and covalent bonds strongly affects the metallic characteristics of the various Ga phases. Intriguingly, the coexistence of solid and liquid phases in Ga nanoparticles (NPs) can be controlled in a highly reversible and reproducible fashion, both by their epitaxial relationship with substrates[4] and by e-beam excitation [89].

These characteristics are responsible for the unique plasmonic properties of Ga NPs, recently demonstrated to span the ultraviolet (UV), visible, and near infrared (NIR) spectral regions [90, 43]. Already, Ga nanostructures have been exploited for a variety of applications, including chemical sensing (using UV surface enhanced Raman spectroscopy) [44], molecular sensing [45], delivery of cancer therapy drugs (using transformable liquid-metal nanospheres composed of a liquid-phase gallium core and a thiolated polymeric solid shell) [80], phase-change memories [91], reversible light-induced switching [92], phase change nonlinear systems [46], and “active plasmonics”

[47]. Many of these applications exploit changes in optical reflectivity produced by phase transformations between the various structural forms of Ga, changes stimulated by very low power (\approx nW) optical excitation [93]. The nature of the Ga–Ga bond is of particular interest because the way structural transformations affect optical properties may yield fascinating new mechanisms for photonic functionality, including multifunctional reconfigurable frequency- and polarization-selective surfaces [94].

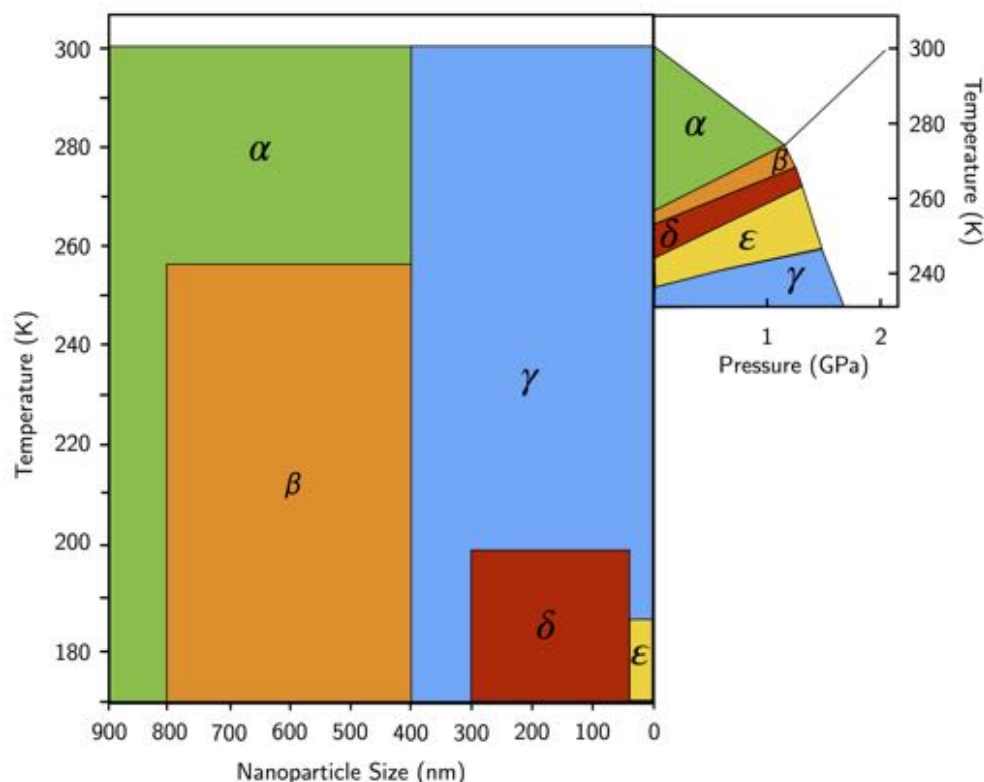


Figure. 4.1 Phase diagram of bulk Ga from Ref. [5] (right panel) and for Ga NPs (left panel), as summarized from data reported in various sources [4, 6, 7], showing the phases expected at the various temperatures.

Unfortunately, the potential applicability of such Ga-based systems for photonics and plasmonics has been severely hampered by the lack of information about the dielectric properties of the five primary phases of Ga (liquid “ l ” and α , β , γ , δ solids), and even less is known about amalgams composed of a mixture of these phases. To date the only dielectric dispersion profiles that have been modelled are a linear combination of the liquid and α -Ga phases [23]. And since these Ga phases change with temperature, accurate knowledge of the optical response of the various Ga phases is needed for predicting and modeling the temperature dependence of Ga-containing optoelectronic devices [95]. Such phase changes are becoming even more important for predicting

the plasmonic behavior of Ga when confined to nanostructures, whose high Laplace pressure and interactions with substrates [4, 12] or solvents [6] can stabilize them into a variety of phase distribution mixtures.

In this chapter we report a comprehensive theoretical and experimental investigation of the optical response of these five Ga phases, including their correlation with the respective crystalline structures and band diagrams, using dielectric functions calculated by first principles methods and experimentally validated by spectroscopic ellipsometry. In Section 4.1 are presented the computational details for the first principles calculations of the electronic structure and optical properties, and also those details concerning the electromagnetic simulations. It is included a subsection devoted to the detailed description of the fabrication of the Ga layers studied in this work along with their complete X-ray diffraction (XRD) analysis. In Section 4.2 are shown the main results arising from the study of the electronic structure (band diagrams and density of states) and optical properties of the analyzed Ga phases. We show that α -Ga and β -Ga possess strong interband transitions at low energies while γ -Ga, δ -Ga, and l -Ga have an almost ideal Drude-like metallic response. In fact, we demonstrate that the cooling of liquid phase Ga produces a mixture of solid phases whose distribution depends on the cooling rate and the presence of impurities. The implications of the different optical properties of the Ga phases are evaluated in thin film waveguides and plasmonic Ga NPs. Finally, the main conclusions of this work are gathered in Section 4.3

4.1 Methods

4.1.1 Computational Details

Density functional first-principles calculations based on a numerical atomic orbital method were carried out using SIESTA code [96]. All the calculations have been performed with the Generalized Gradient Approximation (GGA), using the exchange-correlation potential parametrized by Perdew-Burke-Ernzerhof [97] (PBEsol) to simulate the electronic exchange and correlation.

Core electrons are described by ab-initio optimized norm conserving pseudopotentials, generated following the recipe given by Hamann[98], available in the PSEUDODOJO¹ [99] in the Kleinman-Bylander fully non-local separable representation. The $3s$, $3p$, $3d$, $4s$ and $4p$ were considered as valence electrons of Ga and explicitly included in the calculations. The reference configuration, cut-off radii for each angu-

¹NC SR (ONCVSP v0.4) stringent

lar momentum shell, and the matching radius between the full core charge density and the partial core charge density for the on-linear-core-corrections (NLCC) for the pseudopotentials used in this work are shown in Table 4.1 .

Table 4.1 Reference configuration, cutoff radii and matching radius between the full core charge and the partial core charge for the pseudopotentials used in the study.

Reference	Ga			
	$3s^2$	$3p^6$	$3d^{10}$	$4s^2 4p^1$
Core radius	s		1,2	
	p		1,3	
	d		1,5	
Matching radius NLCC	0.34145 Bohr			

The one-electron Kohn Sham eigenvectors were expanded in a basis of localized numeric atomic orbitals (NAO) as implemented in SIESTA code. The size of the basis set chosen was single ζ for the semicore $3s$ and $3p$, double ζ for $3d$ and $4p$, and triple ζ for $4s$ orbitals. All the parameters required to describe the shape and the range of the NAO were variationally optimized following the recipe in Refs. [100, 101] . The range and shape of the basis set was also controlled by the soft-confinement potential described in Ref. [100] given by,

$$V(r) = V_0 \frac{e^{-\frac{r_c - r_i}{r - r_i}}}{r_c - r} \quad (4.1)$$

where V_0 is the prefactor of the soft-confinement potential, r_i is the inner radius where the soft-confinement potential starts off and r_c is the cutoff radius of each ζ . The parameters of each ζ used to describe each orbital are summarized in Table 4.2.

Table 4.2 Soft-confinement pseudopotential parameters.

	ζ	V_0 (Ry)	r_i (Bohr)	r_c first- ζ (Bohr)	r_c second- ζ (Bohr)	r_c third- ζ (Bohr)
$3s$	1	40.60081	0.68869	3.18621	–	–
$4s$	3	4.44968	0.95568	5.01495	3.29267	2.21895
$3p$	1	18.25305	0.89533	3.48396	–	–
$4p$	2	2.31196	3.46672	7.90001	5.97070	–
$3d$	2	51.40577	51.40577	6.30213	3.08367	–

The electronic density, Hartree, and exchange correlation potentials, as well as the corresponding matrix elements between the basis orbitals, were calculated in a uniform

real space grid. The equivalent plane wave cut-off used to represent the charge density was 800 Ry. For the Brillouin integrations, we use a Monkhorst-Pack[102] sampling of $10 \times 10 \times 10$ for the α -, β -, and δ -phases and $6 \times 6 \times 10$ for the γ -phase.

For the structural characterization atoms and unit cell were allowed to relax until the maximum component of the force acting on all atoms were smaller than $0.01 \text{ eV}/\text{\AA}$, and the maximum component of the stress tensor was smaller than $0.0001 \text{ eV}/\text{\AA}^3$.

4.1.2 Optical Response

The frequency dependent interband contribution to the optical response of the studied structures was obtained using first-order time-dependent perturbation theory to calculate the dipolar transition matrix elements between occupied and unoccupied single-electron eigenstates as implemented in SIESTA code [96]. The frequency dependent interband contribution to frequency-dependent dielectric function $\epsilon(\omega) = \epsilon_1(\omega) + \epsilon_2(\omega)$ can be written within the dipole approximation as

$$\epsilon_2(\omega) = \frac{2\pi}{mN} \frac{\omega_P^2}{\omega^2} \sum_{v,c} \int_{\text{BZ}} \frac{d\mathbf{k}}{(2\pi)^3} |M_{cv\mathbf{k}}|^2 \delta(\epsilon_{c\mathbf{k}} - \epsilon_{v\mathbf{k}} - \hbar\omega), \quad (4.2)$$

where m is the electron mass, N is the number of electrons per unit volume, and $\omega_P^2 = 4\pi N e^2/m$ is the plasma frequency, with e being the electron charge. The single-particle electronic states $|\psi\rangle$ of energy ϵ are labeled by their crystal momentum \mathbf{k} and their valence v or conduction c band index. The sum is over connecting valence and conduction states and over all the \mathbf{k} points in the first Brillouin zone. The optical matrix element is given by $M_{cv\mathbf{k}} = \langle \psi_{c\mathbf{k}} | \hat{\mathbf{e}} \cdot \mathbf{p} | \psi_{v\mathbf{k}} \rangle$, where $\hat{\mathbf{e}}$ is the polarization of the incident light and \mathbf{p} is the momentum operator. The real part of the dielectric function $\epsilon_1(\omega)$ can be obtained from the imaginary part $\epsilon_2(\omega)$ using the Kramers-Kronig relation.

In order to analyze the origin of the peaks appearing in the $\epsilon_2(\omega)$ spectra due to interband transitions, we have calculated the values of the optical matrix element $M_{cv\mathbf{k}}$ for every pair of conduction and valence bands at each \mathbf{k} point with an energy difference equal to the photon energy at which the peak appears. In this way, we can analyze the pair of bands contributing to the interband transition visible in $\epsilon_2(\omega)$ spectra.

All bands have been included in the optical calculations of each Ga phase. The optical mesh used for is $40 \times 40 \times 40$ for the α -, β -, and δ -phases and $40 \times 40 \times 50$ for the γ -phase. The gaussian broadening has been set to 0.20 Ry for α - and δ -phases, 0.25 Ry for β -Ga and 0.1 for γ -Ga.

4.1.3 Electromagnetic Simulations

The reflectance calculations have been performed using the Transfer Matrix Method (TMM) [103]. TMM allows to calculate the reflectance (R), transmittance (T), and absorbance (A) spectrum of an arbitrary system of homogeneous and non-magnetic multilayers. We have considered Ga films of thicknesses $h = 20$ and 150 nm deposited on a sapphire substrate and exposed to air. These values of h have been chosen according to typical experimental values found in the literature [104, 47]. The angle between the wave-vector k and the surface's normal (angle of incidence, AOI) has been fixed to 0° . Both s - and p -polarizations (perpendicular and parallel to the plane of incidence respectively), along with AOI have been chosen to mimic usual conditions in ellipsometry experiments.

The plasmonic response of nanoparticles has been calculated using the finite difference time-domain method. Total-field/scattered field light source conditions were used in all simulations. An illuminating linearly-polarized plane-wave was set to propagate perpendicular to the substrate. The wavelength spectral range analyzed was set from 200 to 1500 nm to mimic experimental conditions. A non-uniform mesh was used in the simulation region. A finer mesh was defined in the vicinity of the NP. In this region, the mesh step was fixed to $d_x = d_y = d_z = 1$ nm. The absorption cross-section was calculated within the total-field/scattered-field formalism

4.1.4 Ga layers formation and analysis

The solid gallium samples were obtained by cooling a gallium layer of about $2 \mu\text{m}$ thickness deposited on a sapphire slide. The back of the sapphire slide was titanium coated in order to assure thermal contact between the gallium slide and the temperature-programmable stage. The cooling speed, the ultimate temperature and the controlled atmosphere during the cooling were the experimental parameters affecting the polycrystalline structure. Specifically, the slide was positioned on a plate whose temperature can be controlled and programmed from the liquid nitrogen temperature (-196°C) up to 300°C . The stage is in a closed cell purged with a N_2 ultrahigh pure flow to avoid condensation of water and impurities on the Ga layer.

- Sample **Ga#1** was prepared by cooling to -40°C with a cooling rate of $20^\circ\text{C}/\text{min}$ while flowing 1 l/min of N_2 . This sample was found to be a homogeneous mixture of α - and metastable β -Ga phases. This is consistent with the partial metallic bonding of the β -Ga, whose crystallization is characterized by monoatomic packing, a generally fast process.

- Sample **Ga#2** was cooled to -150°C with a cooling rate of $5^{\circ}\text{C}/\text{min}$ while flowing 1 l/min of N_2 . It was found to be a polycrystalline mixture of α - and γ -Ga phases.

The cell had optical ports and was mounted on the stage of a spectroscopic ellipsometer so that the dielectric function spectra of the cooled Ga solid films could be obtained in the spectral range $0.75 - 6.5$ eV with 0.01 eV resolution (see experimental data in Fig. 4.4). Those samples were also analyzed by low temperature x-ray diffraction (XRD) to identify the solid phase from the measured d -spacing, as shown in Table 4.3.

Table 4.3 Measured d -spacings for Ga samples and d-spacings from ICSD database.

Measured Ga# 1 d -spacings (\AA)	Measured Ga# 2 d -spacings (\AA)	α -Ga orthorhombic <i>Bmab</i> no 64	β -Ga monoclinic <i>C2/c</i> no 12	γ -Ga orthorhombic <i>Cmca</i> no 63	Ga orthorhombic <i>Cmca</i> no 63
		$a = 4.519 \text{ \AA}$ $b = 4.526 \text{ \AA}$ $c = 7.658 \text{ \AA}$	$a = 2.776 \text{ \AA}$ $b = 8.053 \text{ \AA}$ $c = 3.332 \text{ \AA}$	$a = 10.593 \text{ \AA}$ $b = 13.523 \text{ \AA}$ $c = 5.203 \text{ \AA}$	$a = 2.90 \text{ \AA}$ $b = 8.13 \text{ \AA}$ $c = 3.17 \text{ \AA}$
3.759	3.819	3.82900	4.02650 (020)	5.29650 (200)	4.06700
2.934	2.946	2.95093	3.33200 (001)	4.41400 (1-11)	2.73158
2.603	2.712	2.92323	2.61452 (110)	2.77970 (330)	2.50023
2.243	2.652	2.26300	2.56608 (021)	2.62053 (150)	2.06931
1.941	2.502	2.25950	2.01325 (040)	2.60152 (200)	2.03350
1.915	2.253	1.99501	1.92575 (1-30)	2.49938 (241)	1.98054
1.755	1.985	1.95632	1.66495 (002)	2.48346 (112)	1.71161
1.645	1.991	1.94819	1.64950 (131)	1.98476 (351)	1.67967
1.390		1.94595	1.39200 (1-50)	1.85585 (402)	1.58500
		1.91459			1.47681
		1.78772			1.45000
		1.76324			1.36579
		1.59894			1.35567
					1.29502

4.2 Results

4.2.1 Crystal and electronic structure of the Ga phases

Figure 4.2(c) summarizes the unit cell structure for each of the four solid Ga phases. With a melting point of $T_m = 302.9$ K, α -Ga is the only stable phase for bulk gallium

at atmosphere pressure. It crystallizes in a face-centered orthorhombic structure with space group symmetry $Bmab$ (no. 64) and a unit cell that contains eight atoms [81, 85, 86]. β -Ga, with a melting point of 256.8 K, is one of the metastable phases of Ga and has a face-centered monoclinic structure with space group symmetry $C2/c$ (no. 15) and four atoms in the unit cell [82, 85]. γ -Ga is also a metastable phase in bulk with a similar melting point (253.8 K) but is stable at room temperature in the form of Ga NPs. It has a more complicated crystalline structure consisting of an orthorhombic unit cell with $Cmcm$ (no. 63) space group symmetry and 40 atoms in it [83]. Finally, δ -Ga has the lowest melting point (237.6 K) with a rhombohedral crystallographic cell whose space group symmetry is $R-3m$ (no. 166) with 22 atoms in the unit cell [84].

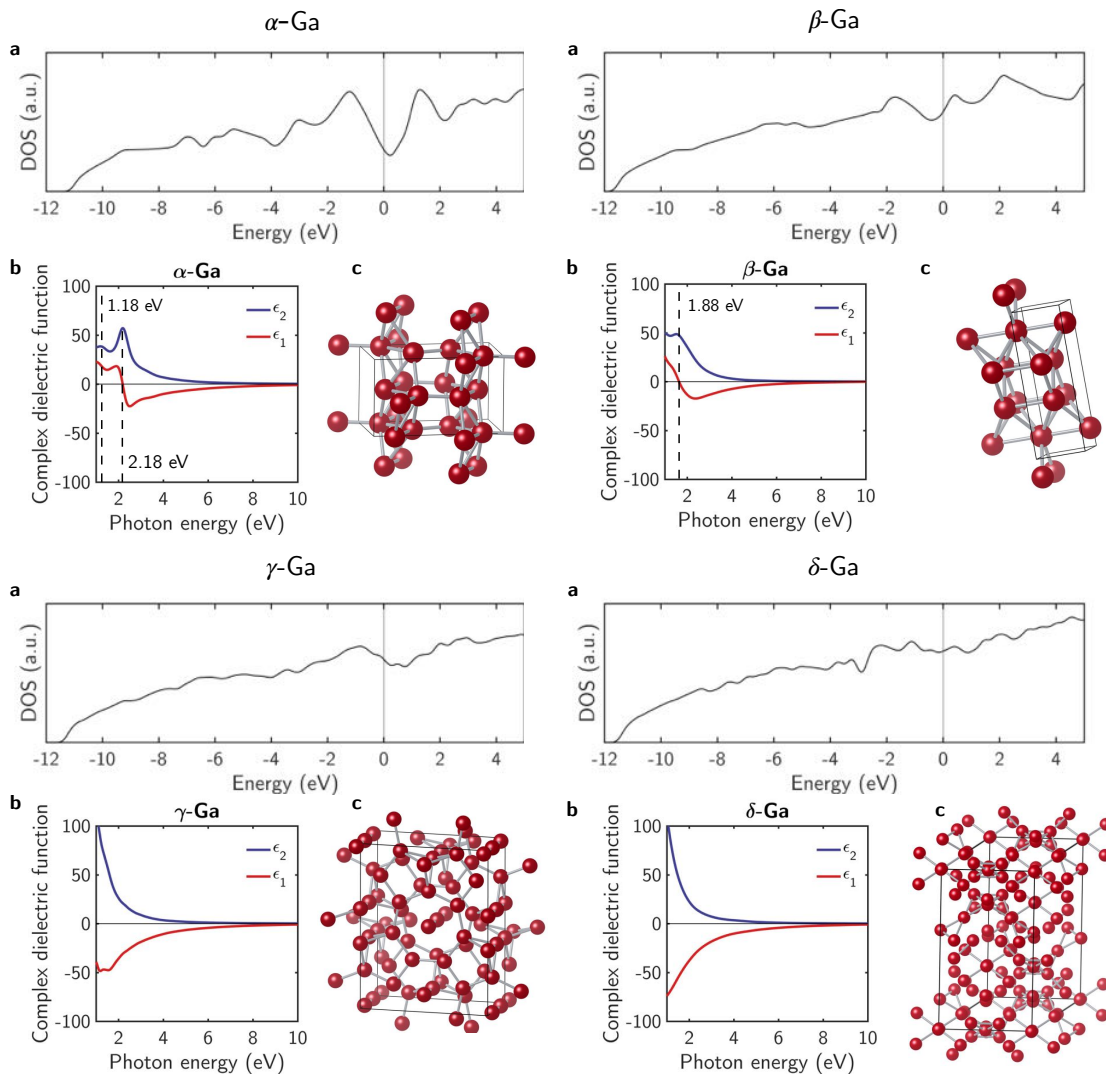


Figure 4.2 (a) Density of states (DOS), (b) complex dielectric function and (c) structure of the unit cell of α -Ga, β -Ga, γ -Ga and δ -Ga.

Table 4.4 Lattice constants and structural parameters of α -Ga, β -Ga, γ -Ga and δ -Ga.

α -Ga			β -Ga		
Property	This work	Exp. [81]	Property	This work	Exp. [82]
Lattice parameters			Lattice parameters		
$ a $ (Å)	4.528	4.511	$ a $ (Å)	2.777	2.766
$ b $ (Å)	4.494	4.517	$ b $ (Å)	8.062	8.053
$ c $ (Å)	7.645	7.645	$ c $ (Å)	3.215	3.332
θ_{bc} (°)	90.00	90.00	θ_{bc} (°)	90.00	90.00
θ_{ac} (°)	90.00	90.00	θ_{ac} (°)	90.01	92.02
θ_{ab} (°)	90.00	90.00	θ_{ab} (°)	90.00	90.00
Coordinates			Coordinates		
x_{GaI}	2.2639	2.2553	x_{GaI}	1.4044	1.3830
y_{GaI}	0.3737	0.3544	y_{GaI}	2.9525	2.9715
z_{GaI}	5.0118	4.9882	z_{GaI}	2.4377	2.4990
γ -Ga			δ -Ga		
Property	This work	Exp. [83]	Property	This work	Exp. [84]
Lattice parameters			Lattice parameters		
$ a $ (Å)	10.540	10.593	$ a $ (Å)	9.063	9.087
$ b $ (Å)	13.395	13.523	$ b $ (Å)	9.063	9.087
$ c $ (Å)	5.178	5.203	$ c $ (Å)	16.869	17.020
θ_{bc} (°)	90.00	90.00	θ_{bc} (°)	90.00	90.00
θ_{ac} (°)	90.00	90.00	θ_{ac} (°)	90.00	90.00
θ_{ab} (°)	90.00	90.00	θ_{ab} (°)	120.00	120.00
Coordinates			Coordinates		
x_{GaI}	0.0000	0.0000	x_{GaI}	0.0000	0.0000
y_{GaI}	0.0072	0.0121	y_{GaI}	0.0000	0.0000
z_{GaI}	1.2945	1.3007	z_{GaI}	0.0000	0.0000
x_{GaII}	2.9245	2.9596	x_{GaII}	1.3082	1.3111
y_{GaII}	0.6974	0.6815	y_{GaII}	2.2655	2.2717
z_{GaII}	1.2945	1.3007	z_{GaII}	5.6231	5.6733
x_{GaIII}	0.0000	0.0000	x_{GaIII}	2.5175	2.5156
y_{GaIII}	5.2779	5.3375	y_{GaIII}	0.0000	0.0000
z_{GaIII}	0.0171	0.0000	z_{GaIII}	1.0720	1.0847
x_{GaIV}	1.3144	1.3304	x_{GaIV}	0.7896	0.7948
y_{GaIV}	2.7618	2.7884	y_{GaIV}	1.3671	1.3766
z_{GaIV}	1.2945	1.3007	z_{GaIV}	3.0256	3.0142
x_{GaV}	2.4064	2.4173	x_{GaV}	1.8222	1.8283
y_{GaV}	1.8628	1.8769	y_{GaV}	3.1561	3.1790
z_{GaV}	-1.2945	-1.3007	z_{GaV}	1.5082	1.5261
x_{GaVI}	0.0000	0.0000			
y_{GaVI}	2.8624	2.9033			
z_{GaVI}	-1.2945	-1.3007			

Using density functional theory (DFT) calculations implemented on SIESTA [96] and minimizing energy using the standard conjugate-gradients technique, we derived the theoretical lattice parameters and atomic positions as reported in Table 4.4. Their reliability can be assessed by the favorable comparison with experimentally obtained values also reported in the table. The densities of states (DOS), reported in Fig. 4.2(a), show an evolution from α -Ga to δ -Ga phases that goes from a very smooth DOS in this latter case, characteristic of metallic delocalized bonds, to a more jagged profile in the former case, indicating charge localization and a behavior closer to an insulating phase (dielectric character). The α -Ga DOS presents two characteristic humps above and below the Fermi energy that correspond with two nearly parallel bands associated to bonding-antibonding behavior due to covalent bonding. The electronic structure of β -Ga also exhibits some covalent behavior, its DOS present humps above and below Fermi energy and some parallel bands along some high symmetry lines, but several other bands cross the Fermi level exhibiting metallic behavior (see Fig. 4.3). In the case of γ -Ga and δ -Ga, the DOS clearly exhibits metallic behavior since bands are continuously crossing the Fermi level although in the former a dip in the DOS close to the Fermi energy is clearly reflected in the imaginary part of the dielectric function.

Based on these band structures and the dipolar transition matrix elements between occupied and unoccupied single-electron eigenstates, the interband component to the complex dielectric function ($\epsilon(\omega) = \epsilon_1(\omega) + i\epsilon_2(\omega)$) is calculated for the different phases using first-order time-dependent perturbation theory as implemented in SIESTA [96]. The calculated complex dielectric function for each phase is shown in Fig. 4.2(b). The evolution of dielectric function spectra is clearly observed, from interband transitions in α -Ga and β -Ga below 2.5 eV to Drude-like metallic characteristics in γ -Ga and δ -Ga. Specifically, the frequency dependent complex dielectric functions of α -Ga and β -Ga manifest interband transitions ($\epsilon_1(\omega) > 0$): at 1.18 eV and 2.18 eV for α -Ga, and at 1.88 eV for β -Ga. The interband transitions responsible for these features in $\epsilon(\omega)$, indicated with arrows in Fig. 4.3, have been identified by evaluating the values of the optical matrix element $M_{cv\mathbf{k}}$ for every pair of conduction (c) and valence bands (v) at each \mathbf{k} point along the high symmetry lines in the first Brillouin zone. Notice that the highlighted transitions occur in the regions with parallel bands characteristic of a covalent solid. By contrast, the dielectric function of both γ -Ga and δ -Ga are very typical of good metals ($\epsilon_1(\omega) < 0$).

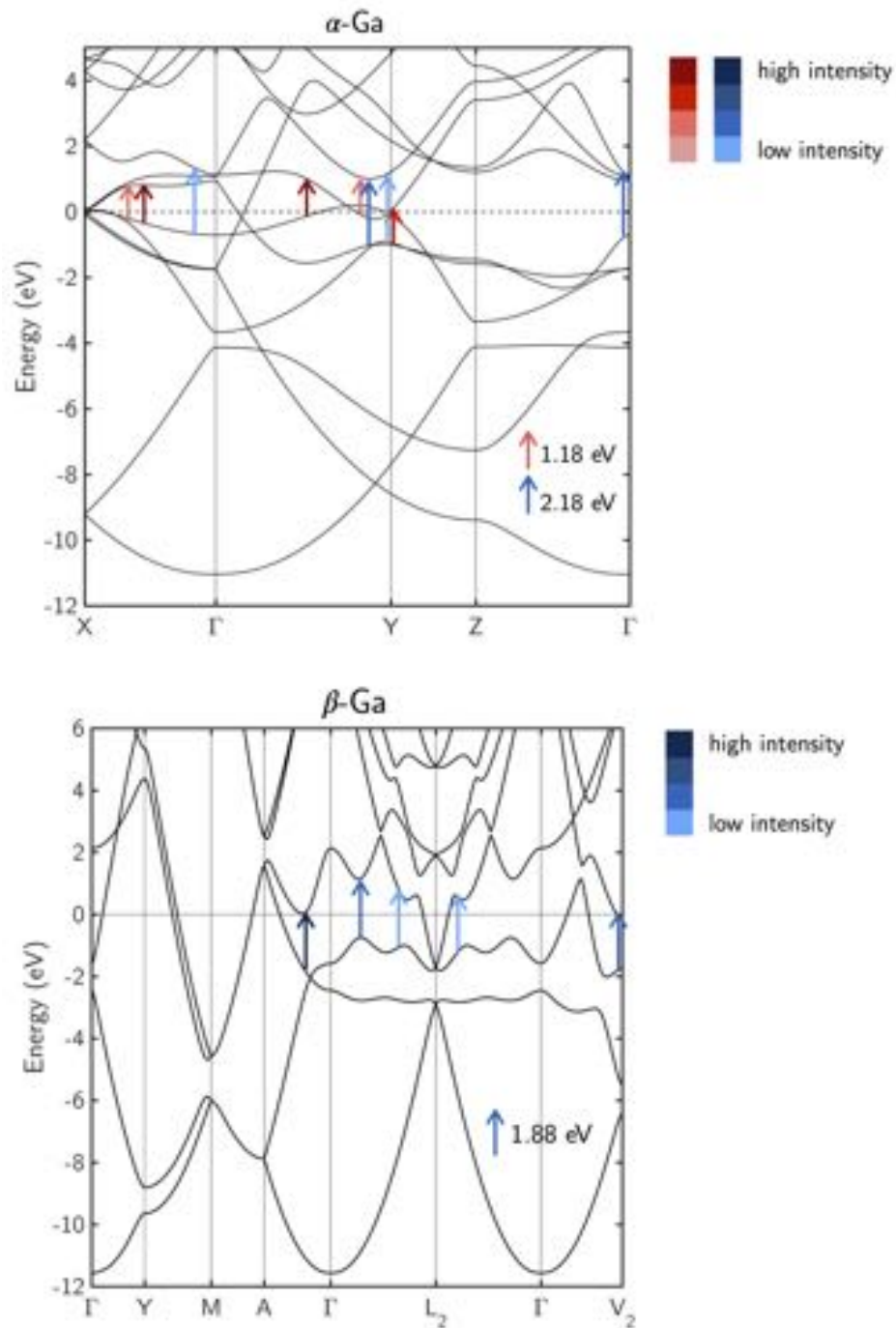


Figure. 4.3 Band diagram of (top) α - and (bottom) β - Ga. With arrows are indicated the interband transitions appearing in the complex dielectric function of α - and β -Ga at 1.18 (red arrows) and 2.18 eV (blue arrows), and 1.88 eV (blue arrows), respectively. With a color code is represented the intensity of the transition based on the evaluation of the optical matrix element M_{cvk} .

In Fig. 4.4(a), the calculated dielectric functions of α -Ga and β -Ga are compared to the reported experimental spectra of solid Ga containing both α -Ga and β -Ga phases [8–10]. The agreement above 3 eV is excellent, while the experimental results below 3 eV are intermediate between the α -Ga and β -Ga phases, as indicated by the dotted lines in Fig. 4.4(a). These differences suggest the experimentally measured solids were a mixture of α -Ga and β -Ga phases, especially since those reports provided no confirmation of the structural purity of the crystallographic phases. Indeed, using the dielectric function of the different phases, we may be able to estimate the contributions of each phase in each sample measured.

To demonstrate this, we have fabricated two solid Ga thin film samples under different cooling conditions, then we measured their ellipsometric spectra and fitted them with the Bruggeman effective medium approximation (BEMA) using a volumetric weighting of two pure phases [105]. The goodness of these fits have been evaluated using the R -square coefficient of determination, and values for each of these fittings are gathered in Table 4.5. For comparison, in Table 4.6 we show the R -square values obtained by fitting the ellipsometric spectra of both samples using the methodology used in Ref. [23]: a weighted average of α -Ga and l -Ga. By comparing both methods, the advantage of the approach proposed here becomes clear. Bruggeman effective medium approximation is the most suitable model since our samples are constituted by a completely random inhomogeneous media whose components are treated symmetrically [105]. Spectroscopic measurements were performed at two locations on each sample (blue and red curves in Figs. 4.4(b,c)), and any differences may be attributed to variability in the distribution of phase mixtures across the samples. For sample Ga#1, formed by rapidly cooling to 243K, Fig. 4.4(b) shows that the spectra at both locations are nearly identical in the metallic regime above 2.5 eV. The best-fit is obtained with a BEMA mixture of 45% α -Ga : 55% β -Ga, a result is consistent with the XRD analysis (see Table 4.3). Discrepancies at lower energies (inset of Fig. 4.4(b)) arise from defects, grain boundaries, and other imperfections in the sample, but the plateauing caused by interband transitions is appropriately captured. For sample Ga#2, formed by slowly cooling to 123K, Fig. 4.4(c) reveals a larger difference in the spectra measured at two locations, but they may both be reproduced with a BEMA mixture of α -Ga and γ -Ga, again consistent with XRD analysis. Interestingly, the α -phase interband transition at 2.18 eV becomes an indicator of the α -Ga to γ -Ga ratio, and the best fit of the two measured spectra reveals a $\pm 10\%$ variability in volume fraction of the two phases: 25% α -Ga : 75% γ -Ga for the red curve and 35% α -Ga : 65% γ -Ga for the blue curve.

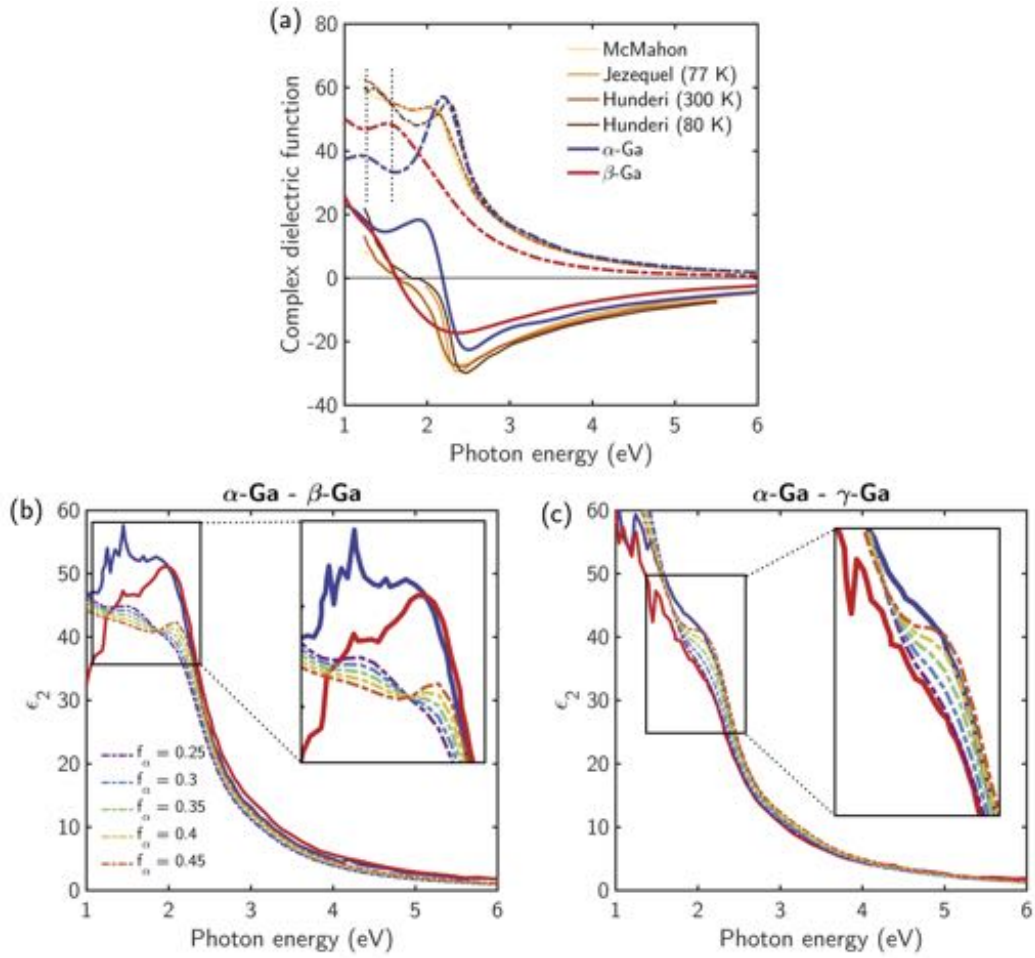


Figure. 4.4 (a) Comparison of measured complex dielectric function of Ga reported by several authors [8–10] and the calculated dielectric function of α -Ga (blue curve) and β -Ga (red curve) for which continuous lines correspond to the real part of the dielectric function and dot-dashed lines correspond to its imaginary part. Ellipsometric measurements of the pseudo-dielectric function (solid lines) of samples with (b) α -Ga/ β -Ga and (c) α -Ga/ γ -Ga content at a 70° angle of incidence for two sample locations (red and blue curves). The dashed lines represent the Bruggeman effective dielectric functions obtained through the mixture of the corresponding theoretical dielectric functions, for which the parameter f_α represents the volume fraction of α -Ga in the sample.

From this we may conclude that the ratio of the coexisting phases may be quantitatively estimated through a simple spectroscopic analysis of Ga samples. Both the analysis of the reported experimental data and the analysis of the dielectric function of solid Ga available in literature, shows that cooling liquid Ga always produces a mixture of different phases. By fitting the experimental data with a BEMA mixture using the

calculated dielectric functions, we provide a tool for estimating the composition of solid Ga films as well as the volumetric fraction of each phase in the samples.

Table 4.5 R -square coefficient of determination for fitting the experimental values with the imaginary part of the dielectric constant of α -Ga/ β -Ga (sample Ga#1) and α -Ga/ γ -Ga (sample Ga#2) to those calculated through Brueggemann EMT using a filling fraction of the α -phase f_α . These fittings are shown in Figs. 4.4(b,c) in the main text.

f_α	α -Ga/ β -Ga (sample Ga#1)		α -Ga/ γ -Ga (sample Ga#2)	
	Blue experimental line	Red experimental line	Blue experimental line	Red experimental line
0.25	0.8878	0.8415	0.9445	0.9331
0.30	0.9154	0.8704	0.9464	0.9424
0.35	0.9377	0.8936	0.9471	0.9501
0.40	0.9553	0.9114	0.9464	0.9563
0.45	0.9681	0.9241	0.9446	0.9609

Table 4.6 R -square coefficient of determination for fitting the experimental values with the imaginary part of the dielectric constant of sample Ga#1 and sample Ga#2 with those calculated through a weighted average of α -Ga and l -Ga using a filling fraction of the α -phase f_α . This methodology is used in Ref. [23] to model the dielectric function of solid Ga

f_α	α -Ga/ β -Ga (sample Ga#1)		α -Ga/ γ -Ga (sample Ga#2)	
	Blue experimental line	Red experimental line	Blue experimental line	Red experimental line
0.10	0.5549	0.3170	0.7509	0.8011
0.20	0.6481	0.4590	0.8185	0.8704
0.30	0.7255	0.5817	0.8696	0.9192
0.40	0.7874	0.6850	0.9044	0.9478
0.50	0.8335	0.7689	0.9227	0.9559
0.60	0.8640	0.8335	0.9245	0.9437
0.70	0.8789	0.8787	0.9099	0.9112
0.80	0.8781	0.9046	0.8790	0.8583
0.90	0.8616	0.9111	0.8315	0.7851

4.2.2 Implications of Ga phases in plasmonic nanostructures

In order to evaluate the performance of the Ga-phases in different plasmonic systems, we have theoretically analyzed two different metrics: one related to extended modes such as surface plasmon polaritons (SPPs) in thin films, and other related to localized surface

plasmons (LSPs) in nanoparticles. In the quasistatic approximation, we respectively define these two quality factors as $Q_{SPP} = \epsilon_1^2/\epsilon_2$ and $Q_{LSP} = -\epsilon_1/\epsilon_2$ [106]. Within this approximation, the Fröhlich energy ($\epsilon_1 = -2$) corresponds to the energy at which localized surface plasmon resonances (LSPRs) may be excited in isolated metallic particles whose size is much smaller than the incident illumination wavelength. Figure 4.5 plots the spectral values of Q_{SPP} and Q_{LSP} for each of the Ga phases. The largest values of Q_{SPP} are achieved by l -Ga ($Q_{SPP} = 150$), δ -Ga (65), and γ -Ga (50) at energies below 2.5 eV. The more covalent solids, α -Ga and β -Ga, have much smaller Q_{SPP} values, and they fall to $Q_{SPP} = 0$ at the interband transition energies (2.18 eV for α -Ga and 1.88 eV for β -Ga). The high contrast in the values of Q_{SPP} values between l -, γ -, δ -Ga and α -, β -Ga below 2.5 eV points out the possibility of building plasmonic switches by the structural transformation of Ga from l -, γ - or δ -phases to the α - or β -phase. For each analyzed phase, Q_{LSP} exhibits a broad resonance, with a peak near 8 eV in accordance with the Fröhlich energy, except for β -Ga whose peak is near 6.5 eV. This makes Ga an excellent candidate for UV plasmonic applications, regardless of its phase. Since the more metallic phases should have greater plasmonic performance than the more covalent phases, the Q_{LSP} spectra confirm that the most efficient phase for LSPR generation is l -Ga, followed by δ -Ga and γ -Ga, while β -Ga and α -Ga are inferior but still retain plasmonic behavior above 2.5 eV.

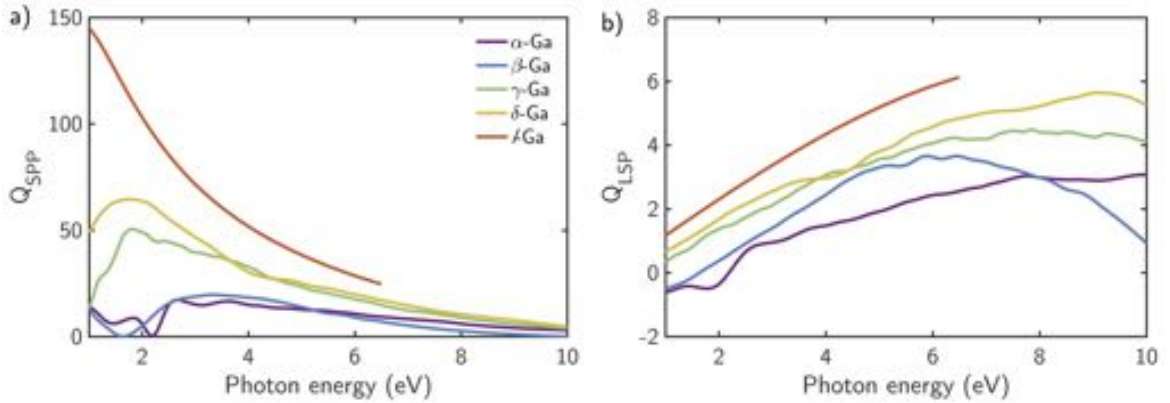


Figure. 4.5 (a) Q_{SPP} and (b) Q_{LSP} spectra for each of the analyzed phases for a Ga NP.

Gallium layers have been used for waveguides, plasmonic switches, and phase changing devices in which α -Ga and/or l -Ga homogeneous phases were assumed [46–48]. However, considering that a pure α -Ga solid phase film cannot be achieved simply by cooling liquid Ga, we simulated the reflectance spectra of α -Ga/ β -Ga and α -Ga/ γ -Ga thin films by varying the content of the α -phase. Figure 4.6 shows the

normal incidence reflectance spectra (angle of incidence $\text{AOI} = 0^\circ$) of α -Ga/ β -Ga and α -Ga/ γ -Ga thin films on a Si substrate, calculated using the Transfer Matrix Method (TMM) [103] by varying the α -phase fraction f_α . For normal incidence, both polarizations are equivalent. The dielectric function in each case has been calculated using the Bruggeman effective medium theory for mixing both phases, and the film thicknesses have been chosen to mimic the thicknesses used in actual devices ($h = 20$ and 150 nm) [46–48]. It can be seen that the reflectance spectra vary significantly with h and f_α between the limits set by the pure phases, indicating that a simple spectral reflectance measurement could be used to identify the relative content of each phase in the sample. The variation with f_α for α -Ga/ γ -Ga is greater because it represents a mixture of covalent and metallic phases, especially below 2.5 eV where the evolution from interband transitions in α -Ga contrasts most strongly with the Drude-like behavior of γ -Ga. The differences between α -Ga/ β -Ga are smaller since both of them have interband transitions below 2.5 eV and metallic character above 2.5 eV.

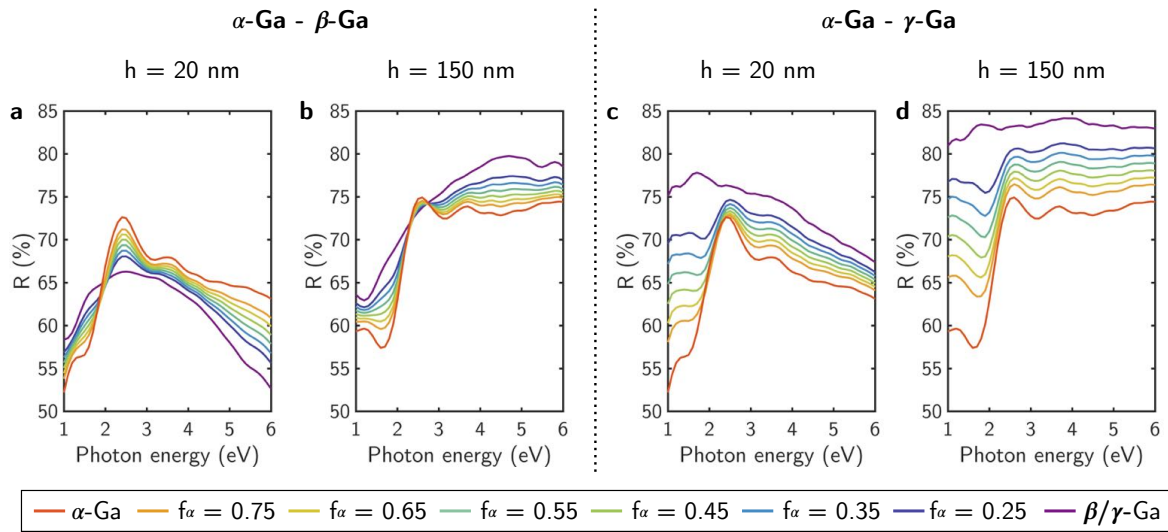


Figure 4.6 Reflectance spectra (R) of α -Ga/ β -Ga (a, b) and α -Ga/ γ -Ga (c, d) thin films on a sapphire substrate (refractive index $n=1.78$). The dielectric function considered in each case is calculated through the Bruggeman effective medium approximation, with the α -phase filling fraction f_α indicated in the legend. The thin films have thicknesses of $h = 20$ (a, c) and 150 nm (b, d) and are illuminated at normal incidence ($\text{AOI} = 0^\circ$).

Synthesized solid Ga nanoparticles have been reported to present the coexistence of different phases whose structural transformation can be driven by low power (\approx nW) optical or e -beam excitation [107, 89]. In order to model the plasmonic response of these NPs, and due to the lack of information on the dielectric dispersion profiles of the

different Ga-phases, the optical properties of the Ga polymorphs were approximated through the linear combination of the dielectric function of l - and α -Ga [107, 93, 23]. Therefore, we have simulated the plasmonic response of NPs with different geometries made of the different Ga-phases. Figure 4.7(a-c) shows the absorption cross-section spectra C_{abs} of spherical NPs and nanorods made of the different Ga phases. Both have radii of $R = 10$ nm, while the nanorods are $L = 250$ nm long.

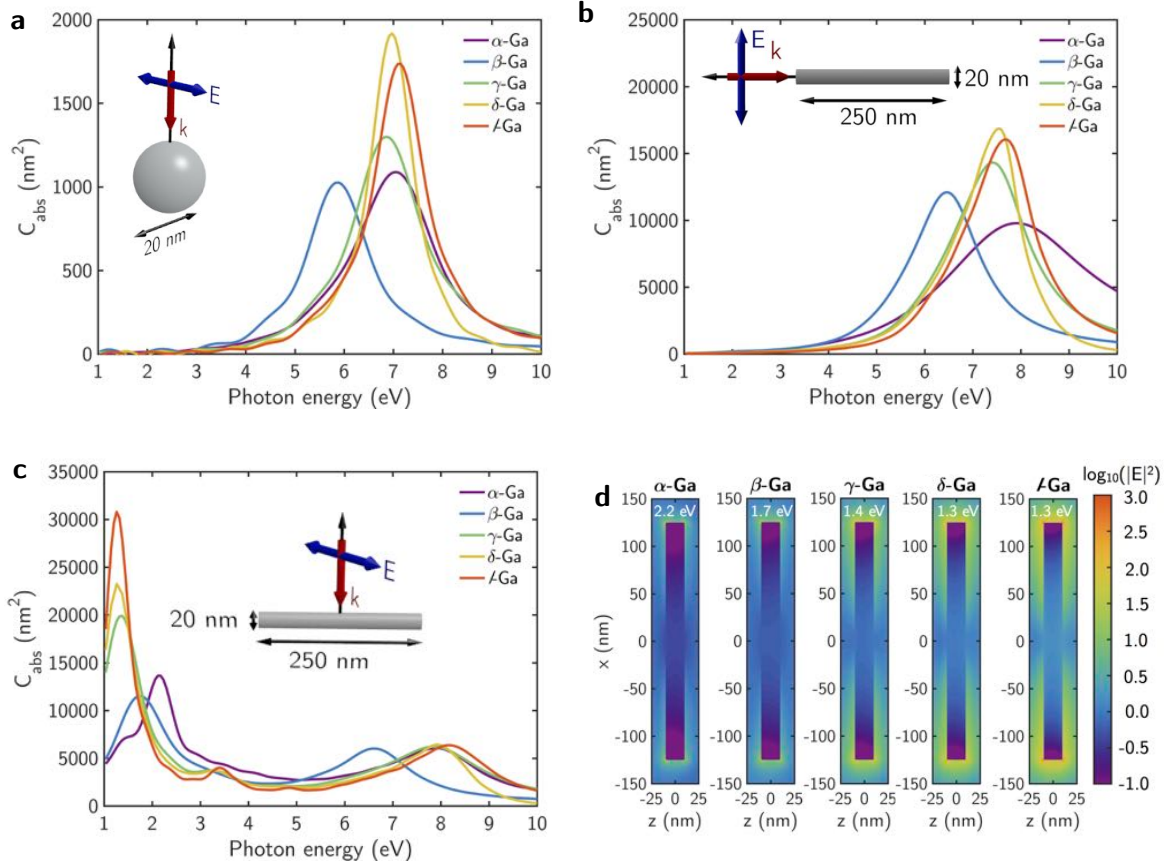


Figure. 4.7 (a) Absorption cross-section (C_{abs}) of spherical NPs with radius $R = 10$ nm made of the different Ga-phases. (b,c) C_{abs} of nanorods of length $L = 250$ nm and radius $R = 10$ nm made of the different Ga-phases: (b) nanorod illuminated along its symmetry axis, and (c) nanorod illuminated perpendicular to it with a polarization angle 45°. The insets indicate the propagating direction of the illuminating beam (\mathbf{k}) and its polarization (\mathbf{E}). (c) Near-field ($\log_{10}(|\mathbf{E}|^2)$) color maps of the nanorods made of each Ga-phase, excited at their low energy (longitudinal) mode.

Because the nanospheres are so much smaller than the wavelengths considered, only the electric dipolar mode of each phase is observed, with an ultraviolet plasmonic resonance near 7 eV for all phases except β -Ga, whose peak is near 6 eV. Similar results present the nanorod illuminated along its symmetry axis. In these two cases, l -

and δ -Ga phases show the highest values of C_{abs} , followed by γ -, β -, and α -Ga. The simulated excitation beam for the rods was polarized 45° from the rod axis so that both longitudinal and transverse modes were excited. The intensity of each plasmonic transverse dipolar mode (near 8 eV except for β -Ga near 6.5 eV) is very similar for all phases because they each have a metallic character at these energies. On the contrary, the longitudinal mode resonances occurred below 2.5 eV where α - and β -Ga undergo interband absorption while γ -, δ -, and l -Ga remain Drude-like. Consequently, the C_{abs} for α - and β -Ga are lower than for the rest of the phases. It is important to point out that depending on the metallic/dielectric character of the Ga phase at the resonant energy the nature of the resonance is different. In the case of those phases with metallic behavior (i.e., γ -, δ -, and l -Ga in all spectral range and α - and β -Ga above ≈ 2.5 eV. See Figures 1(b)) the resonance has a purely plasmonic nature (oscillation of the conduction electrons). However, for those phases with dielectric character ($\epsilon_1(\omega) > 0$, i.e., α - and β -Ga below ≈ 2.5 eV) the peaks are attributed to the Mie resonances whose origin comes mainly from the displacement currents inside the NPs due to the bound electrons contribution. The near-field electric field enhancement maps ($\log_{10}(|\mathbf{E}|^2)$) shown in Fig. 4.7(d) confirm the maximum absolute value for the longitudinal mode increases with the free-electron behavior of the Ga-phase considered. In this way, the value of the near-field enhancement increases as Ga progresses from the α - and β - to the γ -, δ -, and l -phases.

The utility of this becomes clear when these plasmonic structures are used for surface enhanced Raman spectroscopy (SERS) or surface enhanced fluorescence (SEF) spectroscopy in which target molecules adsorb on the surface of the NPs. Figure 4.8 compares the spectral absorption cross-section (C_{abs}) and near-field enhancement ($\langle |\mathbf{E}|^2 \rangle$) averaged over the surface of Ga hemispheres with radius $R = 60$ nm and supported by a sapphire substrate. Spectroscopic signatures from adsorbed target molecules are greatest at a given photon energy when NPs have a large near-field enhancement over as much of the surface as possible. For each solid phase, each curve exhibits two resonant modes: one at low energy (between 1.5 - 2 eV which for α - and β -Ga are Mie resonances and for the rest of the phases are plasmonic modes) and another at higher energies (between 4.5 - 5 eV a plasmonic nature for all considered phases). The low energy C_{abs} peak is blue-shifted (≈ 0.2 eV) with respect to the low energy $\langle |\mathbf{E}|^2 \rangle$ peak, but both curves share the same high energy peak. Since the values of $\langle |\mathbf{E}|^2 \rangle$ for the high energy mode are higher, it is the more appropriate mode for surface-enhanced spectroscopy. Fortunately, a far-field measurement of this high energy resonant mode can be used to tune the laser energy to achieve the maximum near-field

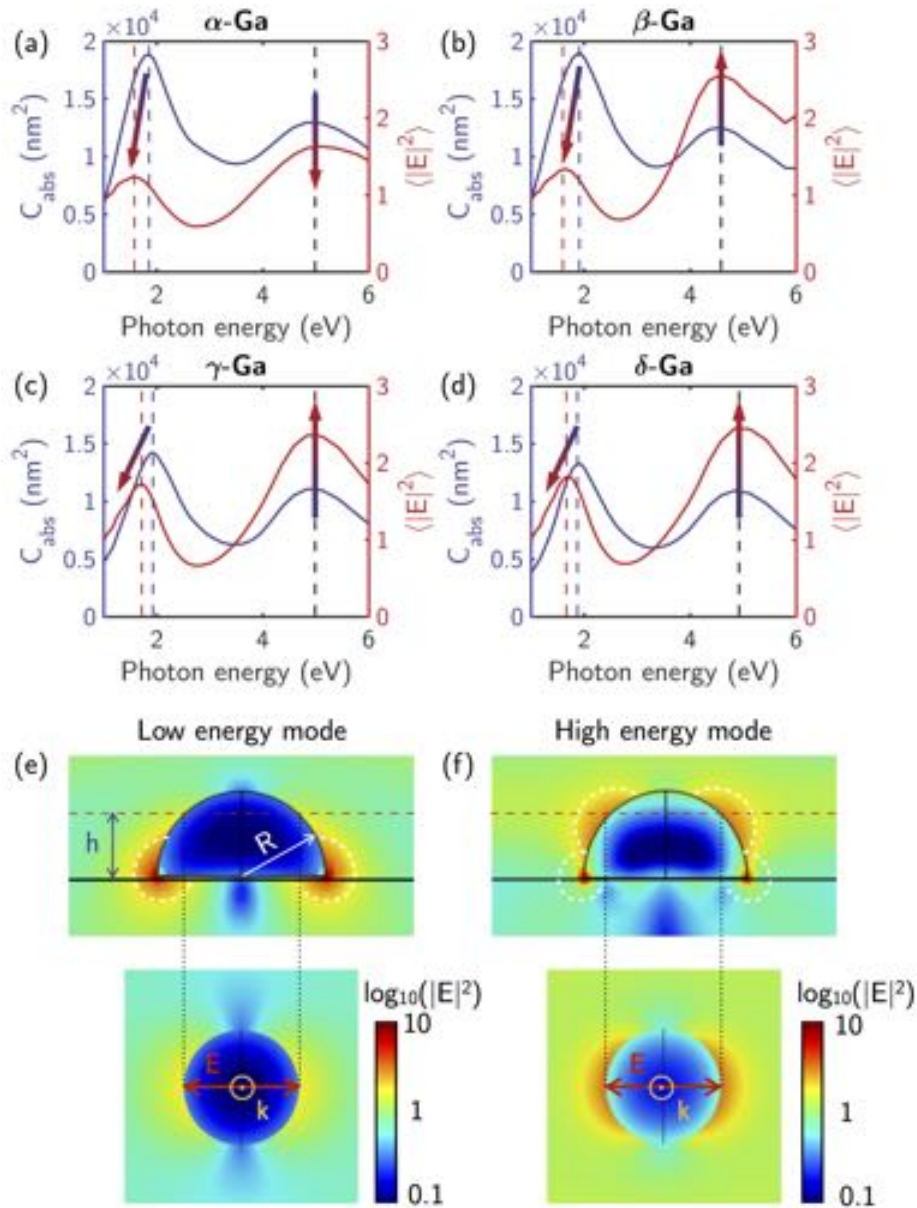


Figure. 4.8 Absorption cross-section (C_{abs} , blue curve) and near-field enhancement ($\langle |\mathbf{E}|^2 \rangle$, red curve) averaged over the surface of a $R = 60$ nm (a) α -Ga, (b) β -Ga, (c) γ -Ga, and (d) δ -Ga hemispherical NP on a sapphire substrate. Near-field distribution ($\log_{10}(|\mathbf{E}|^2)$) of the (e) low and (f) high energy modes. The top panels show the plane containing the wave (\mathbf{k}) and electric field vector (\mathbf{E}). The bottom panels present $\log_{10}(|\mathbf{E}|^2)$ in a plane lifted $h = 45$ nm above the substrate, near where most adsorbates will attach. Although the near-field maps correspond to δ -Ga, the near-field distribution is the same for all phases.

enhancement. And comparison of the near-field distribution of both modes reveals that the low energy mode exhibits a greater but more spatially localized enhancement, while the high energy resonant mode is slightly weaker but more evenly distributed above the surface. Thus, this high energy mode is advantageous for surface enhanced spectroscopy, since the location of the molecules on the surface is not as critical, while the low energy mode produces hot spots localized at the interface with the support and requires target molecules to be placed precisely to achieve maximum enhancement.

4.3 Conclusions

In summary, we report the first detailed analysis of the optical properties of the different α -, β -, γ - and δ -Ga phases and its correlation with their crystalline and electronic structures. It is found that there are significant differences in the dielectric function of the various Ga polymorphs, especially in the spectral region below 2.5 eV, with interband transitions in α - and β -Ga and Drude metallic behavior for γ -Ga and δ -Ga. Until present, although the different phases have been identified in confined systems (nanostructures), the lack of information on the dielectric dispersion of the different Ga-phases has hampered the accurate electromagnetic modeling of this Ga nanostructures, pushing experimentalists to approximate the optical constants as linear combinations of the liquid and solid (α -Ga) phase [107, 93]. Furthermore, we demonstrate that optical constants attributed to α -Ga in the literature [8–10], obtained by supercooling l -Ga, actually corresponds to the mixture of α - with other Ga phases. XRD analysis of our thin film samples, shows that cooling l -Ga always produces a mixture of different phases, either α -/ β -Ga or α -/ δ -Ga depending on the cooling rate. In light of this, we propose a new approach for estimating the phase composition and concentration of solid Ga films by fitting measured dielectric function spectra with a Bruggeman effective medium approximation using the calculated dielectric functions for the pure phases. Bearing this in mind, we have evaluated the electromagnetic response of localized and surface plasmons (LSPs and SPPs) excited in nanostructures and films of Ga polymorphs by showing their different electromagnetic behavior from NIR to UV. The results of this research will facilitate the controllable use of Ga for phase change applications in photonics and plasmonics by allowing the design and accurate modeling of these Ga-based active phase-change plasmonics systems. Finally, this work opens new paths for preparing “à la carte” Ga plasmonic devices.

Chapter 5

Dielectric Function of High-Pressure Gallium Phases

In the previous chapter we paid attention to the wide polymorphism of Ga at atmospheric pressure. At this pressure, depending on temperature, Ga can exist in six different phases (see Fig. 5.1(a)): above 302.7 K Ga is a liquid metal (*l*-Ga), and below that temperature, α -Ga is the only stable phase [5]. At lower temperatures, there are several metastable Ga-phases: β -Ga with a melting temperature of $T_m = 256.8$ K [82], γ -Ga ($T_m = 237.6$ K) [83], ϵ -Ga ($T_m = 244.6$ K) [108] and δ -Ga ($T_m = 253.8$ K) [84].

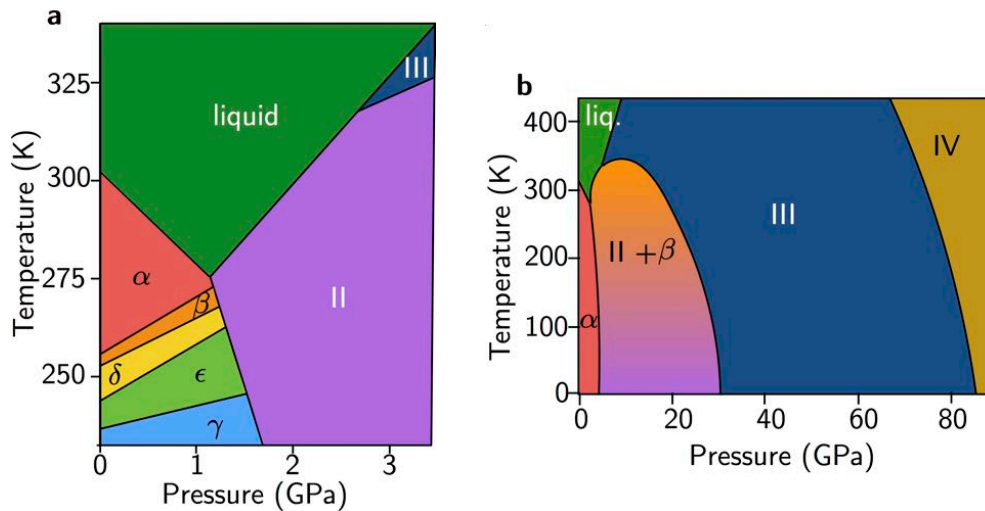


Figure. 5.1 (a) Phase diagram of bulk Ga adapted from Ref. [5] and (b) extended pressure temperature phase diagram adapted from Ref. [11].

This characteristic polymorphism, along with the recently demonstrated plasmonic response of Ga NPs that span from the near-infrared to the UV [43, 90] and low oxidation

tendency [109, 4], has presented Ga as a material exploited in phase-change memories [110], reversible light-induced switching [92], phase-change nonlinear systems and the so-called “active plasmonics” [47, 48]. Most of these applications take advantage of the change of reflectivity produced by the phase transition between Ga-phases induced by either optical [93]/e-beam [89] excitation or heating [46]. Indeed, pressure is another parameter to be exploited in active and phase-change plasmonics. Although several high-pressure Ga-phases have been reported in literature (see Fig. 5.1(b)), i.e., Ga(II), Ga(III), Ga(IV) and Ga(V) [111, 11, 112, 95], none of previous studies have reported optical properties of these high-pressure Ga-phases.

In this chapter, we report a comprehensive theoretical investigation of the optical response of Ga(II) and Ga(III), including their correlation with the respective crystalline structures and band diagrams, using dielectric functions calculated by first principles methods. Moreover, we evaluate the plasmonic response of Ga(II) and Ga(III) and we compare it with the plasmonic response of the phase expected at atmospheric pressure to evaluate the plasmon sensitivity to pressure changes. These results open the path for the design of pressure driven phase-change Ga plasmonic devices.

5.1 Methods

5.1.1 Computational Details and Optical Response

Both first-principles and optical response calculations have been performed following the same method presented in Sections 4.1.1 and 4.1.2 of the previous chapter.

Specifically, in this case we have set the equivalent plane wave cut-off to represent the charge density to 800 Ry. For the Brillouin integrations, we use a Monkhorst-Pack [102] sampling of $10 \times 10 \times 10$. In the calculation of the optical response we have used all bands. The optical mesh has been set to $40 \times 40 \times 40$ and the gaussian broadening to 0.20 eV.

5.1.2 Reflectance Calculations

The reflectance calculations have been performed using the Transfer Matrix Method (TMM) [103]. TMM allows the calculation of the reflectance (R), transmittance (T), and absorbance (A) spectra of an arbitrary system of homogeneous, non-magnetic multilayers. We have considered Ga films of thickness $h = 150$ nm deposited on an infinite sapphire substrate (refractive index $n = 1.78$ [113]) and exposed to air. These value of h have been chosen according to typical experimental values found in the

literature [48, 46]. The angle between the wave-vector \mathbf{k} and the surface's normal (AOI) has been fixed to 0° (normal incidence).

5.2 Results

5.2.1 Crystal and Electronic Structures

Figures 5.2(a,d) summarizes the unit cell for the Ga(II) and Ga(III) phases. Ga(II) crystallizes in a body-centered cubic structure with space group symmetry $I-43d$ (no 220) and a unit cell that contains 12 atoms. Ga(III) crystallizes in a body-centered tetragonal cell with space group symmetry I_4/mmm (no 139) and two atoms in its unit cell.

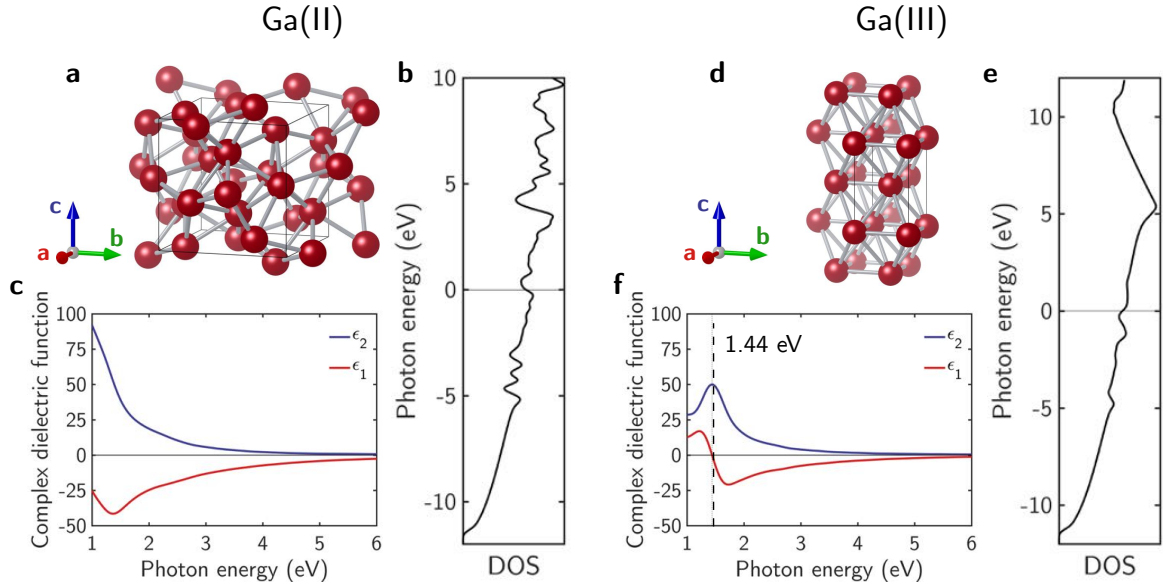


Figure. 5.2 (a,d) Structure of the unit cell, (b,e) density of states DOS and (c,f) complex dielectric function ($\epsilon = \epsilon_1 + i\epsilon_2$) of Ga(II) (left) and Ga(III) (right)

Using density functional theory (DFT) calculations as implemented in SIESTA (see Methods) and minimizing the energy with standard conjugate-gradient techniques, we computed the theoretical lattice parameters and atomic positions as reported in Table 5.1. Their reliability can be assessed by the favorable comparison with the experimentally obtained values also reported in the table. The density of states (DOS) for both phases exhibit metallic behavior although the dip appearing around the Fermi energy is clearly reflected in the optical properties.

Table 5.1 Theoretical lattice constants, structural parameters and atomic coordinates of Ga(II) and Ga(III). Some experimental values are added for reference.

Ga(II)			Ga(III)		
Property	This work	Exp. [5]	Property	This work	Exp. [5]
Lattice parameters			Lattice parameters		
$ a $ (Å)	5.991	5.951 ± 0.005	$ a $ (Å)	2.967	2.813 ± 0.003
$ b $ (Å)	5.991	5.951 ± 0.005	$ b $ (Å)	2.967	2.813 ± 0.003
$ c $ (Å)	5.991	5.951 ± 0.005	$ c $ (Å)	4.109	4.452 ± 0.005
θ_{bc} (°)	90.00	90.00	θ_{bc} (°)	90.00	90.00
θ_{ac} (°)	90.00	90.00	θ_{ac} (°)	90.00	90.00
θ_{ab} (°)	90.00	90.00	θ_{ab} (°)	90.00	90.00
Coordinates			Coordinates		
x_{GaI}	2.247	2.096	x_{GaI}	0.000	0.000
y_{GaI}	0.000	0.000	y_{GaI}	0.000	0.000
z_{GaI}	1.498	1.398	z_{GaI}	0.000	0.000

Based on these band structures and the dipolar transition matrix elements between occupied and unoccupied single-electron eigenstates, the interband contribution to the complex dielectric function ($\epsilon = \epsilon_1 + i\epsilon_2$), is calculated for the different phases using first-order time-dependent perturbation theory as implemented in SIESTA [96]. The interband contribution to the calculated complex dielectric function for each phase is shown in Figs. 5.2(c,f). On the one hand, Ga(II) present metallic behavior ($\epsilon_1 < 0$) in all the studied spectral range. However, the dip in the DOS around the Fermi energy is reflected in the increasing value of ϵ_1 below 1.5 eV. On the other hand, Ga(III) present interband transitions at 1.44 eV. Therefore, below that energy the material has dielectric character ($\epsilon_1 > 0$) whereas above 1.44 eV behaves as a metal ($\epsilon_1 < 0$). These interband transitions are indicated with arrows in Fig. 5.3 and have been identified by evaluating the values of the optical matrix element $M_{c\mathbf{k}}$ for every pair of conduction (c) and valence bands (v) at each \mathbf{k} point along the high symmetry lines in the first Brillouin zone (see Methods). With a color code in the arrows is indicated the intensity of the transition based on the evaluation of $M_{c\mathbf{k}}$.

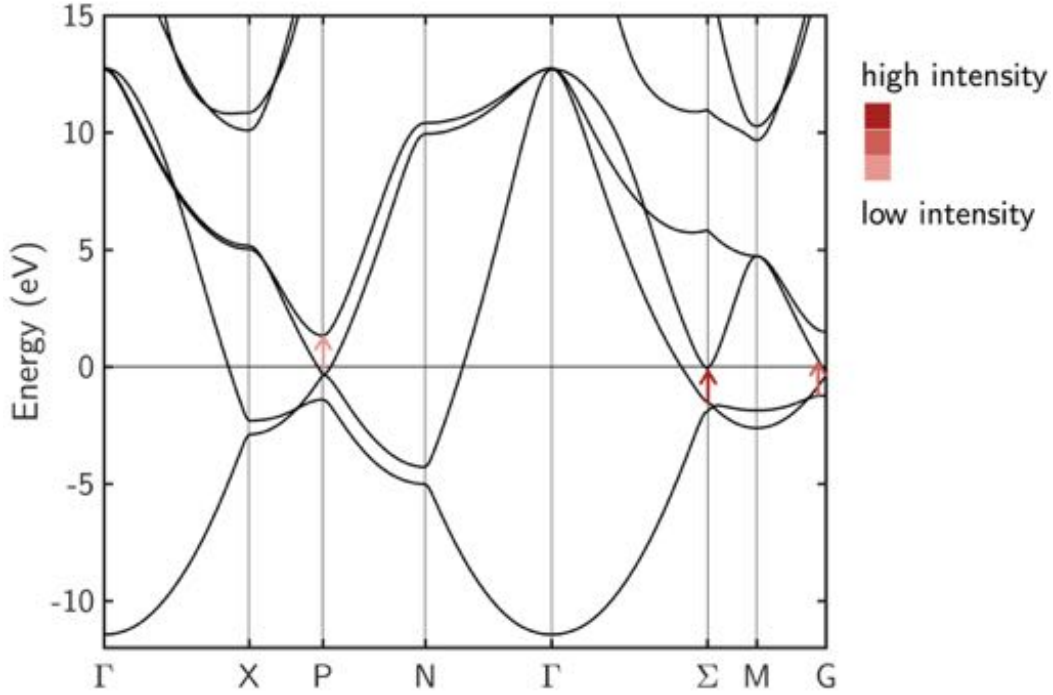


Figure. 5.3 Band diagram of Ga(III). The arrows indicated the interband transitions appearing in its complex dielectric function at 1.44 eV. With a color code in the arrows is indicated the intensity of the transition based on the evaluation of M_{cvk} .

The extended pressure temperature phase diagram reported by Schule and Holzapfel in Ref. [11] shows that Ga(II) coexists with β -Ga (see Fig. 5.1(b)). Therefore, the optical response of Ga in that region should be modeled with an effective complex dielectric function built as mixture of the dielectric functions of Ga(II) and β -Ga respectively. Among the different effective medium approximations, Bruggeman (BEMA) is the most suitable mixing rule to model this system since it is constituted by a completely random inhomogeneous media whose components (Ga(II) and β -Ga) are treated symmetrically [105]. Already in the previous chapter this procedure has been used to model the dielectric function of cooled liquid Ga samples whose XRD spectra have shown to be composed by a mixture of α -/ β -Ga and α -/ γ -Ga. Figure 5.4 shows the effective dielectric function of a mixture of Ga(II) and β -Ga calculated using BEMA with different Ga(II) filling fractions ($f_{\text{Ga(II)}}$). The dielectric function of pure Ga(II) and β -Ga are plotted for reference.

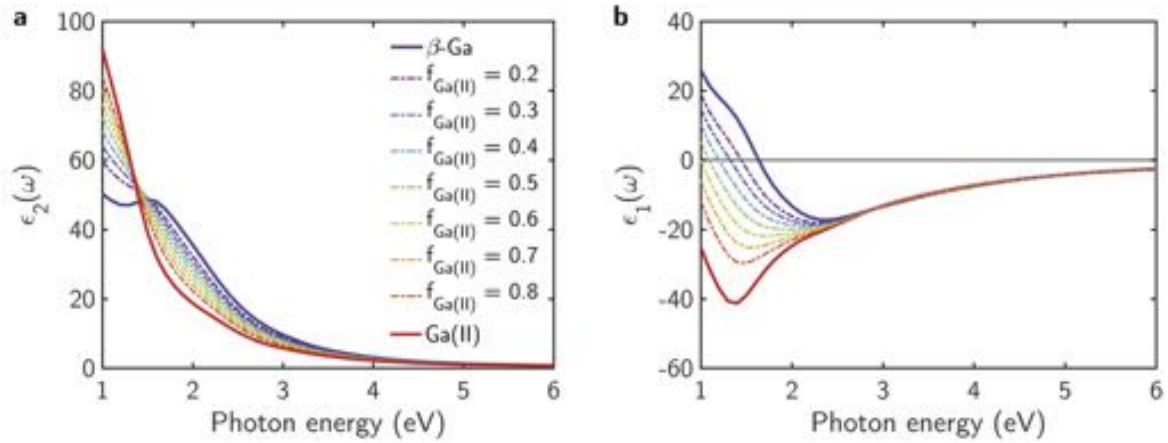


Figure. 5.4 (a) Imaginary and (b) real part of the effective dielectric function ($\epsilon = \epsilon_1 + i\epsilon_2$) of a mixture of Ga(II) and β -Ga obtained using Bruggeman effective medium approximation with different Ga(II) filling fractions $f_{\text{Ga(II)}}$ (dashed lines). With red and blue solid lines are represented the dielectric function of Ga(II) and β -Ga respectively.

5.2.2 Plasmonic Behavior

The plasmonic performance of Ga(II) and Ga(III) phases has been compared with that of other Ga-phases by the evaluation of two metrics related to localized surface plasmons (LSP) in nanoparticles. Within the quasistatic approximation, the Fröhlich frequency (E_{Fr}) (i.e., frequency at which $\epsilon_1 = -2$) corresponds to the energy at which localized surface plasmon resonances LSPRs are excited in isolated spherical metallic particles whose size is much smaller than the illuminating wavelength. The Faraday number (Fa), as proposed by Lalissee et al. in Ref. [114], is a dimensionless metric that quantifies the ability of a nanoparticle to enhance the electric field intensity in its surrounding medium. Thus, good plasmonic materials are characterized by high Fa numbers. Again, this parameter is defined in the framework of the quasistatic approximation. Figure 5.5 shows the values of the Fa number of each Ga-phase, including those phases stable at room pressure (i.e., α -, β -, γ -, δ - and l -Ga), versus their Fröhlich frequency. The Faraday number can be also related to the presence of interband transition in each phase. Good plasmonic metals should present low values of ϵ_2 and values of $\epsilon_1 < 0$. Therefore, the lower the values of ϵ_2 the higher Fa numbers. Keeping this in mind, the plasmonic performance Ga(II) is superior to that of α - and β -Ga. This behavior can be related to the optical properties of these materials: Ga(II) has metallic behavior in all the analyzed spectral range whereas α - and β -Ga present interband transitions below 2 eV. Conversely, Ga(III), that has interband transitions at 1.44 eV has a plasmonic performance comparable to that of α -Ga. Therefore, if we

correlate the values of Fa to the presence of interband transitions of each phase, we can list the Ga-phases in increasing order of importance of the interband contribution as: Ga(II), α -Ga, β -Ga, Ga(III), γ -Ga, δ -Ga and l -Ga. This is consistent with results reported in the previous chapter. All Ga-phases present a Fröhlich energy in the UV range (photon energies above 3 eV) which makes Ga a promising candidate for UV plasmonics applications [12, 49]. Although Ga-phases have lower Faraday numbers than other metals that have proposed for UV plasmonics (i.e., like Al ($Fa = 1391$ and $E_{Fr} = 8.9$ eV) or Mg ($Fa = 6542$ and $E_{Fr} = 5.7$ eV) [109]) the oxide shell that forms on Ga NPs stabilizes to only ≈ 1 nm thick. Conversely, in the case of Al or Mg, oxidation can consume all metal in the nanoparticles inhibiting their plasmonic response [115, 116]. Rh has been recently proposed as an alternative to Al and Mg in UV plasmonics applications due to its stability against various environments [117, 118]. However, its plasmonic performance is lower than that of the different Ga-phases ($Fa = 59$ and $E_{Fr} = 8.1$ eV) [49].

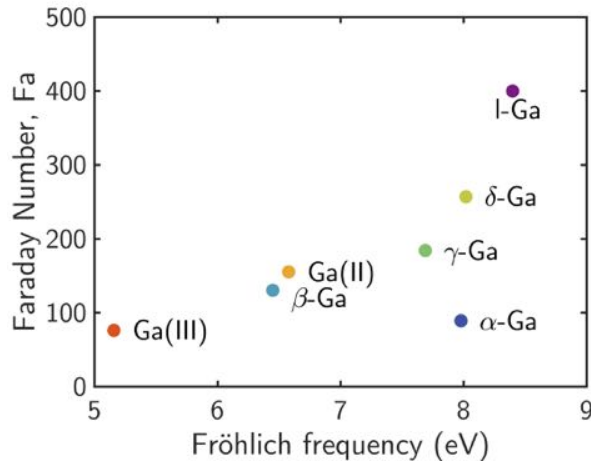


Figure. 5.5 Faraday number and Fröhlich frequency of the different Ga-phases.

Indeed, the near-field enhancement produced by hemispherical l -Ga NPs has already been exploited in surface-enhanced Raman spectroscopy (SERS) experiments [44, 52]. Due to the increasing interest in performing SERS experiments at high pressure [119–121], Ga(II) and Ga(III) NPs seem promising candidates as substrates for high-pressure SERS. The reported values of their optical constants can help the rational design of Ga(II) and Ga(III) nanostructures for this purpose. In order to explore this possibility, we have calculated the absorption cross-section, C_{abs} , and the average near-field enhancement, $\langle |\mathbf{E}|^2 \rangle$, over the surface of hemispherical NPs with radius $R =$

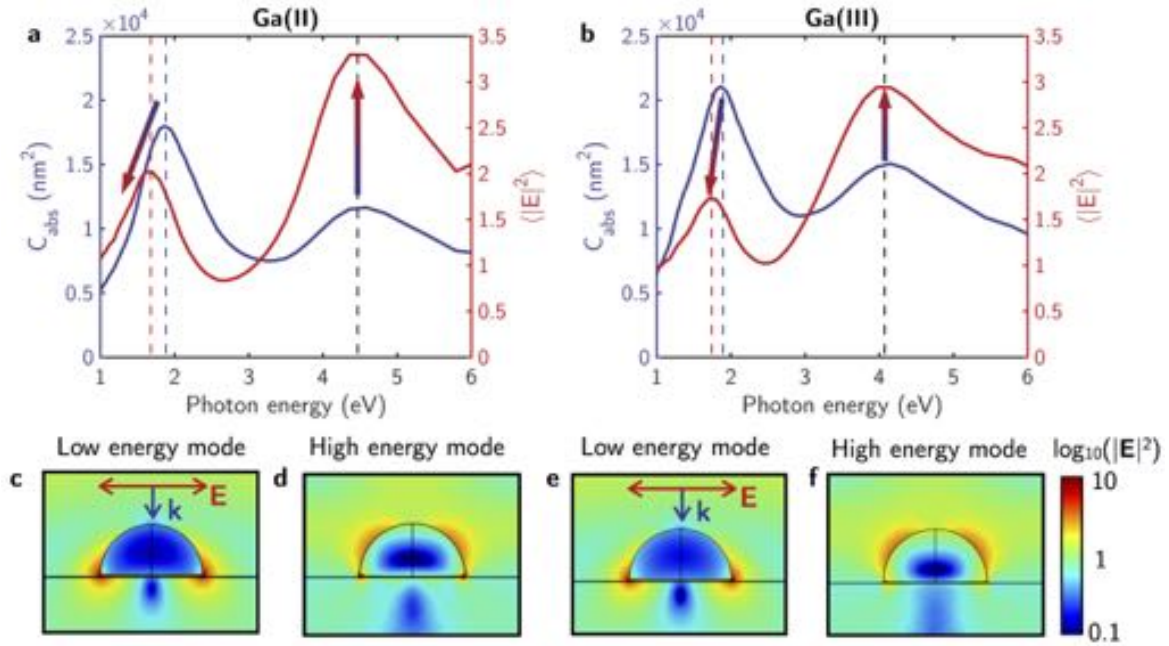


Figure. 5.6 Absorption cross-section (C_{abs} , blue line) and near-field enhancement averaged $\langle |\mathbf{E}|^2 \rangle$ red line) over the surface of (a) Ga(II) and (b) Ga(III) $R = 60$ nm hemispherical NPs on an infinite sapphire substrate embedded in air. Respective near-field distributions ($\log_{10}(|\mathbf{E}|^2)$) of their (c, e) low and (d, f) high energy modes. Red and blue arrows indicate the electric field (\mathbf{E}) and wave vectors (\mathbf{k}), respectively.

60 nm, made of Ga(II) and Ga(III), respectively, and located on a sapphire substrate (see Figure 5.6(a) and 5.6(b) red lines).

As reported for the other Ga-phases in the previous chapter, the hemispherical NPs present two modes: a low energy mode of dipolar character, where the near-field is highly localized in the interface between the NPs and the substrate (see Figure 5.6(c) and 5.6(e)), and a high energy mode of higher order, where the field is more evenly distributed over the hemisphere's surface (see Figure 5.6(d) and 5.6(f)). In light of the near-field distribution, the excitation of the high energy mode seems to be more convenient for SERS experiments: due to the even distribution of the near-field, the deposition of the molecules is not as a critical factor as in the low energy mode for which the molecules have to be precisely deposited in the NP-substrate interface. In addition, the evaluation of the near-field enhancement $\langle |\mathbf{E}|^2 \rangle$ over the NPs surface indicates that for the high energy mode, its magnitude is ≈ 1.5 times higher than for the low energy one. Specifically, Ga(II) hemispheres produce higher near-field enhancement than those made of Ga(III) at both modes (in agreement with Fig. 5.5), although the values of their absorption cross-sections C_{abs} are lower. By comparing C_{abs} and $\langle |\mathbf{E}|^2 \rangle$ in

Figures 5.6(a) and 5.6(b), we discover that the spectral positions of their corresponding high energy peaks are the same. This feature presents an additional advantage when designing SERS substrates from hemispherical NPs: a far-field measurement (C_{abs}) indicates the exact photon energy that produces the maximum near-field enhancement. Conversely, the low energy peak in the C_{abs} spectrum is red-shifted with respect to that of the $\langle |\mathbf{E}|^2 \rangle$ spectrum. This red-shift phenomenon has already been reported for dipolar nano-antennas [122] and is smaller for the Ga(III) hemispheres than for Ga(II) (0.1 vs 0.2 eV, respectively).

Many of the reported Ga-based phase change devices reported in the literature rely in the change of reflectivity produced by the phase transition between Ga-phases induced by either optical [93]/e-beam [89] excitation or heating [46]. In order to explore the change in reflectivity by a transition between Ga-phases induced by an applied pressure, Fig. 5.7(a) plots the reflectance spectrum at normal incidence of a layer $h = 150$ nm thick made of the different Ga-phases on a sapphire substrate (see Methods). The largest differences in the reflectance spectra of the different Ga-phases is produced below ≈ 2 eV. Those phases with interband transitions below ≈ 2 eV (i.e., α -, β -Ga and Ga (II)) show lower reflectance values because of their dielectric behavior ($\epsilon_1 > 0$). Above 2 eV, their reflectance increases because at those energies they become metallic ($\epsilon_1 < 0$). Those phases with metallic character in all the analyzed spectral range (i.e., γ -Ga, δ -Ga, l -Ga and Ga(III)) present almost constant reflectance. For the sake of comparison, in Table 5.2 are gathered the values of reflectance of each Ga-phase at 1 and 6 eV. Whereas for α -, β -Ga and Ga (III) the change in reflectance from 1 to 6 eV is $\approx 20\%$, for γ -Ga, δ -Ga, l -Ga and Ga(III) the change is $\approx 5\%$.

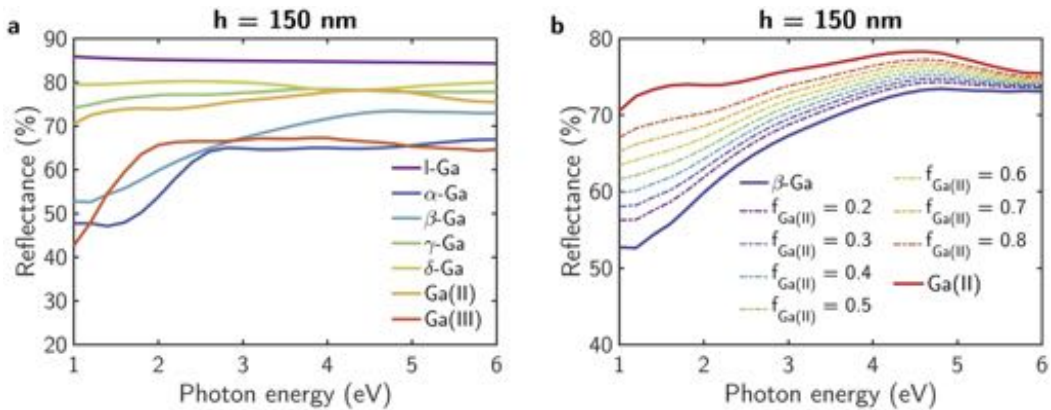


Figure. 5.7 (a) Reflectance spectra at normal incidence of a layer $h = 150$ nm thick made of the different Ga-phases on a sapphire substrate. (b) Reflectance spectrum at normal incidence of a layer $h = 150$ nm thick made of a mixture of β -Ga and Ga(II) on a sapphire substrate with different Ga(II) filling fractions $f_{Ga(II)}$.

Since the extended pressure temperature phase diagram reported by Schule and Holzapfel in Ref. [11] shows that Ga(II) coexists with β -Ga, Fig. 5.7(b) shows the reflectance of a layer $h = 150$ nm thick made of a mixture of β -Ga and Ga(II) on a sapphire substrate with different Ga(II) filling fractions $f_{\text{Ga(II)}}$. The optical constants of each mixture have been obtained using Bruggeman effective medium approximation (see Fig. 5.4).

Table 5.2 Reflectance at normal incidence of a layer $h = 150$ nm thick made of the different Ga-phases on a sapphire substrate at 1 and 6 eV.

Photon energy (eV)	l -Ga	α -Ga	β -Ga	γ -Ga	δ -Ga	Ga(II)	Ga(III)
1 eV	85.9	47.7	52.7	74.1	79.5	70.5	42.6
6 eV	84.3	66.9	72.9	77.8	79.9	75.4	64.6

5.3 Conclusions

In conclusion, we have reported the first detailed analysis of the optical properties of two of the high-pressure Ga phases (i.e., Ga(II) and Ga(III)) and the correlation with their crystalline and electronic structures. It is found that whereas Ga(II) has metallic character in the 1-6 eV spectral range, Ga(III) presents interband transitions at 1.44 eV. We have compared the plasmonic performance of these two high pressure phases with those stable and metastable at atmospheric pressure. Ga(III) has a plasmonic performance comparable to that of α -Ga, the phase stable at atmospheric pressure and room temperature. Ga(II) has a plasmonic performance superior to that of α - and β -Ga. Because many phase-change rely in the change of reflectivity produced by the phase transition between Ga-phases, we have compare the reflectance spectra of a thin film made of the different Ga-phases. These results demonstrate that the largest differences are produced below 2 eV, where some of the Ga-phases have interband transitions (α -, β - and Ga(III)). Finally, this work opens new paths for pressure driven phase-change Ga plasmonic devices.

Part II

Novel Plasmonics Systems for UV and Photocatalysis

Chapter 6

Experimental Methods

In this chapter we will review the experimental techniques employed to obtain some of the results presented in this dissertation. In Section 6.1 we present the basis of Raman and Fourier Transform Infrared Spectroscopy (FTIR). Section 6.2 is devoted to X-ray photoelectron spectroscopy. Finally, Section 6.3 is dedicated to spectroscopic ellipsometry and how it can be employed to investigate the plasmonic response of nanoparticles.

6.1 Raman and Fourier Transform Infrared Spectroscopy

Raman and Fourier Transform Infrared (FTIR) are two spectroscopic techniques used to detect and analyze vibrational and rotational modes in molecules and solids [123]. Both techniques provide characteristic fundamental vibrations that can be used to identify the molecular or material structure that constitutes the sample under study.

Raman spectroscopy is a vibrational spectroscopy technique in which monochromatic light is focused on a sample [124]. The laser radiation interact with the molecules producing a change in their polarizability and originating scattered light. The majority of the scattered photons have the same frequency as the illuminating beam and constitute the Rayleigh scattering (elastic scattering). Only a small fraction of the scattered photons have a frequency different from the incident radiation and constitutes Raman scattering. The Raman spectrum is expressed in a form of intensity of the inelastic scattered light versus Raman shift (difference between the wavenumber of the scattered and incident light). A peak appearing in the Raman spectrum comes from a specific molecular or lattice vibration. The peak position shows the specific vibrational

mode of each functional group in the material. Therefore, by analyzing the peaks and their position it is possible to identify the material under study.

FTIR is a form of vibrational spectroscopy that relies in the reflectance, transmittance or absorption of infrared radiation to identify the composition and structure of the molecules in either a gaseous, liquid or solid sample. This technique irradiates with infrared electromagnetic waves the sample under study. Each type of molecular bonds absorb specific amounts of energy at distinct frequencies which causes a change on the dipole moment of the molecules. Therefore, the vibrational energy levels of the bonds in the molecules are excited from the ground to excited states. The number of absorption bands are related with the vibrational freedom of the molecule. The frequency of the absorption bands in the spectrum is determined by the energy difference between the vibrational levels. The intensity of absorption peaks is related to the change in the dipole moment and the probability of the transition between vibrational energy levels. Thus, by analyzing the infrared spectrum it is possible to identify the composition of the sample.

Raman and FTIR spectroscopy are complementary techniques and both are required to completely measure the vibrational modes of a molecule [123]. While some vibration can be both Raman and IR active, since both techniques are based in different processes (change in polarizability and change in the dipolar moment), the selection rules are also different. In general, Raman spectroscopy is best at symmetric vibrations of non-polar groups while FTIR is more reliable at asymmetric vibration of polar groups.

6.2 X-Ray Photoelectron Spectroscopy

X-ray photoelectron spectroscopy (XPS) is a technique used to analyze the surface chemistry of a material [125]. Based on the photoelectric effect, XPS detects the kinetic energy of emitted photoelectrons from the sample when irradiated by X-rays to subsequently determine their binding energy (BE). The obtained spectra has a series of photoelectron peaks, whose binding energies are specific of each element (with the exception of H and He, that can not be detected through XPS). Therefore, the binding energy of each peak allow us to determine the composition of the sample under study. By studying the peak areas, the concentration of each element in the sample can be quantified. Moreover, the shape and BE of the peaks can be slightly altered by the chemical state of the emitting atom. Therefore, XPS also provides information about the chemical bonding.

6.3 Spectroscopic Ellipsometry

Section 3.3 covers the foundations of spectroscopic ellipsometry (SE). Conventionally, SE, which is a nondestructive, nonintrusive, and noninvasive, contactless optical technique, has been applied to the optical characterization of bulk materials and thin films [78]. In this dissertation SE will be applied to the characterization of the plasmonic response of nanoparticles by the study of their pseudodielectric function.

The applicability of SE to the analysis of nanoparticles arises from the fact that the optical properties of these nano-systems have peculiar characteristics that arise from the quantum confinement and surface states induced by the nanodimensionality [78]. In this way, SE provides a way to monitor the LSPR on nanoparticle systems. Exciting a LSPR produces an increase in the absorption cross-section, C_{abs} , of the nanoparticle. This phenomenon can be correlated with the peaks appearing in the imaginary part of the pseudodielectric function $\langle\epsilon_i\rangle$ measured through SE, a magnitude also associated with the absorption of the system under study. Therefore, the peaks appearing in the C_{abs} spectrum can be associated to those appearing in that of $\langle\epsilon_i\rangle$. To illustrate this, Fig. 6.1 shows SE measurements and electromagnetic simulations on equivalent systems. Figure 6.1 (a) the C_{abs} spectrum calculated for a 52 nm radius Ga hemisphere on a Al_2O_3 substrate and (b) the $\langle\epsilon_i\rangle$ spectrum measured on a sample of Ga hemispheres deposited on a Al_2O_3 substrate whose mean radius $\langle R \rangle$ has been estimated to be 55 nm attending to the atomic force microscopy (AFM) measurements. Both simulated C_{abs} and measured $\langle\epsilon_i\rangle$ spectra show one peak at ≈ 2.7 eV that correspond to the LSPR longitudinal mode of the hemisphere [126]. Therefore, the good agreement between both magnitudes allow us to correlate electromagnetic simulations with the SE measured data on NPs. The discrepancies in the peak position and width not only arises from the polydispersity of the real samples. Another factor to take into account when comparing both systems is that in the electromagnetic simulations, as input, bulk optical constants are considered. However, it is known the optical constants of the nanoparticles depend on their size [127]. Therefore, only qualitative comparison can be performed between SE and electromagnetic simulations.

Another interesting capability of SE is the possibility of monitoring in real time chemical reactions in which nanoparticles interact with other elements such as hydrogen or nitrogen. During this reactions, new compounds are formed on the surface of the nanoparticles and/or atoms from the reactant are incorporated into the nanoparticle's crystalline lattice. Both processes lead to changes in the pseudodielectric constant of the nanoparticles detectable through SE measurements. Therefore, the chemical reaction kinetics can also be monitored attending to the change of $\langle\epsilon_i\rangle$ in time.

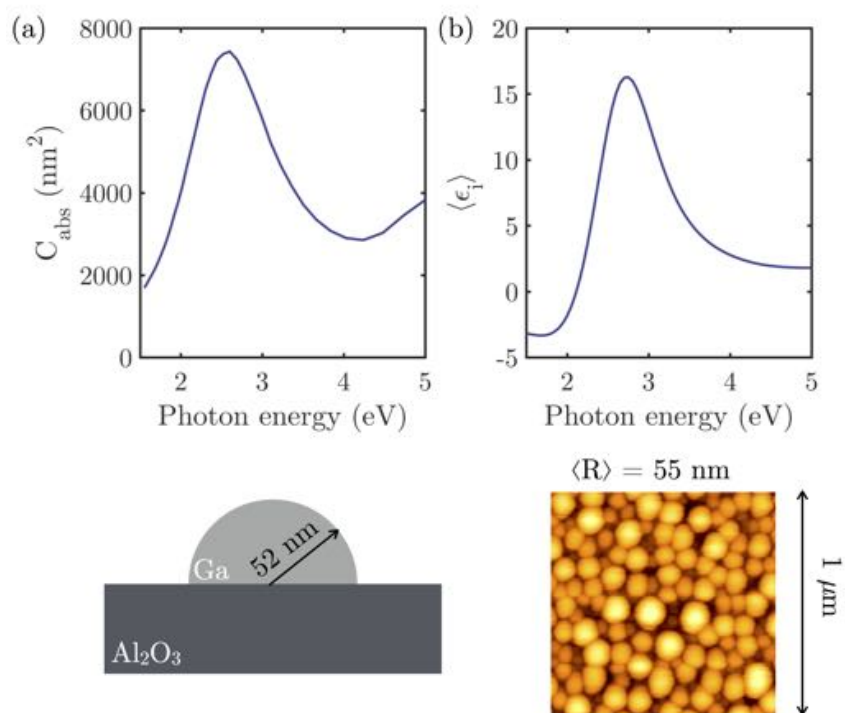


Figure. 6.1 (a) the C_{abs} spectrum calculated for a 52 nm radius Ga hemisphere on a Al_2O_3 substrate and (b) the $\langle \epsilon_i \rangle$ spectrum measured on a sample of Ga hemispheres deposited on a Al_2O_3 substrate whose mean radius $\langle R \rangle$ has been estimated to be 55 nm attending to the AFM measurements.

Chapter 7

UV plasmonics: State of the Art

In this chapter we will review the state of the art on UV plasmonics. In Section 7.1 we will discourse about its applications, current challenges, as well as the most promising materials for these purpose. In Sections 7.2 and 7.3 we will study the properties and related work on four selected metals with good plasmonic performance in the UV range. These metals have been divided in two different groups depending on their high/low oxidation tendency. Finally in Section 7.4 we will compare the plasmonic performance in the UV of NPs with simple geometries made of these four metals.

7.1 State of the Art

In the last two decades, nanoplasmonics has experienced a huge impulse from both theoretical and experimental points of view. This branch of nanophotonics studies the distribution of the electromagnetic field, and its local charge resonances (Localized Surface Plasmon Resonances, LSPRs) in sub-wavelength metallic nanostructures. These LSPRs localize and strongly enhance the incident field near the nanostructure at dimensions much smaller than its wavelength [128]. This phenomenon has been exploited for many applications in several scientific fields such as medicine [129], optical communications [130], spectroscopy [51], chemical sensing [131] or photocatalysis [132].

Many studies have analyzed how the LSPRs can be spectrally tuned by varying the shape, size and material of the nanoparticle, as well as its surrounding conditions [133]. Most of this research has been done in the visible and near-infrared ($\lambda > 400$ nm) where Au nanoparticles have played a leading role due to their oxide-free nature and biocompatibility.

Extending nanoplasmonics to the UV range has become a topic of interest due to the new challenges arising in specific areas. For example, many biological compounds,

such as nucleotide bases, nucleic acids or aromatic amino acids in cells, have absorption bands in the UV (below $\lambda = 300$ nm) [50, 134, 135]. By using hot spots excited by LSPRs in the UV it is possible to improve surface enhanced spectroscopy techniques (SERS [51], TERS [53], etc.) that ease the detection and recognition of these kinds of biomolecules. Also, biosensing assisted by LSPRs monitors the spectrum around the plasma resonance looking for shifts produced by changes in the extinction curves related to some target analyte. Bioimaging is another area that benefits from using UV radiation since the diffraction limit is proportional to the wavelength. Another example is photocatalysis, an area of research which has experienced a great development in the last decade. It has been recently discovered that metallic NPs are photocatalytically active, driving chemical reactions with photo-generated hot carriers originated from the LSPRs' decay [132, 68, 136]. These hot carriers and their subsequent transfer to adsorbates can affect reactions pathways. By tuning the photon and LSPR energies so that hot carriers are injected into specific orbitals of reaction intermediates, product selectivity can be achieved. However, not all metals can be used for these kind of applications, only those with good plasmonic and catalytic behaviors.

Because conventional metals such as Au or Ag cannot operate in the UV range due to the presence of interband transitions, several researches have analyzed possible new metallic alternatives in order to find those whose plasmonic performance could be suitable for the new challenges arising for photon energies above 3 eV [10, 12]. Among the studied metals are aluminum (Al), gallium (Ga), indium (In), rhodium (Rh), ruthenium (Ru), tungsten (W), titanium (Ti), chromium (Cr), palladium (Pd), copper (Cu), platinum (Pt), and magnesium (Mg). Figure 7.1 shows the dimensionless Faraday number, Fa (or field-enhancement factor) [114] for different materials including all the above mentioned plus gold (Au), silver (Ag) and bismuth (Bi), which has been recently presented as a promising candidate for plasmonics in the UV range [15]. Fa is a dimensionless parameter that allows the quantification and comparison of the ability of a material to enhance the electromagnetic field in the proximity of its surface. This expression has been proposed as a refinement to the plasmonic efficiency used in previous studies [10, 12]. Figure 7.1 shows that Mg, Al, Ga and Rh present the highest value of Fa while having LSPRs in the UV. Although In also presents a value of Fa comparable to that of Ga, its oxidation process (5 nm vs 1 nm oxide shell thickness) prevents its application in the UV [10].

The plasmonic performance of these metals strongly depends on the surrounding dielectric environment. All of them, except Rh, form native oxides shells that wrap the NP and whose thickness highly depends on the exposure conditions: temperature and

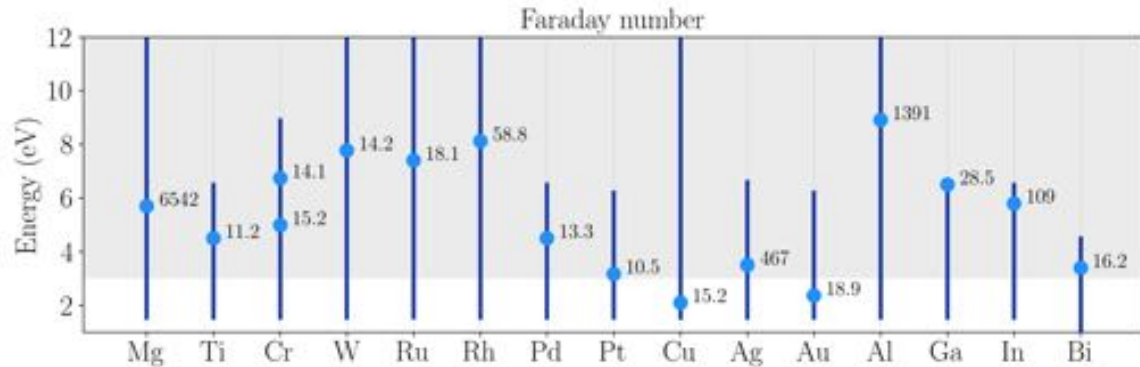


Figure. 7.1 Faraday number (Fa) for different metals. The blue dot represents the resonant energy (Fröhlich frequency, frequency at which $Re(\epsilon) = -2$ [12]) and the shadowed region the exciting photon energies above 3 eV. The blue solid line represents the range of energies studied in each case (this depends on the optical constants available in the literature [13–15, 4]).

pressure. The thickness of this oxide shell can go from 1 nm, as in the case of Ga, to the complete destruction of the metal content of the NP, as in the case of Mg [137]. So, knowing how this oxide shell affects the plasmonic behavior of this type of NPs is a key point for researchers in UV plasmonics [115, 109, 44]. An overview on the oxidation of the four most significant metals able to sustain UV LSPRs will be addressed in the next two sections. However, this issue will be more systematically studied in the following chapter. It is worth mentioning that materials with UV plasmonic response can also be achieved by alloying elemental materials [138].

7.2 High Oxidation Tendency: Aluminum and Magnesium

7.2.1 Aluminum

Aluminum is the third most abundant element in the Earth's crust, only behind oxygen and silicon. This makes it to be 2-3 orders of magnitude cheaper than other conventional plasmonic metals like Au or Ag. It presents a strong plasmonic response in the UV range, and unlike precious metals, its interband transitions lie in the near infra-red (NIR around 800 nm) [139]. For instance, Al is compatible with optoelectronic devices and CMOS technology. Most importantly, there is a high number of processing methods for manufacturing Al NPs of different sizes and shapes [140]. Among these methods are lithography, laser ablation and chemical synthesis. Synthesizable geometries

include nanorods [141–143], nanodisks [115] or flat triangles [144, 145] among others. The main disadvantage of this material is its inherent high tendency to oxidation. When exposed to air, a thin layer of oxide wraps the NP [146]. Although the layer thickness is small (a few nanometers), it is highly sensitive to ambient conditions (temperature and humidity). As a consequence, plasmonic resonances of Al NPs are spectrally modified and usually, hampers a stable plasmonic response. It has been experimentally and theoretically shown that the growth of this oxide layer leads to both a red-shift and a weakening of the resonance peaks in Al NPs with different shapes [144, 109, 147, 115]. On the other hand, the self-terminating oxide layer can prevent further oxidation, producing natural encapsulation that protects the metal in the NP. This is why this oxide layer is sometimes described as a “protective” layer. Recent experiments on Al nanorods, have shown that high-order resonant modes are more confined inside the oxide-shell [143].

Recently, a lot of attention has been paid to Al in photocatalysis applications. Traditionally, transition metals like Rh, Ru or Pd have been used in heterogeneous catalysis to lower the activation energy of chemical reactions. However, these metals present lower absorption and weaker LSPRs than Al in the UV spectral region. This is a disadvantage for photocatalytic applications due to the poor overlap with either conventional laser sources or the solar spectrum. For these reasons, it has been proposed to couple a plasmonic antenna directly to the catalytic nanoparticle. This antenna-reactor complex allows absorption enhancements in poorly light-absorbing catalytic metals [148]. The feasibility of these heterostructures has been demonstrated using Al as “antenna” and Pd as “reactor” heterodimers [148] and decorated spherical nanoparticles [149]. Aluminum-cuprous oxide antenna-reactor nanoparticles have also been proven to be an efficient photocatalytic heterostructure [150]. More recently, it has been reported the possibility of producing Al nanocrystals decorated with transition metal nanoislands [151]. These metals include among others Rh, Ru or Pd, which, as aforementioned, have already been used in heterogeneous catalysis. Although Al by itself is a poor catalytic metal, it has been demonstrated that Al nanocrystals can also act as photocatalysts for hydrogen dissociation [152]. Densely distributed Al NPs have been also used to assist photocatalytic processes [153, 154].

Aluminum nanostructured films have been widely used as substrate for enhanced fluorescence spectroscopy in the UV for detection of biomolecules [155, 156]. Al nanoapertures have been studied as a tool for the modification of fluorescence decay rate of p-terphenyl dye molecules [157, 158]. Wang et al. [158] reported a lifetime reduction of $\approx 7.2 \times$, exceeding the previously reported value $\approx 3.5 \times$ by Jiao et

al. [157]. Concerning SERS, recently it has been reported the fabrication of an Al film-over substrate for UV SERS at the deepest UV wavelength used to date ($\lambda = 229$ nm) [159].

7.2.2 Magnesium

Magnesium nanoparticles presents the strongest plasmonic response in the UV among the analyzed elements. The efficiency of them is higher than those of Al for the same wavelength range. However, the oxidation of Mg NPs is more aggressive. The native oxide MgO forms unstoppingly upon exposure to air as oxygen rapidly diffuses through porous oxide into the metal [12, 109]. This process leads to a complete destruction of the plasmonic effects on Mg NPs unless they are manipulated under controlled atmospheres [160]. In order to prevent their oxidation and preserve their UV plasmonic performance, a coating procedure with gallium has been recently proposed [161].

A very appealing property of Mg is that it can absorb up to 7.6% wt of hydrogen gas [162]. This, together with its abundance and low cost, makes Mg a very attractive material for hydrogen storage and hydrogen sensing purposes in the looming hydrogen economy [31, 29]. Recently, it has been experimentally demonstrated how the plasmonic response of Mg NPs (more precisely, nanodisks fabricated by colloidal hole-mask lithography) can be switched from “on” to “off” states by exposing them to molecular hydrogen (H_2). Mg upon exposure to H_2 turns into MgH_2 , which, as a dielectric material, does not support plasmonic resonances. The hydrogenation process is reversible by exposure to oxygen, turning MgH_2 into metallic Mg again [160]. This feature makes Mg very appealing for creating new active plasmonic devices. For example, this metal-dielectric transition has been experimentally used in the construction of an hybrid plasmonic metamolecule with hydrogen-regulated chiroptical response [163] and the construction of hydrogen-regulated dynamic color displays [164].

In the field of bio-sensing, the modification of the ultraviolet (UV) fluorescence decay rate of p-terphenyl dye molecules by Mg nanoapertures in free solution has been reported by Wang et al. [158]. Mg nanoapertures exhibit a lifetime reduction of up to $\approx 7.2 \times$. This value is higher than that reported for Al ($\approx 5.3 \times$). Single Mg nanohelices with strong chiroptical response have also been reported as plasmonic sensors for molecular detection [165].

7.3 Low Oxidation Tendency: Gallium and Rhodium

7.3.1 Gallium

Gallium is a standard material in optoelectronics that is becoming attractive also for its plasmonic properties. It presents a broad plasmon tunability, it is stable along a wide range of temperatures and its deposition is simple even at room temperature [44]. Moreover, the new range of bottom-up fabrications techniques that allow the production of Ga NPs make this material very appealing for practical purposes. These fabrication methods include molecular beam epitaxy (MBE) [43, 44], optically regulated self-assembly [107], thermal evaporation [88], and colloidal synthesis [6]. In addition, unlike either Al or Mg, its very low tendency to oxidation (1-2 nm oxide shell thickness), minimally affects its optical properties, keeping them stable over months or even years [44, 109]. Ga NPs form liquid droplets with a melting point of 29.7°C, so when deposited on a substrate at room temperature, they produce a close-packed array of smooth truncated spheres whose mean radii and size distributions vary with growth conditions. Wu et al. [43] presented the optical evolution of Ga NPs surface plasmon resonance during deposition by *in-situ* spectroscopic ellipsometry to control and tune the plasmon resonance photon energy. This work reported both longitudinal and transverse modes for the hemispherical Ga NPs supported on a sapphire substrate. Similar results were obtained by Albella et al. [126] through a numerical study based on the Discrete Dipole Approximation (DDA) [72]. Other methods used to study this type of nanoparticles include variable-angle spectroscopic and Mueller matrix ellipsometry [166] or hyperspectral cathodoluminescence imaging [167]. The utility of these Ga NPs seeded substrates has been demonstrated for UV surface-enhanced Raman spectroscopy, fluorescence, and photodegradation following excitation by a HeCd laser operating at 325 nm [52].

Other studies have explored the possibility of alloying or coating these Ga NPs with other metals such as Mg. Wu et al. [168] experimentally analyzed the plasmonic properties of this type of NPs. These bimetallic NPs allow a new degree of freedom for tuning the LSPRs since their optical constants are dependent on the mixture composition. The resulting Ga-Mg NPs exhibit a plasmon resonance tunable from the UV to the IR by playing with the particle size and the Ga/Mg ratio [161]. Electromagnetic simulations based on DDA numerically corroborated these experimental results [161].

Considering the wide polymorphism of Ga, already discussed in Chapter 4, Krasavin et al. [48] proposed a new concept for active plasmonics that exploits light-induced nanoscale structural transformations in the waveguide material. Specifically, they

showed that surface plasmon polaritons signals in a metal-on-dielectric waveguide containing a Ga section a few microns long can be effectively controlled by switching the structural phase of gallium. They were able to induced the phase change by thermal or optical excitation. Taking advantage of the gallium's solid-liquid phase transition, Vivekchand et al. [46] fabricated liquid Ga gratings which exhibited reversible and switchable phase-dependent plasmonic properties. The liquid phase showed higher surface plasmon polaritons coupling efficiencies and narrower resonance line widths compared to the solid phase. Concerning NPs, very recently, it was experimentally shown, through real-time ellipsometry, the stable coexistence of a solid-phase core and a liquid shell in substrate-supported Ga NPs [4]. Other authors have reported the coexistence of other phases in Ga NPs, specifically β - and γ -Ga, controlled by e-beam excitation [89].

7.3.2 Rhodium

Although Ga NPs form an oxide shell only 1-2 nm thick, oxide-free metals, like Pd, Pt, Ru or Rh, should be even more desirable. Among these noble metals, Rh presents the strongest plasmonic response in the UV range. Moreover, the possibility of synthesizing Rh NP with sizes smaller than 10 nm through chemical methods [117, 118] and its potential for photocatalytic applications, makes this material very attractive for building plasmonic tools in which photon energies are well above 3 eV [117]. As a disadvantage, Rh is less abundant than metals like Al or Mg. This fact has a logical impact on the price: its price is more than 10^4 higher than that of Al or Mg.

Among the different synthesizable Rh NPs' shapes, two geometries have been reported to be fabricated with nanometer size control: tripod stars [117, 169] and nanocubes [118]. On the one hand, Watson et al. [117] synthesized and experimentally examined the properties of Rh tripods by means of SERS, surface enhanced fluorescence, and photoinduced degradation of a typical compound like p-aminothiophenol (PATP). They found that Raman and fluorescence spectra were enhanced and photodegradation was accelerated in the presence of Rh under resonant UV excitation. In addition they observed that for more tightly focused UV illumination, fluorescence spectra often increased for many minutes. This is an indication that photo-excited hot electrons efficiently transferred from the Rh NPs to the attached PATP before photodamage ultimately quenched the fluorescence. These efficient photodegradation and photo-induced charge transfer processes confirmed the potential of Rh nanostructures for UV plasmonic and photocatalytic applications. On the other hand, a similar study was carried out by Zhang et al. [118]. They were able to synthesize uniform Rh NCs

with controlled side length ranging between 10 to 59 nm. They observed that the UV LSPRs of the NCs accelerated the rate of PATP chemical decomposition.

Rh has also been presented as a promising metal for plasmonic photocatalysis. Supported Rh nanoparticles and molecular complexes are widely used in industrial hydrogenation, hydroformylation and ammonia oxidation reactions. However, its main industrial application is in three-way catalytic converters to reduce NO_x , where Rh is often alloyed with Pt and Pd because of its corrosion resistance [170–172]. Very recently, Zhang et al. [27] reported that plasmonic Rh nanoparticles are photocatalytic, simultaneously lowering activation energies and exhibiting strong product photo-selectivity, as illustrated through the CO_2 hydrogenation reaction. These results have opened an exciting new pathway in the long history of heterogeneous catalysis by offering a compelling advantage of light over heat.

Other authors have proposed to use Rh nanoparticles for deep-UV bio-chemical sensing [173]. They proposed nanostructures composed of nanorings dimer-type antennas and an infinity shape structure built by a pair of split rings with a nanodisk. These nanostructures support Fano resonances that can be used for deep-UV biochemical sensing applications.

7.4 Comparison of the Plasmonic Response of Simple Geometries

In this section we will compare the plasmonic response in both the near- and far-field regimes of nanostructures made of Al, Mg, Ga and Rh. The parameter of interest in the far-field regime will be the absorption cross-section C_{abs} , while for the near-field we calculate the enhancement of the local intensity averaged over the NP surface $\langle |\mathbf{E}|^2 \rangle$. From now on, we will refer to $\langle |\mathbf{E}|^2 \rangle$ as *averaged local enhancement* for brevity. In the case of Al, Mg and Ga, NPs will be modeled with an oxide thickness of 3, 5 and 1 nm respectively to be consistent with previous numerical and experimental studies [115, 160, 4].

Figure 7.2 shows the complex dielectric function ($\epsilon = \epsilon_r + i\epsilon_i$) of these metals and their corresponding oxides. The values of the complex dielectric function have been taken from different sources in the literature [16, 13, 4]. Note the similar optical behavior shown by Mg and Al oxides, while Ga_2O_3 shows absorption in the UV region above 3 eV.

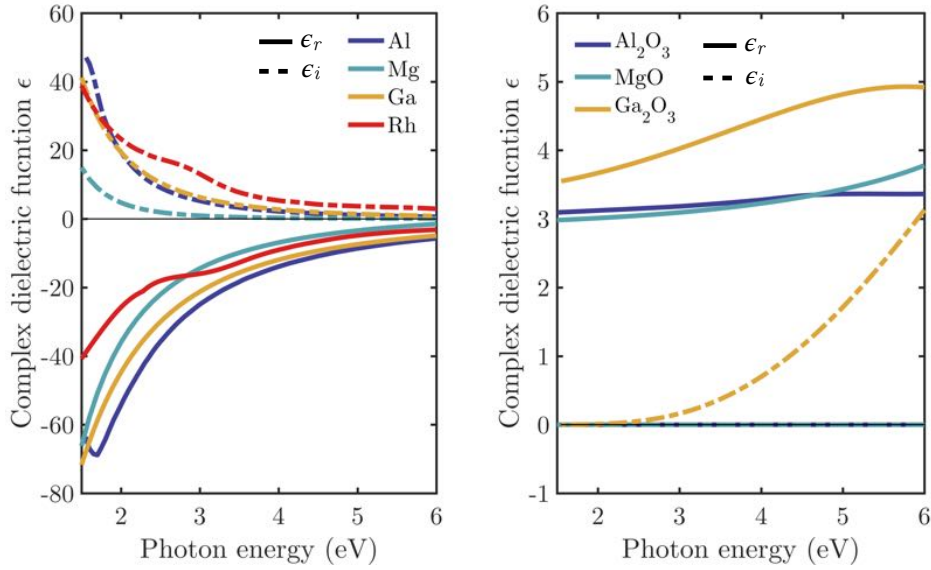


Figure. 7.2 Real (solid line) and imaginary (dashed line) parts of the complex dielectric function ($\epsilon = \epsilon_r + i\epsilon_i$) of Al, Mg, Ga, Rh (left) and their corresponding oxides (right) as a function of the photon energy of the incident beam. The values of the complex dielectric functions have been taken from different sources from the literature [16, 13, 4].

As in a previous work [174], we have considered tripod stars ($l = 10$ nm, $w = 5$ nm and $h = 5$ nm), cubes ($L = 8.1139$ nm) and spheres ($R = 5.0335$ nm) with equivalent volume. By choosing nanoparticles with the same volume but different shape, it is possible to explore the relative contribution of the shape (corners and edges effects included) and the material. Such small NPs are highly demanded in photocatalysis applications. It is well known that small NPs have higher catalytic activity than larger ones due to their increased surface to volume ratio. The hot-electrons produced by LSPR excitation in these small NPs are more likely to reach the surface and enter anti-bonding orbitals of adsorbed molecules, thereby weakening a critical bond and accelerating the reaction [151].

Figure 7.3 shows the absorption cross-section C_{abs} (top row) and averaged local enhancement $\langle |\mathbf{E}|^2 \rangle$ (bottom row) for equivalent tripod stars, spheres, and cubes made of Al + Al₂O₃, Mg + MgO, Ga + Ga₂O₃ and Rh. The oxide shell thickness in each case has been set to 3, 5 and 1 nm respectively [115, 160, 44]. The aforementioned dimensions for the tripod stars, cubes and spheres already include the thickness of oxide shell in each case. The percentage of metal content in each nanoparticle is shown in Table 7.1. This magnitude is defined as $V(metal)/V(metal + oxide) \cdot 100$, where V represents the volume of either metal or metal+oxide within the NP.

Table 7.1 Percentage of metal content in each of the studied nanoparticles.

Metal	Tripod Star	Cube	Sphere
Al + Al ₂ O ₃	0 %	1.8 %	6.6 %
Mg + MgO	0 %	0 %	0 %
Ga + Ga ₂ O ₃	22 %	42 %	51 %
Rh	100 %	100 %	100 %

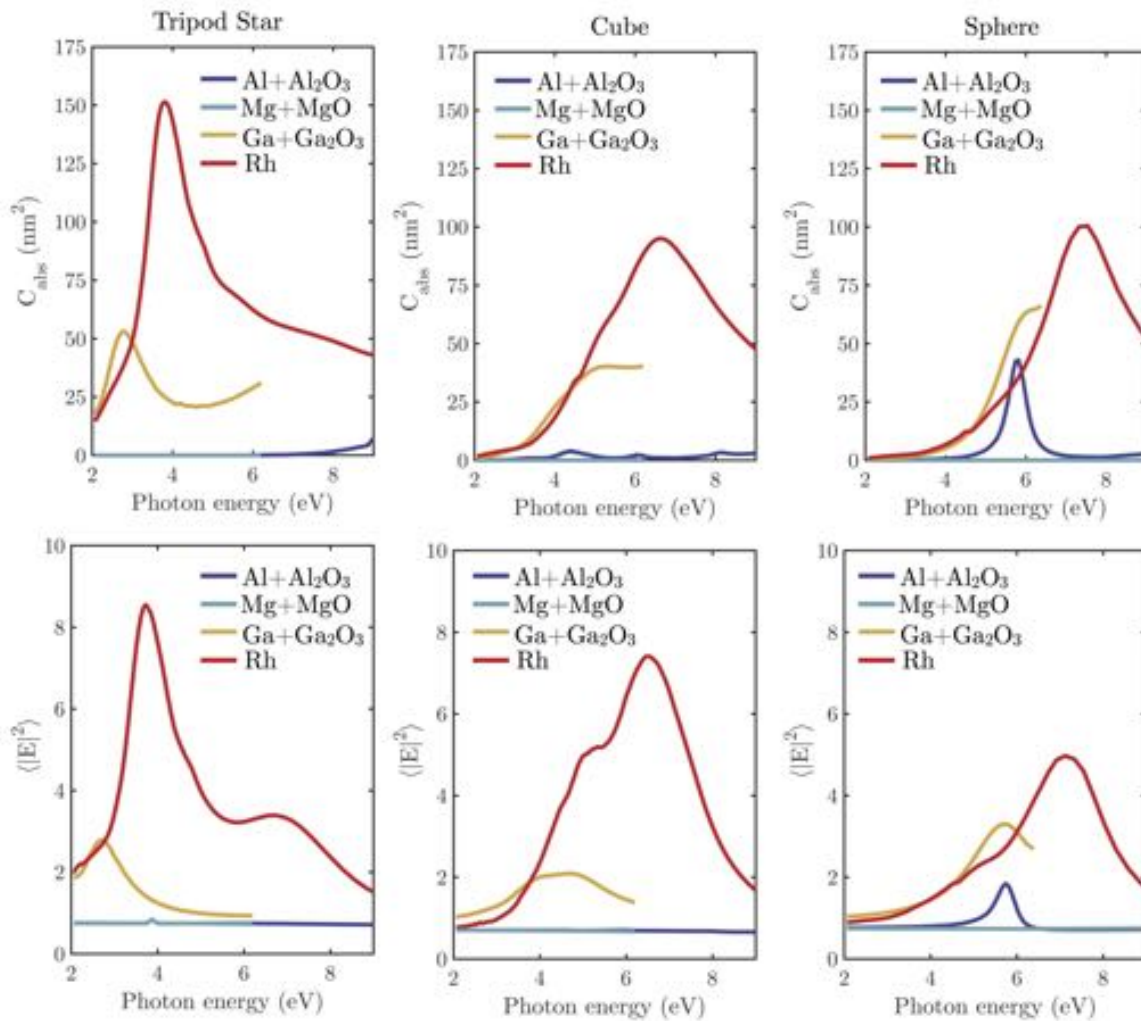


Figure. 7.3 Spectral enhancement of the local intensity averaged over the NP surface $\langle |E|^2 \rangle$ (left column) and the absorption cross-section C_{abs} for equivalent tripod stars ($l = 10$ nm; $w = h = 5$ nm), cubes ($L = 8.1139$ nm) and spheres ($R = 5.0335$ nm) composed of Al + Al₂O₃, Mg + MgO, Ga + Ga₂O₃ and Rh, illuminated under normal incidence.

Figure 7.4 shows the $|\mathbf{E}|^2$ maps (logarithmic scale) at $E = 3.82$ eV ($\lambda = 325$ nm, HeCd laser) for Rh and Ga + Ga₂O₃ tripod stars ($l = 10$ nm, $w = 5$ nm and $h = 5$ nm), nanocubes ($L = 8.1139$ nm) and spheres ($R = 5.0335$ nm). These two materials have been chosen in order to show how the near-field distribution is affected by the presence of an oxide shell. A deeper analysis of this topic on Al + Al₂O₃, Mg + MgO and Ga + Ga₂O₃ spherical and hemispherical geometries will be made in the following chapter.

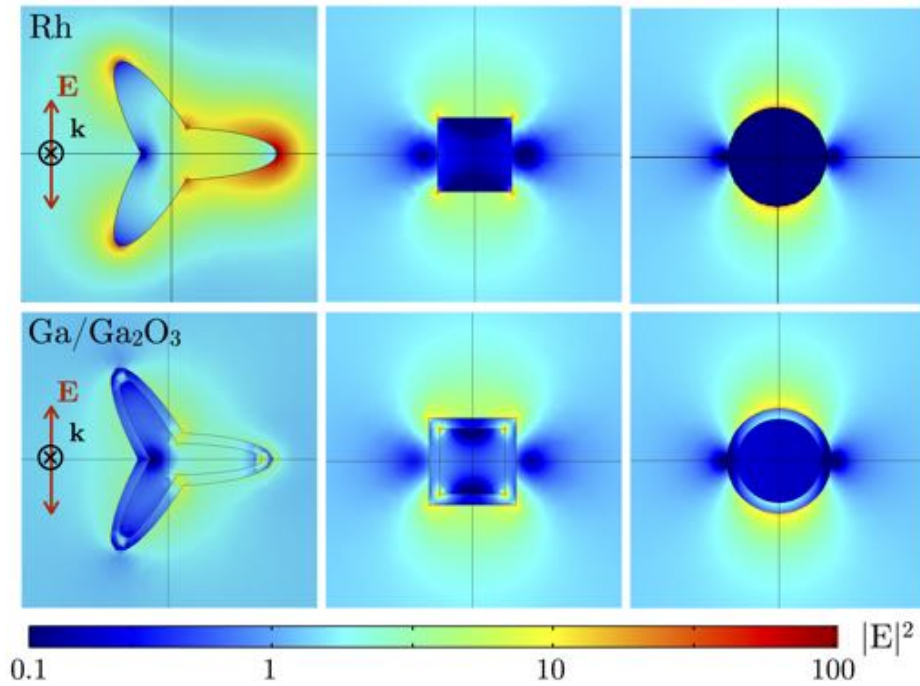


Figure. 7.4 $|\mathbf{E}|^2$ maps (logarithmic scale) at $E = 3.82$ eV ($\lambda = 325$ nm, HeCd laser) for Rh (top row) and Ga + Ga₂O₃ (bottom row) tripod stars ($l = 10$ nm; $w = h = 5$ nm), cubes ($L = 8.1139$ nm) and spheres ($R = 5.0335$ nm).

The plasmonic response of Al and Mg is completely deteriorated by the formation of the oxide layer, specially in the case of Mg, for which the metal content drops to 0% after oxidation. This aggressive oxidation process limits the performance of Mg NPs with sizes smaller than 10 nm. It is surprising how the absorption cross section of the Al sphere (with a metal content of just 1.8 %) is comparable to that of Ga and Rh spheres at energies around 6 eV. However, when looking at the value of $\langle |\mathbf{E}|^2 \rangle$, for Al spherical NPs, it is approximately half the value for Rh and Ga spherical ones.

By comparing Ga and Rh (low oxidizing tendency), in general, the former presents LSPRs at lower energies than the latter (coherent with their Fröhlich frequencies, 6.5 and 8.1 eV respectively). Moreover, for energies above 3 eV both C_{abs} and $\langle |\mathbf{E}|^2 \rangle$ are

higher for Rh NPs than for Ga NPs. The only exception occurs for the sphere geometry, for which Ga presents higher absorption and electric field enhancement between 5 and 6 eV approximately. From this comparison, it can be concluded that oxidation prevents Al and Mg to be optimum candidates as plasmonic materials. On the contrary, Ga and Rh show a good plasmonic response, specially Rh, which presents almost highest values of C_{abs} and $\langle |\mathbf{E}|^2 \rangle$ all over the studied spectral range.

Electric field hot-spots can be observed in specific locations for each geometry (see Fig. 7.4). Also, the effect that oxide shell have on them is shown in the bottom row for Ga+Ga₂O₃ NPs. In absence of oxide, hot-spots are produced on the surface of the particle, where they can be in direct contact with the analytes in surface enhanced applications. When an oxide shell is present, for very thin shells and specific geometries, hot-spots produced on the surface of the oxide are more intense than those at the interface metal-oxide (see the Ga+Ga₂O₃ sphere). However, for other geometries like Ga+Ga₂O₃ tripod stars and nanocubes, hot-spots produced in the metal-oxide boundary are more intense. So, as for the case of Ga, the oxide shell can have a critical effect on the UV plasmonic performance of metallic nanostructures and its relevance to real applications.

Finally, it is important to point out that, although Rh in principle presents not as good plasmonic properties as Al or Mg (lower Fa , see Fig. 7.1), because its does not oxidize, its plasmonic response is more adequate for practical purposes.

7.5 Conclusions

UV plasmonics constitutes a new focus of research due to new challenges arising in fields such as biology, chemistry or spectroscopy. In our quest to find suitable metals for the UV range, we have analyzed recent work developed for four metals that present plasmonic behavior in this spectral region: aluminum, magnesium, gallium and rhodium. These metals have been classified into two categories: those with high oxidation tendency (Al and Mg) and those with low oxidation tendency (Ga and Rh). By comparing the plasmonic response of small NPs (sizes smaller than 10 nm) made of these metals with their corresponding oxide layers, it can be concluded that the plasmonic performance of Al and Mg NPs is strongly affected by an oxide layer. This weakens their absorption efficiency and near-field enhancement. This effect is less noticeable as the size of the particle increases, specially for Al, which forms a self-terminating oxide shell. Recently, Rh, an oxide-free metal, has drawn the attention because it enhances its already favorable catalytic activity by UV illumination near

its plasmonic resonance. From the experimental point of view, two geometries can be chemically synthesized: tripod stars and nanocubes. Rhodium NPs have shown the best UV plasmonic performance as compared with the other metals (highest values of absorption cross-section and near-field enhancement, specially on those geometries with edges and corners).

Chapter 8

Oxide Effects on Al, Ga and Mg Nanoparticles

As exposed in the previous chapter, aluminum (Al) [175, 156, 12, 142, 115, 176], gallium (Ga) [12, 176, 126, 166, 161], magnesium (Mg) [12, 160], and rhodium (Rh) [117, 174, 118] have been identified as particularly promising candidates for UV plasmonics. Their properties approaches those of silver (Ag) and gold (Au), which are the most widely used metals in plasmonic applications in the VIS-NIR [176, 177]. Already these metals have proven their utility in surface-enhanced spectroscopy techniques [44, 117, 52, 178, 158] or photocatalysis [154, 27, 179, 28]. For these applications exploiting the localized surface plasmon resonances (LSPRs) it is crucial the precise tuning of their efficiency and spectral position. However, these parameters depend sensitively on the NP's surrounding dielectric environment. Al, Mg and Ga NPs form native oxides that wrap the NP with a shell whose thickness depends on both the metal and the environmental exposure conditions (temperature and pressure) that clearly affects their LSPRs. Consequently, it is essential to understand the effect of oxidation on their UV plasmonic response for a rational design of Al, Mg and Ga NPs for real UV plasmonic applications [12, 115, 180].

In this chapter a detailed numerical investigation into how the thickness of a surface oxide shell affects the UV plasmonic performance of nanostructures made of Ga, Al, and Mg. In Section 8.1 we describe the nanostructures on which we perform this study. Specifically isolated spherical and hemispherical-on-substrate particles are considered in order to mimic typical experimental conditions used in applications like colloidal chemistry or surface enhanced spectroscopy. Also, we do a detailed description of the electromagnetic simulations performed. We have used both discrete dipole approximation (DDA) method [72] and finite element method (FEM). Section 8.2

shows the main results of this work. It includes the comparison of the plasmonic absorption efficiency and the near-field distribution for each material and geometry, and its dependence with a growing oxide shell thickness. Finally, in Section 8.3 are summarized the main conclusions of this chapter.

8.1 System Geometry and Numerical Methods

Two basic core-shell geometries have been considered: an isolated spherical NP of radius R (“spherical” case), and second, a hemispherical NP with the same radius located on a dielectric sapphire substrate with refractive index $n = 1.78$ (“hemispherical” case). In this way, with the former we mimic experimental conditions in colloidal chemistry and with the latter, the experimental conditions for metallic nanostructures made of either Ga or M on substrates [126, 166, 161, 160]. Although the typical Al NP geometry is usually not hemispherical, we use this geometry to facilitate comparison. However, Al NPs with other shapes such as disks, are often deposited on a dielectric substrates [142, 144]. In the present analysis the total NP size will be fixed at $R = 40$ nm, and the metal oxide shell thickness will vary from 0 nm (bare metal NP) to 20 nm. Therefore, the metallic core radius will range from $R_{core} = 20$ to 40 nm (pure metallic NP) (Fig. 8.1). Al and Ga have very large enthalpies of oxide formation [181], and the oxide formed is quite dense, preventing oxide diffusion and slowing dramatically the oxidation process after only a few monolayers (Ga) or nanometers (Al). On the contrary, Mg has a moderate enthalpy of oxide formation [181] and the native oxide MgO forms aggressively upon exposure to air, leading to a complete and rapid destruction of the plasmonic response [90] unless this process is performed under controlled conditions [160]. In all these cases, oxide layers of a few nanometers are formed. Taking into account the influence of the ambient conditions on the oxidation processes, it is interesting to analyze the whole thickness range since control of it would allow the UV plasmon resonance to be tuned, as we will see later on.

The spectral dependence of two parameters has been studied: the absorption efficiency Q_{abs} and the enhancement of the local electric field averaged over the NP surface $\langle |\mathbf{E}|^2 \rangle$. Obviously both magnitudes depend on the wavelength λ , this dependence being the key of our plasmonic study. For particles much smaller than the wavelength, Q_{abs} can be associated with the far-field extinction efficiency and it is defined as the ratio between the particle absorption cross-section (difference between extinction and scattering cross-sections) and its geometrical cross-section. $\langle |\mathbf{E}|^2 \rangle$ gives an estimate of the local field enhancement or, more precisely, the local enhancement of the local energy

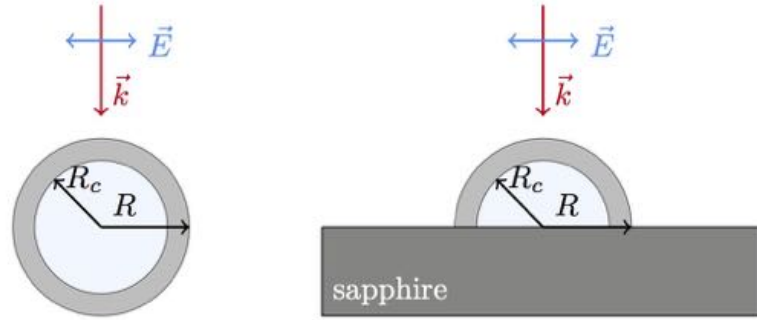


Figure. 8.1 The two analyzed scattering geometries: a) Isolated spherical geometry, b) Hemispherical geometry on a dielectric substrate. ($R = 40$ nm, R_{core} will range from 20 nm to 40 nm).

density, close to the particle surface in the near-field regime, whose spectral distribution is generally red-shifted with respect to Q_{abs} due to the dominant evanescent character of the near electromagnetic field [182, 122]. $\langle |\mathbf{E}|^2 \rangle$ is useful for predicting the plasmonic performance in surface-enhanced applications such as Raman (SERS) or fluorescence (SEF) spectroscopy [51], while Q_{abs} helps to describe the ellipsometric response of surfaces with metallic nanostructures, especially that related to the imaginary part of the measured pseudodielectric function [166].

The Discrete Dipole Approximation (DDA) and Finite Element Methods (FEM) like COMSOL Multiphysics have been employed for the numerical analysis of the Q_{abs} and $\langle |\mathbf{E}|^2 \rangle$. The DDA method, also known as coupled dipole method [72], is based on a direct-space dipole discretization scheme to calculate light scattering and absorption by irregular particles and inhomogeneous structures. In our case, both the NP and the substrate were discretized with a large number of cells. This number was optimized for each calculation in order to guarantee convergence in a reasonable time without loss of accuracy (typically $\sim 150,000$). Although for the isolated core-shell spherical NPs there is an analytical expression that describes the absorption efficiency [2], it has been also calculated with DDA and checked with the exact solution in order to be consistent with the hemispherical-on-substrate case. Although Q_{abs} has a simple expression for the small particle limit coming only from the dipolar contribution [2], this approximation is not longer valid for the $R = 40$ nm particles analyzed in this study. The local electric field distribution and the corresponding $\langle |\mathbf{E}|^2 \rangle$ in both core and shell surfaces have been calculated employing finite-element simulations.

The dielectric constants of Al, Mg, Al_2O_3 , MgO, and Ga_2O_3 have been taken from different sources in the literature [13, 16], but the values for Ga were obtained *in-situ* by spectroscopic ellipsometry [12] and confirmed by those reported in the literature

[183]. Figure 8.2 plots the real and imaginary parts of the dielectric function $\epsilon = \epsilon_r + i\epsilon_i$ for the three metals and their corresponding oxides. Note the similar optical behavior shown by oxides of Mg and Al, while Ga_2O_3 shows a clear absorption in the UV region below 300 nm. The optical behavior of the three oxides is found to be roughly equivalent ($\text{Re}(\epsilon) \approx 3 - 4$ with low absorption) above 400 nm.

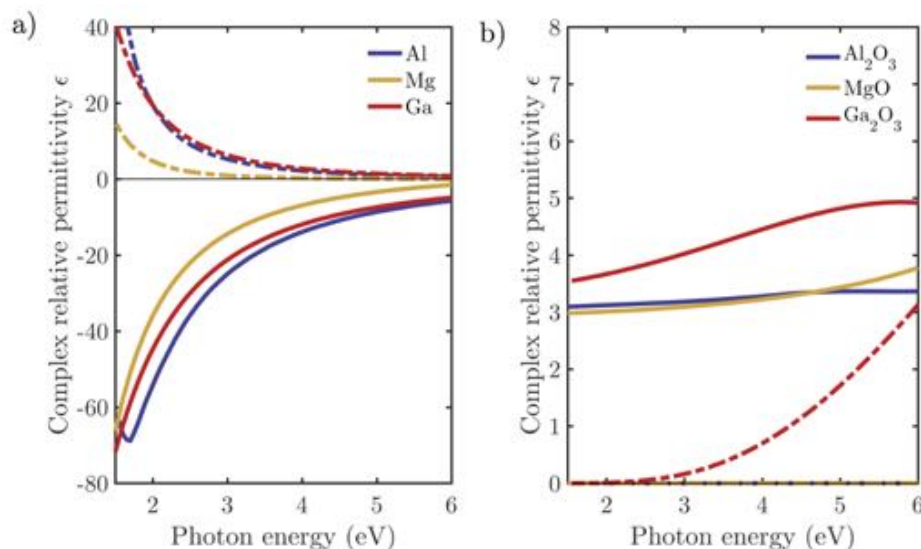


Figure. 8.2 Real (solid line) and imaginary (dashed line) part of the dielectric function for (a) Al, Mg, and Ga and (b) their corresponding oxides.

A dimensionless parameter to quantify the near field enhancement has been recently proposed by Lalis et al. [114] The so called Faraday number (Fa) takes the following values for the analyzed metals at their resonant wavelengths: $Fa^{Mg} = 6542$, $Fa^{Al} = 1404$ and $Fa^{Ga} = 53$. Whereas $\langle |\mathbf{E}|^2 \rangle$ gives an estimate of the local field enhancement averaged over the particles surface, Fa is a local enhancement indicator at the point where the maximum electric field is produced. A large value of Fa indicates a higher ability to enhance the optical near field, and it is expected that Mg will show the highest near field enhancement.

8.2 Results and Discussion

8.2.1 Comparative Study in the Far-Field: Influence of NP Shapes

Ellipsometry has been used to measured the pseudo-dielectric function of particle-on-substrate nanostructures in order to determine their plasmonic response [166, 161].

The measured imaginary part of this pseudo-dielectric function $\langle \epsilon_2 \rangle$ correlates directly with the absorption efficiency Q_{abs} that is easier and more accurate to determine numerically. In Fig. 8.3, the absorption efficiency Q_{abs} for the two geometries is plotted as a function of the wavelength λ and the core radius R_{core} for NPs with a total radius $R = 40$ nm. For an isolated spherical nanoparticle made of either magnesium or aluminum (first two plots in the left column of Figs. 8.3(a,b)), the location of the main resonance is only slightly sensitive to shell thickness and follows a similar tendency as their oxide shell thickens. Specifically, their absorption dipolar resonances increase and narrow as their shells become thicker. For Ga, Q_{abs} also narrows with increasing oxide thickness, but its strength first increases to a maximum value near $R_{core} = 30$ nm before decreasing with increasingly thicker oxide shells, a behavior influenced by a given value of the shell thickness, this being related to the higher absorption of its oxide at shorter wavelengths (see Fig. 8.2). Note that the frequency shift caused by NP oxidation depends on two factors that produce opposite behaviors with increasing oxide thickness: a blue-shift due to a reduction of the core size, and a red-shift due to an increase of the effective refractive index surrounding the core. As the oxide shell increases, the blue-shift compensates and slightly dominates the red-shift for Al, while the red-shift dominates the blue-shift for Mg and Ga. These balanced behaviors are more clearly evidenced in Fig. 8.3(b).

In Fig. 8.3(a) some quadrupolar behavior can be observed. This is clearly visible in form of narrow peaks for Mg between 200 and 300 nm. For Al and Ga, this resonance shifts to the blue, and the quadrupolar response lies out of the analyzed range.

For hemispherical nanoparticles located on a sapphire substrate (right column of Figs. 8.3 (a,b)) [126, 161, 160], the plasmonic performance is substantially modified by the geometry and the substrate. In general, interactions with the dielectric substrate tend to red-shift the dipolar resonance with respect to the isolated sphere of the same radius [126]. For aluminum and magnesium the absorption is stronger for the hemispherical case than for the spherical case, due to the volume reduction of the metallic core. As a consequence of this, the plasmonic absorption reaches a maximum for these Al and Mg hemispherical nanoparticles for certain values of the core radius within the studied interval, in contrast with the isolated spherical nanoparticles for which the absorption increases as the core shrinks. Conversely, the absorption for Ga hemispheres decreases with decreasing core radius but reaches a maximum value for an intermediate spherical core radius. In general, if left and right plots of Fig. 8.3(b) are compared, we can conclude that the overall effect of going from the sphere case to the hemisphere one is a shift of the peak absorption to larger core radius and to longer

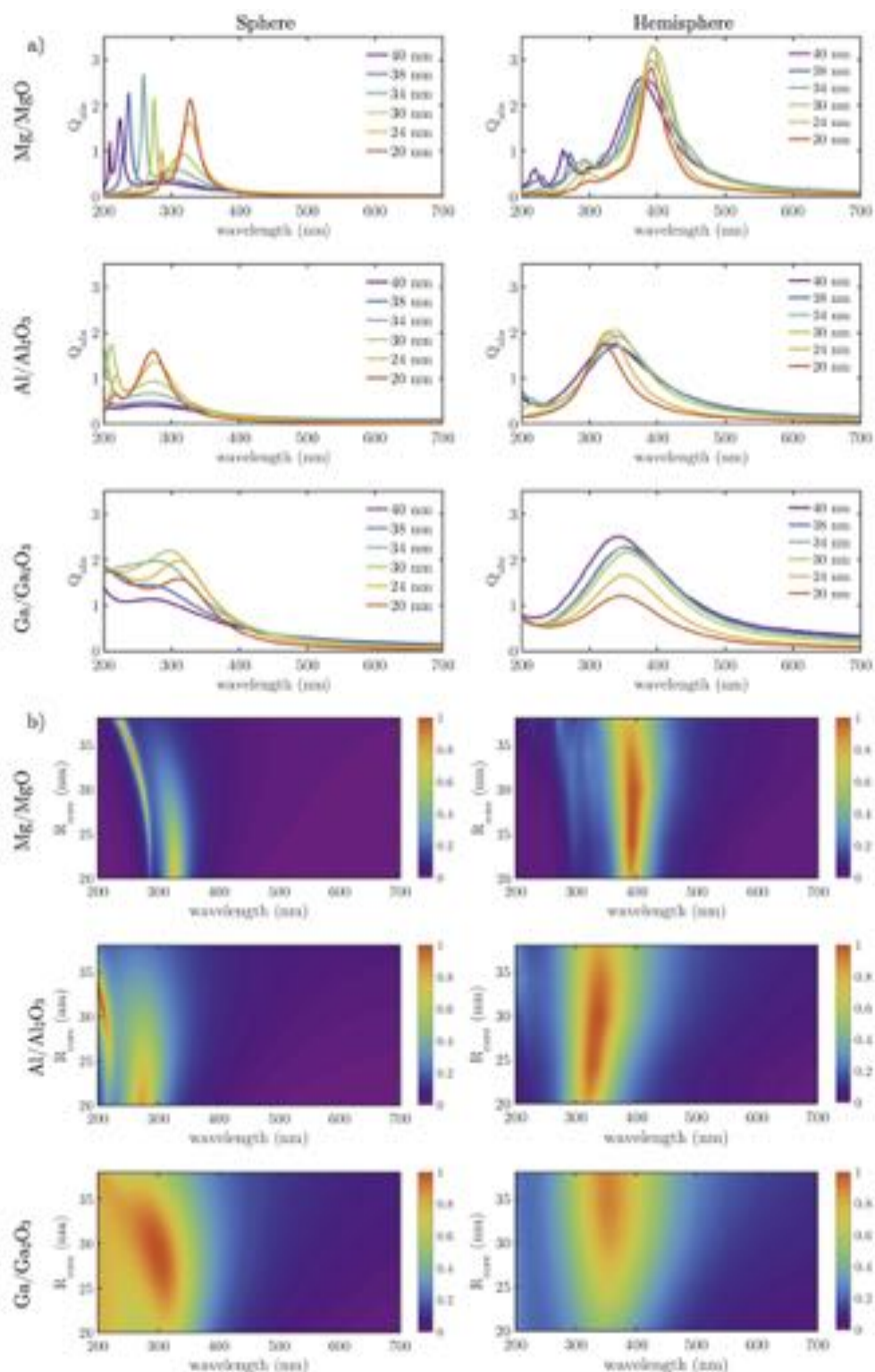


Figure 8.3 (a) Absorption efficiency, Q_{abs} , of a core-shell spherical (left column) and a hemispherical NP (right column), for Mg/MgO (first row), Al/Al₂O₃ (second row) and Ga/Ga₂O₃ (third row). The particle total radius is $R = 40$ nm while the core radius varies from $R_{core} = 20$ to 40 nm. (b) 2D color map of the normalized absorption efficiency as a function of the wavelength and the core radius R_{core} for Mg/MgO (first row), Al/Al₂O₃ (second row) and Ga/Ga₂O₃ (third row) spherical (right column) and hemispherical on substrate NPs (right column).

wavelengths. However, the hemispherical-on-substrate geometry is less sensitive to the value of R_{core} . Note that the substrate and the oxide shell have a similar refractive index, so the effective refractive index surrounding the metallic core is larger for the hemispherical nanoparticles than for the isolated spherical nanoparticle with the same oxide thickness. Consequently, the associated blue-shift produced by the oxidation is less for the hemisphere than for the isolated sphere. Finally, it is worth mentioning that the hemisphere geometry presents weaker quadrupolar resonances.

By considering the dielectric constants of each studied metal and their corresponding oxides (Fig. 8.2), it would be expected that Mg would have the lowest values of Q_{abs} since it has the smallest values of the imaginary part of the dielectric function, but Al Q_{abs} peaks are lower. This apparently contradictory behavior may be understood by recognizing that it is the area under the Q_{abs} curve, not the peak, that is related to the power absorbed by the particle. The Al absorption peak is weaker but wider than that of Mg, so it is not clear which one absorbs more. Furthermore, the real part of the dielectric function has also an effect on the absorption efficiency. In the region of interest (200-300 nm), Al acts as a better conductor than Mg since the real part of its dielectric constant is more negative and is thus better able to limit field penetration.

8.2.2 Near-Field Enhancement

The analysis of the near field enhancements is of great interest for Raman (SERS) or fluorescence (SEF) spectroscopy techniques where surface field and its interaction with adsorbed analytes play a crucial role. The local electric field distribution has been calculated and analyzed by FEM method, for the two geometries and for different values of the core size and oxide shell thickness. For brevity, and as a representative example of the general behaviour, in Fig. 8.4 the local electric field distribution is only plotted for a core-shell (metal-metal oxide) spherical (top row) and hemispherical-on-substrate (bottom row) with $R_{core} = 30$ nm and a oxide shell of 10 nm. The illuminating beam is a monochromatic linearly polarized plane wave whose propagation (\mathbf{k}) and polarization directions (\mathbf{E}) are indicated in the inset. The illuminating wavelength corresponds to the electric dipolar resonance in the Q_{abs} spectrum. The main conclusion is that hot-spots corresponding to a surface electric field enhancement are observed on both the core and the shell, especially for the spherical case. These enhancements correspond to charge concentrations induced by the polarization of the incident field and are manifested by non-propagating evanescent waves. For thick oxide shells, these evanescent waves remain attached to the metallic core and dissipate within the oxide shell. However, for thin oxide shells, part of this evanescent field reaches beyond the

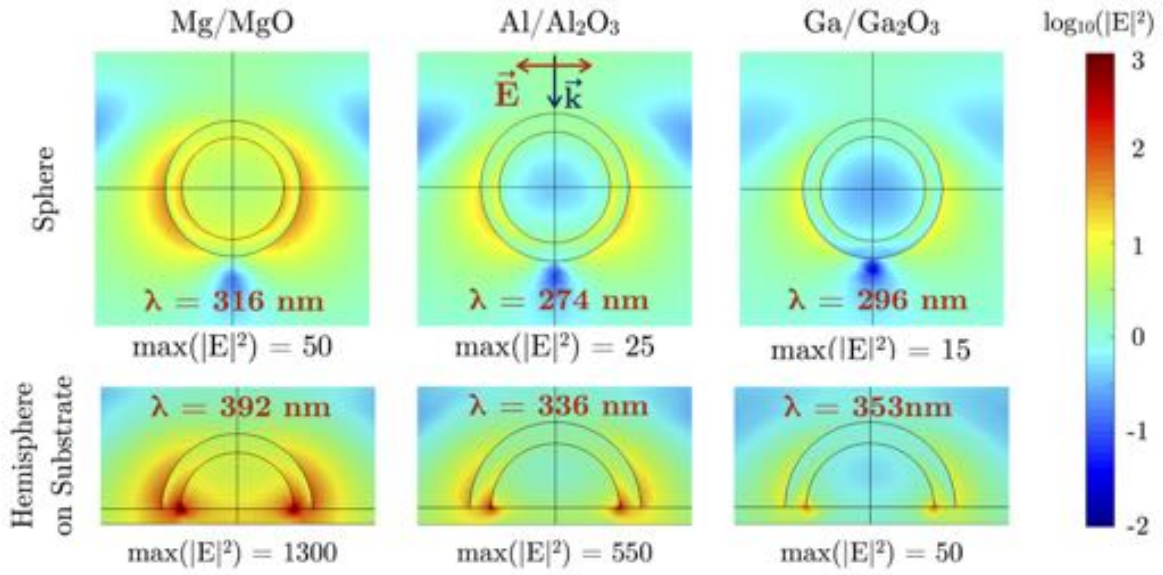


Figure. 8.4 Local electric field distribution for an isolated core-shell spherical and hemispherical nanoparticle for each metal, with $R = 40$ nm, $R_{core} = 30$ nm, and a 10 nm thick oxide shell. The illuminating wavelength in each case corresponds to the one that makes Q_{abs} maximum.

surface of the particle, creating external hot-spots with evident practical interest. For the hemisphere geometry, these hot-spots are located mainly where the metallic core touches the substrate, i.e. where the metallic core has sharp edges. Because they are not accessible from outside, they are of little practical interest.

In order to quantify how these enhancements are distributed between core and shell surfaces, the ratio between the average of $|\mathbf{E}|^2$ on the core and shell surfaces is represented in Fig. 8.5. These ratios are plotted as a function of the core size for the two geometrical configurations at the wavelength at which $\langle |\mathbf{E}_{shell}|^2 \rangle$ takes its maximum value in the electric dipolar resonance. For both cases, it can be observed that for a small metal core with thick oxide shells, $\langle |\mathbf{E}|^2 \rangle$ is much higher at the core than in the shell, with $\langle |\mathbf{E}_{core}|^2 \rangle / \langle |\mathbf{E}_{shell}|^2 \rangle > 1$. As the oxide shell thins, the value of this ratio generally decreases until the shell enhancement becomes larger than the core enhancement, and the hot-spots are clearly located on the shell surface ($\langle |\mathbf{E}_{core}|^2 \rangle / \langle |\mathbf{E}_{shell}|^2 \rangle < 1$). This happens for the spherical geometry for all the three materials analyzed. For the hemispherical geometry, we get similar results, except that this ratio is considerably larger because of the high field enhancements where the metallic core meets the substrate.

Ratios $\langle |\mathbf{E}_{core}|^2 \rangle / \langle |\mathbf{E}_{shell}|^2 \rangle < 1$ can be interpreted by considering boundary conditions for the normal component of the displacement vector $\mathbf{D} = \epsilon \mathbf{E}$. At hot-spot

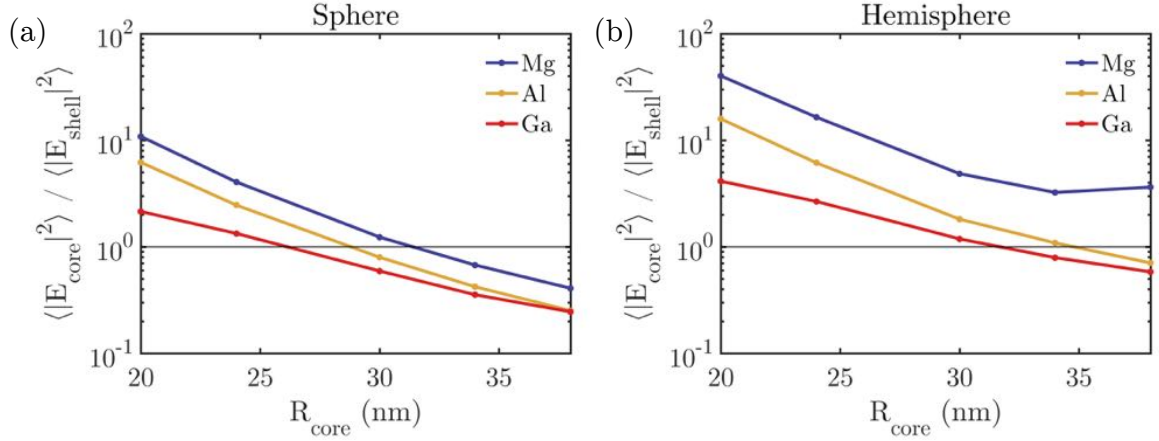


Figure. 8.5 Evolution of $\langle |\mathbf{E}_{core}|^2 \rangle / \langle |\mathbf{E}_{shell}|^2 \rangle$ for each metal as a function of the metallic core size for a spherical and hemispherical nanoparticle of radius 40 nm at the wavelength at which $\langle |\mathbf{E}_{shell}|^2 \rangle$ takes its maximum in the electric dipolar resonance.

positions, the near field is mostly composed of evanescent waves, and its electric field direction is predominantly radial, normal to the spherical surface. In this situation, the component of the displacement vector \mathbf{D} normal to the surface separation between the oxide shell and vacuum is conserved. Because the shell electric permittivity is larger than that of the surrounding vacuum, the electric field inside the shell is smaller than outside of it.

For hemispherical nanoparticles, the electromagnetic field tends to be confined at the edges of the hemisphere (lightning rod effect [184]). Due to this confinement, thinner shells are required to achieve $\langle |\mathbf{E}_{core}|^2 \rangle / \langle |\mathbf{E}_{shell}|^2 \rangle < 1$; indeed, for Mg this ratio is always > 1 . As can be seen in Fig. 8.4, the maximum value $|\mathbf{E}|^2$ is much larger for all three metals because of this confinement. By contrast, in the isolated spherical geometry the electromagnetic energy is spread in larger regions instead of being bound around the edges.

For practical purposes it is interesting to be in the $\langle |\mathbf{E}_{core}|^2 \rangle / \langle |\mathbf{E}_{shell}|^2 \rangle < 1$ region, where the enhancement is primarily located in the shell surface and therefore accessible. The fact that for the Mg hemisphere this condition can not be fulfilled indicates that this type of structure cannot be effectively used for surface enhanced applications.

Concerning the analyzed materials, magnesium presents the highest values of these electric field enhancements because Mg and MgO are the least lossy materials. On the contrary, gallium and its oxide shell present the poorest plasmonic performance. It is interesting to point out that the core size for the condition $\langle |\mathbf{E}_{core}|^2 \rangle / \langle |\mathbf{E}_{shell}|^2 \rangle = 1$ increases as the Faraday number [114] (Fa) of the metal becomes larger, but the

enhancement depends more sensitively on core radius. Figure 8.5 indicates that for a given geometry, the sensitivity of $\langle |\mathbf{E}_{core}|^2 \rangle / \langle |\mathbf{E}_{shell}|^2 \rangle$ to increasing R_{core} is larger for the Mg and Al than for Ga.

8.2.3 Influence of the Oxidation on Plasmonic Performance

Figure 8.6 plots the evolution of the peak value and wavelength of the dipolar resonance for both Q_{abs} and $\langle |\mathbf{E}|^2 \rangle$ in terms of the core radius for both geometries of Ga, Mg, and Al. The way the peak value of $\langle |\mathbf{E}|^2 \rangle$ evolves with increasing oxide-shell thickness is similar for the three studied metals. Whereas for the spherical particle (red squares-solid line) its value reaches a maximum for the intermediate values of the analyzed shell thicknesses, in the case of the hemispherical nanoparticle (blue squares-solid line), the value of $\langle |\mathbf{E}|^2 \rangle$ decreases monotonically as the shell becomes thicker. Both behaviors are influenced by two factors: the way the oscillating charges in the metallic core are increasingly separated from the surface where the near field is calculated [185], and the fact that the evanescent field is increasingly confined inside the thicker oxide layers [186]. Since the intensity is calculated as an average of the electric field on the particle surface, its value depends sensitively on the oxide layer thickness.

Regarding the peak location, the hemisphere peaks are red-shifted from the spherical peaks, as expected [126], following the same behavior for both geometries but differing from metal to metal. For Mg and Ga, the resonance peak red-shifts from the bare metal value as the shell thickens, ultimately approaching a constant value. Although, the Al peak red-shifts with initial oxidation, it then blue-shifts with increasing oxide thickness, eventually to wavelengths shorter than its unoxidized wavelength. These idiosyncratic behaviors derive from the respective dielectric functions of the growing native oxide shell (red-shift) and shrinking metal core (blue-shift) [12, 126], an effect foreshadowed in an early investigation of Al NPs [144] and consistent with more recent studies [115, 160].

The characteristic spectral red-shift of the near field $\langle |\mathbf{E}|^2 \rangle$ (circles-dashed line) from the far field [182, 122], Q_{abs} (squares-solid line) is clearly observed for all geometries. The magnitude of this shift depends on the value of the imaginary part of the dielectric function [122]. When the imaginary part of the dielectric function is low, as for Mg, the red-shift is smaller, but when its imaginary part is higher, as for Ga, the red-shift is larger. The quantification of this shift allows an optimization of the near fields based on their far-field counterparts, which are, in general, easier to measure.

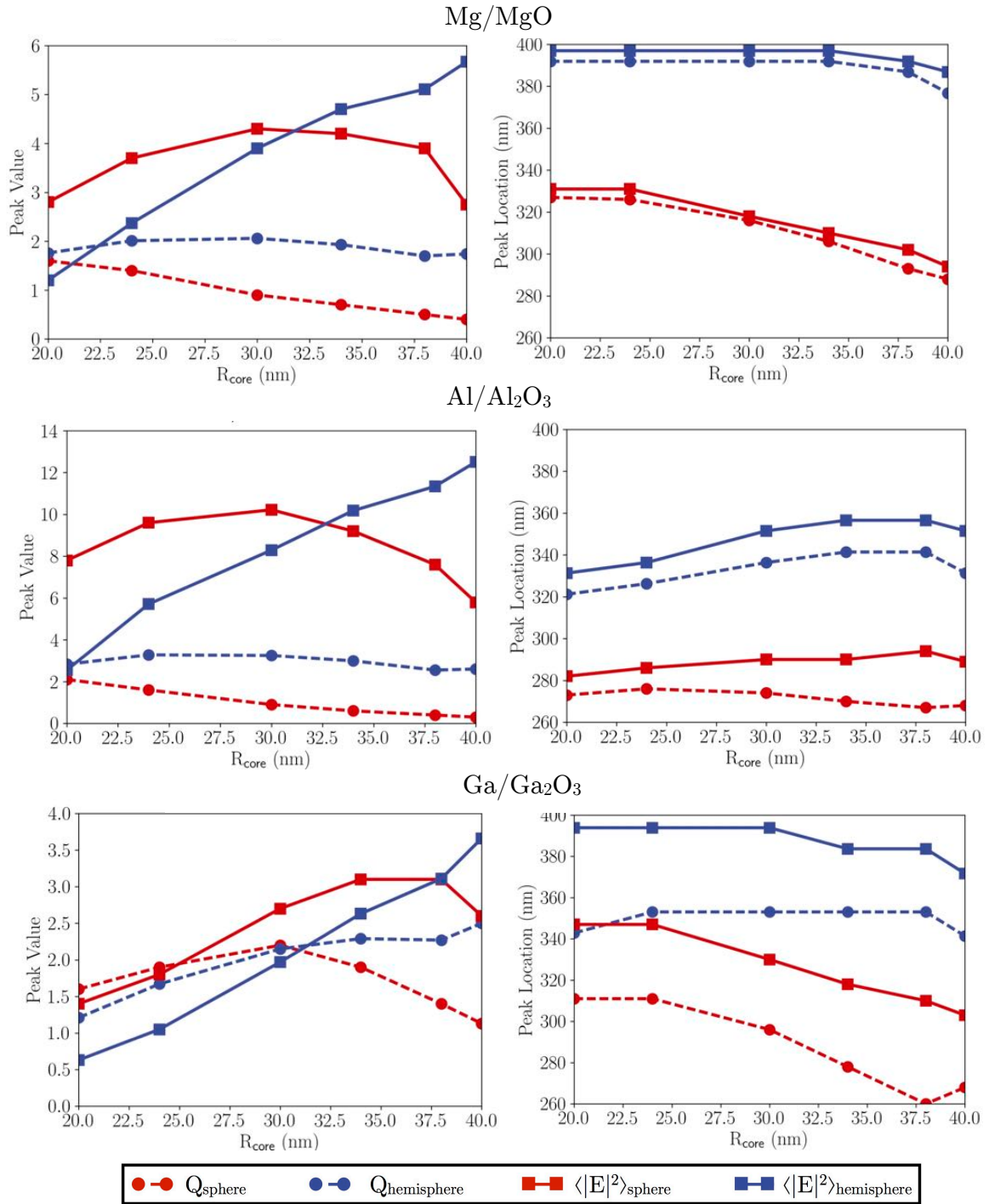


Figure 8.6 Evolution of the peak value (top) and location (bottom) for the Q_{abs} (circles) and the $\langle |E|^2 \rangle$ (squares) for spherical (red) and hemispherical (blue) nanoparticles of Mg/MgO, Al/Al₂O₃ and Ga/Ga₂O₃.

From an experimental point of view, Al and Mg show an interesting plasmonic behavior in the UV [12], and both are quite stable metals in absence of humidity [160] and at moderate temperatures [146]. Unfortunately, nanostructures of these metals are quite susceptible to oxidation during or after fabrication, and further investigations are needed to understand and control nanoscale oxide formation [115, 160]. For example, if ambient temperature increases over 400°C, Al can oxidize almost completely due to the high mobility of oxygen [146]. In this way, the heating action produced by a powerful light source interacting with the strong plasmonic absorption of Al NPs could produce a deleterious effect by inducing additional oxidation. Consequently, both humidity and Joule heating can produce efficiency losses in both metals and blue-shifts of the resonances in Al after several uses. Although gallium shows the weakest resonance and strongest oxide sensitivity, it is of interest because its oxide is thin and stable, its resonances in the UV [126, 166] are broad, and its low melting point makes it suitable for eutectic alloys that may improve its plasmonic performance [187].

8.3 Conclusions

In summary, we have studied the effect of NP oxidation on the UV plasmonic performance of three promising metals: gallium, magnesium, and aluminum [12, 142, 126, 161]. The growth of an oxide shell on a hemispherical NP surface made of Ga, Mg, or Al produces a decrease in the near-field amplitude of $\langle |\mathbf{E}|^2 \rangle$ for all cases. However, for the spherical nanoparticles, the value of $\langle |\mathbf{E}|^2 \rangle$ increases for intermediate values of the analyzed shell thicknesses. The values of Q_{abs} in hemispherical NPs actually increases for the three metals under study for some intermediate value of the oxide thicknesses. For Al and Mg spherical NPs, Q_{abs} increases as the size of the core decreases. On the contrary, for Ga spherical nanoparticles, the Q_{abs} maximum is found for a 10 nm thick oxide shell. The resonance could be red- or blue-shifted depending on the material and the thickness of the shell. Furthermore, the systematic, monotonic reduction of the field intensity on the particle surface may be used as an estimate of the oxide thickness. These results indicate how UV plasmonic resonances of Ga, Mg, and Al may be optimized for SERS-like applications, allowing control of the near field peak intensity and its spectral location.

Chapter 9

The Tarnishing of Mg/MgO Nanoparticles

Recently, magnesium (Mg) is gaining renewed interest because of the innovation it is introducing in a multitude of application fields spanning from hydrogen storage as magnesium hydride (MgH_2) [38], to electronics as transparent semiconductor magnesium hydroxide ($\text{Mg}(\text{OH})_2$) [188], to plasmonics as Mg nanostructures supporting tunable LSPRs from the near-infrared (NIR) to the ultraviolet (UV) [49, 12] for sensing [51] and photovoltaic [189] enhancement, and photocatalysis [132], and to photonic applications such as dynamic plasmonic color displays based on Mg/ MgH_2 system [164] and on the Mg (metal)/MgO (dielectric) platform recently proposed for transient photonics [190]. For all those applications exploiting the localized surface plasmon resonances (LSPRs) it is crucial the precise tuning of the efficiency and spectral position of LSPRs as well as its stability, which are affected by the surface reactivity. In light of this, attention has been paid in the previous chapter to the effect of the oxide shell that forms upon air exposure on the surface of nanostructures made of plasmonic metals such as Mg, aluminum (Al) and gallium (Ga) [109, 180]. So far, the limit of Mg has been reported to consist mainly in its oxidation to MgO [191].

However, oxidation is not the only chemical surface transformation that can occur at the surface of metal NPs. Surface tarnishing is a well known phenomenon on Ag, and its origins have been extensively investigated: the main product is silver sulfide (Ag_2S) due to reaction with sulfur (S) contaminations (sulfidation), OCS and H_2 , in ambient laboratory air [192, 193].

Indeed, sulfur dioxide (SO_2) is among the most important trace oxidants in the indoor and outdoor atmosphere, which can be responsible of Mg corrosion [194]. On the other hand, nanosized Mg and MgO have emerged as appealing materials for the

removal of fluoride and other anions from water, considering that fluoride is one of the major pollutants of groundwater. MgO has been suggested to be an attractive defluoridation agent due to its high adsorption capacity, non-toxic nature and limited solubility in water [195].

The work presented in this chapter demonstrates the tarnishing of oxidized Mg nanoparticles (Mg/MgO NPs) by the heterogeneous adsorption of SO₂ and fluorides (F-species) from air and the formation of MgSO₄, MgF₂ and other Mg-oxyfluorides (MgO_{1-x}F_x) compounds on the surface of Mg/MgO NPs in the form of micron-size crystals. Section 9.1 presents the sample fabrication methods, the different techniques used for the structural, chemical and optical characterization of the samples, and how they have been exposed to an hydrogen plasma treatment. Additionally, it is detailed the electromagnetic methods employed to model the change in the plasmonic response and color of the samples when MgSO₄ and MgF₂ forms on the surface of the Mg/MgO NPs. In Section 9.2 are gathered the main results of this chapter: it is shown that the “thought inert” oxide MgO shell has the potential to adsorb air contaminants. The products from the heterogeneous adsorption and reaction of F and S on Mg/MgO surfaces have been chemically, structurally and optically investigated by X-ray photoelectron (XPS), Raman and FTIR spectroscopies, atomic force microscopy (AFM) and spectroscopic ellipsometry. On one side we discuss the implication of this tarnishing on the plasmonic behavior of Mg/MgO nanoparticles, while on the other side we show that nanostructured Mg/MgO can be used as sink of contaminants and therefore as purifier. Moreover, it is demonstrated that the tarnish layers can be removed by a hydrogen plasma afterglow at 100°C in a matter of seconds. Finally, Section 9.3 summarizes the main conclusions of this chapter.

The relevance of the work presented in this chapter pop ups from the need of new systems for air purification that absorb, monitor and detect the presence of sulfur (S) and fluorine (F) containing gases in air that pose a risk for human health and the environment [196]. In fact, the World Health Organization has reported that, annually, there are 7 million deaths caused by air pollution. Already, systems based on carbon allotropes have been reported as nanoadsorptive structures capable of adsorbing NO_x, CO₂, HF, CF_x or H₂S, among other pollutants and greenhouse effect gases [196].

9.1 Methods

9.1.1 Sample Fabrication

Mg self-assembled nanoparticles samples were prepared by evaporating Mg on an Al_2O_3 substrate at room temperature under ultra-high-vacuum (UHV) 10^{-10} Torr conditions in a VEECO GENII molecular beam epitaxy system (MBE) to make sure that the prepared samples were not contaminated. The nanoparticles samples provided a range of case studies with different active surface area for adsorption. The samples were exposed to laboratory atmosphere with a humidity of 60%.

9.1.2 Sample Characterization

Chemical characterization was performed by Raman spectroscopy (LabRam Horiba) excited by a 532 nm laser, X-ray photoelectron spectroscopy (XPS) using a monochromatic Al $K\alpha$ source (PHI 5400 VERSAPROBE) at a take-off angle of 45° , and Fourier-transform infrared spectroscopy (FTIR) (Vertex 70V Bruker). Morphology and phase analysis was performed by atomic force microscopy (AFM) (AutoProbe CP, ThermoMicroscope). Overlayer thickness and optical properties, namely spectra of the complex pseudodielectric function, $\langle\epsilon\rangle = \langle\epsilon_r\rangle + \langle\epsilon_i\rangle$, were measured by spectroscopic ellipsometry (UVISEL Horiba) in the photon energy range 0.75 – 6.5 eV with a resolution of 0.01 eV.

9.1.3 Hydrogen Plasma Treatment

The tarnish layer was removed by exposing the samples to a hydrogen plasma afterglow and this interaction was investigated in real time in a reactor that combines a remote hydrogen plasma source with an *in-situ* spectroscopic ellipsometer (UVISEL Horiba), allowing us to optical monitoring the hydrogen interaction and resulting modification of Mg samples and their optical properties. Hydrogen exposure occurred at 1 Torr with a H_2 flow rate of 200 sccm, whereas atomic hydrogen was produced by a radiofrequency (r.f.) 13.56 MHz plasma at the low power of 50 W to study the direct interaction with H-atoms. Kinetic data were acquired with a time resolution of 1 sec.

9.1.4 Electromagnetic simulations

The formation of MgO , MgF_2 and MgSO_4 on the surface of Mg nanoparticles and its effect in the plasmonic response of the system has been modeled by using Mie

theory for a multilayered sphere. The absorption efficiency has been calculated for spheres with a total radius $R = 50$ nm and a shell thickness varying from 0 to 50 nm. The complex refractive index of Mg, MgF_2 , MgSO_4 and MgO have been taken from different sources in the literature [13, 181, 197, 198]. The color coordinates have been obtained from the reflectance of a multilayered system calculated at normal incidence through the Transfer Matrix Method. The color coordinates are expressed in the $L^*a^*b^*$ system. For the color coordinates calculations, it has been considered the CIE standard Illuminant D65 and the CIE 1931 Standard Observer [199].

9.2 Results

Figure 9.1(a,c) shows the real time evolution of the imaginary part of the pseudodielectric constant, $\langle \epsilon_i \rangle$, of Mg NPs recorded during their deposition on Al_2O_3 . The spectral evolution clearly shows the appearance of localized surface plasmon resonance (LSPR) peaks. At first, a LSPR peak appears at approximately 5 eV that remained almost at a constant position during the deposition process. With further Mg deposition a peak at lower energies appears that red-shifts with increasing NP density due to their aggregation forming clusters with increasing size [116]. Figure 9.1(b) and 9.1(d) shows the effect of 1 day of air exposure on the $\langle \epsilon_i \rangle$ of the two samples of Mg NPs, i.e., a quenching of the plasmon peak upon exposure to air is observed, which has been attributed in previous literature to oxidation of the NPs, transforming Mg to its dielectric oxide MgO [12]. This is supported by electromagnetic simulations performed on a Mg/MgO core-shell sphere with total radius $R = 50$ nm in which the thickness of the MgO is varied from 0 (100% Mg nanoparticle) to 50 nm (100% MgO nanoparticle) (see Fig. 9.1(e)). Figure 9.1(f) shows the 2D color map of the spectral absorption efficiency (Q_{abs}) as a function of the MgO shell thickness. It can be seen how for the thicker MgO shells the plasmon peak is completely quenched. Therefore, we can conclude that the oxide has consumed almost all metal content in the nanoparticles i.e., radius of the Mg core $R < 10$ nm.

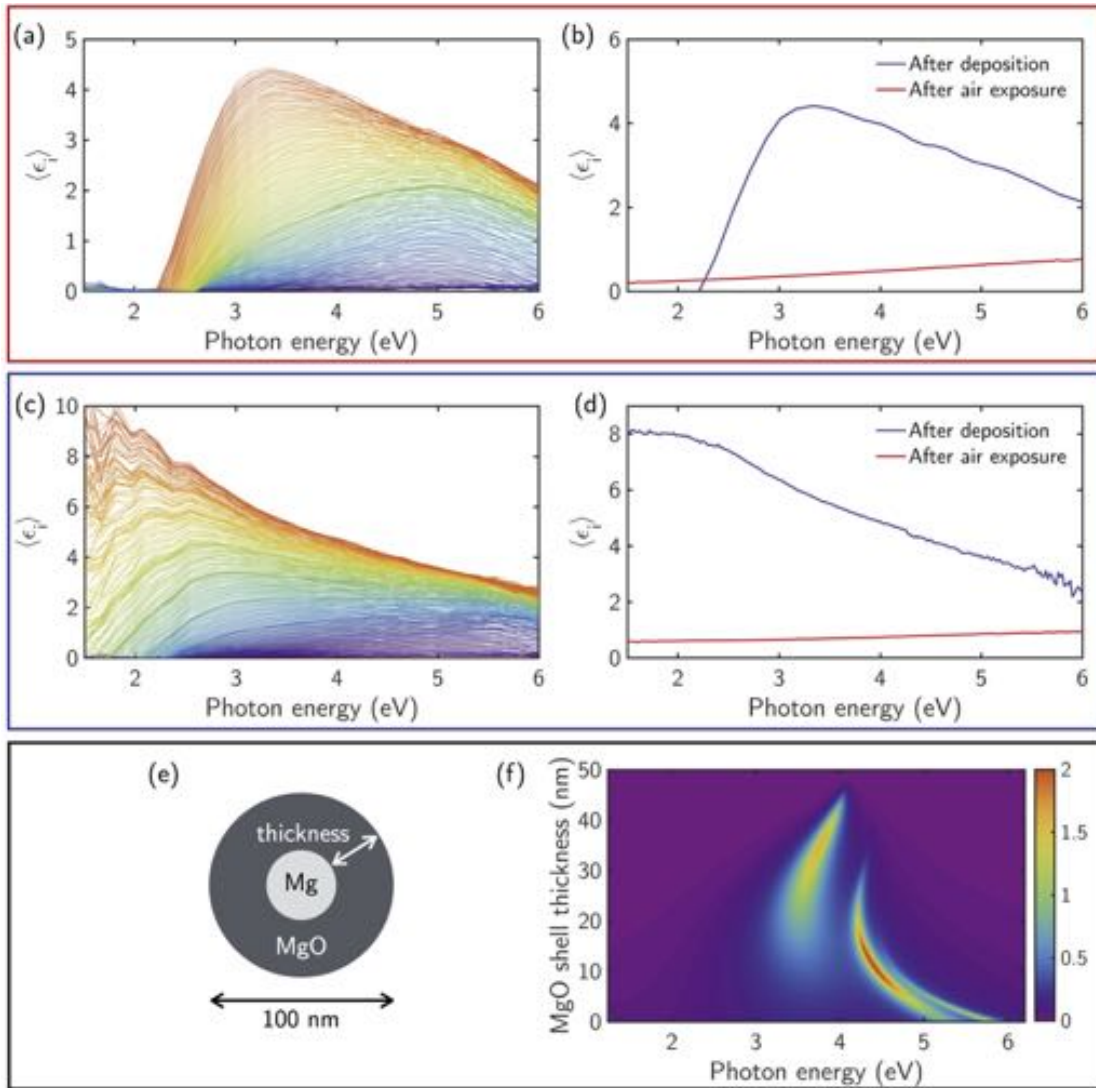


Figure. 9.1 (a,c) Real time evolution of the imaginary part of the pseudodielectric function ($\langle \epsilon \rangle = \langle \epsilon_r \rangle + \langle \epsilon_i \rangle$) for Mg NPs grown on Al_2O_3 ; (a) shorter Mg deposition time corresponding to smaller NPs, and (c) larger Mg deposition time corresponding to higher density and larger NPs as well as aggregates of NPs. (b,d) Mg NPs LSPR quenching due to air exposure. (e) Scheme of the geometry in which electromagnetic simulations have been performed: Mg/MgO core-shell spherical NP of total radius $R = 50$ nm. (f) 2D color map of the spectral absorption efficiency (Q_{abs}) of a Mg/MgO core-shell as a function of the MgO shell thickness.

Figure 9.2 shows the initial morphology of the Mg NPs samples and the changes in the surface morphology after 1 month of air exposure. We verified that all the analyzed samples could be grouped in two categories of morphology changes shown in Fig. 9.2. Initial Mg NPs have similar NPs sizes with histogram radius distribution peaked at ≈ 30 nm but different shape and density resulting in different values of the peak-to-valley

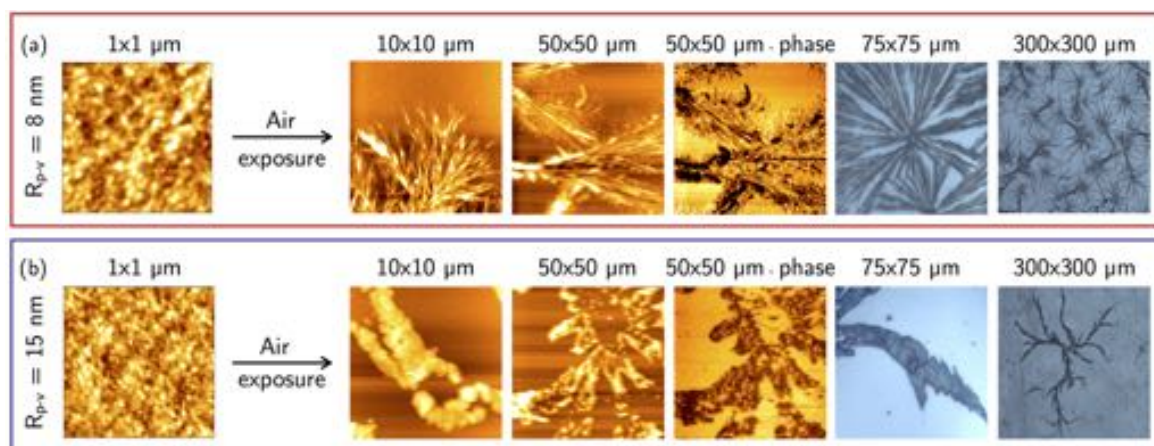


Figure. 9.2 AFM topography of Mg NPs of different R_{p-v} (value is indicated) soon after the deposition and after air exposure. Different scan size images after air exposure are reported to better show the different shape of those crystals. The phase images of both samples after air exposure, indicating the different chemical nature of those crystals are also reported. Larger size optical microscopy images are also shown to put in evidence the distribution of those different shape microcrystals.

roughness, R_{p-v} also reported in Fig. 9.2. Upon 1 month of air exposure, micron-size dendritic crystals of different shape and density form depending on the different R_{p-v} . Those crystals increase in size and density until they cover the whole sample surface over the prolonged checked period of 6 months. The contrast in the phase image shown in Fig. 9.2 indicates that those crystals are of a different chemical nature than the Mg/MgO nanoparticles.

The nature of those crystals was determined combining Raman, FTIR absorbance spectra, and XPS Mg2p, O1s, F1s and S2p photoelectron core level spectra reported in Fig. 9.3. The Raman spectra taken on the crystal (blue circle in the inset) and substrate region (red circle in the inset) of the sample clearly show peaks due to vibrational modes in MgF_2 (blue arrows) and MgSO_4 (yellow arrows). The MgF_2 peaks are located at 240 and 469 cm^{-1} , consistent with the values reported by Neelamraju et al. [200]. The peaks corresponding to MgSO_4 located at 607 , 986 and 1082 cm^{-1} , consistent with values reported in literature [201], are due to the vibrational modes of SO_4 . Figure 9.3(b) shows the corroborating FTIR absorbance spectra in the $600 - 1700\text{ cm}^{-1}$ spectral range. The peak shadowed in yellow, composed by two overlapping peaks at 1095 and 1122 cm^{-1} , corresponds to the ν^3 band of SO_4 in MgSO_4 . The position of this band is highly dependent on the relative humidity of the air and the substrate in which the MgSO_4 is deposited. Reported values in literature show a variation between 1100 and 1150 cm^{-1} [202]. The very strong broad band around

1600 cm^{-1} includes the contribution of the 1640 cm^{-1} band corresponding to adsorbed water and the absorption at 1620 cm^{-1} attributed to bridging hydroxy or oxy groups in intermediate alkoxy/hydroxy compounds [203]. Bicarbonates are also found on the surface as shown by the 1460 cm^{-1} band. The strong absorption around 900 cm^{-1} is due to MgO vibrations in the sample. Correspondingly, the XPS analysis in Fig. 9.3(c) shows the F1s, O1s, S2p and Mg2p photoelectron core levels. The F1s peak could be fit by two components, with the higher binding energy peak due to Mg-F (BE = 685.5 eV) and/or MgF_2 (BE = 685.52 eV [204]), and the lower binding energy peak (BE = 684.2 eV) due to Mg-F-O compounds, probably amorphous as indicated by the sketch of possible arrangement of the Mg-F-O compounds in Fig. 9.3(c) and consequently not originating peaks in the Raman spectrum. The S2p core level showed one main component peaked at 169.3 eV, consistent with values reported in the literature for MgSO_4 [205]. The O1s can be deconvoluted into two main components, i.e., one due to metallic oxides of both MgO and Al_2O_3 (from the substrate), and another one at higher binding energy consistent with MgSO_4 . Correspondingly, the Mg2p peak is also formed by two components. In this case, the one at lower energy corresponds to metallic Mg (BE = 49.7 eV [206]), and the one at higher energy that corresponds to MgO, MgSO_4 , Mg-F and Mg-F-O compounds (50.6 eV). All these components cannot be resolved in the Mg2p since they all have approximately the same binding energy (MgO BE = 50.8 eV [207], MgF_2 BE = 50.9 eV [208] and MgSO_4 BE = 51.4 eV [209]).

Interestingly, by analyzing several samples with different density of nanoparticles and morphology, we found that all samples could be grouped into two categories as indicated in Fig. 9.4, and that the tarnishing to mainly fluoride or sulfate depends on the sample morphology. Specifically, Fig. 4(a) shows the contaminants oxygen (O), fluorine (F), and sulfur (S) to Mg ratios as determined by XPS (Fig. 9.4(a)) on two samples with different morphology and surface roughness quantified by measuring the mean value of the peak-to-valley distance R_{p-v} (Fig. 4(b)). The R_{p-v} is related to the area exposed to ambient conditions i.e., the rougher the surface, the more area exposed to air. From Fig. 9.4 it can be inferred that the sample with the higher roughness and surface area (blue bars) shows larger amount of O/Mg and comparable amount of F (F/Mg = 0.55) and S (S/Mg = 0.30), while the sample with lower roughness (red bars) shows lower amount of oxygen and larger amount of fluorine with a F/Mg \approx 1 and negligible amount of S (S/Mg = 0.05). This dependence of contaminants on surface roughness and surface-active area indicates that the higher the values of R_{p-v} , the higher area exposed to air and the higher oxygen uptakes that further oxidizes both fluorine and sulfur from air forming sulfates and oxyfluorides. Conversely, smaller and

more packed nanoparticles with lower oxygen content react preferentially with fluorine contamination forming MgF_2 and oxyfluorides.

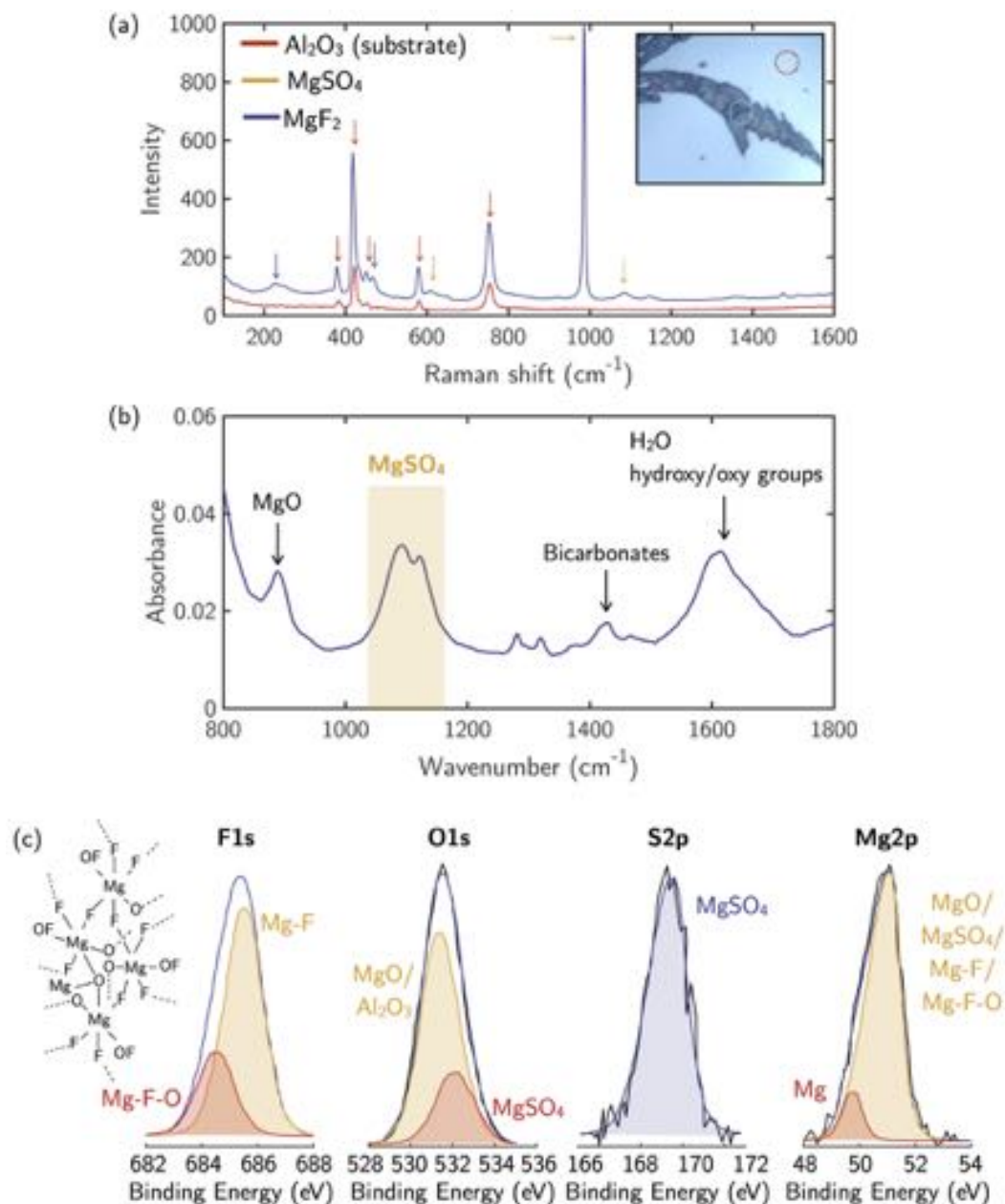


Figure. 9.3 (a) Raman spectra taken on the crystal (blue line, blue circle in the inset) and on the Al_2O_3 substrate (red line, red circle in the inset). With red, yellow and blue arrows are indicated those peaks assigned to Al_2O_3 , MgSO_4 and MgF_2 . (b) FTIR absorbance spectra. In yellow is shadowed ν^3 band of SO_4 in MgSO_4 . (c) XPS spectra of the $\text{F}1s$, $\text{O}1s$, MgSO_4 and $\text{Mg}2p$ photoelectron core level. As an inset in the $\text{F}1s$ spectra is indicated the possible Mg-F-O arrangement.

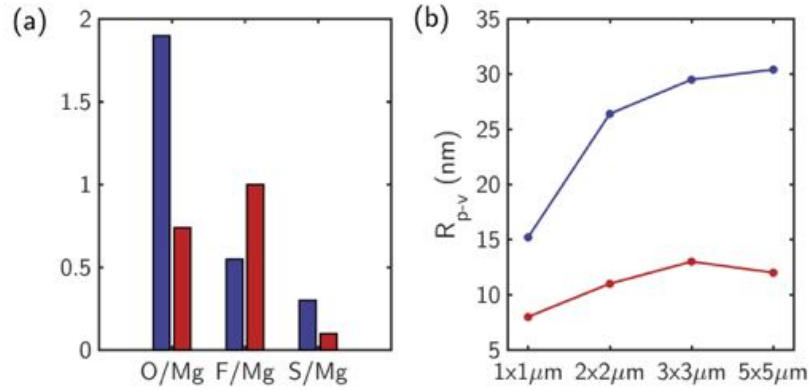
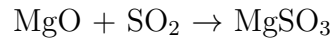
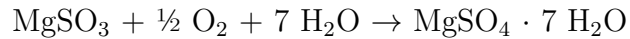


Figure. 9.4 (a) Oxygen, (O), fluorine (F), and sulfur (S), to Mg ratios measured by XPS for the two representative samples in Fig. 9.2; (red and blue colours refer to samples (a) and (b)). (b) Mean peak-to-valley distance (R_{p-v}) values measured through AFM in both samples after deposition as function of the sampled area.

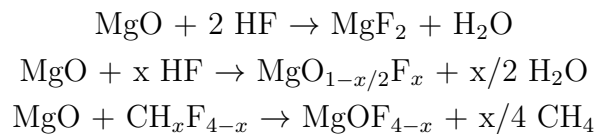
The formation of MgSO_4 can be explained in two steps. First, the heterogeneous reaction of adsorbed SO_2 on acidic magnesium sites (Mg^{2+}) of MgO to form MgSO_3



This reaction has already been observed by Czyżewski et al. on MgO loaded porous carbons [210]. Secondly, the further oxidation of MgSO_3 leading to MgSO_4 , as reported by Luque et al., occurs in presence of air humidity through the reaction [211].



It has also been suggested by the theoretical study of Pacchioni et al. [212] that sulfate can also form heterogeneously by interaction of the sulfur atom in sulfite with two surface five-coordinated O^{2-} anions, in other words, two oxide anions on the unreconstructed MgO surface. On the other hand, oxyfluorides may arise from the reaction of hydrogen fluoride (HF) and hydrocarbon fluoride $\text{CH}_x\text{F}_{4-x}$ contamination in air with MgO , i.e.,



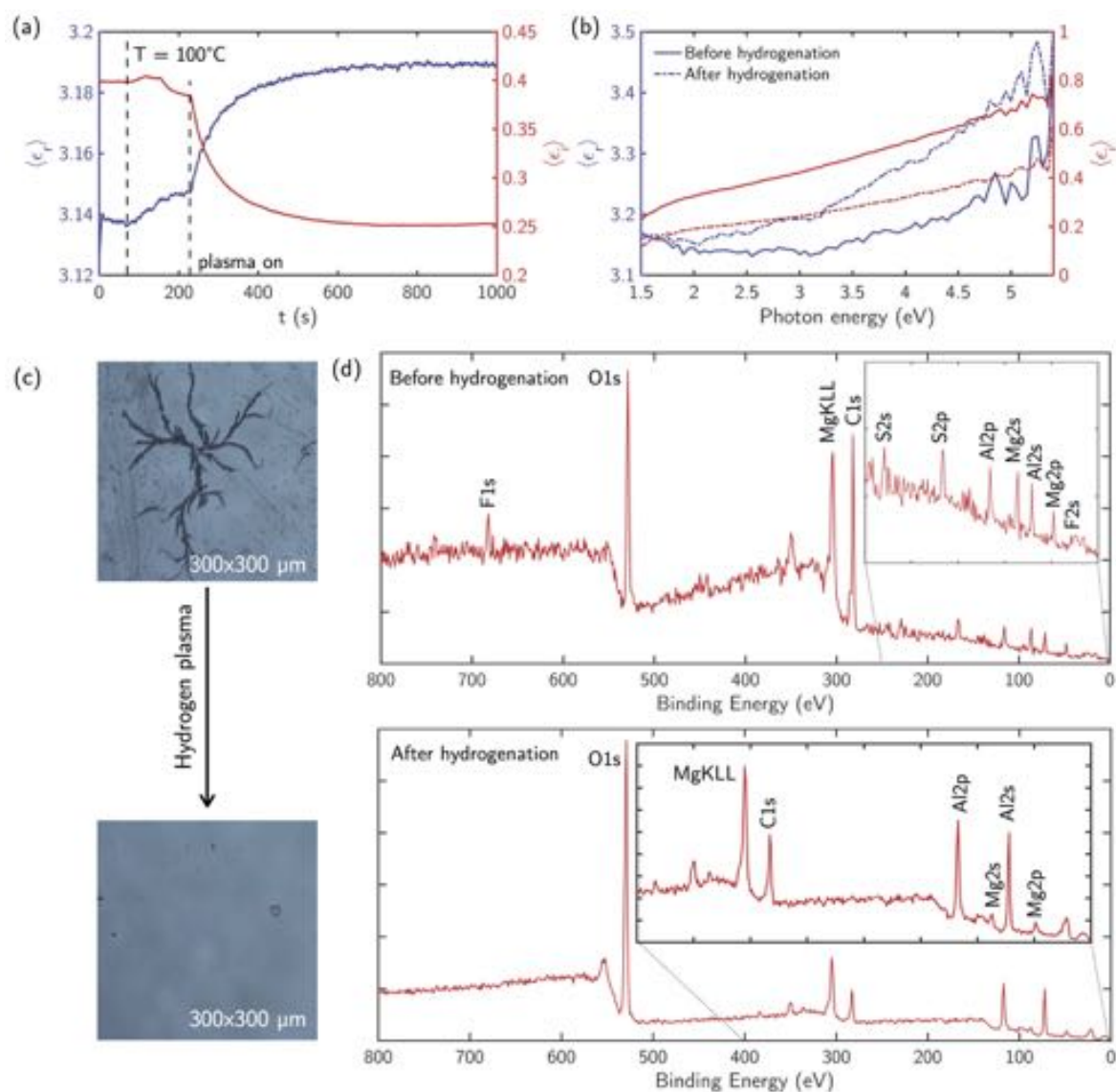


Figure. 9.5 (a) *In-situ* ellipsometry monitoring at 2.75 eV of the real (blue line) and imaginary part (red line) during the H_2 plasma exposure. (b) Experimental real (blue line) and imaginary (red lines) parts of pseudodielectric function of a sample of oxidized Mg NPs before (solid line) and after (dashed line) hydrogenation. (c) Micrography of the surface of the sample before and after the hydrogenation process. (d) XPS survey spectra of the sample before (top) and after (bottom) the hydrogenation process.

Interestingly, we verified if Mg/MgO samples could be regenerated from eliminating the F and S contaminant. Therefore, in order to remove the $\text{MgF}_2/\text{MgOF}_x$ and MgSO_4 from the surface of the samples we have exposed the sample to a remote hydrogen plasma at a temperature of 100°C . The interaction of the samples with atomic hydrogen has been monitored in real time by *in-situ* ellipsometry. Figure 9.5(a) shows the *in-situ*

ellipsometry monitoring at 2.75 eV of the real (blue line) and imaginary part (red line) of the pseudodielectric function during the H₂ plasma exposure. It can be seen that the exposure to the H₂ plasma causes a decrease of $\langle\epsilon_i\rangle$ and an increase of $\langle\epsilon_r\rangle$. The decreasing values of $\langle\epsilon_i\rangle$ is compatible with the desorption of elements from the surface of the sample. The increasing values of $\langle\epsilon_r\rangle$ correspond to the removal of MgF₂/MgOF_x and MgSO₄, both of them with lower refractive index than MgO, and the transformation of MgO into MgH₂, whose refractive index is higher (1.94 [13] vs 1.73 [17]). These effects can be spectrally extrapolated as shown in Fig. 9.5(b). Figure 9.5(b) shows the spectral dependence of the real (blue lines) and imaginary (red line) part of the pseudodielectric function before (solid lines) and after (dashed lines) the hydrogen plasma. Figure 9.5(c) shows micrography of the sample before and after the hydrogenation of the surface. It can be seen how the surface has been cleaned after exposure to the hydrogen plasma. Figure 9.5(d) shows the XPS survey spectra of the sample before and after the hydrogen plasma. Both survey spectra show peaks corresponding to Mg (MgKLL, Mg2p and Mg2s) from the NPs and Al (Al2p and Al2s) from the sapphire substrate. Before hydrogenation, the XPS survey spectrum present peaks ascribed to S (S2p and S2s) and F (F1s) that disappear after H treatment.

Figure 9.5a and 9.5b demonstrate that the heterogeneous adsorption of sulfur dioxide (SO₂) and fluorides (F-species) entails a change in the pseudodielectric function of the Mg/MgO NPs. This phenomenon opens the possibility of using the LSPRs or colorimetry measurements of the Mg/MgO NPs samples to detect and monitor the uptake of S- and F-compounds on the surface of the nanoparticles.

LSPRs are very sensitive to changes in the refractive index of their surroundings. This phenomenon is widely used for sensing applications. For example, in LSPR assisted biosensing, the spectrum around the plasma resonance is monitored looking for shifts produced in the extinction curves related to some target analyte [131]. Therefore, the spectral shift in the LSPRs can be used to monitor the transformation of the MgO shell that wraps the Mg core into MgSO₄ or MgF₂. To demonstrate this, we have performed electromagnetic simulations on a Mg/MgO core-shell spherical nanoparticle (total radius $R = 50$ nm and core radius $R_c \subseteq [0, 25]$ nm) in which the MgO shell is transformed progressively into either MgSO₄ or MgF₂ until MgO is completely consumed (100% MgSO₄/MgF₂ shell). The values of R_c have been chosen in order to mimic the almost complete oxidation of the Mg NPs reported by the ellipsometric data in Fig. 9.1. This geometry is illustrated in Fig. 9.6(a). Figure 9.6(c) and 9.6(d) plots the spectral shift ($\Delta\lambda$) of the LSP dipolar resonance as the MgO shell is converted to MgSO₄ and MgF₂ with respect to the spectral position of the 100% MgO shell.

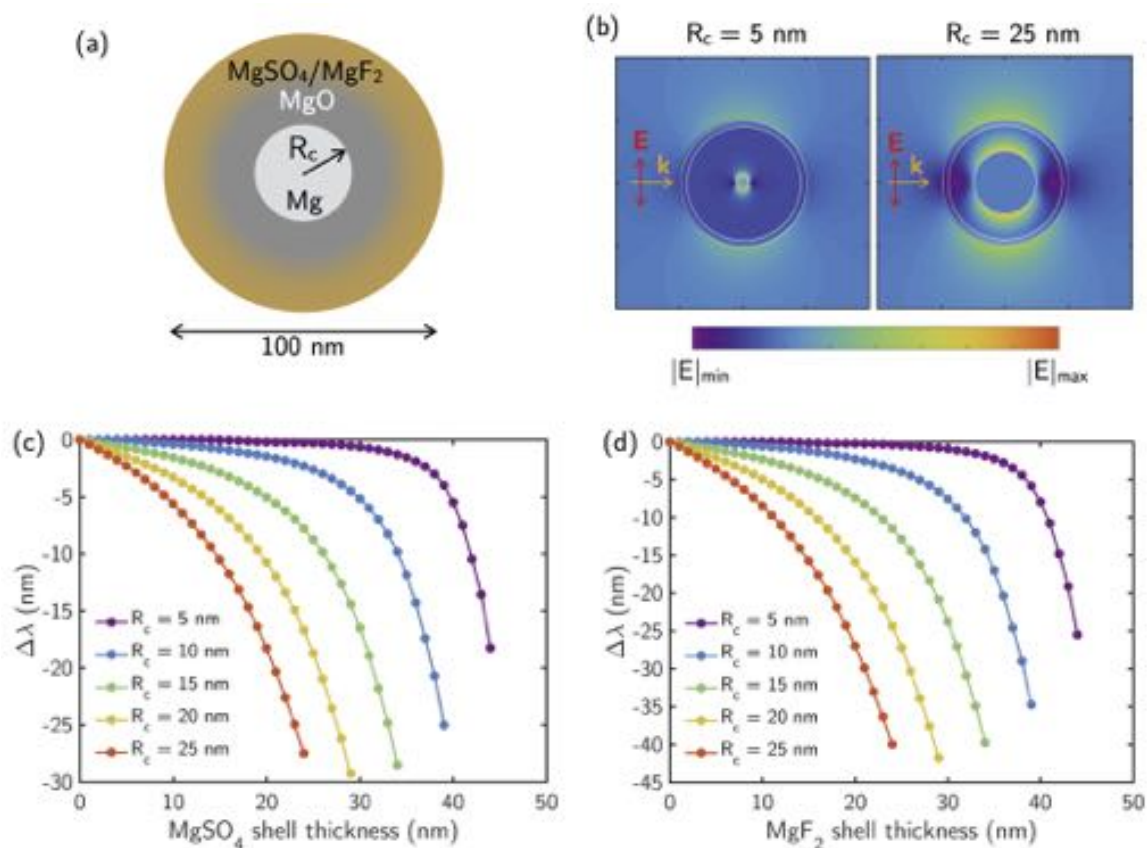


Figure. 9.6 (a) Scheme of the geometry in which the electromagnetic simulations have been performed: Mg/MgO core shell of total radius $R = 50$ nm and core radius R_c . The MgO shell is converted progressively into MgSO₄/MgF₂ until it is completely consumed (100% MgSO₄/MgF₂ shell). (b) Near-field $|E|$ map for Mg/MgO/MgF₂ multilayered sphere with $R_c = 5$ and 25 nm and MgF₂ shell thickness of 5 nm. With arrows are indicated incident electric field E polarization (red) and propagation direction k (yellow). (c,d) Spectral shift ($\Delta\lambda$) of the LSP dipolar resonance as the MgO shell is converted to MgSO₄/MgF₂ with respect to the spectral position of the 100% MgO shell. This calculation has been performed for different values of R_c while keeping the total radius fixed to $R = 50$ nm.

This calculation has been performed for different values of R_c while keeping the total radius fixed to $R = 50$ nm. In both cases, the transformation of the MgO shell into either MgSO₄ or MgF₂ produces a blue-shift of the LSPR. This is consistent with the fact that both MgSO₄ and MgF₂ have lower refractive indices n than MgO (1.54 and 1.41 vs 1.73): as the thickness of the MgSO₄/MgF₂ layers become thicker, the refractive index of the effective surrounding medium of the Mg core is lower, producing a blue-shift of the LSPR. Because the contrast between the refractive indices of MgO and MgF₂ is higher than that of MgO and MgSO₄, the blue-shift in the former case is

larger. In both cases, the sensitivity of the LSPR to the thinner shells of MgSO₄/MgF₂ increases with the value of R_c . For instance, for the highest and lowest values of R_c (25 and 5 nm) the values of $\Delta\lambda$ for a MgSO₄/MgF₂ shell thickness of 5 nm are -2.3 and 0 / -3.6 and 0 nm respectively. Therefore, the sensitivity to the conversion of the MgO shell into MgSO₄/MgF₂ increases with the amount of metallic Mg in the NPs (larger values of R_c). This trend can be understood attending to the change in the refractive index experienced by the near-field around the Mg core. Figure 9.6(b) plots the near-field $|\mathbf{E}|$ maps for a Mg/MgO/MgF₂ multilayered spheres with $R_c = 5$ and 25 nm, and a MgF₂ shell of 5 nm. Note that, although they are not shown here, the maps for the Mg/MgO/MgSO₄ are very similar. For the smallest cores and the thinner MgSO₄/MgF₂ shells, the extension of the near-field, which decays with the square of the distance, does not reach the boundary between the MgO and MgSO₄/MgF₂, being its response insensitive to the MgSO₄/MgF₂ growing shell (see Fig. 9.6(b) left). However, in NPs with higher values of R_c , the extension of the near-field produced by the Mg core reaches boundary between MgO and MgSO₄/MgF₂, therefore, even for the thinner shells a blue-shift of the LSPR is experienced (see Fig. 9.6(b) right).

The appearance of an over layer of these compounds on MgO surfaces entails a change of color. A similar effect is appreciated on Ag surfaces, which turn from shiny to dull blackened ones due to their tarnishing. This feature may allow the detection, or even the evolution, of MgSO₄/MgF₂ formation on Mg/MgO surfaces using colorimetric measurements. In order to study the change of color in our samples we have performed colorimetric simulations in systems as the one schemed in Fig. 9.7(a): a multilayer system constituted by an infinite Al₂O₃ substrate, a Mg layer of thickness h , a layer of MgO which is converted into either MgSO₄ or MgF₂ and air as surrounding medium. The total thickness of the Mg and MgO layers has been fixed to 50 nm. We have calculated the color coordinates $L^*a^*b^*$ for Mg layer thicknesses h ranging between 5 and 20 nm (see Fig. 9.7(a)). These values have been chosen to be consistent with the low Mg content of our samples confirmed by the ellipsometric data in Fig.9.1. Each point in the Fig.9.7(b-d) correspond to the increasing thickness of the MgSO₄/MgF₂ layer that consumes the MgO. The swept goes from 100% MgO to 100% MgSO₄/MgF₂ in steps of 1 nm. The extremes of this swept are labeled with the name of the compound in the layer. The color of each dot corresponds to the color of the film. As the value of h increases (more Mg in the system), the value of the luminosity L^* increases, leading to a shinier appearance more characteristic of metallic surfaces. The samples have a brownish color that becomes lighter as h increases. In order to objectively evaluate how the color of the system changes as the thickness of MgSO₄/MgF₂ layer increases

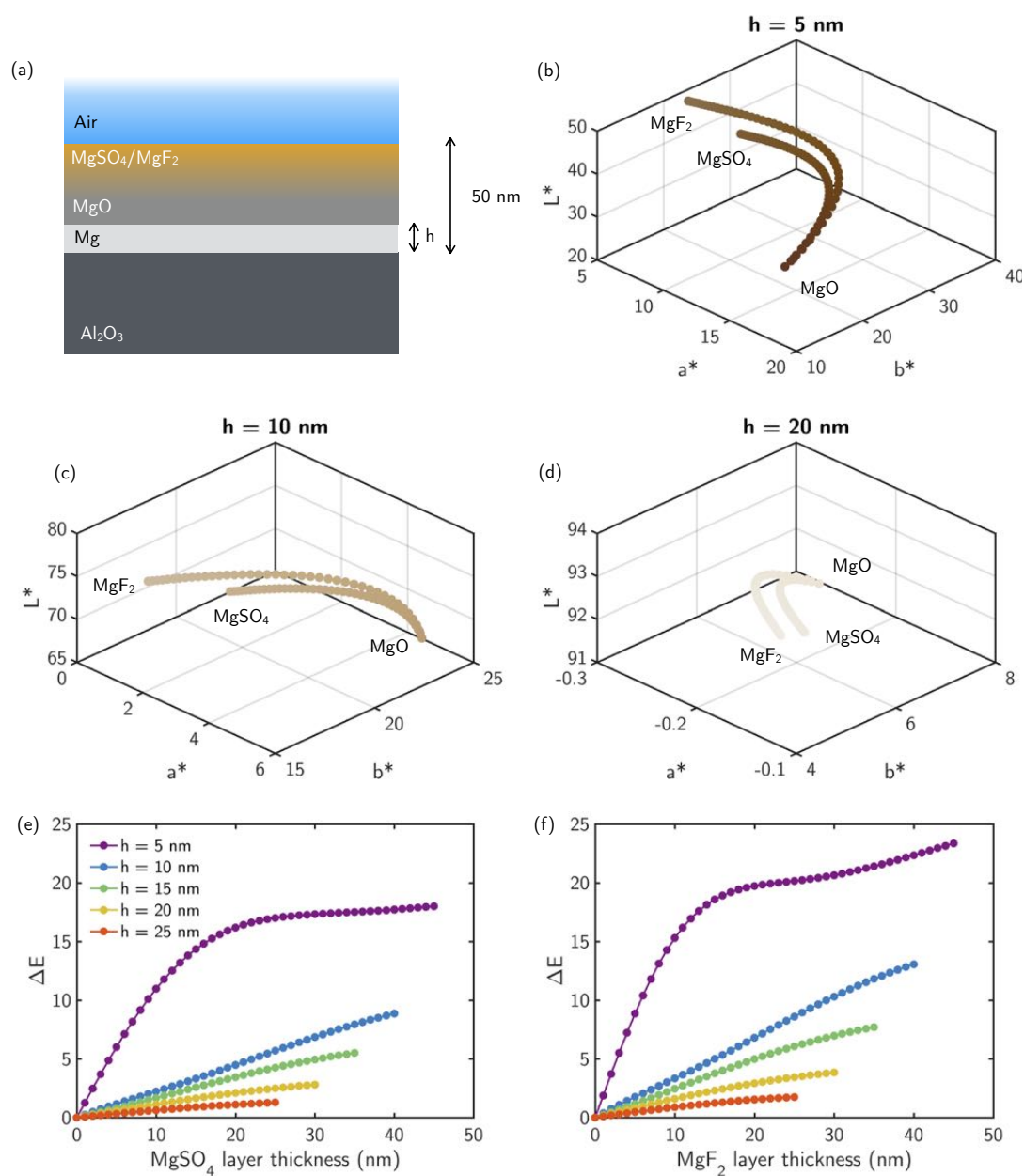


Figure. 9.7 (a) Scheme of the geometry in which the colorimetric simulations have been performed: multilayer system constituted by an infinite Al₂O₃ substrate, a Mg layer of thickness h , a layer of MgO which is converted in MgSO₄/MgF₂ and air as surrounding medium. The total thickness of the Mg and MgO layers have been fixed to 50 nm. (b-d) Color coordinates in $L^*a^*b^*$ space of Mg thin films with thickness (b) $h = 5$ nm, (c) and $h = 10$ nm and (d) $h = 20$ nm covered by MgO layer converted progressively into MgF₂ and MgSO₄. The color of each dot corresponds to the color of the film. (e,f) Color difference ΔE between the 100% MgO layer and the progressive conversion into (e) MgSO₄ and (f) MgF₂.

with respect to the 100% MgO layer, we have calculated the value of ΔE between these two situations for different values of h as a function of the thickness of the MgSO₄/MgF₂ layer (see Fig. 9.7(e,f)). The color difference between two points in the $L^*a^*b^*$ space is defined as $\Delta E = \sqrt{(a_1^* - a_2^*)^2 + (b_1^* - b_2^*)^2 + (L_1^* - L_2^*)^2}$. In our case $L_1^*a_1^*b_1^*$ corresponds to the color coordinates of the system with 100% MgO layer and $L_2^*a_2^*b_2^*$ corresponds to the color coordinates of the system with different thicknesses of the MgSO₄/MgF₂ layers. The values of ΔE are higher for a growing MgF₂ layer than for the MgSO₄ one. Again, this difference is related with the contrast in the refractive index between the oxide and MgSO₄/MgF₂. In light of these results, the ΔE can be used to detect and monitor the uptake of S- and F-compounds in Mg/MgO NPs.

9.3 Conclusions

In this chapter, we have demonstrated tarnishing of Mg nanoparticles by the heterogeneous uptake of SO₂ and fluorine contamination in air at room temperature on MgO. The Raman, XPS and infrared data showed that sulfate and oxyfluoride compounds formed on the Mg surfaces at room temperature in addition to or subsequently to MgO. Therefore, the tarnishing of Mg has to be taken into account similarly to the tarnishing of Ag, for all application of Mg in hydrogen storage, corrosion of ultralight Mg-based alloys (e.g. MgAl) and plasmonics. Specifically, we have theoretically show how the localized surface plasmons resonances of oxidized Mg NPs are blue shifted by their tarnishing, and the change of color that these phenomena entail in the appearance of the sample. This theoretical study reveals the possibility of using these two magnitudes to monitor the S- and F-compounds uptake in Mg/MgO samples. Indeed, on the positive side Mg/MgO nanostructured samples have a huge potential in environmental remediation, since they can be useful for purification of air and water, being Mg and MgO non-toxic. Furthermore, those purifying elements can be regenerated and reused by reducing the contaminated samples again to Mg by 100°C hydrogen plasma treatments.

Chapter 10

Optical Monitoring the Interacion of H with Mg/MgO Films and Nanoparticles

The interaction of magnesium, Mg, and its oxide, MgO, with hydrogen is of paramount importance for an hydrogen based economy due to magnesium hydride, MgH₂, which has high gravimetric and volumetric hydrogen densities of $\rho_m = 7.6$ wt % H and $\rho_V = 110$ kg H/m³. Therefore, Mg has been the subject of intensive studies in order to assess its potential as a hydrogen storage system alone, doped, in alloys [213], and as nanostructures [214, 41, 39]. Nevertheless, critical issues related to hydrogen desorption temperature, higher than 300°C, sluggish kinetics of the hydrogen adsorption/desorption processes (as an example de-hydrogenation from a 30 nm Mg layer in 19 h has been reported) [164] and fast Mg oxidation/tarnishing/corrosion by air exposure limit its hydrogen technology uptake. Thus, Mg is currently being studied so we can understand and overcome these drawbacks.

Very recently, the plasmonic properties of Mg nanodisks [160] have been exploited to investigate their hydrogenation/de-hydrogenation processes, the so called “hydrogenography”, based on the different dielectric function of metallic Mg and dielectric MgH₂ [215]. Indeed, most of those previous studies have reported the low activity of Mg in dissociating H₂. Consequently, Mg was covered or alloyed with Ti and Pd that were the catalytic metals inducing the dissociation of H₂. Nevertheless, Mg-Pd-Ti alloying at interfaces, Pd and Ti themselves, and TiH₂ [214] can affect the diffusion of hydrogen as well as the Mg hydrogenation kinetics and the optical response of the overall system. Furthermore, Mg films and Mg nanoparticles samples are extremely reactive when they are exposed to air, water, and oxygen, and usually covered with a stable oxide

MgO/Mg(OH)₂ nanometric layer [214] that, as seen in the previous chapter, can trigger a further tarnishing process. Therefore, the first step of the interaction with hydrogen would involve the reduction of the MgO/Mg(OH)₂ layer. This interaction is also important considering that the hydrogen production by hydrolysis of Mg also produces MgO/Mg(OH)₂ (i.e. $\text{Mg} + \text{H}_2\text{O} \rightarrow \text{MgO} + \text{H}_2$). Therefore, any eco-friendly and practical hydrogen production system should consider recycling/reusing MgO/Mg(OH)₂ to regenerate Mg/MgH₂, e.g., by cascading re-use or regeneration by H₂ plasma processes. Furthermore, another challenge is related to the air stability of the MgH₂ phase and the effect of this instability on the MgH₂ thermal decomposition, which has not been thoroughly defined [216].

In this chapter the hydrogenation/de-hydrogenation processes of a Mg/MgO film and plasmonic nanoparticles (NPs) are investigated via optical measurements by real time spectroscopic ellipsometry in the broad spectral range of 0.75 – 6.5 eV. Section 10.1 presents the experimental set-up used during the hydrogenation/de-hydrogenation process. In this study, we have used atomic hydrogen produced by a remote H₂ plasma source to investigate the direct interaction of clean Mg with hydrogen to avoid any interference from primer Ti and capping Pd layers (energy barriers for H₂ dissociation on pure Mg and MgO surfaces have been reported to be 1.05 and 1.33 eV vs 0.39 eV for dissociation on catalyzed Pt/Pd-doped Mg [217]). Another benefit of the H₂ plasma approach is the reduction of MgO surface layer and penetration of energetic hydrogen into the subsurface region increasing the hydrogenation yield and thickness even for Mg thick films that have been in contact to air. This can add more flexibility to the implementation of Mg-hydrides formation routine operating a “plasma hydrogenation activation”. Additionally, this section contains the details about how the samples were prepared, how they have been optically, structurally and chemically characterized, and the electromagnetic simulations performed to rationalize the experimental data. In Section 10.2 are presented the main results of this research. We have evaluated the conversion of a Mg/MgO film and plasmonic NPs into Mg/MgH₂ and the air stability of MgH₂. Specifically, the real time ellipsometric data obtained during the hydrogenation process is explained and modeled by electromagnetic simulations, whereas the chemical description of the Mg/MgO/H₂ interaction has been supported by Raman spectroscopy and X-ray photoelectron spectroscopy. Further relevance of this optical study can also be gained considering that it allows monitoring any variation of Mg NPs localized surface plasmon resonance (LSPR) whose importance pops out from latest studies proposing Mg/MgH₂ nanostructures hydrogenation/de-hydrogenation for plasmonic

color displays [163, 164]. Finally, in Section 10.3 are summarized the main conclusions of this work.

10.1 Methods

10.1.1 Sample Fabrication

Mg thick films (> 50 nm) were prepared by ion milling. Mg self-assembled nanoparticle samples were prepared by evaporating Mg on an Al_2O_3 substrate at room temperature under ultra-high-vacuum (UHV) 10^{-10} Torr conditions in a VEECO GENII molecular beam epitaxy system (MBE) to make sure that the as prepared samples were not contaminated.

10.1.2 Hydrogenation and Sample Characterization

The direct interaction with hydrogen was investigated in a reactor that combines a remote hydrogen plasma source with an *in-situ* spectroscopic ellipsometer (UVISEL Horiba), allowing us to optical monitoring the hydrogen interaction and resulting modification of optical properties. Hydrogen exposure occurred at 1 Torr with a H_2 flow rate of 200 sccm, whereas atomic hydrogen was produced by a radiofrequency (r.f.) 13.56 MHz plasma at the low power of 50 W to study the direct interaction with H-atoms (since we are not using any Pd capping of Mg for the catalytic dissociation of H_2). The temperature during the hydrogenation/de-hydrogenation was investigated in the range room 25-300°C, the latter being the MgH_2 de-hydrogenation temperature [30]. Each sample was measured (*i*) soon after the preparation, (*ii*) after their exposure to air, (*iii*) after the hydrogenation step *in-situ* and (*iv*) finally, again after exposure to air. The experimental ellipsometric spectra of the complex pseudodielectric function, $\langle\epsilon\rangle = \langle\epsilon_r\rangle + i\langle\epsilon_i\rangle$, were acquired in the range 1.5 – 6.5 eV with an energy resolution of 0.1 eV, and the kinetic data were acquired with a time resolution of 1 sec. The optical data were corroborated by chemical characterizations of Raman spectroscopy (LabRam Horiba) excited by a 532 nm laser, X-ray photoelectron spectroscopy (XPS) using a monochromatic Al $K\alpha$ source (PHI 5400 VERSAPROBE) at a take-off angle of 45°, and atomic-force-microscopy (AFM) (AutoProbe CP, ThermoMicroscope).

10.1.3 Electromagnetic Simulations

In order to model the experimental results measured by ellipsometry in both thin films and nanoparticles, we have performed electromagnetic simulations in equivalent systems. In the case of the Mg thin films, spectral reflectance calculations in multilayer systems were calculated using the Transfer Matrix Method (TMM) [103].

The formation of MgO and MgH₂ on Mg nanoparticles was modeled as multilayered spheres. The absorption efficiency of this type of nanoparticles were modeled using Mie theory [2]. The complex dielectric function, $\langle\epsilon\rangle = \langle\epsilon_r\rangle + i\langle\epsilon_i\rangle$, of Mg, MgO and MgH₂ used in the simulations were taken from different sources in the literature [13, 17]. For the knowledge of the reader, the optical properties about the mentioned materials are shown in Figs. 10.1(a,b). These dielectric function spectra are used for comparison with experimental pseudodielectric function to understand qualitatively the findings.

10.2 Results

10.2.1 Mg Films

Figures 10.1(a,b) shows a huge contrast in the dielectric function of the metallic Mg and dielectric MgO, as well as between Mg and the dielectric MgH₂. The layers of Mg after preparation and exposure to air for *ex-situ* measurements showed an oxide overlayer of approximately 25 nm; this can be read in Fig. 10.1(c) when comparing the dielectric function of pure Mg (red curves) with that of the air exposed film (blue curve): the oxide dielectric overlayer decreases $\langle\epsilon_i\rangle$ and increases $\langle\epsilon_r\rangle$ (less negative) reducing the metallic behavior. The oxide overlayer has been quantitatively estimated (25 nm) by analyzing the experimental pseudodielectric function spectra (blue curve) using the one-layer model sketched at the bottom of Fig. 10.1(e). Figure 10.1(b) shows that MgO and MgH₂ are both dielectric and differ mainly in the UV region above 5 eV. Reported bandgap for MgO and MgH₂ are 7.8 and 5.6 eV [13, 17]. The refractive index of MgH₂ is slightly higher than MgO, e.g. 1.7 for MgO and 1.9 for MgH₂ at 2 eV. The consequence of this, as shown by both kinetic ellipsometric data in Figs. 10.1(c,d) and the transfer matrix method reflectance calculations in Figs. 10.1(e,g), is that when realistic Mg layers with the thin overlayer of MgO are exposed to atomic hydrogen, the reduction of MgO and the conversion of the outmost layer to MgH₂ results in small changes of the dielectric function in the visible range.

Specifically, Fig. 10.1(c) shows the pseudodielectric function $\langle\epsilon\rangle = \langle\epsilon_r\rangle + i\langle\epsilon_i\rangle$ of the Mg layer before and after its exposure to a H₂ plasma. As reference the dielectric

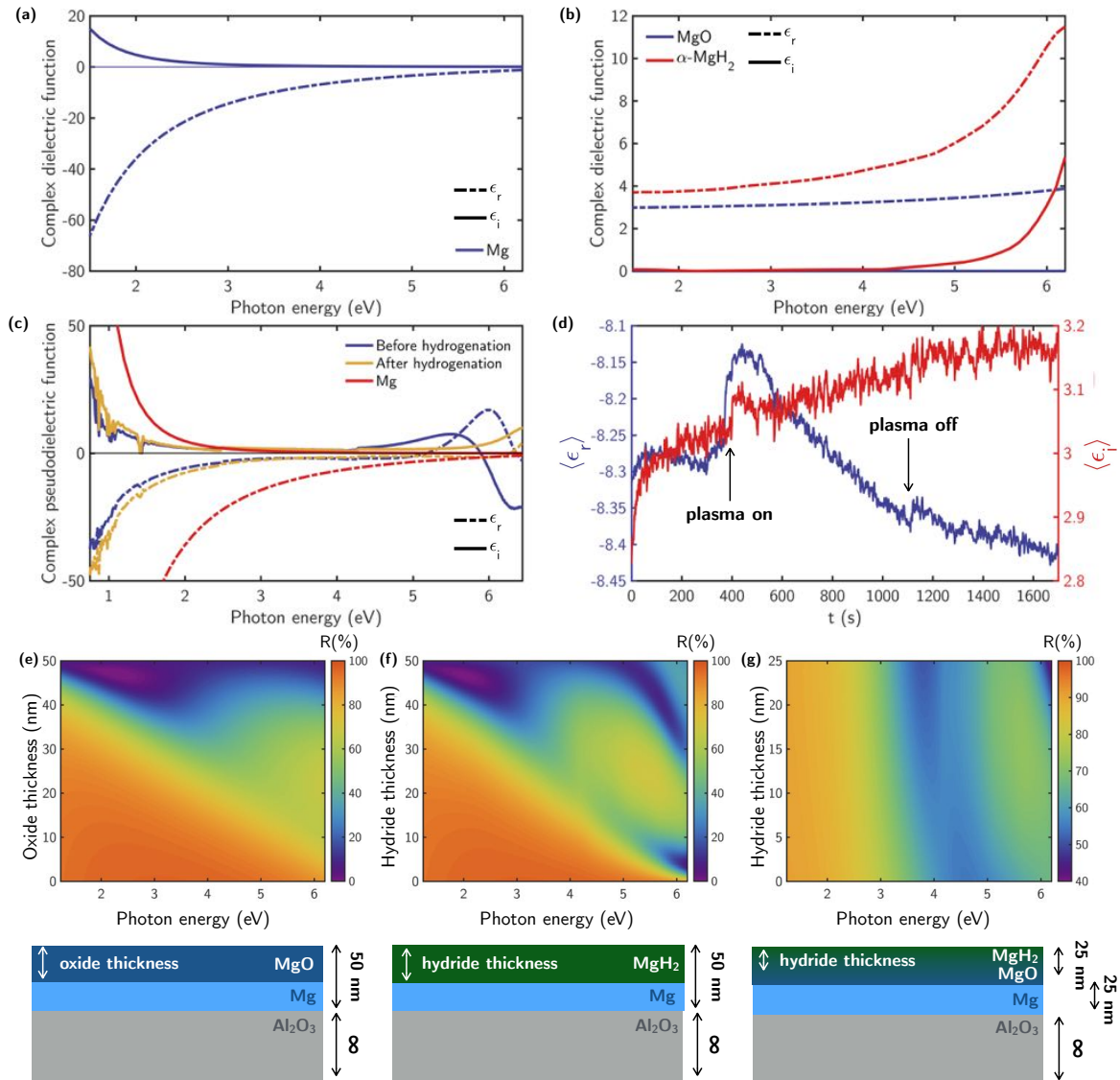


Figure. 10.1 Complex dielectric function ($\epsilon = \epsilon_r + i\epsilon_i$) of (a) Mg [13] and (b) MgO [13] and α -MgH₂ [17]. (c) Experimental complex pseudodielectric function ($\langle \epsilon \rangle = \langle \epsilon_r \rangle + i\langle \epsilon_i \rangle$) of a layer of Mg before (blue line) and after exposure (yellow line) to a H₂ plasma. As a reference, the dielectric function of Mg (red line) from Ref. [13] is also plotted (d) *In-situ* ellipsometry monitoring at 2 eV of the real (blue line) and imaginary part (red line) of the pseudodielectric function during the H₂ plasma exposure. Reflectance color map as a function of the photon energy and the (e) Mg and (f,g) MgH₂ layer thickness under normal incidence. The multilayer configuration in each case is presented underneath.

function of Mg from literature [13] is also plotted. By comparing the pseudodielectric function of the initial state of the layer sample with that of reference Mg, it can be inferred that the layer already has a ≈ 25 nm oxide layer as indicated by the less negative real part of the dielectric function, $\langle \epsilon_r \rangle$ and by the decreased losses in the imaginary part, $\langle \epsilon_i \rangle$. When exposed to the hydrogen plasma, the *in-situ* ellipsometry monitoring shown in Fig. 10.1(d) indicates a decrease of $\langle \epsilon_r \rangle$, which would be consistent with the reduction of MgO, and an increase of $\langle \epsilon_i \rangle$, consistent with its transformation to MgH₂.

Furthermore, the hydrogenation kinetics is saturating because it is limited by the slow diffusion of H-atoms into the already-grown “blocking” MgH₂ layer since the diffusion coefficient of hydrogen in MgH₂ is lower (eighth to ten order of magnitude lower) than in Mg. Specifically, the diffusion coefficient of H-atoms through forming MgH₂ layer is $D = 2.24 \cdot 10^{-21}$ m²/s [218] which is orders of magnitude lower than H-atoms diffusion into Mg, ($D = 4.1 \cdot 10^{-13}$ m²/sec) [219]. Therefore, most of Mg in the thick layers stays metallic and only the outmost layers (including the reduction of MgO) can be converted into MgH₂. This two-layer structure of the sample (as schematized at the bottom of Fig. 10.1(f)) -inner Mg-metal layer covered by the thin MgH₂ dielectric overlayer- explains also the still Drude behavior observed in Fig. 10.1(c), since the penetration depth of light is still probing both layers. By fitting the hydrogenated sample (orange spectrum in Fig. 10.1(c)) the two-layer model Al₂O₃-substrate/Mg/MgH₂ sketched at the bottom of Fig. 10.1(f), a thickness of 24 ± 1 nm has been estimated for the MgH₂ overlayer. Reflectance calculations under normal incidence of multilayer systems have been performed in order to evaluate the sensitivity of the optical response of a Mg layer grown on an Al₂O₃ substrate when MgO or MgH₂ layers are formed. We have modeled this situation by considering a Mg layer 50 nm thick on an Al₂O₃ substrate of infinite thickness. The formation of the MgO and MgH₂ has been taken into account by reducing the thickness of the Mg thin film and by adding a layer of MgO or MgH₂ on top in order to keep the 50 nm thick of the system. Figures 10.1(e)-(f) shows the reflectance color maps as function of the photon energy and the MgO/MgH₂ layer thickness. The most significant differences can be spotted in the high energy range, where MgH₂ presents absorption and MgO has a loss less behavior. However, at lower energies both reflectance spectra are very similar no matter the thickness of the layer. The real experimental situation is modeled in Fig. 10.1(g) where a 25 nm Mg layer on top of an Al₂O₃ substrate of infinite thickness is covered by a 25 nm MgO oxide which is converted progressively in MgH₂. The reflectance color map as a function of the photon energy and the thickness of the MgH₂

layer shows almost no difference as we go from MgO to a MgH₂ overlayer. The higher differences are found at the high energy regime, where the contrast in the optical constants between the oxide and the hydride is bigger. This is consistent with the experimental values of the pseudodielectric constant before and after plasma exposure (see Fig. 10.1(c)).

10.2.2 Mg Nanoparticles

In order to check if the self-limiting hydrogenation kinetics also applies to nanostructures, Mg nanoparticles (NPs) samples have been prepared. Figure 10.2(a) shows the real time evolution of the imaginary part of the pseudodielectric function for a sample constituted of closely packed Mg NPs grown on Al₂O₃. The spectra evolution clearly shows the appearance of localized surface plasmon resonances (LSPR) peaks (see arrows in Fig. 10.2(a)). Specifically, initially a LSPR peaked at 4.8 eV appears that stays constant in position and increases in amplitude with the increase of density of NPs whose diameter has been estimated by AFM to be 70 nm (see inset AFM Fig. 10.2(a)). With further deposition of Mg, an additional LSPR peak at lower energy appears, which red-shifts with increasing Mg deposition. It has been reported [160] that the Mg plasmon resonance can be tuned from the ultraviolet to the infrared. In our case, the red-shifting LSPR is due to the increasing size of agglomerates of the 70 nm nanoparticles as detailed by the AFM in inset in Fig. 10.2(a). Despite the presence of those plasmon resonances, no plasmon catalytic effect of the Mg LSPR has been observed on the H₂ dissociation when those NPs have been exposed to H₂. Fig. 10.2(b) shows the complete damping of the Mg NPs LSPR by air exposure and consequent oxidation of the Mg NPs, demonstrating one of the limits of the Mg NPs in plasmonics, which is the full oxidation of the Mg NPs with time. Indeed, when the lower $\langle\epsilon_i\rangle$ (full oxidation) spectrum in Fig. 10.2(b) was recorded, XPS showed mainly the MgO component in the Mg2p photoelectron core level (see Fig. 10.3(a)), indicating that most of the NPs were oxidized. This is consistent with the electromagnetic modeling and absorption efficiency, Q_{abs} , of a multilayer Mg-core/MgO-shell sphere, with the thickness of the shell increases consuming all the metal content in the NP, shown in Fig. 10.2(e). For the Mg-core the Mg dielectric function from Ref. [13] has been used, while for the MgO-shell or the outer MgH₂-shell the MgO and MgH₂ respective dielectric functions from Ref. [13, 17] have been used. Since the surrounding media of our particles are the air and the substrate Al₂O₃, the spheres have been placed in an effective surrounding medium of refractive index $n_{med} = 1.5$ to consider the effect of the substrate, the air and the rest of the aggregates (see AFM images in Fig. 10.2(a)).

The refractive index of the effective medium is defined as $n_{med} = (1 - \gamma) \cdot n_{air} + \gamma \cdot n_{subs}$ [220], where the substrate refractive index and that of the rest of particles has been considered in n_{subs} with a value of 1.7, and the weight $\gamma = 0.7$. The parameter γ can be interpreted as the fraction of the volume surrounding the particle with refractive index 1.7.

Figure 10.2(e) shows the absorption efficiency, Q_{abs} , color map of Mg-MgO core-shell as function of the photon energy and of the MgO shell thickness. It can be seen how the localized plasmon peaks visible in Q_{abs} due to the Mg core are completely quenched when the NP is fully MgO. This is expected since the imaginary part of its dielectric constant is zero in all the analyzed spectral range. Figure 2(f) shows the case of a growing MgH₂ shell on a Mg nanoparticle. In this case, below ≈ 5 eV ($\epsilon_i(\text{MgH}_2) = 0$), the Q_{abs} color map shows the same behavior as in the case of the MgO shell: the localized plasmon peaks are quenched as the shell of the hydride increases. However, above 5 eV, an absorption band appear due to the losses introduced by the MgH₂ shell. Thus, the growing of either a MgO or a MgH₂ shell can be clearly distinguished in the high energy range. When mimicking the real situation, the conversion of the MgO shell into a MgH₂ upon H₂ plasma exposure (see Fig. 10.2(g)), the main differences in the Q_{abs} color map as function of the photon energy and the hydride layer thickness can be seen again at energies above 5 eV. When metallic core is covered by the pure oxide shell, the absorption at high energies is zero. However, as the outer layers of oxide become to be replaced by the hydride, the values of Q_{abs} start to increase reaching a maximum when the oxide is completely converted in the hydride.

Therefore, even the hydrogenation of the Mg NPs without any capping has to consider as first step the reduction of the native oxide overlayer. Figure 10.2(c) shows the real time kinetics for the variation of both the real, $\langle \epsilon_r \rangle$, and imaginary part, $\langle \epsilon_i \rangle$, at 3 eV of the pseudodielectric function, during exposure to H-atoms. An increase in $\langle \epsilon_r \rangle$ and decrease in $\langle \epsilon_i \rangle$ are observed, which are consistent with MgH₂ formation, until a saturation value is reached, which corresponds to the maximum uptake of hydrogen from the Mg NPs. This saturation level does not change even increasing further the temperature or H₂ pressure during the hydrogenation.

Interestingly, no variation is observed when the H₂ is stopped, indicating that the hydrogenated state of the particles remains fixed when in N₂, Ar or UHV, i.e., no hydrogen desorption occurs at $T < 300$ °C, when H₂ is dropped off the surrounding atmosphere. Contrarily, as soon as the hydrogenated NPs are exposed to air, in a few hours, the $\langle \epsilon_i \rangle$ spectrum increases again (see Fig. 10.2(d)). Those modifications of the optical spectra can be rationalized on the basis of the XPS results in Fig. 10.3.

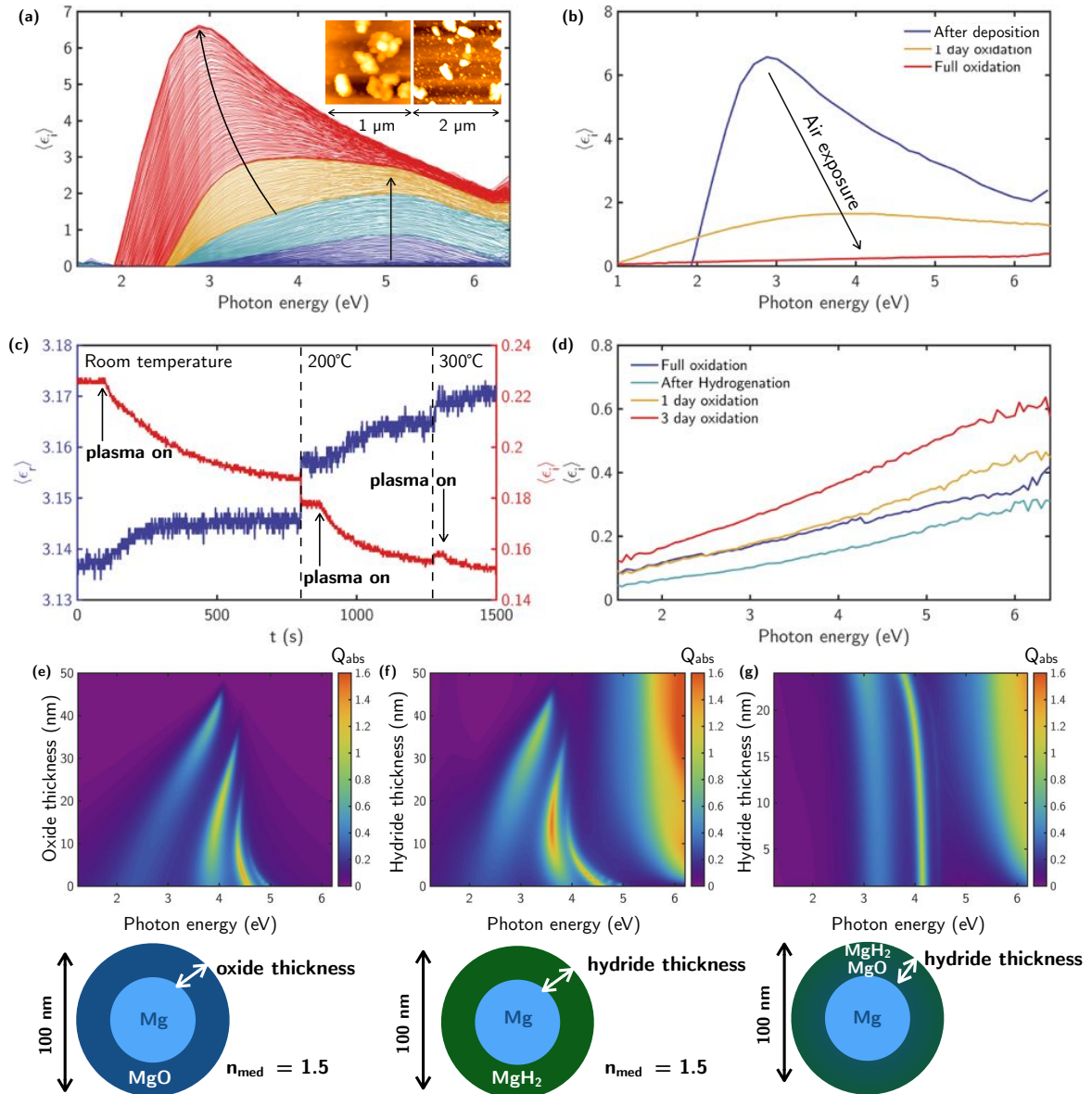


Figure. 10.2 (a) Real time evolution of the imaginary part of the pseudodielectric function ($\langle \epsilon \rangle = \langle \epsilon_r \rangle + i\langle \epsilon_i \rangle$) for Mg NPs grown on Al_2O_3 . With arrows are indicated the evolution in time of the two LSPRs. As inset are shown AFM images of the samples under study. (b) Mg LSPR damping by air exposure and oxidation. (c) *In-situ* ellipsometry monitoring at 3 eV of the real (blue line) and imaginary part (red line) during the H_2 plasma exposure at different temperatures. (d) Experimental pseudodielectric function of a sample of oxidized Mg NPs before and after hydrogenation, and its evolution after air exposure. Absorption efficiency color map as a function of the photon energy and the (e) Mg and (f,g) MgH_2 shell thickness. The core-shell configuration in each case is presented underneath. The NPs are placed in a medium with refractive index $n_{\text{med}} = 1.5$ to take into account the effect of the substrate and the rest of the NPs in the sample.

Specifically, the increase of $\langle \epsilon_i \rangle$ of the air exposed MgH_2 can be ascribed to $\text{Mg}(\text{OH})_2$ that forms rapidly on the MgH_2 surface when contacting with air humidity [216]. The XPS O1s spectra shows mainly the MgO (including Al_2O_3 from the substrate) component before hydrogenation while for the hydrogenated sample in addition to the Al_2O_3 , a $\text{Mg}(\text{OH})_2$ component can be also resolved.

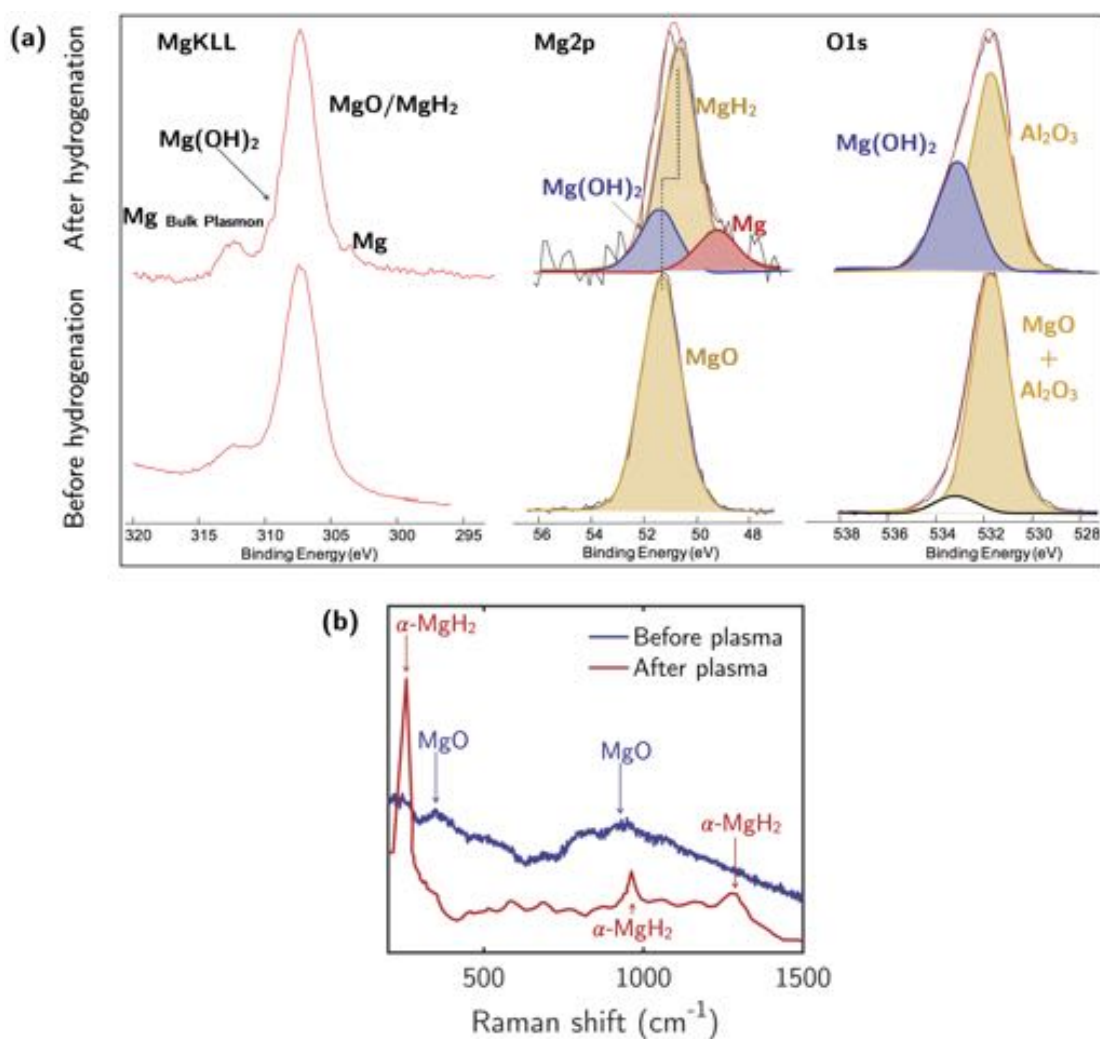


Figure. 10.3 (a) XPS spectra of the MgKLL Auger line, and of the Mg2s and O1s photoelectron core level of the Mg NPs sample before and after hydrogenation, both after air exposure for 5h. (b) Raman spectra of Mg nanoparticles before and after H₂ plasma exposure.

XPS spectra of the Mg photoelectron core level and of the MgKLL Auger line are also reported in Fig. 10.3(a). Here, although the MgO and MgH₂ components cannot be separated in the Mg2p photoelectron core level, before hydrogenation only one symmetric component at 51.4 eV is observed ascribed to MgO. However, upon

hydrogenation, apart from a shift of the peak to 50.8 eV consistent with MgH_2 , a lower binding energy component at 49.3 eV appears due to metallic Mg, indicating that the MgO was reduced and the hydrogenation did not completely hydrogenated all sample, probably because of the barrier effect of the already formed MgH_2 layer. Furthermore, the appearance of the tail peak in Mg2p due to $\text{Mg}(\text{OH})_2$ also indicates that the air exposed MgH_2 is not stable and forms hydroxide. This is also supported by the O1s photoelectron core level that also shows a main component at 531.4 eV due to MgO and the substrate before hydrogenation, and an extra component at 533.2 eV due to the hydroxide $\text{Mg}(\text{OH})_2$ after hydrogenation. Also, the high resolution MgKLL Auger peak of Mg before and after hydrogenation indicates the presence of metallic Mg, a more prominent Mg bulk plasmon peak, and the formation of hydroxide $\text{Mg}(\text{OH})_2$ after hydrogen exposure.

The newly formed phase of MgH_2 upon hydrogenation has been confirmed by the Raman analysis (Fig. 10.3(b)), showing after hydrogenation peaks of the B_{1g} , E_g and A_{1g} phonon modes characteristics of α - MgH_2 , whereas before hydrogenation only a very broad peak of nanocrystalline/amorphous MgO was observed.

The present optical and chemical results are consistent with the heterolytic $-\text{Mg}(\text{H})-\text{O}(\text{H})-$ chemisorption of hydrogen on MgO [221, 222], as schematized in Fig. 10.4. This process produces hydride and hydroxy groups which are partially reversible upon evacuation and desorption of H_2O leaving some Mg sites that can be further hydrogenated or remain as unsaturated Mg, as also evidenced by the XPS.



Figure. 10.4 Scheme of the heterolytic $-\text{Mg}(\text{H})-\text{O}(\text{H})-$ chemisorption of hydrogen on MgO surfaces.

10.3 Conclusions

In summary, the *in-situ* real time ellipsometry study of the interaction of hydrogen with Mg surfaces and Mg plasmonic nanoparticles realistically covered by a thin overlayer

of MgO has revealed the self-limiting character of the Mg hydrogenation kinetics. This effect is due to the reduction of the oxide layer and to the subsequent conversion of the outmost layer into MgH₂, indicating that the MgO layer is converted into MgH₂. Further Mg hydrogenation is limited by the slow diffusion of the hydrogen atoms in the growing “blocking” MgH₂ layer. The MgH₂ also oxidizes to some extent by air exposure forming the hydroxide Mg(OH)₂. Furthermore, we have demonstrated that Mg NPs, although they present a tunable plasmonic response in a wide spectral, their use is limited by the complete quenching of the LSPRs when exposed to air due to the complete oxidation of the nanoparticle if a capping layer is not used.

Chapter 11

Rh Nanocubes in Photocatalysis Applications

As presented in Chapter 7, a particularly intriguing metal whose UV plasmonic behavior has only recently been discovered is rhodium, already well known for its catalytic activity produced by a partially filled *d*-shell and its commensurately low tendency to oxidize [12, 117, 174, 118, 27, 223]. Rh nanoparticles (NPs) may be synthesized into a variety of shapes through chemical methods with nanometer size control [117, 118, 27]. Already, size-controlled Rh tripod stars and nanocubes (NCs) have been grown, a systematic numerical study has been performed for the tripod stars, and activity for UV SERS, surface enhanced fluorescence, and photoinduced degradation of *p*-aminothiophenol has been demonstrated [174, 117, 118]. However, its most exciting potential may lie with the possibility of enhancing rhodium's already favorable catalytic activity by UV illumination near its plasmonic resonance. Very recently Zhang et al. [27] discovered that Rh NCs on Al₂O₃ supports exhibit plasmonic photocatalytic activity in the carbon dioxide methanation reaction by simultaneously lowering the activation energy of the rate determining step and strongly selecting the desired product CH₄ over the undesired product CO.

In plasmonic photocatalysis, chemical reactions are driven on the surface of illuminated metallic NPs [224, 132]. The most commonly accepted mechanism for this is the so called direct transfer mechanism, by which excitation of the LSPR generates hot carriers that migrate to the surface and enter anti-bonding orbitals of adsorbed molecules, thereby weakening a critical bond and accelerating the reaction. Since the LSPR of the NP drives this mechanism, mapping the location of the surface electromagnetic and carrier hot-spots will indicate regions in which the photochemical processes are enhanced. For thermal catalysis it is well-known that the most active

sites on metal NPs are corners and edges because adsorbed chemical intermediates may have higher coordination with surface atoms there [223, 225]. Therefore, for plasmonic photocatalysis to be effective, the photogenerated hot carriers from LSPR decay must also reach these most active sites.

In this chapter we report a detailed numerical analysis of the UV plasmonic behavior and charge distribution of Rh NCs, a geometry easily fabricated with precise size control [118]. In Section 11.1 is presented the system under study along with the numerical methods employed during this work. In Section 11.2 are shown the main results of this research. It will be shown that the strongest plasmonic hot-spots are located at the corners and edges of the NCs, exactly where they are the most catalytically active, and that distortions of the cubical shape significantly affect their plasmonic and photocatalytic properties. The fact that the highest fields and highest carrier concentrations occur in the corners and edges of Rh NCs confirms their tremendous potential for plasmon-enhanced catalysis. Transmission electron microscopy of the largest Rh NCs indicated that the surfaces are not flat but slightly concave with even more pointed corners, so the effects of surface concavity will be explored to understand how the lightning rod effect concentrates field and carriers there. Because intense catalytic activity at corners and edges will reshape these regions, we also explore how the electromagnetic and charge distributions evolve as the shape evolves from concave cubical to convex cubical to spherical with corners and edges of increasing radii of curvature. By this, we can quantify how the photocatalytic activity of these nanostructures deteriorates, a critical concern for the practical application of any catalyst. Finally, we explore how the charge distribution is affected when these NCs are on a dielectric (Al_2O_3) support, where again it is fortuitously demonstrated that the most chemically active sites at the interface of the metal NC and the support are where the highest field and charge concentrations reside. Section 11.2 summarizes the main conclusions of this chapter.

11.1 System Geometry and Methods

The electromagnetic interaction between the Rh NCs and light has been modeled using finite element (FEM) simulations implemented using the commercial software COMSOL Multiphysics 5.2 [226].

The spectral dependence of three parameters has been studied: the absorption cross-section (C_{abs}), the local field enhancement of the electric field ($|\mathbf{E}|^2$), and the surface charge density (σ), all of which depend on the energy of the illuminating

electromagnetic field. For particles much smaller than the wavelength, C_{abs} can be associated with the far-field extinction efficiency and helps to describe the ellipsometric response of surfaces with metallic nanostructures, especially those related to the imaginary part of the measured pseudodielectric function [126]. $|\mathbf{E}|^2$ represents the local field enhancement. The areas with greatly enhanced field intensity, the so called hot-spots, are the regions where the hot-electron generation process takes place. The evaluation of $|\mathbf{E}|^2$ allows us to identify the regions over the NP surface where hot electrons are being generated [227], being this information useful for photocatalysis research [224]. A deeper analysis of this aspect is made through the evaluation of σ : the regions with highest charge concentrations are the most reactive with the highest probability of charge transfer.

We have performed finite element simulations on Rh nanostructures and have compared them with identical ones made of Ag. These NPs have been illuminated with a monochromatic linearly polarized plane wave within a spectral interval of interest: 2-8 eV. The illumination geometry (wave vectors and polarization) is properly described in Figure 11.1.

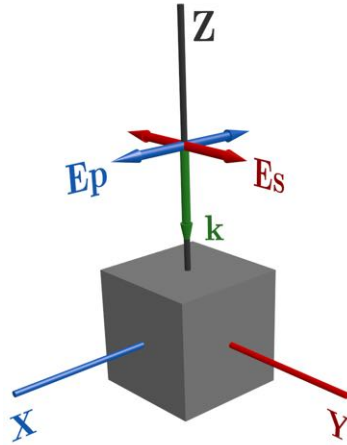


Figure. 11.1 Diagram of a nanocube. It is illuminated by a monochromatic plane wave propagating (\vec{k}) along the Z-axis with either P- or S-polarization.

In this work we use the complex dielectric functions of Rh and Ag shown in Fig. 12.1. The oxide Ag_2O that constitutes the Ag coating is also included. These values have been obtained from different sources in the literature [13, 228]. Figure 12.1 shows the complex dielectric permittivity of these materials. The Frölich frequency ($\epsilon_r = -2$) of Ag lies in the near UV, but Rh's is deep in the UV region. Furthermore, Ag presents interband transitions in the UV which inhibit plasmonic performance in this spectral range.

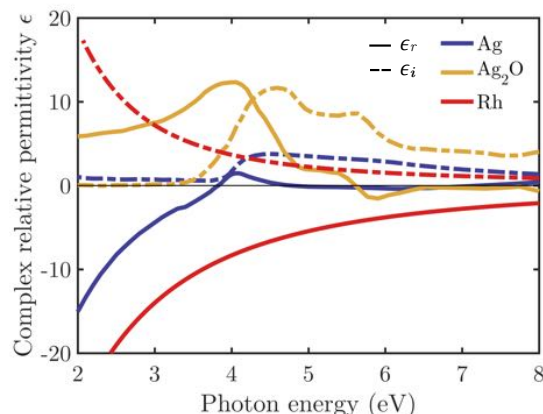


Figure. 11.2 Real (solid line) and imaginary (dashed line) parts of the complex relative permittivity (ϵ) of Ag (blue), Ag_2O (yellow) and Rh (red) as a function of the photon energy of the incident beam.

11.2 Results and Discussion

11.2.1 Comparison of Ag and Rh in Simple Geometries.

Silver, when synthesized in cubic NPs, has shown to present good plasmonic performance and has been used as a metallic photocatalytic enhancer below 3 eV [224]. Oxidation and strong interband transitions above 3 eV prevent its use for applications in the UV range, especially when size is below 10 nm, as preferred in photocatalysis. In this section, we present a direct comparison of cubical silver and rhodium NPs to show how the latter presents two clear advantages for UV applications: its lack of oxidation, especially important for NPs of very small sizes (less than 10 nm [117, 118]), and its lack of interband transitions above 3 eV.

As a first step, we consider cubic monomers of Rh and Ag with an edge length of 30 nm and rounded edges (curvature radius $R_c = 2$ nm). This size has been chosen because it allows a good comparison with silver when oxidation effects have no appreciable effect, and also because this size has been recently used in photocatalysis and SERS experiments with rhodium [27]. For smaller sizes [117, 118], silver becomes useless because oxidation destroys its plasmonic performance. The nanostructure is illuminated with a monochromatic plane wave under normal incidence and P-polarization (see Fig. 11.1). To explore the relative contributions of the dielectric function and the geometry, calculations for a sphere and a disk with equivalent volume are also presented. The radius of the equivalent sphere is $R = 18.6$ nm. The equivalent disk is considered to have the same radius R and height h ($R = h = 20.5$ nm).

Figure 11.3 plots the absorption cross-section C_{abs} (left column) and spectral electric field intensity averaged ($\langle |\mathbf{E}|^2 \rangle$) over the NP's closed surface (right column) for equivalent spheres, disks, and cubes made of Rh and Ag. As expected, the two metals have different behaviors: Ag presents LSPRs within the interval 3 - 4 eV whereas the Rh plasmonic response is located between 4 - 10 eV. This behavior is commensurate with their respective values of the Fröhlich energies E_{Fr} [12] ($E_{Fr}^{Ag} = 3.5$ eV and $E_{Fr}^{Rh} = 8.2$ eV). Also, it can be observed how the shape of NP has a strong influence on the LPSRs and their spectral position.

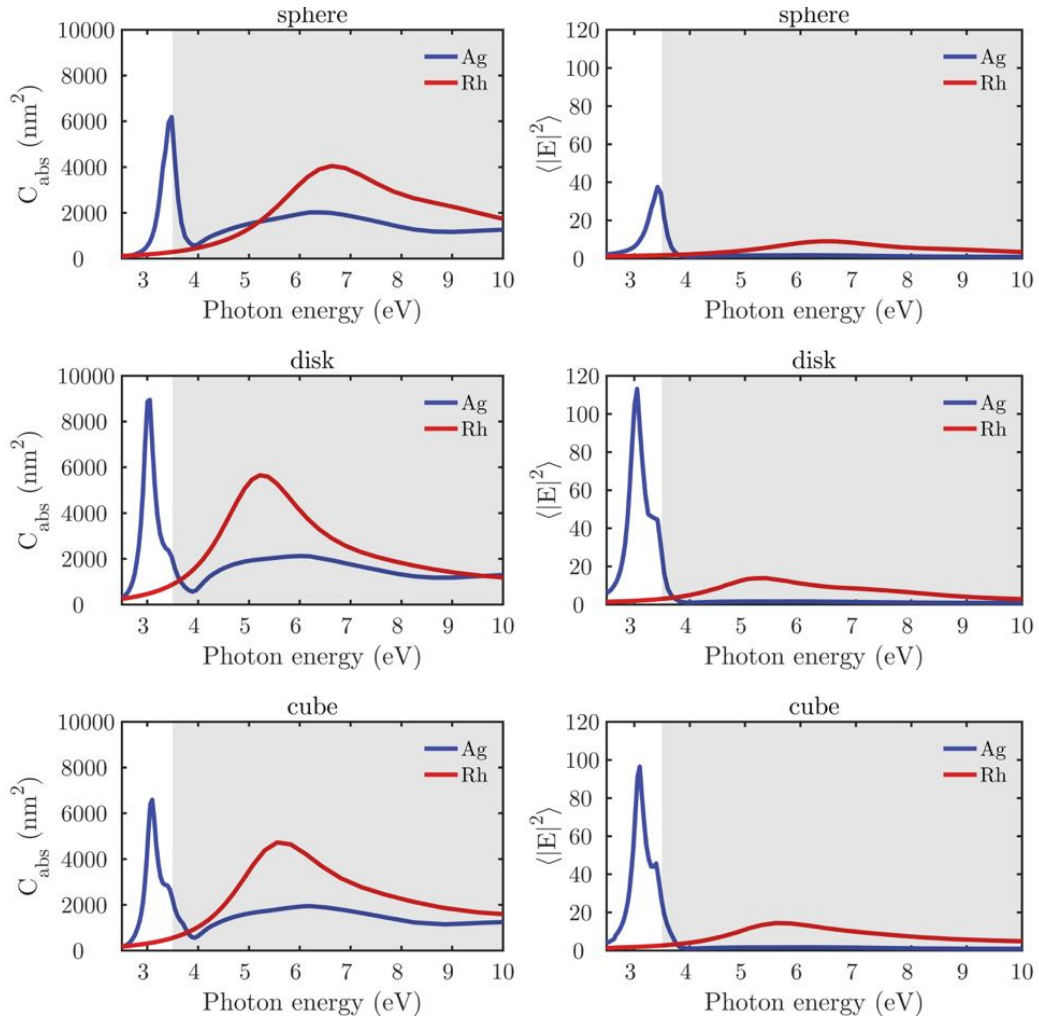


Figure. 11.3 Absorption cross-section (C_{abs}) (left column) and spectral electric field intensity ($\langle |\mathbf{E}|^2 \rangle$) averaged over the NP's closed surface (right column) for spheres ($R = 18.6$ nm), disks ($R = h = 20.5$ nm), and cubes ($L = 30$ nm) composed of Rh (red) or Ag (blue) illuminated under normal incidence, and embedded either in air.

11.2.2 Rh Nanocubes: Perfect Shape

As mentioned before, Rh NCs can be easily fabricated with precise size control [118]. Figure 11.4 shows the optical behavior and TEM images of Rh perfect cubes embedded in ethanol synthesized through seeded and unseeded slow-injection polyol methods. Their experimental UV-Vis normalized extinction spectra are compared with those obtained through FEM electromagnetic simulations. As seen in the TEM images, the Rh NCs before being repeatedly used as photocatalyst, present almost a perfect cubical shape. However, slight rounded corners and concave faces can be appreciated. These defects may be responsible for the deviation of the experimental LSPR energy with respect to the simulated one.

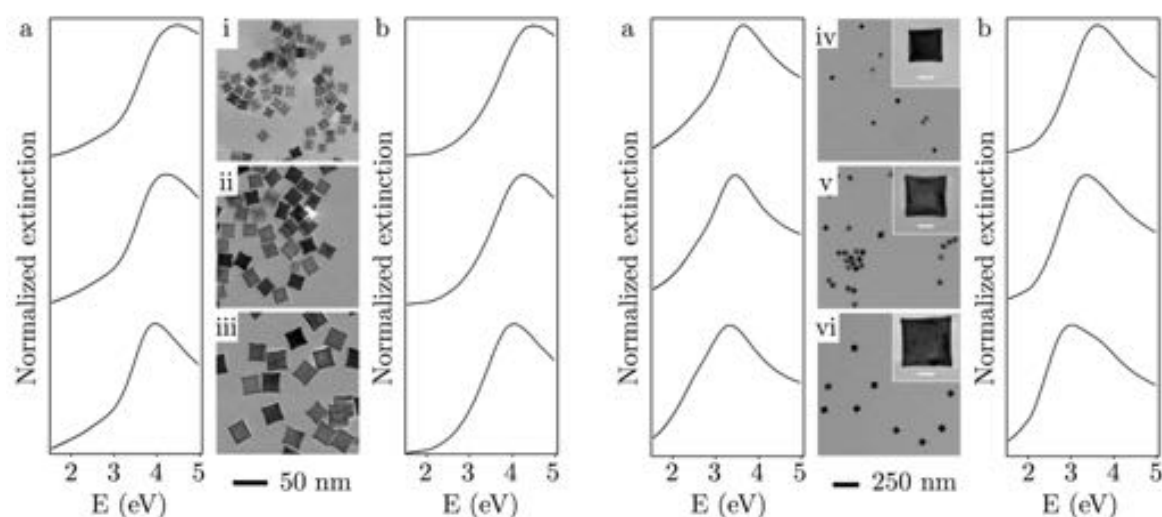


Figure 11.4 UV-Vis normalized extinction spectra (a) experimental and (b) theoretical of monodisperse Rh nanocubes embedded in ethanol with their corresponding TEM images. The average sizes are: (i) 15, (ii) 21, (iii) 27, (iv) 39, (v) 47 and (vi) 59 nm respectively. The scale bars of the inset images are 20 nm.

Figure 11.5 shows the relation between the size of the Rh NCs and the LSPR energies from the simulations and the experiment. The x-error bars of experimental data are the standard deviations of the edge lengths of Rh NCs measured by TEM in each sample. The y-error bars are the peak widths at which 99% of maximum intensity in extinction spectra occurs. It can be seen that the peak of extinction spectra is in the UV range (above 3 eV) for all the analyzed sizes. For the smallest cubes the peak is produced at ≈ 4.5 eV. The resonant energy is red-shifted as the side length is increased.

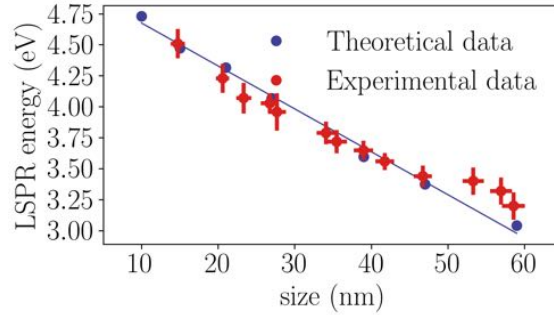


Figure. 11.5 Relationship of size and LSPR energies from experimental measurements (red circles) and numerical simulations (blue circles) of Rh NCs in ethanol. The blue line is a linear fitting of the simulated results.

11.2.3 Rh Nanocubes: Effect of a Deformation

Given this strong dependence of the optical response on the geometry of the NP [133], we now consider the dependence of the LSPR for an isolated NC with the deviations from the perfect cubical geometry that could appear during chemical synthesis or from the extended use of the NCs as catalysts. Specifically, we will study the effect of rounding the edges and corners of the NC with different radius of curvature (R_c) varying from 0 (perfect cube) to 15 nm (perfect sphere) while keeping the distance between flat opposite faces constant. The effect of introducing a concavity (decreasing volume) or convexity (increasing volume) from 0 (flat) to 4 nm (most depressed or extended) on the faces of the NC will be also analyzed. Both studies have been done starting from a perfect NC with side length $L = 30$ nm illuminated with a monochromatic plane wave under normal incidence and P-polarization.

Figure 11.6 shows the effect on the absorption cross-section C_{abs} and the local field enhancement of rounding the edges of a NC with $L = 30$ nm.

When increasing R_c two main effects can be seen in the absorption cross-section spectra: a blue-shift and a decrease of the resonance peak caused by competing effects. The first is associated with the volume reduction as NCs evolve from a perfect cube to a perfect sphere (27000 to 14137 nm³) while keeping constant the distance between the center of opposite faces. Also, the amplitude of charge oscillations is reduced because of less localized charges when the NC edges and corners are rounded. By looking at the near-field (NF) distribution over the particle surface (Figs. 11.6(b,c)), it can be seen how the hot-spots are less intense and charge density less localized as R_c increases. In these cases the depolarizing field, which appears as reaction to the applied field [229, 230] is weaker, leading to resonance peaks at higher energies. Also,

it is important to emphasize that the near-field resonance (Figs. 11.6(b)) is red-shifted in comparison to the far-field one (C_{abs}), as has been pointed out previously [122, 182]. For rhodium, this shift is small (≈ 0.1 eV for a plasmon resonance located on 6 eV), so far-field magnitudes like C_{abs} give accurate enough spectral information about what is happening close to the particle.

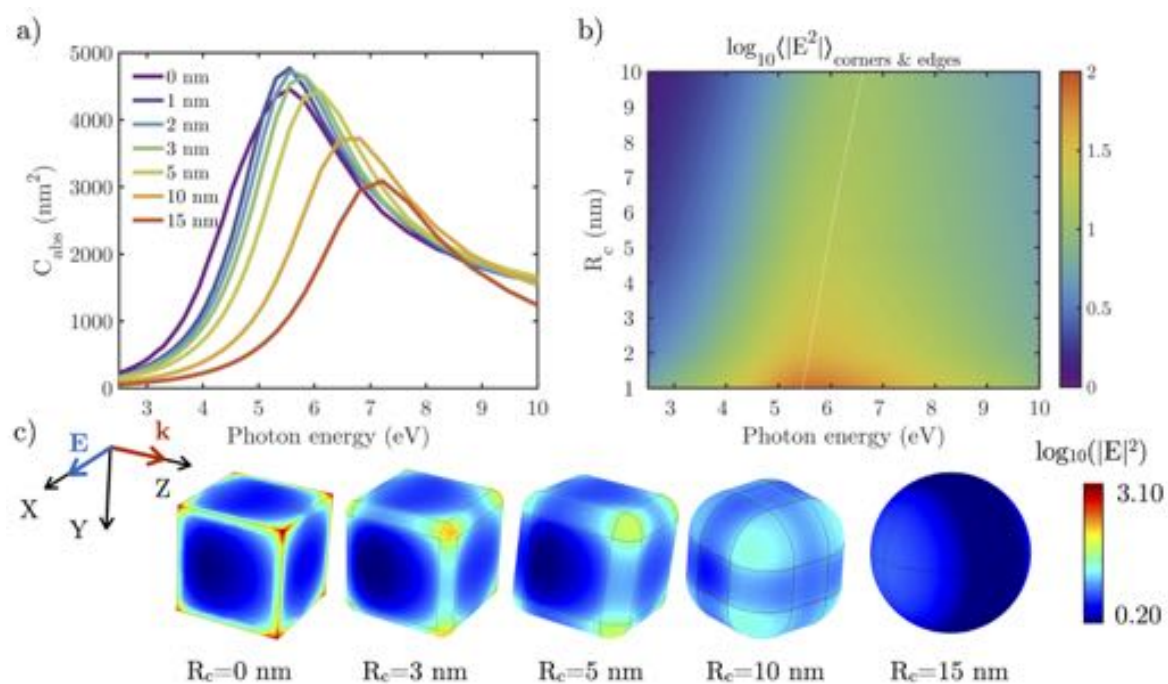


Figure. 11.6 (a) Absorption cross-sections (C_{abs}) of edge length $L = 30$ nm Rh NCs with rounded edges and corners with a curvature radii R_c varying from 0 (perfect cube) to 15 nm (perfect sphere). (b) Local field enhancement ($|E|^2$) averaged over the corners and edges (where charge is most concentrated) of the NC with different R_c . (c) Local field enhancement in logarithmic scale ($|E|^2$) over the surface of the different NCs when illuminated with the corresponding resonant wavelength.

In order to discriminate the contribution to C_{abs} of both aforementioned aspects separately we consider a reference NC with $L = 30$ nm and $R_c = 5$ nm. Fig. 11.7(a) shows the effect of varying the volume of the nanocube while keeping $R_c = 5$ nm constant and, Fig. 11.7(b) illustrates the effect of varying R_c while keeping the volume of the NP constant. The spectral blue-shift introduced by these effects are $\Delta E = 0.4$ eV and $\Delta E = 1.2$ eV, respectively caused by volume reduction and charge delocalization. This blue-shift is also manifested in Fig. 11.6(b), where the spectral values of averaged over the rounded edges and corners of the NCs decreases an order of magnitude as R_c is reduced from 1 to 10 nm.

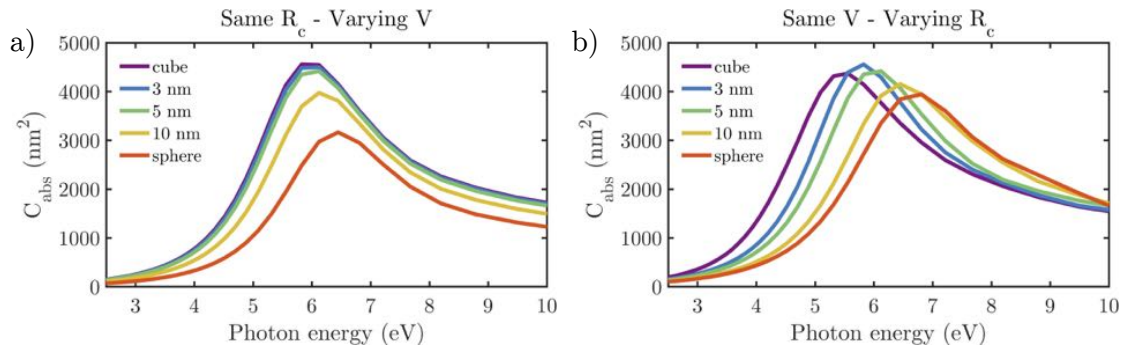


Figure. 11.7 Absorption cross-sections (C_{abs}) spectra of (a) cubes with $R_c = 5$ nm with the same volume as those with $L = 30$ nm and R_c indicated by the legend and (b) cubes with the same volume as a cube with $L = 30$ nm and $R_c = 5$ nm, but with a R_c given by the legend.

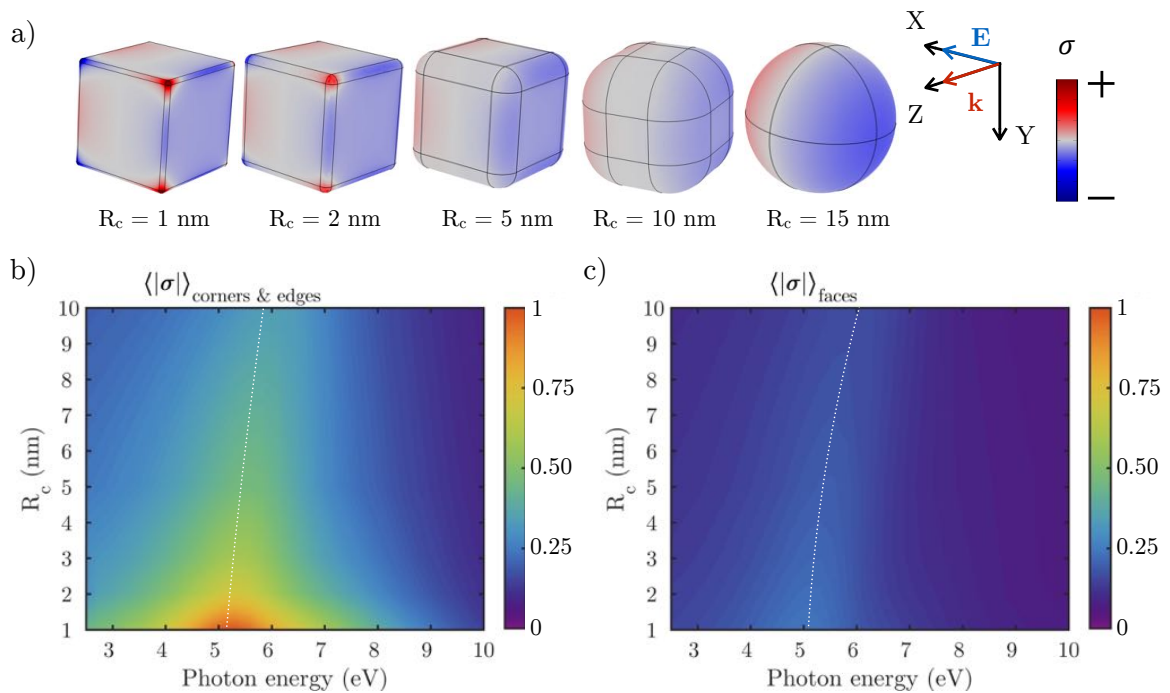


Figure. 11.8 (a) Surface charge distribution (σ) over Rh NCs with rounded edges and tips with a curvature radii R_c when illuminated at the resonant wavelength. The red/blue regions represent positive/negative charge densities. (b) Normalized values of σ averaged over the edges and corners, and (c) over the flat faces of the NCs.

To better illustrate the aforementioned delocalization of the charge distribution, Fig. 11.8(a) shows the surface charge density (σ) on the cube's faces as R_c increases. Large values of σ are associated with a high chemical reactivity [225, 223]. The red/blue regions represent positive/negative charge densities. Fig. 11.8(b) and (c) show the normalized absolute value of the averaged surface charge density $\langle|\sigma|\rangle$ on the corners and edges, and on the flat faces of the cube, respectively. It can be seen how the highest concentrations of surface charge density are produced at the corners and edges of NCs with smallest R_c . As we go from $R_c = 1$ to $R_c = 4$ nm, the value of $\langle|\sigma|\rangle$ goes down to 1/4 of its original value. However, the value $\langle|\sigma|\rangle$ on the faces remains almost constant no matter the value of R_c .

Experimentally it has been observed that as the cubes are re-used in photocatalytic processes they are reshaped. The longer the catalyst is used, the more spherical they become, leading to a loss of reactivity. This effect is related with the lowering of σ as R_c increases [223].

Figure 11.9 shows the effect on the absorption cross-section C_{abs} and the local field enhancement when a concavity/convexity is introduced in a NC with $L = 30$ nm and $R_c = 2$ nm. This deformation is parametrized by d , which indicates the maximum amount that the convex or concave surface is deformed above or below the flat surface of the original NC. Positive/negative values of d are associated with a convex/concave deformation.

As convexity and volume increases, a blue-shift of C_{abs} is produced, while C_{abs} red-shifts when a concavity increases and volume decreases. This seems to be in contradiction with previous observation that increasing/decreasing the volume of a NP produces a red/blue-shift of the resonance peak due to a increase/decrease of the depolarizing field inside the particle [229]. However, as in the previous case, it is necessary to consider how the charge is distributed in each case. The lightning rod effect [184] states that the charge density is higher in sharper tips. If we compare both concave and convex NCs, it can be seen how the concave NCs have sharper corners and edges, so the charge density is higher in these regions, leading to a more intense depolarizing field that causes the resonance peak to red-shift. The great sensitivity of plasmonic response to the degree of deformation agrees with experimental results obtained by Romo-Herrera et al. in gold NCs [231].

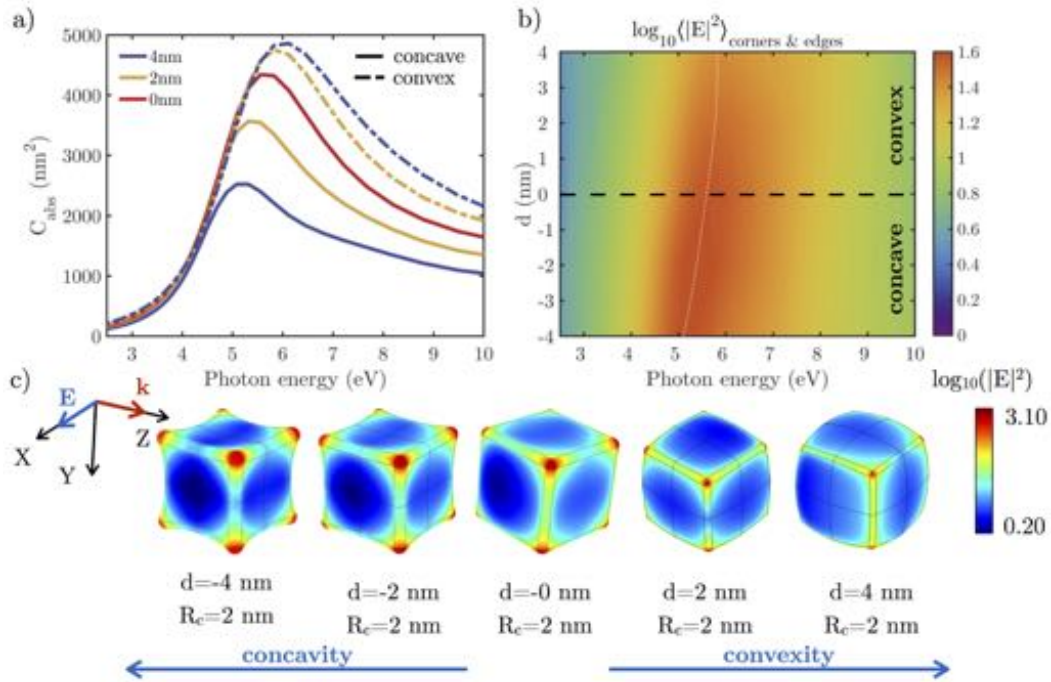


Figure. 11.9 (a) Absorption cross-sections (C_{abs}) of $L = 30$ nm and $R_c = 2$ nm Rh NCs as a function of concave/convex deformation parameter d indicated in the legend. (b) Local field enhancement ($|\mathbf{E}|^2$) averaged over the corners and edges of NC with different d . (c) Local field enhancement in logarithmic scale ($|\mathbf{E}|^2$) over the surface of the different NCs when illuminated at resonance.

Figure 11.9(b) shows the local field enhancement averaged over the corners and edges of the nanocubes. It can be seen that the maximum value also blue-shifts as NCs go from concave to convex. Also, the maximum value decreases as d is increased. The distribution of over the particle surface is shown in Fig.11.9(c). Not only do concave cubes present higher values of in the corners and edges, they represent a larger fraction of the surface. Concave cubes are therefore expected to be more reactive than convex ones.

Figure 11.10(a) shows the surface charge density σ over a Rh NC with $R_c = 2$ nm and $d = 2$ nm concave/convex deformation when illuminated at resonance. Higher concentrations of charge can be found on the edges and corners of the NC. Figure 11.10 shows the normalized absolute value of the averaged surface charge density $\langle|\sigma|\rangle$ over (b) corners and edges, and (c) the deformed faces of the cube. The values of $\langle|\sigma|\rangle$ on the corners and edges are ≈ 2.5 times greater than on the faces. Higher values of d lower $\langle|\sigma|\rangle$. The value of $\langle|\sigma|\rangle$ on the faces remains almost constant, increasing slightly as the cube becomes more convex.

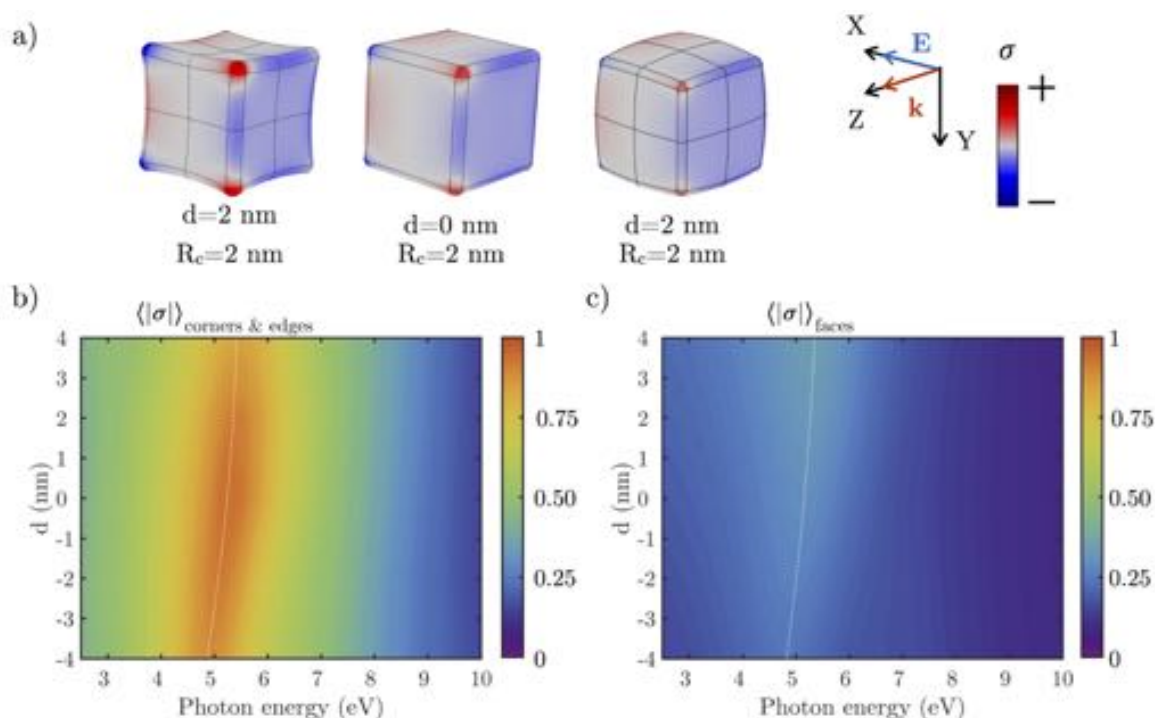


Figure. 11.10 (a) Surface charge distribution (σ) over concave and convex Rh NCs with $L = 30$ nm and $R_c = 2$ nm when illuminated at resonance. The red/blue regions represent positive/negative charge densities. Normalized values of σ averaged over (b) the edges and corners, and (c) over their deformed faces of the NCs.

11.2.4 Rh Nanocubes: Effect of a Dielectric Substrate

To mimic common experimental configurations in SERS and photocatalysis [4, 126, 166], we consider a Rh NC located on a dielectric substrate of different refractive indices. Examples commonly used in experiments are glass or sapphire with refractive indices of 1.5 and 1.78, respectively. Figure 11.11(a) plots the absorption cross-section (C_{abs}) for $L = 30$ nm Rh/Ag NCs with two R_c (2 and 10 nm) on different dielectric substrates. As the refractive index of the substrate increases, two peaks in the C_{abs} spectra appear, a phenomenon previously reported by Sherry et al. [232] on Ag NCs. One of these two peaks is slightly blue-shifted with respect to the peak of the isolated cube, and the other is red-shifted. The latter is associated with large fields near the surface of the substrate, whereas the former is associated with large fields away from the substrate. This shift towards lower energies can be understood by considering that the corners and edges of the cube touching the substrate are surrounded by a higher effective refractive index [12, 126, 166] (see Fig. 11.11(c)). These results are in agreement with

those reported by Nicoletti et al. [233], who studied Ag NCs on a dielectric substrate through electron energy-loss spectroscopy (EELS).

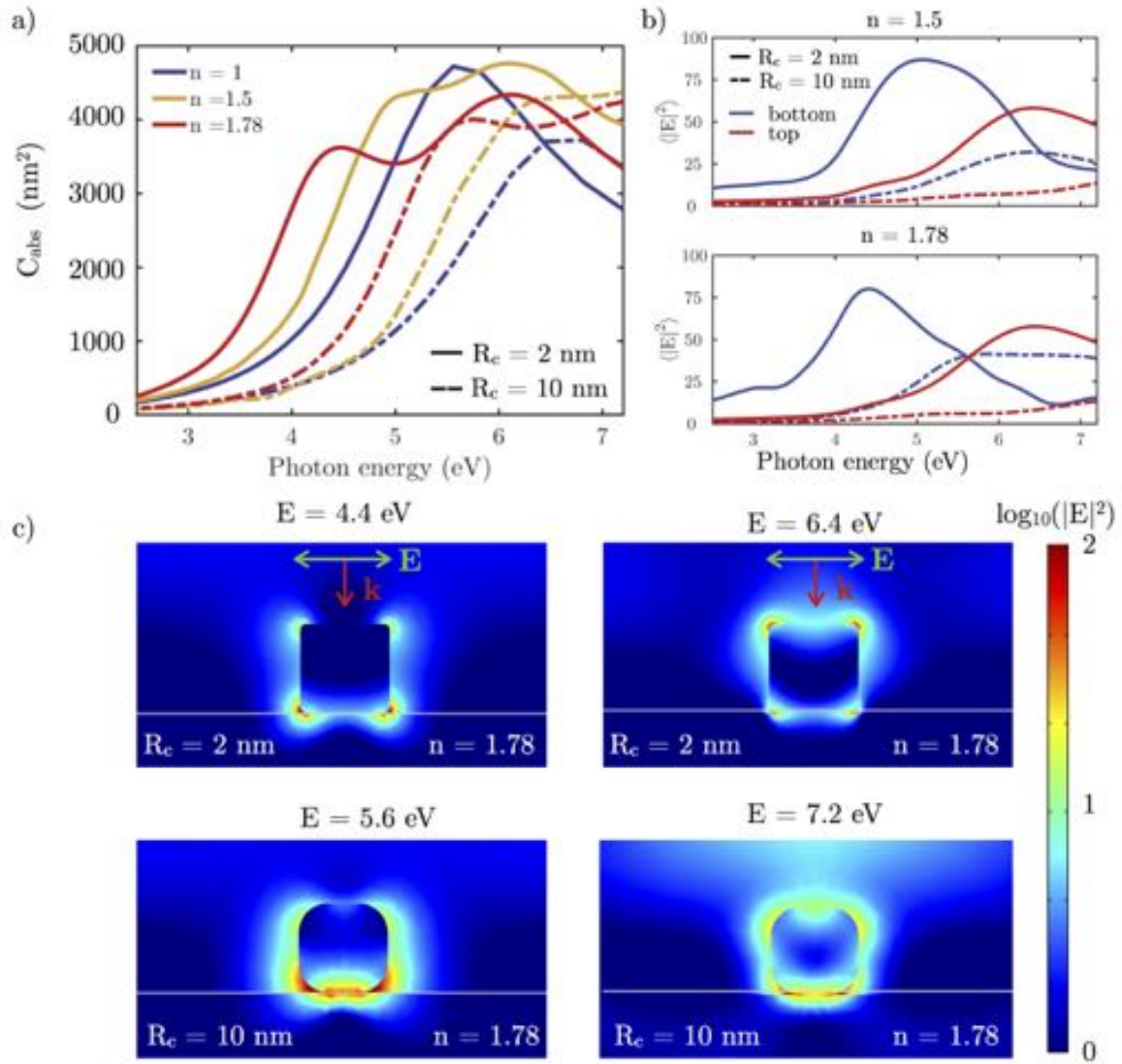


Figure. 11.11 (a) Absorption cross-section (C_{abs}) of a $L = 30$ nm and $R_c = 2/10$ nm (solid/dashed line) Rh NC under normal incidence with a P-polarization beam on substrates with different refractive indexes. (b) averaged over the corners and edges in the bottom (contact with the substrate, blue line) and top (red line) faces of the cube on a glass ($n = 1.5$) and sapphire ($n = 1.78$) substrates. (c) Logarithmic scale near-field maps for $R_c = 2/10$ nm Rh NC (top/bottom) on sapphire substrate ($n = 1.78$) at $E = 4.4/5.6$ eV and $E = 6.4/7.2$ eV.

Figure 11.11(b) shows the value of averaged over the edges and corners of the bottom (in contact with the substrate, blue lines) and top faces (in contact with air,

red lines) of the Rh NC. The peak associated with the bottom face is red-shifted with respect to the top face peak because the corners and edges of the bottom face are surrounded by a higher refractive index than the top ones. In fact, the peak associated with the sapphire substrate is shifted towards lower energies than the one corresponding to the glass because the refractive index of sapphire is greater than glass (1.78 vs 1.5). Conversely, the spectral value of averaged over the edges and corners of the top face (in contact with air), take approximately the same values no matter the substrate. The maximum average enhancement at the edges in contact with the substrate is higher than for those at the top face. This means that at the interface between particle and substrate, a large concentration of plasmonically-excited carriers is produced, making this region the most reactive location.

Two near-field maps for cubes with $R_c = 2$ and 10 nm on a sapphire substrate are plotted in Fig 11.11(c), respectively. The chosen photon energies for each map are those at which the aforementioned averages take their maximum value: $E = 4.4/5.6$ eV in the case of the bottom face, and $E = 6.4/7.2$ eV for the top face. It can be seen how in bottom surface, very intense hot spots are produced in the interface between the cube and the substrate. Although there are still hot spots on the top, especially in the top corners of the NC. The main differences between the results for each value of R_c analyzed is that for $R_c = 10$ nm Rh NC, the spectra are blue-shifted with respect to those of $R_c = 2$ nm in accordance with the results reported in Fig. 11.6(a) for isolated NCs. Also, the values are lower for the $R_c = 10$ nm Rh NCs as for the case of the isolated NCs (see Fig.11.6(b) and (c)).

Figure 11.12(a) compares the C_{abs} spectra for Ag and Rh $L = 30$ nm and $R_c = 2$ nm NCs on glass and sapphire substrates. The spectra for isolated NCs are plotted too (red lines). As mentioned previously, Ag NCs are restricted for applications below the 3.5 eV because of its interband transitions, while Rh can operate in a wide range of the UV (4-7 eV).

As a final remark, consider that some commercial low cost light sources used in photocatalysis experiments operate in the near-UV and blue regions of the spectrum [27]. Optimum photocatalysis requires a good catalyst metal with efficient plasmonic behavior in these spectral ranges. Ag shows an excellent plasmonic response around 3 eV, but it suffers from oxidation and is a poor catalyst. Although Rh has a weaker plasmonic response in the near-UV, it is much better than other catalytic metals such as Pt or Pd [12], and its catalytic behavior is very good even off resonance. Fig. 11.12(b) shows the absorption efficiency of a 5 nm Rh NC as compared to that of a Ag NC of the same size with 1 nm Ag_2O shell. These sizes have been chosen because they

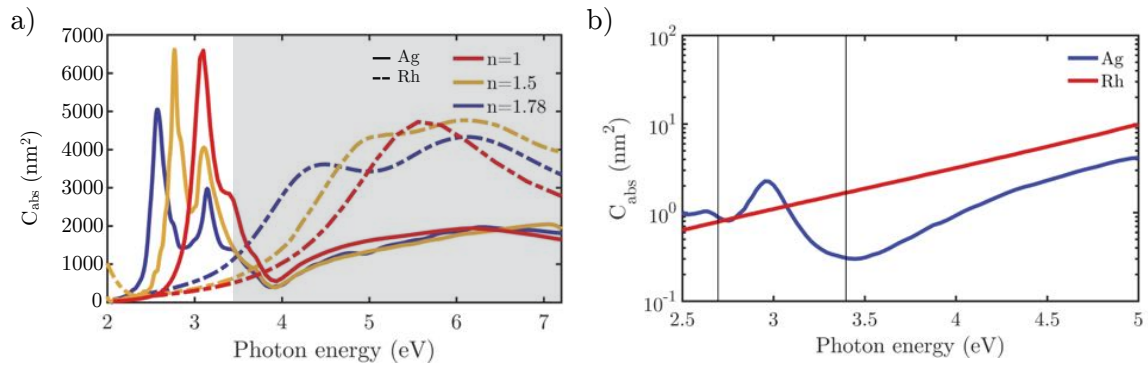


Figure. 11.12 (a) Absorption cross-section (C_{abs}) of a $L = 30$ nm and $R_c = 2$ nm Rh (dashed line) and Ag (solid line) NC under normal incidence with a P-polarization beam on substrates with different refractive indices. The shadowed region corresponds to the UV range. (b) Absorption cross-section (C_{abs}) for $L = 5$ nm Rh and Ag (with 1 nm Ag₂O shell). The vertical lines indicate two commercial wavelengths (460 nm (2.7 eV) and 365 nm (3.4 eV), respectively).

are typical in photocatalysis experiments [234, 171, 235]. As can be observed, above 3 eV, and in particular for widely available UV sources at 365 nm (3.4 eV) marked with a vertical line in the plot, Rh has better plasmonic and photocatalytic performance than Ag.

11.3 Conclusions

This research is a consequence of the recent interest in UV plasmonics, the consequent search for new metallic materials with good UV plasmonic performance, and enhancement of chemical reactions assisted by light such as photosynthesis and photocatalysis. Because rhodium has good plasmonic and catalytic behaviors, we have numerically studied the electromagnetic behavior of NPs made of Rh with cubical geometry in the UV range. This study has been performed by analyzing practical parameters like their absorption cross-section, local field enhancement, and surface charge density. From this study, the general conclusion is that Rh is a promising candidate for applications in plasmon enhanced spectroscopy and catalysis. Through chemical synthesis and repeated photocatalytic processes, NCs may have concave/convex faces or rounded corners and edges. In this research, we have analyzed their effect on the plasmonic response of Rh nanocubes. In general, a concavity/convexity on the NC faces leads to a blue/red-shift of the LSPR peak. Depositing the cube on a substrate or rounding its edges and corners also generates a red/blue-shift of the resonance peak. Both the local

field enhancement and the surface charge density reach their highest values at both the edges and the corners of the NC. The smaller the curvature radius of the edges and corners, the higher the values of the local field enhancement and surface charge density. These results serve as a guide to experimentalists for how Rh NC resonances may be optimized for photocatalytic process or SERS-like applications, leading to a control of the near-field and surface charge densities over the NP surface.

Chapter 12

The search for High Refractive Index materials in the UV

Plasmonics has been an extremely active area of research in the last decade [63]. The potential of using metallic nanoparticles (NPs) as electromagnetic field enhancers has opened up new possibilities in fields like chemistry, surface-enhanced spectroscopies, nanosensing, and medicine [128]. Although, in general, metallic NPs exhibit good plasmonic performance [114], their intrinsic Joule losses limit their use for many applications [55, 56]. To overcome this problem, a lot of attention has been paid to dielectric nanostructures made of High-Refractive-Index (HRI) materials, working in the Visible (VIS) and near-infrared (NIR) ranges. These materials are characterized by a high real part $n > 2$ and a low imaginary part $k \approx 0$ of their refractive indices (some examples can be found in R ef. [236]). They show the “ability” of enhancing the electromagnetic field both in the near and far-field regimes without much absorption [58, 55, 56] in those spectral ranges. In addition, they support magnetic resonances originated from the excited displacement currents. Moreover, HRI dielectric NPs manifest interesting properties of scattering directionality arising from the coherent effects between the excited electric and magnetic dipolar components [58, 57]. Under some specific conditions, scattered radiation from a single HRI dielectric spherical nanoparticle can be concentrated either in the backward or forward scattering regions. When the electric and magnetic dipoles oscillate in- or out-of-phase, two special situations appear, the so-called *zero-backward condition* (null scattering in the backward direction) and the *minimum forward condition* (minimum scattering in the forward direction), respectively. Up to now, most of the studies concerning these effects have been done in the visible (VIS) and near-infrared (NIR) ranges using common

semiconductors such as Si [237, 238] or GaAs [239], because of their interest for optical communications applications.

Unlike metals, when HRI dielectric materials show negligible absorption in the VIS-NIR spectral ranges (see ref. [236] for some examples), no localized heat appears. Consequently, neither the surrounding medium nor the nanostructure is heated, something that could have a clear negative effect. For instance, it could limit the performance of nano-antennas [240, 241] by altering the refractive index of both the nanostructure and surrounding medium through the thermo-optic effect [242]. Also, depending on the incident power, the nanoantenna could be reshaped, or even melted [243]. In addition, the heat generated by the nanoparticle can either vaporize the solvent media, affect or even destroy molecules and proteins. Heat can also affect the SERS signal, and has connection to problems or anomalies found in several processes including thermal annealing, modified adsorption/desorption kinetics of surface molecules, and changes in the dielectric properties of both, medium and particle [244]. In consequence, HRI dielectric materials have been proposed as an alternative to metals in surface-enhanced spectroscopies [55, 56].

As explained in Chapter 7, extending plasmonics into the UV (3–6 eV or 200 < wavelength < 400 nm) has triggered immense interest due to new challenges arising in specific areas [245]. A clear example is biosensing because many biological compounds such as nucleotide bases, nucleic acids, or aromatic amino acids in cells have absorption bands in the ultraviolet (UV). By using the local electric field enhancement generated by nanoparticles when illuminated at resonant wavelength, surface enhanced spectroscopy techniques [51–53] (SERS, TERS, etc.) can be improved to ease the detection of biomolecules. Other biosensing techniques rely on monitoring the spectral shifts induced by some target analytes in the extinction peaks of the NPs acting as nanoantennas. Bioimaging can also benefit from using UV radiation, since the diffraction limit is proportional to the wavelength (the lower the wavelength the higher the resolution). Most of these studies on UV plasmonics have been done using metals with strong UV plasmonic response such as aluminum, magnesium, gallium, or rhodium [12], but, to the best of our knowledge, HRI dielectric NPs have not been explored in this spectral range yet.

In this chapter it is presented a numerical analysis of several candidate dielectric materials that show HRI dielectric properties at energies above 3 eV. The dielectric materials chosen for this study are aluminum phosphide (AlP), aluminum arsenide (AlAs), aluminum nitride (AlN), diamond, cerium dioxide (CeO₂), and titanium dioxide (TiO₂). TiO₂ and CeO₂ are commonly used in photocatalysis [25, 246]. AlN, AlP, and

AlAs have undergone extensive study because of their potential use in the fabrication of light-emitting diodes (LEDs) [247]. In fact, in 2010 an AlN LED was presented with an emission wavelength of 210 nm, the shortest ever reported [248]. AlP and AlAs are materials commonly alloyed with GaP and GaAs to form AlGaP and $\text{Al}_x\text{G}_{1-x}\text{As}$ for their use in LED design. Nanodiamonds are being used in several areas of research and for various applications that include catalysis, drug delivery, and biomedical imaging [249].

The analysis of the aforementioned materials consists in a detailed numerical investigation of their directionality properties and their near-field enhancement in the UV. For the sake of comparison, we specifically consider isolated spheres of different sizes. It is worth mentioning that the results obtained for the spheres can be generalized for other NP's shapes. To mimic common typical experimental conditions, interaction effects in dimers are explored by comparing the near-field enhancement and the temperature generated in the nanoparticles and its surroundings. This work is aimed to introduce some HRI dielectric materials that can offer high quality directional properties and high near-field enhancement without heat generation in the UV regime. These features are closely connected with UV light-trapping applications and sensing. We envision that this study can open a new landscape for optimizing the efficiency of solar energy harvesting, photocatalysis, photodetection, and spectroscopic techniques in the UV regime.

This chapter is organized as follows. In Section 12.1, we briefly review the theoretical concepts and methods used to perform the electromagnetic and temperature calculations. In Section 12.2, we describe the criteria used to select the analyzed materials. In addition, the optical properties of these materials are presented. Section 12.3 includes the results and discussion of this research: an analysis of the near-field enhancement, directionality properties and cooperative effects in spherical NPs made of the selected materials. Finally, in Section 12.4 the main conclusions of this work are summarized.

12.1 Methods

12.1.1 Mie theory

The electromagnetic interaction between isolated nanospheres and light has been modeled following the Mie formalism for scattering and absorption of light by small particles [2]. The scattering efficiency by a spherical particle is given by,

$$Q_{sca} = \frac{2}{x^2} \sum_{n=1}^{\infty} (2n+1)(|a_n|^2 + |b_n|^2) \quad (12.1)$$

where a_n and b_n are the scattering coefficients of the Mie theory. These depend on the particle size and on the optical properties of the NP relative to its surrounding medium. The size parameter x is defined as $(2\pi m_{med}R)/\lambda$, where λ is the wavelength of incident light in the surrounding medium of refractive index m_{med} , and R is the radius of the sphere. From a physical point of view, coefficients a_n and b_n represent the weighting factors of the different multipolar contributions of order n , electric or magnetic, respectively. In particular, a_1 and b_1 correspond to the electric and magnetic dipolar modes, respectively. When $a_1 = b_1$ the zero backward condition is fulfilled and, as a result [58], there is null scattering in the backward direction, assuming that the rest of the coefficients are negligible (small size limit).

In the far-field region, the scattered electric field E^{sca} is related to the incident one E^{inc} through the scattering amplitude matrix $S(\theta, \phi)$ [36]. The scattered p -/ s -components are given by

$$\begin{pmatrix} E_{p,sca} \\ E_{s,sca} \end{pmatrix} \propto \begin{pmatrix} S_2 & S_3 \\ S_4 & S_1 \end{pmatrix} \begin{pmatrix} E_{p,inc} \\ E_{s,inc} \end{pmatrix} \quad (12.2)$$

where θ and ϕ are the scattering and azimuthal angles, respectively. The $S_i(\theta, \phi)$ elements are related to the coefficients a_n and b_n , and specific angular functions [2].

In order to quantify the efficiency of the zero backward scattering condition, the forward to backward scattering intensity ratio (I_{Fwd}/I_{Bck}) is introduced. This magnitude is defined as the ratio between the integrated scattered intensity in the forward and backward hemispheres. A key point to consider is that although a particle can have a high value of I_{Fwd}/I_{Bck} , its scattering efficiency may be negligible, making its scattering directionality properties useless. Therefore, it is important to find NPs made of materials that have high values of both I_{Fwd}/I_{Bck} and Q_{sca} [2]. Keeping this in mind, we have evaluated the product between these two magnitudes: $Q_{ZB} = I_{Fwd}/I_{Bck} \cdot Q_{sca}$. We will refer to this magnitude as zero backward efficiency (Q_{ZB}).

As aforementioned, the electromagnetic response of the nanospheres excited with light has been modeled using the Mie formalism. On the other hand, the interaction of light with dimers has been solved with finite element (FEM) calculations.

12.1.2 Temperature Calculations

The general heat generation process involves optical absorption, heat generation by itself and heat transfer to the surrounding medium. For the mechanism of heat release, the electric field strongly drives mobile carriers inside the NPs, and the energy gained turns into heat. Then, the heat diffuses away from the NP and leads to an increase of the temperature of the surrounding medium [250]. In metallic nanoparticles, the heat generation rate is especially strong under plasmon resonance. However, in semiconductors, this is much weaker since heat dissipation occurs through an interband absorption process with the creation of a single mobile electron-hole pair (exciton). In absence of phase transformations, the temperature distribution around an optically excited NP is described by the heat transfer equation [250, 251].

$$\rho(r) c(r) \frac{\partial T(r, t)}{\partial t} = \nabla \kappa(r) \nabla T(r, t) + Q_e(r, t) \quad (12.3)$$

where r and t are the spatial coordinate and the time, $T(r, t)$ is the local temperature, and the material parameters $\rho(r)$, $c(r)$ and $\kappa(r)$ are the density, specific heat and thermal conductivity, respectively. The magnitude $Q_e(r, t)$ represents a heat source produced by light dissipation in NPs. This term is composed by both resistive and magnetic losses. $Q_e(r, t)$ has been obtained by solving a system of Maxwell's equations including appropriate boundary conditions [55]. In our case, the whole process of light absorption and subsequent heat transfer between the nanostructure and the surrounding medium has been modeled by means of finite element simulations (following the same method as in [55, 56]).

12.2 Materials

In the search for materials with an appropriate HRI dielectric properties in the UV range, we look for real materials whose optical properties fulfill the two following constraints on their complex dielectric function $\epsilon = \epsilon_1 + i\epsilon_2$:

- A real part of the dielectric function $\epsilon_1 > 4$ in the UV allow the generation of electric and magnetic dipolar responses in the nanoparticle. This is necessary to satisfy the zero backward and minimum forward conditions.
- An imaginary part of the dielectric function that meets the condition $\epsilon_2 < 1$ at energies higher than 3 eV. This opens a low-absorption window above 3 eV, since

it can be easily derived that, provided that $\epsilon_1 > \epsilon_2$, the corresponding imaginary part of the refractive index ($k \approx \epsilon_2/2\sqrt{\epsilon_1}$) would be of the order of 0.1.

The materials we have analyzed that fulfill these requirements are the following: aluminum phosphide (AlP), aluminum arsenide (AlAs), aluminum nitride (AlN), diamond, cerium dioxide (CeO₂), and titanium dioxide (TiO₂). Table 12.1 shows the photon energy at which $\epsilon_2 = 1$ for each of the selected materials. In the case of AlN and diamond, the photon energy at which this condition is reached is out of the spectral range considered in this study (1–6 eV).

Table 12.1 Photon energy at which $\epsilon_2 < 1$ for each of the selected materials.

Material	E($\epsilon_2 = 1$) / eV
AlP	3.90
AlAs	3.25
AlN	–
Diamond	–
CeO ₂	3.53
TiO ₂	3.39

Some of the wide-bandgap materials have been rejected because they do not fulfill one of the two constraints. This includes GaN, ZnS, ZnO, and AlSb. For all the selected materials, with the exception of AlP and AlAs, NP fabrication methods have been reported and are available in the literature [252, 249, 253, 254].

Figure 12.1(a–f) shows the dielectric function ($\epsilon = \epsilon_1 + i\epsilon_2$) of the selected materials. The region where $\epsilon_1 > 4$ and $\epsilon_2 < 1$ within the UV is shadowed in gray. In Figure 12.1(g,h), the dielectric function of Rh and Al is shown as a reference because these metals are widely used in UV plasmonic applications [49]. Figure 12.1(i) plots the dielectric function of the HRI dielectric materials taken as reference: Si, GaAs and Ge. In the case of the reference materials (Al, Rh, Si, GaAs, and Ge) the shadowed region indicates the UV spectral range.

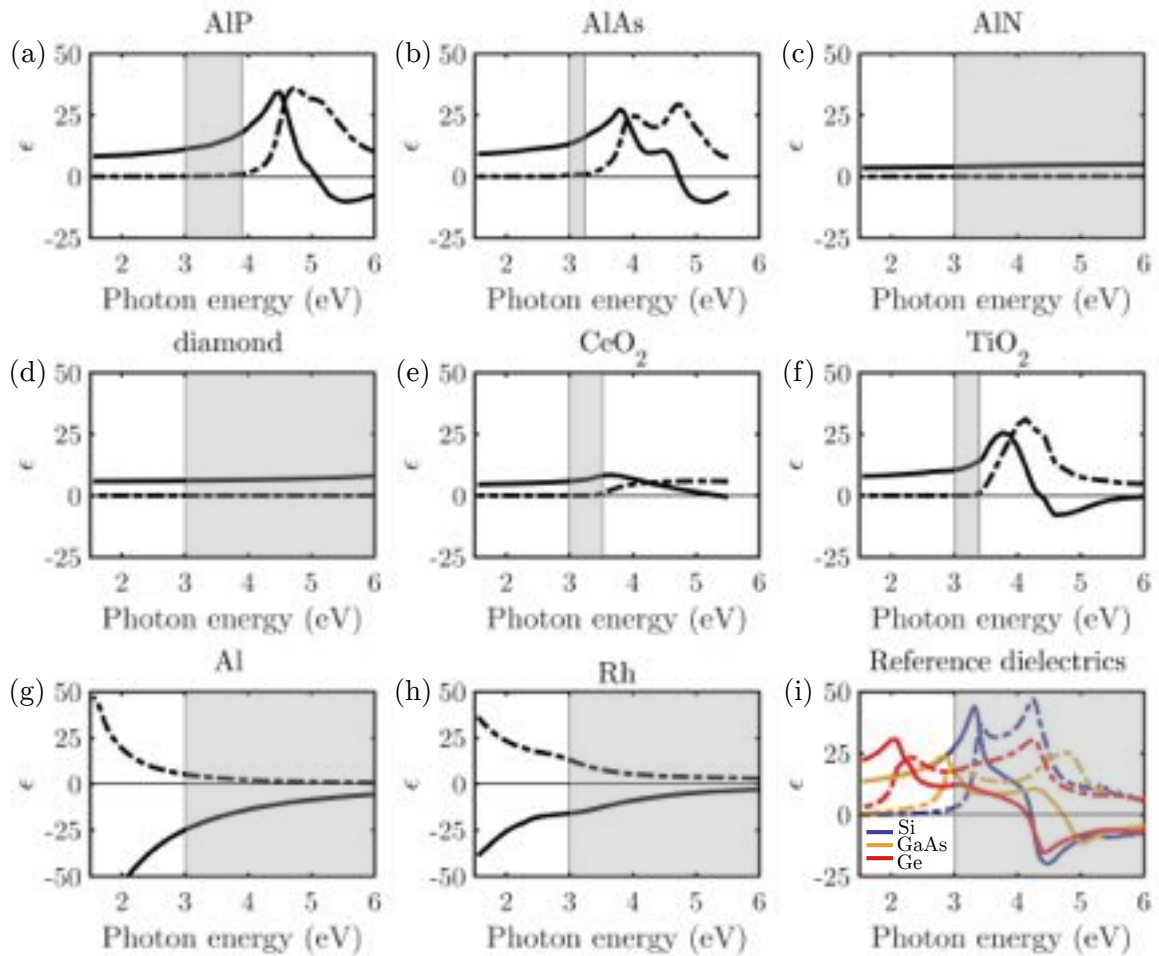


Figure 12.1 Real (solid line) and imaginary (dashed line) parts of the dielectric function ($\epsilon = \epsilon_1 + i\epsilon_2$) of (a) AIP [18], (b) AlAs [19], (c) AlN [20], (d) diamond, (e) CeO₂ [21], (f) TiO₂ [22], (g) Al, (h) Rh [13] and (i) the HRI taken as a reference: Si (blue), GaAs (yellow) and Ge (red)[13]. The region in which $\epsilon_2 < 1$ and $\epsilon_1 > 4$ is shadowed in grey. In the case of the reference materials (Si, Al and Rh) the shadowed region indicates the UV spectral range.

12.3 Results

12.3.1 Near-Field Enhancement

Near-field enhancement produced by NPs when electromagnetically irradiated is essential for applications like SERS (surface enhanced Raman spectroscopy) or SEF (surface enhanced fluorescence). In these spectroscopy techniques, most of the NP surface is covered with the molecules under study, so the electromagnetic field acting on them

can be approximated by an average of the electric field produced over the whole NP surface [56, 51]. Figure 12.2 shows the near-field enhancement averaged over the NP surface $\langle |\mathbf{E}|/|\mathbf{E}_0| \rangle$. Spheres with R varying from 30 to 90 nm have been considered. With dashed and solid white lines are highlighted the energy at which $\epsilon_2 = 1$ and the starting energy of the UV regime respectively (3 eV). For reference, $\langle |\mathbf{E}|/|\mathbf{E}_0| \rangle$ for two common metals for UV plasmonic applications are included: Rh and Al. In the case of Al, a realistic 5 nm thick oxide (Al_2O_3) shell has been considered [115, 109].

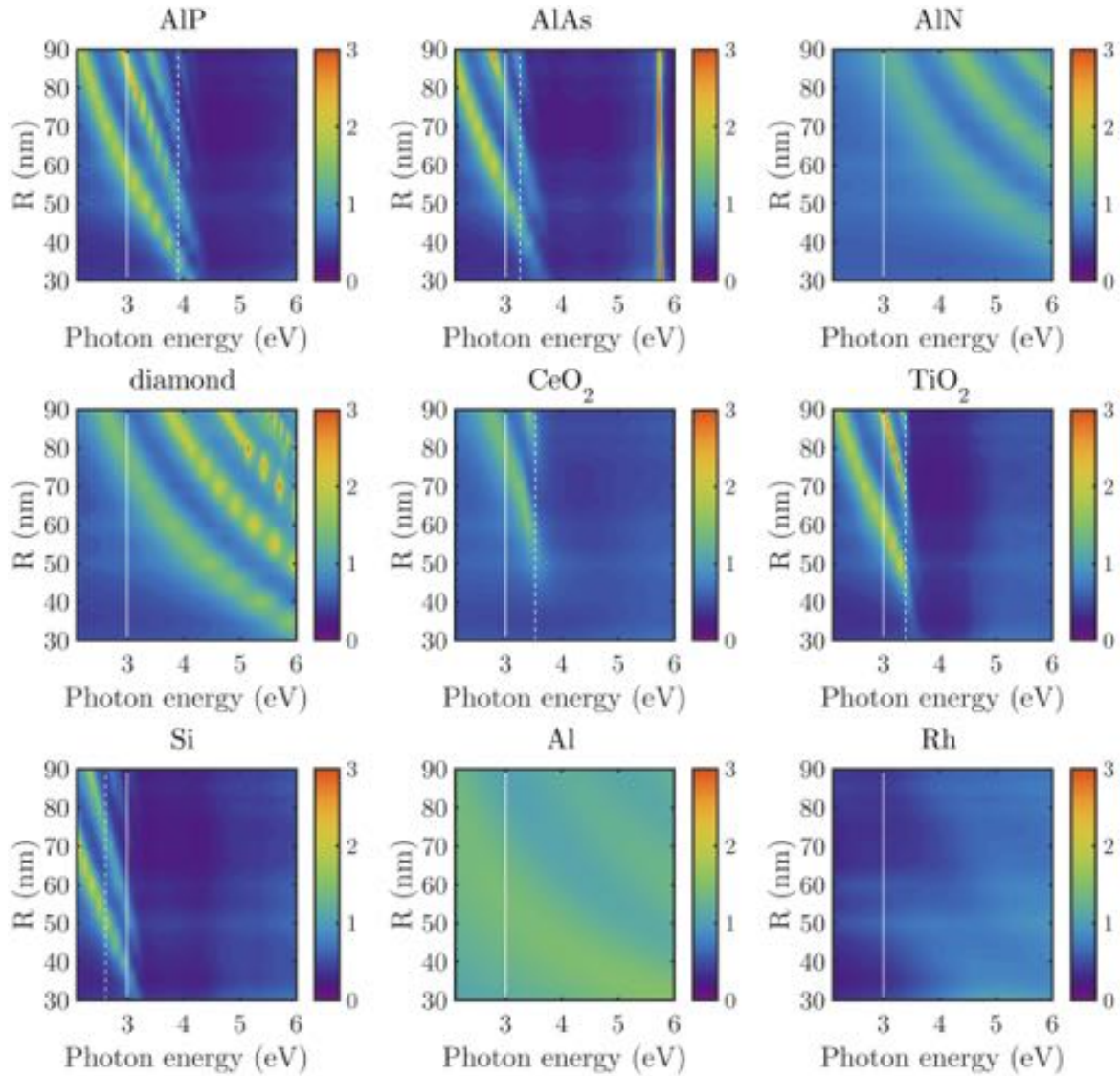


Figure. 12.2 Near-field enhancement averaged over the surface $\langle |\mathbf{E}|/|\mathbf{E}_0| \rangle$ of spheres with radius R (between 30 and 90 nm). A white dashed line represents the energy where $\epsilon_2 = 1$, and a white solid line indicates the energy where we consider the UV regime starts, 3 eV.

Unlike Si, all the HRI dielectric materials analyzed in this research, exhibit its electric field enhancement at energies above 3 eV. AlP, AlAs, CeO₂ and TiO₂ also show similar performance and high values of $\langle |\mathbf{E}|/|\mathbf{E}_0| \rangle$ can be reached between 3 and 3.4 or 4 eV depending on of the material. We would like to emphasize that TiO₂ shows the largest enhancement at energies above 3 eV. AlN and diamond also have very similar behavior since their absorption bands are above 6 eV: they have a HRI dielectric like behavior all along the studied spectral range. In this case, diamond presents the highest enhancement. The values of $\langle |\mathbf{E}|/|\mathbf{E}_0| \rangle$ for Al (with its native oxide shell included) and Rh NPs are also shown for comparison. Rhodium presents very low enhancement because its LSPRs are into deep UV (above 6 eV)[12, 49]. On the contrary, Al/Al₂O₃ nanospheres present wider peaks with moderate intensity. Consequently, the value of $\langle |\mathbf{E}|/|\mathbf{E}_0| \rangle$ is almost constant for all sizes in the studied spectral range.

12.3.2 Directionality Properties: The Full-Forward Condition

The full-forward condition, also known as the first Kerker condition, maximizes the scattered intensity in the forward direction while it minimizes the backward one. This situation has found a great utility in light guiding and light trapping applications [255, 256]. In order to evaluate the full-forward condition, we have considered nanospheres of different radii made of AlP, AlAs, AlN, CeO₂, TiO₂ and Si and we have analyzed the following parameters: photon energy where the zero-backward condition is produced (E_{ZB}), the scattering efficiency (Q_{sca}) and the forward to backward scattering ratios (I_{Fwd}/I_{Bck}) at E_{ZB} . In addition, the combined effect of these two last magnitudes, the zero backward efficiency, defined as $Q_{ZB} = Q_{sca} \cdot I_{Fwd}/I_{Bck}$ will be also analyzed.

Figure 12.3 (a) shows the photon energies where the zero-backward condition holds (E_{ZB}) for spheres of radius R between 30 and 90 nm. The zero-forward condition is not satisfied for all the materials in the analyzed size range. For example, for CeO₂ NPs, R should be larger than 60 nm. On the contrary, nanospheres made of either AlP or diamond, exhibit this condition for all analyzed radii. The rest of materials also shows the zero-backward condition in the UV but not for all radii. Notice that all of them satisfy this condition at higher energies than Si. Those that show the zero-backward condition above 3 eV are AlP ($30 < R < 50$ nm), AlN ($40 < R < 80$ nm), diamond ($40 < R < 70$ nm), CeO₂ ($60 < R < 80$ nm) and TiO₂ ($R = 50$ nm).

High values of Q_{sca} are desirable in order to exploit the maximum amount of incoming intensity in the analyzed condition, the zero-backward [257]. Figure 12.3(b) shows the scattering efficiency Q_{sca} at the photon energy of the zero-backward condition as a function of the sphere radius, R . Among the studied materials, those that show

the highest values of Q_{sca} at the zero-backward condition are diamond, CeO_2 and AlN . AlP, one of the promising candidates for directionality applications in the UV, presents values of Q_{sca} around two times smaller than diamond and CeO_2 , and very similar to those of TiO_2 . It is worth noting that all the analyzed materials show higher values of Q_{sca} than Si.

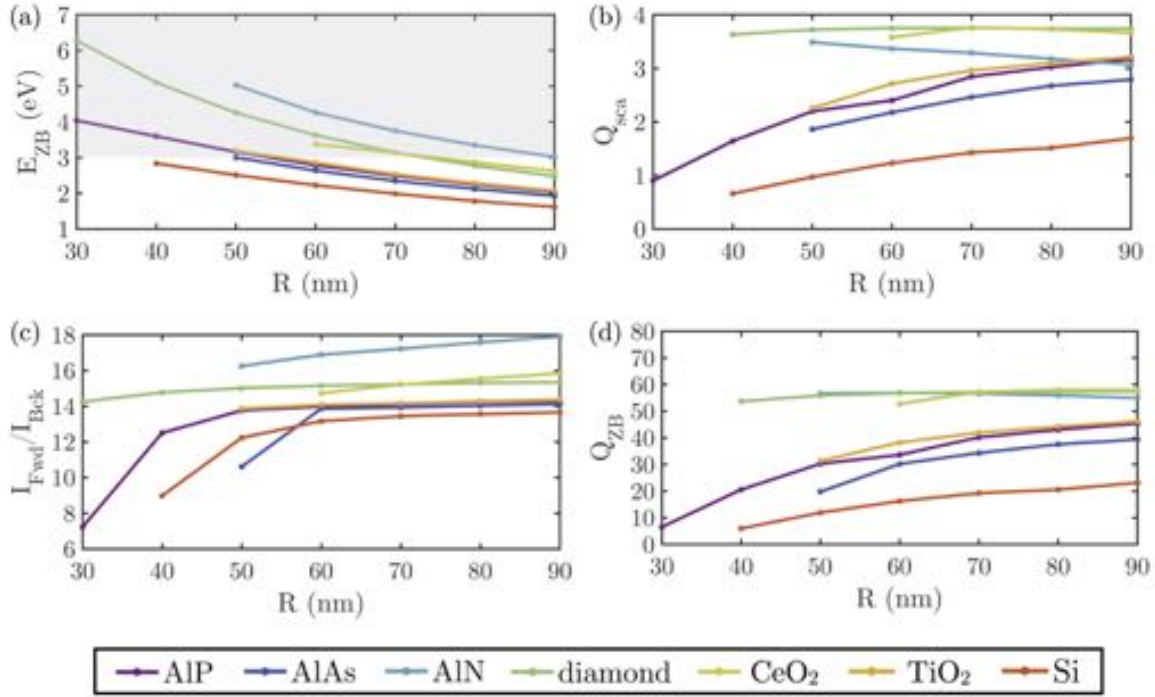


Figure. 12.3 (a) Photon energies where the zero-backward condition holds (E_{ZB}), (b) scattering efficiency Q_{sca} at the photon energy of the zero-backward condition, (c) forward to backward intensity ratio I_{Fwd}/I_{Bck} at the zero-backward condition and (d) zero backward efficiency, Q_{ZB} , for spheres of radius R (between 30 and 90 nm) made of different materials.

Figure 12.3(c) shows the forward to backward intensity ratio I_{Fwd}/I_{Bck} at the photon energy of the zero-backward condition as a function of R . This magnitude will allow us to quantify the asymmetry introduced in the scattered intensity along the propagating direction when imposing the zero-backward conditions. Diamond, CeO_2 and AlN are the materials that present higher ratios I_{Fwd}/I_{Bck} . Values remain almost constant for all the considered sizes. TiO_2 and AlP present the same values of I_{Fwd}/I_{Bck} , and very similar to that of AlAs. Once again, Si shows the lowest ratio.

The ideal zero backward condition is a combination of two effects: a high scattering efficiency and a high forward to backward ratio. Therefore, forward directionality requires the presence of both. This makes necessary to evaluate the zero backward

efficiency, defined as $Q_{ZB} = Q_{sca} \cdot I_{Fwd}/I_{Bck}$. Figure 3(d) shows the values of Q_{ZB} at the photon energy of the zero-backward condition as a function of R . Diamond, CeO₂ and AlN present the same constant value of Q_{ZB} , approximately. The zero backward efficiency for AlP and TiO₂ takes the same values. However, in this case, Q_{ZB} becomes smaller as R decreases. Once again, Si is the material that shows the worst performance. Therefore, all the analyzed materials are better options than Si for scattering directionality applications, both in the VIS and UV ranges.

12.3.3 Interaction Effects

In this section, possible interaction effects are considered by studying the near-field enhancement that can be produced between two NPs in close interaction and the consequences that this interaction may have in the heat generation process. Interaction effects are widely used when designing nanostructures for surface enhanced spectroscopic techniques [56]. A dimer made of spheres with $R = 70$ nm and inter-particle distances (gap) of 10 and 20 nm is analyzed.

TiO₂ and diamond are selected as representative materials of the two type of HRI dielectrics studied previously: those with losses ($\epsilon_2 > 0$) above 3.5 eV (AlP, AlAs, CeO₂ and TiO₂) and those with losses above 6 eV (AlN and diamond). The selected materials for this study (TiO₂ and diamond) when studied as isolated spheres, showed the highest value of $\langle |\mathbf{E}|/|\mathbf{E}_0| \rangle$. We also present the behavior of Al NPs as a reference. Once again, a 5 nm oxide shell (Al₂O₃) has been considered in order to mimic common experimental situations [115].

Figure 12.4 shows the spectral values of $|\mathbf{E}|/|\mathbf{E}_0|$ and ΔT (temperature increase with respect to ambient temperature) at the center of the gap of dimers made of Al/Al₂O₃, TiO₂ and diamond. In all cases, the dimers are excited with a plane wave linearly polarized along the dimer axis (see inset in Fig. 12.4(a)). This polarization is chosen to enhance the interaction effects [258]. By comparing the values of $|\mathbf{E}|/|\mathbf{E}_0|$ for the different materials analyzed, both diamond and TiO₂ produce the highest values above 3 eV. In the case of the Al/Al₂O₃ dimer, the enhancement is significantly smaller than that of either diamond or TiO₂ (around 4 times and one order of magnitude, respectively) and at an energy slightly below 3 eV. Also note that, for diamond and TiO₂, the temperature does not increase ($\Delta T = 0$) when excited at the photon energies of maximum enhancement. However, for Al/Al₂O₃, the temperature is increased.

Similar results to those of TiO₂ are expected for AlP, AlAs and CeO₂: high values of $|\mathbf{E}|/|\mathbf{E}_0|$ and low values of ΔT at energies below their corresponding absorption bands (≈ 3.5 eV). At higher energies, ΔT increases while $|\mathbf{E}|/|\mathbf{E}_0|$ decreases. Also,

mention that for AlN, a behavior similar to diamond is expected, moderate values of $|\mathbf{E}|/|\mathbf{E}_0|$ with $\Delta T = 0$ for energies below 6 eV.

The main difference between having a gap of 10 or 20 nm is that for the shortest one both $|\mathbf{E}|/|\mathbf{E}_0|$ and ΔT , are higher. This is caused by the strength of the interaction: as the distance between particles become smaller the interaction becomes stronger. Also, a red-shift of both $|\mathbf{E}|/|\mathbf{E}_0|$ and ΔT spectra is produced as the gap becomes shorter [258].

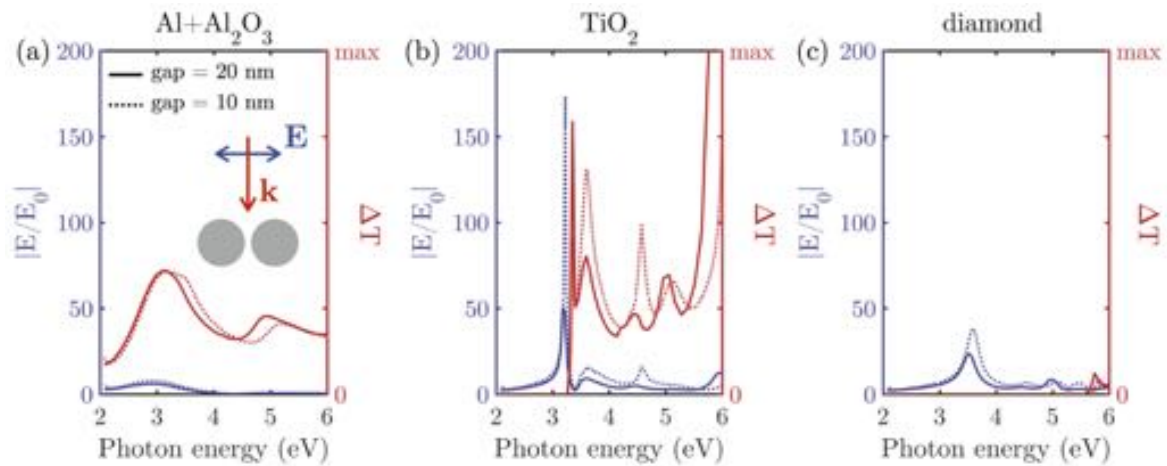


Figure. 12.4 Electric field enhancement $|\mathbf{E}|/|\mathbf{E}_0|$ (blue line, left axis) and temperature difference with respect to ambient temperature ΔT (red line, right axis) at the center of the gap of (a) Al/Al₂O₃, (b) TiO₂ and (c) diamond dimers. The analyzed dimer configuration is shown as inset in (a): a dimer of spheres of $R = 70$ nm with gap = 10 (dashed line) and 20 nm (solid line), illuminated with a plane wave linearly polarized along the dimer axis.

Figure 12.5 shows the near-field enhancement ($|\mathbf{E}|/|\mathbf{E}_0|$) and heat maps (ΔT) for diamond and Al/Al₂O₃ dimers with a gap = 20 nm. Since the temperature increment is proportional to the intensity of the illuminating beam, the temperature scale is arbitrary and for comparison purposes, going from 0 to a *max* value which depends on this intensity [251]. The diamond dimer offers the highest near-field enhancement, together with the smallest heat perturbation. However, this is not the case for Al/Al₂O₃, where the field enhancement is four times smaller and significant heat generation is present, as expected from its absorption. Although the results for gap = 10 nm are not shown, the overall effect of decreasing the gap is an increase of the near-field enhancement and temperature at the center of the gap, while keeping a very similar $|\mathbf{E}|/|\mathbf{E}_0|$ and ΔT , spatial distribution[55].

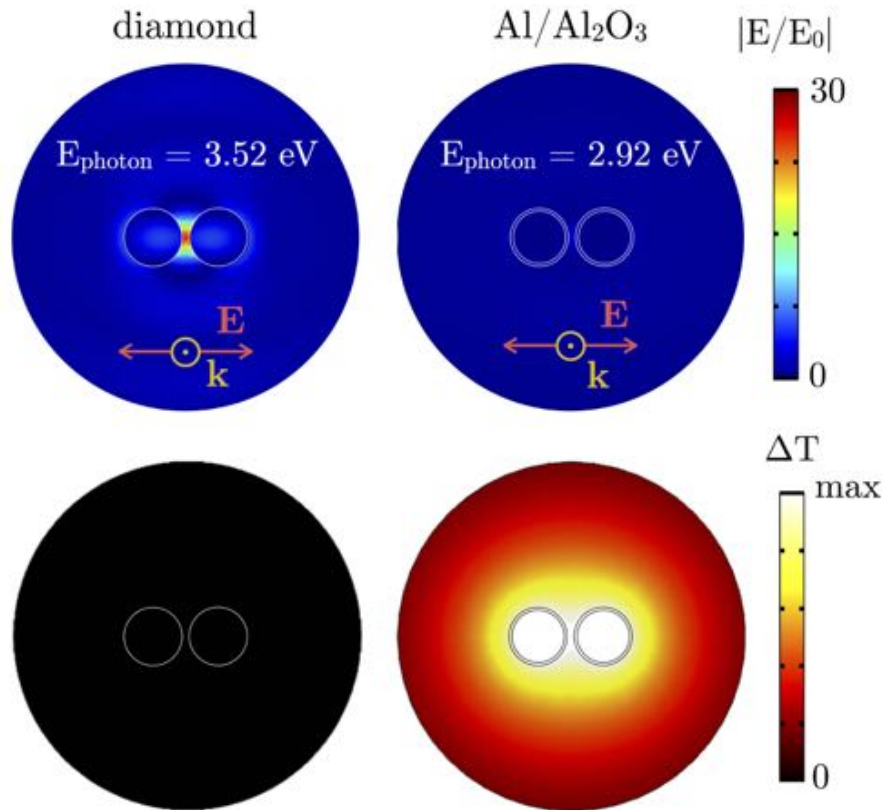


Figure. 12.5 Near field $|\mathbf{E}|/|\mathbf{E}_0|$ (top row) and temperature difference ΔT (bottom row) maps for a diamond and Al/Al₂O₃ dimers with gap = 20 nm. Both dimers are illuminated at resonance (photon energy indicated as an inset), with a p -polarized beam \mathbf{E} and wave vector \mathbf{k} . E_{photon} corresponds to the photon energy of the illuminating beam. The chosen values of E_{photon} are those that produce the maximum near-field enhancement at the center of the gap.

12.4 Conclusions

We have explored the possibilities of a selection of semiconductors –of the low loss High Refractive Index kind- to form nanoparticles with interesting applications in the UV region. The behavior we have considered of interest includes acting as HRI nanoantennas or behaving as unit cells of more complex metamaterials. The analyzed materials include some important semiconductors like AlP, AlAs, AlN, diamond, CeO₂ and TiO₂. When studying its near-field –averaged over the surface of the nanoparticle- some important values of the enhancement have been observed within the UV, in most of the considered materials. In the far-field, the possibility of using nanoparticles of these materials to generate light directionality effects has been explored by means of

the zero-backward efficiency, that accounts for both the scattering efficiency and the backward-to-forward scattering ratio. In fact, all the analyzed materials are better options than Si for scattering directionality applications, both in the VIS and UV ranges. Finally, the near-field enhancement and local temperature effects have been studied for these materials when forming dimers, reaching high values of the near-field. Similarly, to the response of well-known semiconductors used in VIS and Near-IR (Si, GaAs and Ge).

Based on these analyses, some of the studied compounds can be considered as promising High Refractive Index dielectrics in the UV. On the one hand there is diamond, along with AlN, that show loss-less behavior below 6 eV, so they have HRI dielectric character in the entire optical regime (from near-IR to UV). They exhibit the highest values of Q_{ZB} , only matched by CeO₂, but with moderate values of $|\mathbf{E}|/|\mathbf{E}_0|$ all along the UV range. On the other hand, TiO₂, along with AlP, AlAs and CeO₂, present losses above ≈ 3.5 eV. Between 3 and 3.5 eV they present high values of $|\mathbf{E}|/|\mathbf{E}_0|$ but lower Q_{ZB} values than AlN and diamond.

Finally, the analysis of the thermal response in the case of dimers shows that, for both TiO₂ and diamond, high values of $|\mathbf{E}|/|\mathbf{E}_0|$ can be generated at energies above 3 eV and without any losses and consequently no heat.

Chapter 13

Conclusions and Future Work

In this last chapter, and to finish this dissertation, I will summarize the main conclusions of this work along with the future perspectives.

13.1 Conclusions

13.1.1 Dielectric function of Ga polymorphs

Due to the wide temperature-dependent Ga polymorphism (l -, α -, β -, γ - and δ -Ga), and its promising applicability to the fabrication phase-change plasmonic/photonic devices, we have calculated the dielectric function of the different Ga-phases stable at atmospheric pressure using first-principles methods.

The results of this research shows that there are significant differences in the dielectric function of the various Ga phases at atmospheric pressure, specially in the region below 2.5 eV. In this spectral region, α - and β -Ga show interband transitions while γ - and δ -Ga have Drude metallic behavior. We demonstrate that optical constants attributed to α -Ga in the literature, actually correspond to a mixture of α - with other Ga phases. Depending on the cooling rate, this mixture can be α/β -Ga or α/γ -Ga. In light of this, we propose a new approach for estimating the phase composition and concentration of solid Ga films by fitting measured dielectric function spectra with a Bruggeman effective medium approximation using the calculated dielectric functions for the pure phases.

13.1.2 Dielectric function of high-pressure Ga phases

Gallium also presents a wide pressure-dependent polymorphism. Here, we have calculated the dielectric function of those high-pressure Ga-phases appearing closest to atmospheric pressure ((Ga(II) and Ga(III)) using-first principles methods to explore the possibility of designing pressure-driven phase-change plasmonic/photonic devices.

It is found that whereas Ga(II) has metallic character in the 1-6 eV spectral range, Ga(III) presents interband transitions at 1.44 eV. We have compared the plasmonic performance of these two high pressure phases with those stable and metastable at atmospheric pressure. Ga(III) has a plasmonic performance comparable to that of α -Ga, the phase stable at atmospheric pressure and room temperature. Ga(II) has a plasmonic performance superior to that of α - and β -Ga. Because many phase-change devices rely on in the change of reflectivity produced by the phase transition between Ga-phases, we have compared the reflectance spectra of a thin film made of the different Ga-phases. These results demonstrate that the largest differences are produced below 2 eV, where some of the Ga-phases have interband transitions (α -, β - and Ga(III)).

13.1.3 Oxide effects on Al, Ga and Mg nanoparticles

For all those applications exploiting LSPRs, it is crucial the precise tuning of their efficiency, spectral position, as well as their stability in order to have a reproducible plasmonic response. We have studied how the oxide shell that appears upon air exposure on Al, Ga and Mg NPs affect their plasmonic response in the UV.

The growth of an oxide shell on Ga, Mg and Al nanoparticles can either red-shift or blue-shift the localized surface plasmon resonances depending on the oxide shell thickness. The red-shift is produced by the increase of the effective refractive index surrounding the metallic core as the oxide shell thickness, whereas the blue-shift is produced by the size-reduction of the metallic core. Hot-spots corresponding to a surface electric field enhancement, and manifested by non-propagating evanescent fields, are observed on both the core and the shell. For thick oxide shells, these evanescent waves remain attached to the metallic core and dissipate within the oxide. These hot-spots are not useful since they are not accessible from outside. On the contrary, for thinner shells, part of the evanescent field reach beyond the surface of the particle while creating external hot-spots with evident practical interest. This results suggest the possibility of optimizing the near-field intensity peak and its spectral region by controlling the oxide shell thickness.

13.1.4 The Tarnishing of Mg/MgO Nanoparticles

So far, the limit of Mg as a plasmonic material has been reported to consist mainly in its oxidation. Here, we demonstrate that oxidation is not the only chemical surface transformation that can occur at the surface of Mg NPs.

We report the tarnishing of oxidized Mg nanoparticles by the heterogeneous uptake of SO₂ and fluorine contamination in air at room temperature and its regeneration by exposure to a H-plasma. Raman, XPS and FTIR data shows that sulfate and oxyfluoride compounds are formed in the surface of Mg/MgO nanoparticles in the form of micron-size crystals. This effect has to be taken into account in plasmonic and hydrogen storage applications. Change in the color of the sample and the shift of he plasmonic response can be used to monitor the adsorption S- and F-compounds by the sample. On the positive side, Mg/MgO nanoparticles have a great potential for water and air purification being Mg and MgO non-toxic.

13.1.5 Interaction of H with Mg/MgO nanoparticles and films

The interaction of Mg and MgO with H is of paramount importance for an hydrogen based economy due to its hydride MgH₂, which has high gravimetric and volumetric H densities. Nevertheless, critical issues related to H desorption temperature, sluggish (de-)hydrogenation kinetics and the fast oxidation of Mg by air exposure limit the Mg-H technology uptake. Given these challenges, we have studied the direct interaction of Mg with H, as well as implications of its inevitable oxidation by real-time spectroscopic ellipsometry.

The interaction of hydrogen with Mg thin films and plasmonic nanoparticles realistically covered by a thin overlayer of MgO reveals the self-limiting character of the Mg hydrogenation kinetics. This is produced, first, by the reduction of the outmost MgO layer and its conversion into MgH₂. Subsequent Mg hydrogenation is limited by the slow diffusion of the H atoms into the growing “blocking” MgH₂ layer. When exposed to air, the MgH₂ layer oxidizes forming Mg(OH)₂. Furthermore, it is demonstrated that, although Mg NPs have a tunable plasmonic response from the UV to the NIR controlled by the NP size, their use in realistic applications is limited due to their complete oxidation unless a capping layer is used.

13.1.6 Rh nanocubes in photocatalysis applications

Rhodium can be considered a promising candidate for applications in plasmon enhanced catalysis and spectroscopy in the UV because of its low oxidation tendency, its strong

plasmonic response in the UV and its inherent catalytic behavior. Very recently, it has been reported the possibility of synthesizing Rh nanocubes with nanometer size control that have been already used for CO₂ photocatalyzation. In light of this, we have numerically studied the electromagnetic behavior of NPs made of Rh with cubical geometry in the UV range and the deformation that can arise from their use in photocatalysis.

Through repeated photocatalytic processes, Rh nanocubes may get concave/convex faces or rounded corners and edges. In general, concave/convex faces leads to a blue/red-shift of the LSPR peaks. Rounding the edges and corners produces a blue-shift of the LSPR peak. Corners and edges are the most active sites since is in those regions where both the field enhancement and surface charge density reach their highest values. It has been found that the intensity of these two magnitudes at the corners and edges increases as their curvature radius decreases.

13.1.7 High refractive index dielectric materials in the UV

Nanostructured High Refractive Index dielectric (HRID) materials, when acting as nanoantennas, can show peculiar scattering directionality properties, and produce near-field enhancement with very low heat radiation. Up to now, most of the studies on HRID have been explored in the VIS-NIR. Here, we have performed a search for materials with HRID behavior in the UV.

In the quest for HRID materials in the UV we have presented several candidates: AlP, AlAs, AlN, diamond, CeO₂ and TiO₂. Both AlN and diamond show loss-less behavior below 6 eV, so they have HRID character from the near-IR to UV range. They exhibit the better directionality properties, only matched by CeO₂, but present moderate values of the near-field enhancement. On the other hand, TiO₂ along with CeO₂, AlP and AlAs, present losses above ≈ 3.5 eV. Between, 3 and 3.5 eV they present higher values of the near-field enhancement but worse directionality properties.

13.2 Future Work

Many promising ideas have come up during this research. However, many of them could not be properly addressed. Still, some of them deserve future research and development. Some of these ideas are related with: functionalization

- Since the successful production of graphene from graphite in 2004 [259], the 2D materials family has been widely enlarged. Increasing interest in 2D materials has

been triggered by their wide range of unique thermal, electric, mechanical and chemical properties arising from their singular surface chemistry and quantum-confinement effects. Very recently, Kochat et al. reported the successful exfoliation of atomically thin metallic Ga sheets on different substrates using a solid-melt exfoliation technique [260]. They named this new form of 2D Ga “gallenene”. The metallicity of the reported gallene phases exfoliated from the α -phase has been reported to be robust with respect to lattice strain [260, 261], its interaction with different semiconducting substrate [260] and hydrogen surface [261]. Indeed, gallene’s metallic behavior is ideal to complete the last and necessary component in the 2D material family. It is meant to complement the semi-metallic graphene, semiconducting dichalcogenides and insulating h-BN [262]. However, no information on the optical properties of these new form of Ga has been reported yet.

Consequently, the calculation from first-principles calculations of the optical constants of the different gallene phases are of current interest. These calculations are being currently performed and prepared for publication in a high impact journal.

- As discussed in Chapter 8, although Mg has some encouraging properties that make it a good candidate for the hydrogen technology, it also presents several drawbacks that limit its actual use. One of the most critical ones is the formation of an MgO/Mg(OH)₂ overlayer when exposed to ambient conditions that inhibit the dissociation of H₂ and diffusion of H atoms into the bulk [38]. It has been reported that one of the main factors that controls H-sorption is the rate of H₂ dissociation in the surface [30]. Therefore, alloying Mg with effective catalyst in the H₂ dissociation can critically improve the H-sorption kinetics. As an example, the energy barriers for this process in Mg and MgO surfaces are 1.05 and 1.33 eV, explaining the low-reactivity of Mg/MgO. However, when Mg is doped with Pt, the energy barrier drops to 0.39 eV [217].

Recently, it has been demonstrated that Ga is able to dissociate H₂ [263]. This makes Ga a very appealing candidate for creating Ga-Mg alloys capable of dissociate H₂. In fact, the Ga-Mg binary system can be presented in a wide variety of intermetallic compounds (Mg₅Ga₂, Mg₂Ga, MgGa, MgGa₂ and Mg₂Ga₅) in a rather complicated phase diagram [264]. The (de)hydrogenation of some of these intermetallic compounds have already been studied. It has been demonstrated that the (de)hydrogenation of Mg₅Ga₂ is a reversible process governed by the

reaction equation: $\text{Mg}_5\text{Ga}_2 + \text{H}_2 \rightarrow 2 \text{Mg}_2\text{Ga} + \text{MgH}_2$. In fact, reported values in literature for the de-hydrogenation enthalpy of Ga-Mg alloys (68.7 kJ/mol H_2) and pure Mg (77.1 kJ/mol H_2) suggest that the hydrogen storage capacity of Mg can be improved by alloying it with Ga [40].

Metallic nanoparticles (NPs) (e.g. Mg, Ga or Ga-Mg NPs) support localized plasmonic resonance (LSPR) that enables the possibility of plasmon-enhanced photocatalyzed chemical reactions, e.g., the dissociation of H_2 . It has been recently demonstrated that Ga-Mg NPs have tunable LSPRs from the visible to the ultraviolet [43, 90], providing a nanosystem resonant with all possible dissociation and bond formation energies. Therefore, the possibility of plasmon-enhanced photocatalytic dissociation of H_2 , and the higher hydrogen storage capacity and lower de-hydrogenation enthalpy Ga-Mg compounds [40], make Ga-Mg NPs a promising novel platform for the rising hydrogen technology.

Experiment on the H interaction with this type of NPs have already been done. However, work on their analysis and electromagnetic modelization is still needed.

- A current challenge in the plasmonic community is that of calculating the plasmonic response of sub-10 nm particles. In this regime, quantum mechanical effects, not taken into account by classical theories, start to gain importance. Several attempts to solve this problems can be found in the literature. For example, Scholl et al. [127], calculated the absorption spectra of Ag nanoparticles with diameters ranging from 2 to 10.5 nm. These absorption spectra were obtained using a dielectric function calculated from a modified Drude model in which they model the conduction electrons as a free electron gas constrained by infinite potential barriers at the physical edges of her particle. This model was proposed by Genzel [265] and Kraus [266] in 1975 and 1983 respectively. For Ag ($[\text{Kr}] 4d^{10}, 5s^1$), this approximation is good since in this material the energy difference between the d -band electrons and the Fermi level is larger than the plasmon energy. Therefore, the free electron contribution only comes from the $5s^1$ electrons. However, in other materials such as Au, electrons from the d -band can contribute significantly to the free electron gas [267] hampering the use of this model. Other authors, have approach this problem using time-dependt density functional theory (TDDFT). This theory provides an adequate framework to tackle the optical response of nanostructures in which quantum effects appear [268]. Calculations using this formalism are basically limited by the number of electrons that can be taken into account in the calculation. For this reason,

clusters studied using TDDFT are usually made of Na atoms since they only have one valence electron ($[\text{Ne}] 3s^1$). Despite this characteristic of Na, cluster's sizes are still below 1 nm. Performing these calculations with realistic metals for plasmonic applications (materials with more valence electrons coming from the d -bands) imply a further reduction of the atoms conforming the nanostructure. Consequently, even smaller sizes need to be considered. This sizes of nanoparticle lack of a real applicability.

With the appearance of second-principles methods [269], arises the possibility of calculating the optical response of sub 10-nm nanoparticles made of common plasmonic metals. These methods are prepared to deal with up to 100000+ atoms (vs 1000+ atoms that can be considered in first-principles calculations). In light of this, the idea is to employ second-principles methods to study the plasmonic response of these type of particles given their interest in photocatalytic applications due to their increase surface-to-volume ratios.

References

- [1] S. Lal, S. Link, and N. J. Halas, “Nano-optics from sensing to waveguiding,” *Nature Photonics* **1**, 641–648 (2007).
- [2] C. F. Bohren and D. R. Huffman, eds., *Absorption and Scattering of Light by Small Particles* (Wiley-VCH Verlag GmbH, Weinheim, Germany, 1998).
- [3] S. G. Warren, “Optical constants of ice from the ultraviolet to the microwave,” *Applied Optics* **23**, 1206 (1984).
- [4] M. Losurdo, A. Suvorova, S. Rubanov, K. Hingerl, and A. S. Brown, “Thermally stable coexistence of liquid and solid phases in gallium nanoparticles,” *Nature Materials* **15**, 995–1002 (2016).
- [5] L. Bosio, “Crystal structures of Ga(II) and Ga(III),” *The Journal of Chemical Physics* **68**, 1221–1223 (1978).
- [6] M. Yarema, M. Wörle, M. D. Rossell, R. Erni, R. Caputo, L. Protesescu, K. V. Kravchyk, D. N. Dirin, K. Lienau, F. von Rohr, A. Schilling, M. Nachttegaal, and M. V. Kovalenko, “Monodisperse Colloidal Gallium Nanoparticles: Synthesis, Low Temperature Crystallization, Surface Plasmon Resonance and Li-Ion Storage,” *Journal of the American Chemical Society* **136**, 12422–12430 (2014).
- [7] X. F. Li, G. T. Fei, X. M. Chen, Y. Zhang, K. Zheng, X. L. Liu, and L. D. Zhang, “Size-temperature phase diagram of gallium,” *EPL (Europhysics Letters)* **94**, 16001 (2011).
- [8] O. Hunderi and R. Ryberg, “Amorphous gallium—a free electron metal,” *Journal of Physics F: Metal Physics* **4**, 2096–2102 (1974).
- [9] O. Hunderi and R. Ryberg, “Band structure and optical properties of gallium,” *Journal of Physics F: Metal Physics* **4**, 2084–2095 (1974).
- [10] J. M. McMahon, G. C. Schatz, and S. K. Gray, “Plasmonics in the ultraviolet with the poor metals Al, Ga, In, Sn, Tl, Pb, and Bi,” *Phys. Chem. Chem. Phys.* **15**, 5415–5423 (2013).
- [11] O. Schulte and W. B. Holzapfel, “Effect of pressure on the atomic volume of Ga and Tl up to 68 GPa,” *Physical Review B - Condensed Matter and Materials Physics* **55**, 8122–8128 (1997).

- [12] J. M. Sanz, D. Ortiz, R. Alcaraz de la Osa, J. M. Saiz, F. González, a. S. Brown, M. Losurdo, H. O. Everitt, and F. Moreno, “UV Plasmonic Behavior of Various Metal Nanoparticles in the Near- and Far-Field Regimes: Geometry and Substrate Effects,” *The Journal of Physical Chemistry C* **117**, 19606–19615 (2013).
- [13] E. D. Palik, *Handbook of Optical Constants of Solids* (Academic Press, 1998).
- [14] P. B. Johnson and R. W. Christy, “Optical Constants of the Noble Metals,” *Physical Review B* **6**, 4370–4379 (1972).
- [15] J. Toudert, R. Serna, I. Camps, J. Wojcik, P. Mascher, E. Rebollar, and T. A. Ezquerro, “Unveiling the Far Infrared-to-Ultraviolet Optical Properties of Bismuth for Applications in Plasmonics and Nanophotonics,” *The Journal of Physical Chemistry C* **121**, 3511–3521 (2017).
- [16] M. F. Al-Kuhaili, S. M. A. Durrani, and E. E. Khawaja, “Optical properties of gallium oxide films deposited by electron-beam evaporation,” *Applied Physics Letters* **83**, 4533 (2003).
- [17] J. Isidorsson, I. A. M. E. Giebels, H. Arwin, and R. Griessen, “Optical properties of MgH₂ measured in situ in a novel gas cell for ellipsometry/spectrophotometry,” *Physical Review B* pp. 1–15 (2003).
- [18] S. Y. Hwang, T. J. Kim, Y. W. Jung, N. S. Barange, H. G. Park, J. Y. Kim, Y. R. Kang, Y. D. Kim, S. H. Shin, J. D. Song, C. T. Liang, and Y. C. Chang, “Dielectric function and critical points of AlP determined by spectroscopic ellipsometry,” *Journal of Alloys and Compounds* **587**, 361–364 (2014).
- [19] M. Garriga, P. Lautenschlager, M. Cardona, and K. Ploog, “Optical properties of AlAs,” *Solid State Communications* **61**, 157–160 (1987).
- [20] J. M. Khoshman and M. E. Kordesch, “Optical characterization of sputtered amorphous aluminum nitride thin films by spectroscopic ellipsometry,” *Journal of Non-Crystalline Solids* **351**, 3334–3340 (2005).
- [21] H. Shih, W.C., Chen, C.H., Chiu, F.C. Lai, C.M., Hwang, “CeO₂ optical properties and electrical characteristics,” *ECS Transactions* **28**, 435–442 (2010).
- [22] J. R. Devore, “Refractive Indices of Rutile and Sphalerite,” *Journal of the Optical Society of America* **41**, 416 (1951).
- [23] V. A. Fedotov, V. I. Emel yanov, K. F. MacDonald, and N. I. Zheludev, “Optical properties of closely packed nanoparticle films: spheroids and nanoshells,” *Journal of Optics A: Pure and Applied Optics* **6**, 155–160 (2004).
- [24] NASA, “GLOBAL CLIMATE CHANGE <https://climate.nasa.gov/> access date: 2019-03-03,” .
- [25] W. Hou and S. B. Cronin, “A review of surface plasmon resonance-enhanced photocatalysis,” *Advanced Functional Materials* **23**, 1612–1619 (2013).

- [26] X. Zhang, Y. L. Chen, R.-S. Liu, and D. P. Tsai, "Plasmonic photocatalysis." *Reports on progress in physics. Physical Society (Great Britain)* **76**, 046401 (2013).
- [27] X. Zhang, X. Li, D. Zhang, N. Q. Su, W. Yang, H. O. Everitt, and J. Liu, "Product selectivity in plasmonic photocatalysis for carbon dioxide hydrogenation," *Nature Communications* **8**, 14542 (2017).
- [28] X. Zhang, X. Li, M. E. Reish, D. Zhang, N. Q. Su, Y. Gutiérrez, F. Moreno, W. Yang, H. O. Everitt, and J. Liu, "Plasmon-Enhanced Catalysis: Distinguishing Thermal and Nonthermal Effects," *Nano Letters* **18**, 1714–1723 (2018).
- [29] C. Wadell, S. Syrenova, and C. Langhammer, "Plasmonic Hydrogen Sensing with Nanostructured Metal Hydrides," *ACS Nano* **8**, 11925–11940 (2014).
- [30] B. Sakintuna, F. Lamaridarkrim, and M. Hirscher, "Metal hydride materials for solid hydrogen storage: A review," *International Journal of Hydrogen Energy* **32**, 1121–1140 (2007).
- [31] L. Schlapbach and A. Züttel, "Hydrogen-storage materials for mobile applications," *Nature* **414**, 353–358 (2001).
- [32] S. Mukherjee, F. Libisch, N. Large, O. Neumann, L. V. Brown, J. Cheng, J. B. Lassiter, E. A. Carter, P. Nordlander, and N. J. Halas, "Hot electrons do the impossible: Plasmon-induced dissociation of H₂ on Au," *Nano Letters* **13**, 240–247 (2013).
- [33] S. Mukherjee, L. Zhou, A. M. Goodman, N. Large, C. Ayala-Orozco, Y. Zhang, P. Nordlander, and N. J. Halas, "Hot-Electron-Induced Dissociation of H₂ on Gold Nanoparticles Supported on SiO₂," *Journal of the American Chemical Society* **136**, 64–67 (2014).
- [34] S. Linic, P. Christopher, and D. B. Ingram, "Plasmonic-metal nanostructures for efficient conversion of solar to chemical energy," *Nature Materials* **10**, 911–921 (2011).
- [35] D. Sil, K. D. Gilroy, A. Niaux, A. Boulesbaa, S. Neretina, and E. Borguet, "Seeing is believing: Hot electron based gold nanoplasmonic optical hydrogen sensor," *ACS Nano* **8**, 7755–7762 (2014).
- [36] V. M. Silkin, R. Díez Muiño, I. P. Chernov, E. V. Chulkov, and P. M. Echenique, "Tuning the plasmon energy of palladium–hydrogen systems by varying the hydrogen concentration," *Journal of Physics: Condensed Matter* **24**, 104021 (2012).
- [37] V. M. Silkin, I. P. Chernov, P. M. Echenique, Y. M. Koroteev, and E. V. Chulkov, "Influence of hydrogen absorption on low-energy electronic collective excitations in palladium," *Physical Review B - Condensed Matter and Materials Physics* **76**, 1–9 (2007).
- [38] M. Zhu, Y. Lu, L. Ouyang, and H. Wang, "Thermodynamic tuning of mg-based hydrogen storage alloys: A review," *Materials* **6**, 4654–4674 (2013).

- [39] T. Sadhasivam, H.-T. Kim, S. Jung, S.-H. Roh, J.-H. Park, and H.-Y. Jung, “Dimensional effects of nanostructured Mg/MgH₂ for hydrogen storage applications: A review,” *Renewable and Sustainable Energy Reviews* **72**, 523–534 (2017).
- [40] D. Wu, L. Ouyang, C. Wu, H. Wang, J. Liu, L. Sun, and M. Zhu, “Phase transition and hydrogen storage properties of Mg–Ga alloy,” *Journal of Alloys and Compounds* **642**, 180–184 (2015).
- [41] X. Yu, Z. Tang, D. Sun, L. Ouyang, and M. Zhu, “Recent advances and remaining challenges of nanostructured materials for hydrogen storage applications,” *Progress in Materials Science* **88**, 1–48 (2017).
- [42] G. Bo, L. Ren, X. Xu, Y. Du, and S. Dou, “Recent progress on liquid metals and their applications,” *Advances in Physics: X* **3**, 1446359 (2018).
- [43] P. C. Wu, T.-H. Kim, A. S. Brown, M. Losurdo, G. Bruno, and H. O. Everitt, “Real-time plasmon resonance tuning of liquid Ga nanoparticles by in situ spectroscopic ellipsometry,” *Applied Physics Letters* **90**, 103119 (2007).
- [44] P. C. Wu, C. G. Khoury, T.-H. Kim, Y. Yang, M. Losurdo, G. V. Bianco, T. Vo-Dinh, A. S. Brown, and H. O. Everitt, “Demonstration of Surface-Enhanced Raman Scattering by Tunable, Plasmonic Gallium Nanoparticles,” *Journal of the American Chemical Society* **131**, 12032–12033 (2009).
- [45] A. G. Marín, T. García-Mendiola, C. N. Bernabeu, M. J. Hernández, J. Piqueras, J. L. Pau, F. Pariente, and E. Lorenzo, “Gallium plasmonic nanoparticles for label-free DNA and single nucleotide polymorphism sensing,” *Nanoscale* **8**, 9842–9851 (2016).
- [46] S. R. C. Vivekchand, C. J. Engel, S. M. Lubin, M. G. Blaber, W. Zhou, J. Y. Suh, G. C. Schatz, and T. W. Odom, “Liquid Plasmonics Manipulating Surface Plasmon Polaritons via Phase Transitions,” *Nano Letters* **12**, 4324–4328 (2012).
- [47] A. V. Krasavin and N. I. Zheludev, “Active plasmonics: Controlling signals in Au/Ga waveguide using nanoscale structural transformations,” *Applied Physics Letters* **84**, 1416–1418 (2004).
- [48] A. V. Krasavin, A. V. Zayats, and N. I. Zheludev, “Active control of surface plasmon–polariton waves,” *Journal of Optics A: Pure and Applied Optics* **7**, S85–S89 (2005).
- [49] Y. Gutiérrez, R. Alcaraz de la Osa, D. Ortiz, J. M. Saiz, F. González, and F. Moreno, “Plasmonics in the Ultraviolet with Aluminum, Gallium, Magnesium and Rhodium,” *Applied Sciences* **8**, 64 (2018).
- [50] D. Voet, W. B. Gratzer, R. a. Cox, and P. Doty, “Absorption spectra of nucleotides, polynucleotides, and nucleic acids in the far ultraviolet,” *Biopolymers* **1**, 193–208 (1963).
- [51] B. Sharma, R. R. Frontiera, A.-I. Henry, E. Ringe, and R. P. Van Duyne, “SERS: Materials, applications, and the future,” *Materials Today* **15**, 16–25 (2012).

- [52] Y. Yang, J. M. Callahan, T. H. Kim, A. S. Brown, and H. O. Everitt, "Ultraviolet nanoplasmonics: A demonstration of surface-enhanced raman spectroscopy, fluorescence, and photodegradation using gallium nanoparticles," *Nano Letters* **13**, 2837–2841 (2013).
- [53] A. Taguchi, "Plasmonic tip for nano Raman microscopy: structures, materials, and enhancement," *Optical Review* **24**, 462–469 (2017).
- [54] M. Decker and I. Staude, "Resonant dielectric nanostructures: a low-loss platform for functional nanophotonics," *Journal of Optics* **18** (2016).
- [55] P. Albella, R. Alcaraz de la Osa, F. Moreno, and S. a. Maier, "Electric and Magnetic Field Enhancement with Ultralow Heat Radiation Dielectric Nanoantennas: Considerations for Surface-Enhanced Spectroscopies," *ACS Photonics* **1**, 524–529 (2014).
- [56] M. Caldarola, P. Albella, E. Cortés, M. Rahmani, T. Roschuk, G. Grinblat, R. F. Oulton, A. V. Bragas, and S. A. Maier, "Non-plasmonic nanoantennas for surface enhanced spectroscopies with ultra-low heat conversion," *Nature Communications* **6**, 7915 (2015).
- [57] J. Geffrin, B. García-Cámara, R. Gómez-Medina, P. Albella, L. Froufe-Pérez, C. Eyraud, A. Litman, R. Vaillon, F. González, M. Nieto-Vesperinas, J. Sáenz, and F. Moreno, "Magnetic and electric coherence in forward- and back-scattered electromagnetic waves by a single dielectric subwavelength sphere," *Nature Communications* **3**, 1171 (2012).
- [58] A. García-Etxarri, R. Gómez-Medina, L. S. Froufe-Pérez, C. López, L. Chantada, F. Scheffold, J. Aizpurua, M. Nieto-Vesperinas, and J. J. Sáenz, "Strong magnetic response of submicron Silicon particles in the infrared," *Optics Express* **19**, 4815 (2011).
- [59] D. G. Baranov, D. A. Zuev, S. I. Lepeshov, O. V. Kotov, A. E. Krasnok, A. B. Evlyukhin, and B. N. Chichkov, "All-dielectric nanophotonics: the quest for better materials and fabrication techniques," *Optica* **4**, 814 (2017).
- [60] "Why interdisciplinary research matters," *Nature* **525**, 305–305 (2015).
- [61] H. Ledford, "How to solve the world's biggest problems," *Nature* **525**, 308–311 (2015).
- [62] M. I. Stockman, "Nanoplasmonics: past, present, and glimpse into future," *Optics Express* **19**, 22029 (2011).
- [63] J. A. Schuller, E. S. Barnard, W. Cai, Y. C. Jun, J. S. White, and M. L. Brongersma, "Plasmonics for extreme light concentration and manipulation," *Nature Materials* **9**, 193–204 (2010).
- [64] J. D. Jackson, *Classical Electrodynamics* (John Wiley and Sons Inc, 1999), 3rd ed.
- [65] F. Wooten, *Optical Properties of Solids* (Academic Press, 1972).

- [66] S. A. Maier, *Plasmonics: Fundamentals and Applications* (Springer US, Boston, MA, 2007).
- [67] M. L. Brongersma, N. J. Halas, and P. Nordlander, “Plasmon-induced hot carrier science and technology,” *Nature Nanotechnology* **10**, 25–34 (2015).
- [68] S. Linic, U. Aslam, C. Boerigter, and M. Morabito, “Photochemical transformations on plasmonic metal nanoparticles,” *Nature Materials* **14**, 567–576 (2015).
- [69] B. García-Cámara, R. Gómez-Medina, J. J. Sáenz, and B. Sepúlveda, “Sensing with magnetic dipolar resonances in semiconductor nanospheres,” *Optics Express* **21**, 23007 (2013).
- [70] M. Kerker, D.-S. Wang, and C. L. Giles, “Electromagnetic scattering by magnetic spheres,” *Journal of the Optical Society of America* **73**, 765 (1983).
- [71] E. M. Purcell and C. R. Pennypacker, “Scattering and Absorption of Light by Nonspherical Dielectric Grains,” *The Astrophysical Journal* **186**, 705 (1973).
- [72] B. T. Draine and P. J. Flatau, “Discrete-dipole approximation for scattering calculations,” *Journal of the Optical Society of America A* **11**, 1491 (1994).
- [73] COMSOL, “An Introduction to the Finite Element Method,” (2018).
- [74] Kane Yee, “Numerical solution of initial boundary value problems involving maxwell’s equations in isotropic media,” *IEEE Transactions on Antennas and Propagation* **14**, 302–307 (1966).
- [75] A. Taflove, “Application of the Finite-Difference Time-Domain Method to Sinusoidal Steady-State Electromagnetic-Penetration Problems,” *IEEE Transactions on Electromagnetic Compatibility* **EMC-22**, 191–202 (1980).
- [76] M. F. Cohen and S. G. Louie, *Fundamentals of condensed matter physics* (Cambridge University Press, Cambridge, 2016).
- [77] R. M. Martin, *Electronic Structure* (Cambridge University Press, Cambridge, 2004).
- [78] M. Losurdo, M. Bergmair, G. Bruno, D. Cattelan, C. Cobet, A. De Martino, K. Fleischer, Z. Dohcevic-Mitrovic, N. Esser, M. Galliet, R. Gajic, D. Hemzal, K. Hingerl, J. Humlicek, R. Ossikovski, Z. V. Popovic, and O. Saxl, “Spectroscopic ellipsometry and polarimetry for materials and systems analysis at the nanometer scale: State-of-the-art, potential, and perspectives,” *Journal of Nanoparticle Research* **11**, 1521–1554 (2009).
- [79] M. Losurdo and K. Hingerl, *Ellipsometry at the Nanoscale* (Springer Berlin Heidelberg, Berlin, Heidelberg, 2013).
- [80] Y. Lu, Q. Hu, Y. Lin, D. B. Pacardo, C. Wang, W. Sun, F. S. Ligler, M. D. Dickey, and Z. Gu, “Transformable liquid-metal nanomedicine,” *Nature Communications* **6**, 1–10 (2015).

- [81] R. W. G. Wyckoff, *Crystal Structures, Vol. 1* (Wiley, 1963).
- [82] L. Bosio, A. Defrain, H. Curien, and A. Rimsky, "Structure cristalline du gallium β ," *Acta Crystallographica Section B Structural Crystallography and Crystal Chemistry* **25**, 995–995 (1969).
- [83] L. Bosio, H. Curien, M. Dupont, and A. Rimsky, "Structure cristalline de $\text{Ga}\gamma$," *Acta Crystallographica Section B Structural Crystallography and Crystal Chemistry* **28**, 1974 (1972).
- [84] L. Bosio, H. Curien, M. Dupont, and A. Rimsky, "Structure cristalline de $\text{Ga}\delta$," *Acta Crystallographica Section B Structural Crystallography and Crystal Chemistry* **29**, 367–368 (1973).
- [85] M. Bernasconi, G. L. Chiarotti, and E. Tosatti, "Ab initio calculations of structural and electronic properties of gallium solid-state phases," *Physical Review B* **52**, 9988–9998 (1995).
- [86] X. G. Gong, G. L. Chiarotti, M. Parrinello, and E. Tosatti, " α -gallium: A metallic molecular crystal," *Physical Review B* **43**, 14277–14280 (1991).
- [87] R. Li, L. Wang, L. Li, T. Yu, H. Zhao, K. W. Chapman, Y. Wang, M. L. Rivers, P. J. Chupas, H.-k. Mao, and H. Liu, "Local structure of liquid gallium under pressure," *Scientific Reports* **7**, 5666 (2017).
- [88] P. Ghigna, G. Spinolo, G. B. Parravicini, A. Stella, A. Migliori, and R. Kofman, "Metallic versus covalent bonding: Ga nanoparticles as a case study," *Journal of the American Chemical Society* **129**, 8026–8033 (2007).
- [89] S. Pochon, K. F. MacDonald, R. J. Knize, and N. I. Zheludev, "Phase Coexistence in Gallium Nanoparticles Controlled by Electron Excitation," *Physical Review Letters* **92**, 145702 (2004).
- [90] P. C. Wu, M. Losurdo, T.-H. Kim, S. Choi, G. Bruno, and A. S. Brown, "In situ spectroscopic ellipsometry to monitor surface plasmon resonant group-III metals deposited by molecular beam epitaxy," *Journal of Vacuum Science & Technology B: Microelectronics and Nanometer Structures* **25**, 1019 (2007).
- [91] A. I. Denisyuk, F. Jonsson, and N. I. Zheludev, "Phase-change memory functionality in gallium nanoparticles," in "2007 European Conference on Lasers and Electro-Optics and the International Quantum Electronics Conference," (IEEE, 2007), pp. 1–1.
- [92] N. I. Zheludev, "Single nanoparticle as photonic switch and optical memory element," *Journal of Optics A: Pure and Applied Optics* **8**, S1–S8 (2006).
- [93] K. F. MacDonald, V. A. Fedotov, S. Pochon, G. Stevens, F. V. Kusmartsev, V. I. Emel'yanov, and N. I. Zheludev, "Controlling the coexistence of structural phases and the optical properties of gallium nanoparticles with optical excitation," *Europhysics Letters (EPL)* **67**, 614–619 (2004).

-
- [94] S. Ghosh and S. Lim, “A Multifunctional Reconfigurable Frequency-Selective Surface Using Liquid-Metal Alloy,” *IEEE Transactions on Antennas and Propagation* **66**, 4953–4957 (2018).
- [95] L. Comez, A. Di Cicco, J. Itié, and A. Polian, “High-pressure and high-temperature x-ray absorption study of liquid and solid gallium,” *Physical Review B* **65**, 1–10 (2001).
- [96] J. M. Soler, E. Artacho, J. D. Gale, A. García, J. Junquera, P. Ordejón, and D. Sánchez-Portal, “The SIESTA method for ab initio order-N materials simulation,” *Journal of Physics: Condensed Matter* **14**, 2745–2779 (2002).
- [97] J. P. Perdew, A. Ruzsinszky, G. I. Csonka, O. A. Vydrov, G. E. Scuseria, L. A. Constantin, X. Zhou, and K. Burke, “Restoring the Density-Gradient Expansion for Exchange in Solids and Surfaces,” *Physical Review Letters* **100**, 136406 (2008).
- [98] D. R. Hamann, “Optimized norm-conserving Vanderbilt pseudopotentials,” *Physical Review B* **88**, 085117 (2013).
- [99] M. van Setten, M. Giantomassi, E. Bousquet, M. Verstraete, D. Hamann, X. Gonze, and G.-M. Rignanese, “The PseudoDojo: Training and grading a 85 element optimized norm-conserving pseudopotential table,” *Computer Physics Communications* **226**, 39–54 (2018).
- [100] J. Junquera, Ó. Paz, D. Sánchez-Portal, and E. Artacho, “Numerical atomic orbitals for linear-scaling calculations,” *Physical Review B* **64**, 235111 (2001).
- [101] E. Anglada, J. M. Soler, J. Junquera, and E. Artacho, “Systematic generation of finite-range atomic basis sets for linear-scaling calculations,” *Physical Review B* **66**, 205101 (2002).
- [102] H. J. Monkhorst and J. D. Pack, “Special points for Brillouin-zone integrations,” *Physical Review B* **13**, 5188–5192 (1976).
- [103] M. Born, E. Wolf, A. B. Bhatia, P. C. Clemmow, D. Gabor, A. R. Stokes, A. M. Taylor, P. A. Wayman, and W. L. Wilcock, *Principles of Optics* (Cambridge University Press, Cambridge, 1999).
- [104] S. R. C. Vivekchand, C. J. Engel, S. M. Lubin, M. G. Blaber, W. Zhou, J. Y. Suh, G. C. Schatz, and T. W. Odom, “Liquid Plasmonics Manipulating Surface Plasmon Polaritons via Phase Transitions,” *Nano Letters* **12**, 4324–4328 (2012).
- [105] D. A. G. Bruggeman, “Berechnung verschiedener physikalischer Konstanten von heterogenen Substanzen. I. Dielektrizitätskonstanten und Leitfähigkeiten der Mischkörper aus isotropen Substanzen,” *Annalen der Physik* **416**, 636–664 (1935).
- [106] M. G. Blaber, M. D. Arnold, and M. J. Ford, “A review of the optical properties of alloys and intermetallics for plasmonics,” *Journal of Physics: Condensed Matter* **22**, 143201 (2010).

- [107] K. F. MacDonald, V. A. Fedotov, S. Pochon, K. J. Ross, G. C. Stevens, N. I. Zheludev, W. S. Brocklesby, and V. I. Emel'yanov, "Optical control of gallium nanoparticle growth," *Applied Physics Letters* **80**, 1643–1645 (2002).
- [108] L. Bosio, R. Cortes, J. R. Copley, W. D. Teuchert, and J. Lefebvre, "Phonons in metastable beta gallium: neutron scattering measurements," *Journal of Physics D: Applied Physics* **11**, 2261–2273 (1981).
- [109] Y. Gutierrez, D. Ortiz, J. M. Sanz, J. M. Saiz, F. Gonzalez, H. O. Everitt, and F. Moreno, "How an oxide shell affects the ultraviolet plasmonic behavior of Ga, Mg, and Al nanostructures," *Optics Express* **24**, 20621 (2016).
- [110] B. F. Soares, F. Jonsson, and N. I. Zheludev, "All-optical phase-change memory in a single gallium nanoparticle," *Physical Review Letters* **98**, 1–4 (2007).
- [111] T. Kenichi, K. Kazuaki, and A. Masao, "High-pressure bct-fcc phase transition in Ga," *Physical Review B - Condensed Matter and Materials Physics* **58**, 2482–2486 (1998).
- [112] Z. Li and J. S. Tse, "High-pressure bct to fcc structural transformation in Ga," *Physical Review B - Condensed Matter and Materials Physics* **62**, 9900–9902 (2000).
- [113] A. K. Harman, S. Ninomiya, and S. Adachi, "Optical constants of sapphire (α -Al₂O₃) single crystals," *Journal of Applied Physics* **76**, 8032–8036 (1994).
- [114] A. Lalisse, G. Tessier, J. Plain, and G. Baffou, "Quantifying the Efficiency of Plasmonic Materials for Near-Field Enhancement and Photothermal Conversion," *The Journal of Physical Chemistry C* **119**, 25518–25528 (2015).
- [115] M. W. Knight, N. S. King, L. Liu, H. O. Everitt, P. Nordlander, and N. J. Halas, "Aluminum for plasmonics," *ACS Nano* **8**, 834–840 (2014).
- [116] Y. Gutiérrez, M. M. Giangregorio, F. Palumbo, A. S. Brown, F. Moreno, and M. Losurdo, "Optically addressing interaction of Mg / MgO plasmonic systems with hydrogen," *Optics express* **27**, A197–A205 (2019).
- [117] A. M. Watson, X. Zhang, R. Alcaraz de la Osa, J. Marcos Sanz, F. González, F. Moreno, G. Finkelstein, J. Liu, and H. O. Everitt, "Rhodium nanoparticles for ultraviolet plasmonics." *Nano letters* **15**, 1095–1100 (2015).
- [118] X. Zhang, P. Li, Á. Barreda, Y. Gutiérrez, F. González, F. Moreno, H. O. Everitt, and J. Liu, "Size-tunable rhodium nanostructures for wavelength-tunable ultraviolet plasmonics," *Nanoscale Horiz.* **1**, 75–80 (2016).
- [119] Y. Fu and D. D. Dlott, "Single molecules under high pressure," *Journal of Physical Chemistry C* **119**, 6373–6381 (2015).
- [120] P. Podini and J. M. Schnur, "Applicability of sers to the study of adsorption at high pressure," *Chemical Physics Letters* **93**, 86–90 (1982).

- [121] P. Wang, H. Li, J. Jiang, B. Mo, and C. Cui, “An exploration of surface enhanced Raman spectroscopy (SERS) for in situ detection of sulfite under high pressure,” *Vibrational Spectroscopy* **100**, 172–176 (2019).
- [122] F. Moreno, P. Albella, and M. Nieto-Vesperinas, “Analysis of the Spectral Behavior of Localized Plasmon Resonances in the Near- and Far-Field Regimes,” *Langmuir* **29**, 6715–6721 (2013).
- [123] P. Larkin, *Infrared and Raman Spectroscopy* (Elsevier, 2011).
- [124] G. S. Bumrah and R. M. Sharma, “Raman spectroscopy – Basic principle, instrumentation and selected applications for the characterization of drugs of abuse,” *Egyptian Journal of Forensic Sciences* **6**, 209–215 (2016).
- [125] M. Aziz and A. Ismail, “X-Ray Photoelectron Spectroscopy (XPS),” in “Membrane Characterization,” (Elsevier, 2017), pp. 81–93.
- [126] P. Albella, B. Garcia-Cueto, F. González, F. Moreno, P. C. Wu, T. H. Kim, A. Brown, Y. Yang, H. O. Everitt, and G. Videen, “Shape matters: Plasmonic nanoparticle shape enhances interaction with dielectric substrate,” *Nano Letters* **11**, 3531–3537 (2011).
- [127] J. a. Scholl, A. L. Koh, and J. a. Dionne, “Quantum plasmon resonances of individual metallic nanoparticles.” *Nature* **483**, 421–7 (2012).
- [128] P. N. Prasad, *Nanophotonics* (John Wiley & Sons, Inc., Hoboken, NJ, USA, 2004).
- [129] K. Aslan, J. R. Lakowicz, and C. D. Geddes, “Plasmon light scattering in biology and medicine: new sensing approaches, visions and perspectives,” *Current Opinion in Chemical Biology* **9**, 538–544 (2005).
- [130] E. Ozbay, “Plasmonics: Merging Photonics and Electronics at Nanoscale Dimensions,” *Science* **311**, 189–193 (2006).
- [131] J. N. Anker, W. P. Hall, O. Lyandres, N. C. Shah, J. Zhao, and R. P. Van Duyne, “Biosensing with plasmonic nanosensors.” *Nature materials* **7**, 442–453 (2008).
- [132] M. J. Kale, T. Avanesian, and P. Christopher, “Direct photocatalysis by plasmonic nanostructures,” *ACS Catalysis* **4**, 116–128 (2014).
- [133] C. Noguez, “Surface plasmons on metal nanoparticles: The influence of shape and physical environment,” *Journal of Physical Chemistry C* **111**, 3606–3619 (2007).
- [134] Y. Kumamoto, A. Taguchi, N. I. Smith, and S. Kawata, “Deep UV resonant Raman spectroscopy for photodamage characterization in cells,” *Biomedical Optics Express* **2**, 927 (2011).
- [135] Y. Kumamoto, A. Taguchi, N. I. Smith, and S. Kawata, “Deep ultraviolet resonant Raman imaging of a cell,” *Journal of Biomedical Optics* **17**, 0760011 (2012).

- [136] P. Christopher and M. Moskovits, “Hot Charge Carrier Transmission from Plasmonic Nanostructures,” *Annual Review of Physical Chemistry* **68**, annurev-physchem-052516-044948 (2017).
- [137] V. Fournier, P. Marcus, and I. Olefjord, “Oxidation of magnesium,” *Surface and Interface Analysis* **34**, 494–497 (2002).
- [138] C. Gong and M. S. Leite, “Noble Metal Alloys for Plasmonics,” *ACS Photonics* **3**, 507–513 (2016).
- [139] C. J. DeSantis, M. J. McClain, and N. J. Halas, “Walking the Walk: A Giant Step toward Sustainable Plasmonics,” *ACS Nano* **10**, 9772–9775 (2016).
- [140] J. Martin and J. Plain, “Fabrication of aluminium nanostructures for plasmonics,” *Journal of Physics D: Applied Physics* **48**, 184002 (2015).
- [141] Y. Ekinici, H. H. Solak, and J. F. Löffler, “Plasmon resonances of aluminum nanoparticles and nanorods,” *Journal of Applied Physics* **104** (2008).
- [142] M. W. Knight, L. Liu, Y. Wang, L. Brown, S. Mukherjee, N. S. King, H. O. Everitt, P. Nordlander, and N. J. Halas, “Aluminum plasmonic nanoantennas.” *Nano letters* **12**, 6000–6004 (2012).
- [143] J. Martin, M. Kociak, Z. Mahfoud, J. Proust, D. Gérard, and J. Plain, “High-resolution imaging and spectroscopy of multipolar plasmonic resonances in aluminum nanoantennas,” *Nano Letters* **14**, 5517–5523 (2014).
- [144] G. H. Chan, J. Zhao, G. C. Schatz, and R. P. V. Duyne, “Localized surface plasmon resonance spectroscopy of triangular aluminum nanoparticles,” *Journal of Physical Chemistry C* **112**, 13958–13963 (2008).
- [145] A. Campos, A. Arbouet, J. Martin, D. Gérard, J. Proust, J. Plain, and M. Kociak, “Plasmonic Breathing and Edge Modes in Aluminum Nanotriangles,” *ACS Photonics* **4**, 1257–1263 (2017).
- [146] A. Rai, K. Park, L. Zhou, and M. R. Zachariah, “Understanding the mechanism of aluminium nanoparticle oxidation,” *Combustion Theory and Modelling* **10**, 843–859 (2006).
- [147] C. Langhammer, M. Schwind, B. Kasemo, and I. Zoric, “Localized surface plasmon resonances in aluminum nanodisks,” *Nano Letters* **8**, 1461–1471 (2008).
- [148] C. Zhang, H. Zhao, L. Zhou, A. E. Schlather, L. Dong, M. J. McClain, D. F. Swearer, P. Nordlander, and N. J. Halas, “Al–Pd Nanodisk Heterodimers as Antenna–Reactor Photocatalysts,” *Nano Letters* **16**, 6677–6682 (2016).
- [149] D. F. Swearer, H. Zhao, L. Zhou, C. Zhang, H. Robotjazi, J. M. P. Martirez, C. M. Krauter, S. Yazdi, M. J. McClain, E. Ringe, E. A. Carter, P. Nordlander, and N. J. Halas, “Heterometallic antenna reactor complexes for photocatalysis,” *Proceedings of the National Academy of Sciences* **113**, 8916–8920 (2016).

- [150] H. Robotjazi, H. Zhao, D. F. Swearer, N. J. Hogan, L. Zhou, A. Alabastri, M. J. McClain, P. Nordlander, and N. J. Halas, "Plasmon-induced selective carbon dioxide conversion on earth-abundant aluminum-cuprous oxide antenna-reactor nanoparticles," *Nature Communications* **8**, 27 (2017).
- [151] D. F. Swearer, R. K. Leary, R. Newell, S. Yazdi, H. Robotjazi, Y. Zhang, D. Renard, P. Nordlander, P. A. Midgley, N. J. Halas, and E. Ringe, "Transition-Metal Decorated Aluminum Nanocrystals," *ACS Nano* (2017).
- [152] M. J. McClain, A. E. Schlather, E. Ringe, N. S. King, L. Liu, A. Manjavacas, M. W. Knight, I. Kumar, K. H. Whitmire, H. O. Everitt, P. Nordlander, and N. J. Halas, "Aluminum Nanocrystals," *Nano Letters* **15**, 2751–2755 (2015).
- [153] M. Honda, Y. Kumamoto, A. Taguchi, Y. Saito, and S. Kawata, "Plasmon-enhanced UV photocatalysis," *Applied Physics Letters*, 104(6), 061108. **104**, 061108 (2014).
- [154] M. Honda, Y. Kumamoto, A. Taguchi, Y. Saito, and S. Kawata, "Efficient UV photocatalysis assisted by densely distributed aluminum nanoparticles," *Journal of Physics D: Applied Physics* **48**, 184006 (2015).
- [155] K. Ray, M. H. Chowdhury, and J. R. Lakowicz, "Aluminum nanostructured films as substrates for enhanced fluorescence in the ultraviolet-blue spectral region." *Analytical chemistry* **79**, 6480–7 (2007).
- [156] M. H. Chowdhury, K. Ray, S. K. Gray, J. Pond, and J. R. Lakowicz, "Aluminum nanoparticles as substrates for metal-enhanced fluorescence in the ultraviolet for the label-free detection of biomolecules," *Anal. Chem.* **81**, 1397–1403 (2009).
- [157] X. Jiao, E. M. Peterson, J. M. Harris, and S. Blair, "UV Fluorescence Lifetime Modification by Aluminum Nanoapertures," *ACS Photonics* **1**, 1270–1277 (2014).
- [158] Y. Wang, E. M. Peterson, J. M. Harris, K. Appusamy, S. Guruswamy, and S. Blair, "Magnesium as a Novel UV Plasmonic Material for Fluorescence Decay Rate Engineering in Free Solution," *The Journal of Physical Chemistry C* (2017).
- [159] B. Sharma, M. F. Cardinal, M. B. Ross, A. B. Zrimsek, S. V. Bykov, D. Punihaole, S. A. Asher, G. C. Schatz, and R. P. Van Duyne, "Aluminum Film-Over-Nanosphere Substrates for Deep-UV Surface-Enhanced Resonance Raman Spectroscopy," *Nano Letters* (2016).
- [160] F. Sterl, N. Strohfeldt, R. Walter, R. Griessen, A. Tittl, and H. Giessen, "Magnesium as Novel Material for Active Plasmonics in the Visible Wavelength Range," *Nano Letters* **15**, 7949–7955 (2015).
- [161] P. C. Wu, M. Losurdo, T. H. Kim, B. Garcia-Cueto, F. Moreno, G. Bruno, and A. S. Brown, "Ga-Mg Core-shell nanosystem for a novel full color plasmonics," *Journal of Physical Chemistry C* **115**, 13571–13576 (2011).
- [162] A. Zaluska, L. Zaluski, and J. Ström-Olsen, "Nanocrystalline magnesium for hydrogen storage," *Journal of Alloys and Compounds* **288**, 217–225 (1999).

- [163] X. Duan, S. Kamin, F. Sterl, H. Giessen, and N. Liu, "Hydrogen-Regulated Chiral Nanoplasmonics," *Nano Letters* **16**, 1462–1466 (2016).
- [164] X. Duan and N. Liu, "Scanning Plasmonic Color Display," *ACS Nano* **12**, 8817–8823 (2018).
- [165] H.-H. Jeong, A. G. Mark, and P. Fischer, "Magnesium plasmonics for UV applications and chiral sensing," *Chem. Commun.* **52**, 12179–12182 (2016).
- [166] Y. Yang, N. Akozbek, T.-h. Kim, J. M. Sanz, F. Moreno, M. Losurdo, A. S. Brown, and H. O. Everitt, "Ultraviolet–Visible Plasmonic Properties of Gallium Nanoparticles Investigated by Variable-Angle Spectroscopic and Mueller Matrix Ellipsometry," *ACS Photonics* **1**, 582–589 (2014).
- [167] M. W. Knight, T. Coenen, Y. Yang, B. J. M. Brenny, M. Losurdo, A. S. Brown, H. O. Everitt, and A. Polman, "Gallium Plasmonics: Deep Subwavelength Spectroscopic Imaging of Single and Interacting Gallium Nanoparticles," *ACS Nano* **9**, 2049–2060 (2015).
- [168] P. C. Wu, T.-H. Kim, A. Suvorova, M. Giangregorio, M. Saunders, G. Bruno, A. S. Brown, and M. Losurdo, "GaMg Alloy Nanoparticles for Broadly Tunable Plasmonics," *Small* **7**, 751–756 (2011).
- [169] N. Zettsu, J. M. McLellan, B. Wiley, Y. Yin, Z.-Y. Li, and Y. Xia, "Synthesis, Stability, and Surface Plasmonic Properties of Rhodium Multipods, and Their Use as Substrates for Surface-Enhanced Raman Scattering," *Angewandte Chemie International Edition* **45**, 1288–1292 (2006).
- [170] S. Xie, X. Y. Liu, and Y. Xia, "Shape-controlled syntheses of rhodium nanocrystals for the enhancement of their catalytic properties," *Nano Research* **8**, 82–96 (2015).
- [171] Y. Yuan, N. Yan, and P. J. Dyson, "Advances in the Rational Design of Rhodium Nanoparticle Catalysts: Control via Manipulation of the Nanoparticle Core and Stabilizer," *ACS Catalysis* **2**, 1057–1069 (2012).
- [172] M. B. Chambers, X. Wang, N. Elgrishi, C. H. Hendon, A. Walsh, J. Bonnefoy, J. Canivet, E. A. Quadrelli, D. Farrusseng, C. Mellot-Draznieks, and M. Fontecave, "Photocatalytic Carbon Dioxide Reduction with Rhodium-based Catalysts in Solution and Heterogenized within Metal-Organic Frameworks," *ChemSusChem* **8**, 603–608 (2015).
- [173] A. Ahmadvand, R. Sinha, S. Kaya, and N. Pala, "Rhodium Plasmonics for Deep-Ultraviolet Bio-Chemical Sensing," *Plasmonics* **11**, 839–849 (2016).
- [174] R. Alcaraz de la Osa, J. M. Sanz, a. I. Barreda, J. M. Saiz, F. González, H. O. Everitt, and F. Moreno, "Rhodium Tripod Stars for UV Plasmonics," *The Journal of Physical Chemistry C* **119**, 12572–12580 (2015).
- [175] I. Lieberman, G. Shemer, T. Fried, E. M. Kosower, and G. Markovich, "Plasmon-Resonance-Enhanced Absorption and Circular Dichroism," *Angewandte Chemie International Edition* **47**, 4855–4857 (2008).

- [176] E. J. Zeman and G. C. Schatz, “An accurate electromagnetic theory study of surface enhancement factors for silver, gold, copper, lithium, sodium, aluminum, gallium, indium, zinc, and cadmium,” *The Journal of Physical Chemistry* **91**, 634–643 (1987).
- [177] M. Pelton, J. Aizpurua, and G. Bryant, “Metal-nanoparticle plasmonics,” *Laser & Photonics Review* **2**, 136–159 (2008).
- [178] S. Tian, O. Neumann, M. J. McClain, X. Yang, L. Zhou, C. Zhang, P. Nordlander, and N. J. Halas, “Aluminum Nanocrystals: A Sustainable Substrate for Quantitative SERS-Based DNA Detection,” *Nano Letters* **17**, 5071–5077 (2017).
- [179] L. Zhou, C. Zhang, M. J. McClain, A. Manjavacas, C. M. Krauter, S. Tian, F. Berg, H. O. Everitt, E. A. Carter, P. Nordlander, and N. J. Halas, “Aluminum Nanocrystals as a Plasmonic Photocatalyst for Hydrogen Dissociation,” *Nano Letters* **16**, 1478–1484 (2016).
- [180] A. Kuzma, M. Weis, S. Flickyngerova, J. Jakabovic, A. Satka, E. Dobrocka, J. Chlpik, J. Cirak, M. Donoval, P. Telek, F. Uherek, and D. Donoval, “Influence of surface oxidation on plasmon resonance in monolayer of gold and silver nanoparticles,” *Journal of Applied Physics* **112**, 103531 (2012).
- [181] W. M. Haynes, *CRC Handbook of Chemistry and Physics* (Taylor and Francis Group, LLC, 2014), 95th ed.
- [182] P. Alonso-González, P. Albella, F. Neubrech, C. Huck, J. Chen, F. Golmar, F. Casanova, L. E. Hueso, A. Pucci, J. Aizpurua, and R. Hillenbrand, “Experimental verification of the spectral shift between near- and far-field peak intensities of plasmonic infrared nanoantennas,” *Physical Review Letters* **110**, 1–6 (2013).
- [183] G. Jezequel, J. C. Lemonnier, and J. Thomas, “Optical properties of gallium films between 2 and 15 eV,” *Journal of Physics F: Metal Physics* **7**, 1613–1622 (1977).
- [184] P. F. Liao, “Lightning rod effect in surface enhanced Raman scattering,” *The Journal of Chemical Physics* **76**, 751 (1982).
- [185] S. A. Scherbak, O. V. Shustova, V. V. Zhurikhina, and A. A. Lipovskii, “Electric Properties of Hemispherical Metal Nanoparticles: Influence of the Dielectric Cover and Substrate,” *Plasmonics* **10**, 519–527 (2015).
- [186] R. F. Aroca, G. Y. Teo, H. Mohan, A. R. Guerrero, P. Albella, and F. Moreno, “Plasmon-enhanced fluorescence and spectral modification in SHINEF,” *Journal of Physical Chemistry C* **115**, 20419–20424 (2011).
- [187] M. G. Blaber, C. J. Engel, S. R. C. Vivekchand, S. M. Lubin, T. W. Odom, and G. C. Schatz, “Eutectic Liquid Alloys for Plasmonics Theory and Experiment,” *Nano Letters* **12**, 5275–5280 (2012).
- [188] S. Z. Karazhanov, A. Pishtshev, and M. Klopov, “Electronic and optical properties of magnesium and calcium hydroxides: the role of covalency and many-body effects,” *Physica Scripta* **90**, 094015 (2015).

- [189] H. A. Atwater and A. Polman, “Plasmonics for improved photovoltaic devices,” *Nature Materials* **9**, 205–213 (2010).
- [190] T. G. Farinha, C. Gong, Z. A. Benson, and M. S. Leite, “Magnesium for Transient Photonics,” *ACS Photonics* **6**, 272–278 (2019).
- [191] J. S. Biggins, S. Yazdi, and E. Ringe, “Magnesium Nanoparticle Plasmonics,” *Nano Letters* **18**, 3752–3758 (2018).
- [192] T. Graedel, J. Franey, G. Gualtieri, G. Kammlott, and D. Malm, “On the mechanism of silver and copper sulfidation by atmospheric H₂S and OCS,” *Corrosion Science* **25**, 1163–1180 (1985).
- [193] T. W. H. Oates, M. Losurdo, S. Noda, and K. Hinrichs, “The effect of atmospheric tarnishing on the optical and structural properties of silver nanoparticles,” *Journal of Physics D: Applied Physics* **46**, 145308 (2013).
- [194] M. Esmaily, D. B. Blücher, R. W. Lindström, J.-E. Svensson, and L. G. Johansson, “The Influence of SO₂ on the Corrosion of Mg and Mg-Al Alloys,” *Journal of The Electrochemical Society* **162**, C260–C269 (2015).
- [195] R. R. Devi, I. M. Umlong, P. K. Raul, B. Das, S. Banerjee, and L. Singh, “Defluoridation of water using nano-magnesium oxide,” *Journal of Experimental Nanoscience* **9**, 512–524 (2014).
- [196] E. F. Mohamed, “Nanotechnology: Future of Environmental Air Pollution Control,” *Environmental Management and Sustainable Development* **6**, 429 (2017).
- [197] L. V. Rodríguez-de Marcos, J. I. Larruquert, J. A. Méndez, and J. A. Aznárez, “Self-consistent optical constants of MgF₂, LaF₃, and CeF₃ films,” *Optical Materials Express* **7**, 989 (2017).
- [198] V. V. Maslyuk, C. Tegenkamp, H. Pfnür, and T. Bredow, “Properties of Ternary Insulating Systems: The Electronic Structure of MgSO₄·H₂O,” *The Journal of Physical Chemistry A* **109**, 4118–4124 (2005).
- [199] J. Schanda, *Colorimetry: Understanding the CIE System* (John Wiley & Sons, Inc., Hoboken, NJ, USA, 2007).
- [200] S. Neelamraju, A. Bach, J. C. Schön, D. Fischer, and M. Jansen, “Experimental and theoretical study on Raman spectra of magnesium fluoride clusters and solids,” *The Journal of Chemical Physics* **137**, 194319 (2012).
- [201] A. Wang, J. J. Freeman, B. L. Jolliff, and I.-M. Chou, “Sulfates on Mars : A systematic Raman spectroscopic study of hydration states of magnesium sulfates,” *Geochimica et Cosmochimica Acta* **70**, 6118–6135 (2006).
- [202] L. J. Zhao, Y. H. Zhang, Y. A. Hu, and F. Ding, “Observations of supersaturated MgSO₄ and NaClO₄ aerosols by FTIR/ATR spectroscopy,” *Atmospheric Research* **83**, 10–18 (2007).

- [203] H. Thoms, M. Epple, and A. Reller, "The thermal decomposition of magnesium alcoholates to magnesia (MgO): studies by IR and thermal analysis," *Solid State Ionics* **101-103**, 79–84 (1997).
- [204] G. Murch and R. Thorn, "Relation between orbital binding energies and ionicities in alkali and alkaline earth fluorides," *Journal of Physics and Chemistry of Solids* **41**, 785–791 (1980).
- [205] S. Sugiyama, T. Miyamoto, H. Hayashi, and J. B. Moffat, "Oxidative Coupling of Methane on MgO–MgSO₄ Catalysts in the Presence and Absence of Carbon Tetrachloride," *Bulletin of the Chemical Society of Japan* **69**, 235–240 (1996).
- [206] D. R. Jennison, P. Weightman, P. Hannah, and M. Davies, "Calculation of Mg atom-metals XPS and Auger shifts using a Δ SCF excited atom model," *Journal of Physics C: Solid State Physics* **17**, 3701–3710 (1984).
- [207] Y. Inoue and I. Yasumori, "Catalysis by Alkaline Earth Metal Oxides. III. X-Ray Photoelectron Spectroscopic Study of Catalytically Active MgO, CaO, and BaO Surfaces," *Bulletin of the Chemical Society of Japan* **54**, 1505–1510 (1981).
- [208] C. D. Wagner, "Chemical shifts of Auger lines, and the Auger parameter," *Faraday Discussions of the Chemical Society* **60**, 291 (1975).
- [209] N. Craig, A. Harker, and T. Novakov, "Determination of the chemical states of sulfur in ambient pollution aerosols by X-ray photoelectron spectroscopy," *Atmospheric Environment* (1967) **8**, 15–21 (1974).
- [210] A. Czyżewski, J. Kapica, D. Moszyński, R. Pietrzak, and J. Przepiórski, "On competitive uptake of SO₂ and CO₂ from air by porous carbon containing CaO and MgO," *Chemical Engineering Journal* **226**, 348–356 (2013).
- [211] A. Luque, M. V. Martínez de Yuso, G. Cultrone, and E. Sebastián, "Analysis of the surface of different marbles by X-ray photoelectron spectroscopy (XPS) to evaluate decay by SO₂ attack," *Environmental Earth Sciences* **68**, 833–845 (2013).
- [212] G. Pacchioni, A. Clotet, and J. M. Ricart, "A theoretical study of the adsorption and reaction of SO₂ at surface and step sites of the MgO(100) surface," *Surface Science* **315**, 337–350 (1994).
- [213] H. Shao, L. He, H. Lin, and H.-W. Li, "Progress and Trends in Magnesium-Based Materials for Energy-Storage Research: A Review," *Energy Technology* **6**, 445–458 (2018).
- [214] L. Pasquini, "The Effects of Nanostructure on the Hydrogen Sorption Properties of Magnesium-Based Metallic Compounds: A Review," *Crystals* **8**, 106 (2018).
- [215] F. Sterl, H. Linnenbank, T. Steinle, F. Mörz, N. Strohfelddt, and H. Giessen, "Nanoscale Hydrogenography on Single Magnesium Nanoparticles," *Nano Letters* p. acs.nanolett.8b01277 (2018).

- [216] V. Dobrovolsky, O. Khyzhun, A. Sinelnichenko, O. Ershova, and Y. Solonin, "XPS study of influence of exposure to air on thermal stability and kinetics of hydrogen decomposition of MgH₂ films obtained by direct hydrogenation from gaseous phase of metallic Mg," *Journal of Electron Spectroscopy and Related Phenomena* **215**, 28–35 (2017).
- [217] G. Wu, J. Zhang, Y. Wu, Q. Li, K. Chou, and X. Bao, "The effect of defects on the hydrogenation in Mg (0001) surface," *Applied Surface Science* **256**, 46–51 (2009).
- [218] J. Čermák and L. Král, "Hydrogen diffusion in Mg–H and Mg–Ni–H alloys," *Acta Materialia* **56**, 2677–2686 (2008).
- [219] J. L. Anchell, K. Morokuma, and A. C. Hess, "An electronic structure study of H₂ and CH₄ interactions with MgO and Li-doped MgO clusters," *The Journal of Chemical Physics* **99**, 6004–6013 (1993).
- [220] A. Curry, G. Nusz, A. Chilkoti, and A. Wax, "Substrate effect on refractive index dependence of plasmon resonance for individual silver nanoparticles observed using darkfield microspectroscopy," *Optics Express* **13**, 2668 (2005).
- [221] Z. Song, H. Hu, H. Xu, Y. Li, P. Cheng, and B. Zhao, "Heterolytic dissociative adsorption state of dihydrogen favored by interfacial defects," *Applied Surface Science* **433**, 862–868 (2018).
- [222] S. Coluccia, F. Boccuzzi, G. Ghiotti, and C. Morterra, "Infrared study of hydrogen adsorption on MgO, CaO and SrO. Possible mechanism in promoting O–2 formation," *Journal of the Chemical Society, Faraday Transactions 1: Physical Chemistry in Condensed Phases* **78**, 2111 (1982).
- [223] J. K. Nørskov, F. Studt, F. Abild-Pedersen, and T. Bligaard, *Fundamental Concepts in Heterogeneous Catalysis* (John Wiley & Sons, Inc, Hoboken, NJ, USA, 2014).
- [224] C. Boerigter, R. Campana, M. Morabito, and S. Linic, "Evidence and implications of direct charge excitation as the dominant mechanism in plasmon-mediated photocatalysis." *Nature Communications* **7**, 10545 (2016).
- [225] I. Chorkendorff and J. W. Niemantsverdriet, *Concepts of Modern Catalysis and Kinetics* (Wiley-VCH Verlag GmbH & Co. KGaA, Weinheim, FRG, 2003).
- [226] C. Inc., "COMSOL Multiphysics 5.2," (2016).
- [227] H. Harutyunyan, A. B. F. Martinson, D. Rosenmann, L. K. Khorashad, L. V. Besteiro, A. O. Govorov, and G. P. Wiederrecht, "Anomalous ultrafast dynamics of hot plasmonic electrons in nanostructures with hot spots." *Nature Nanotechnol.* **10**, 770–774 (2015).
- [228] F. Pei, S. Wu, G. Wang, M. Xu, S.-Y. Wang, L.-Y. Chen, and Y. Jia, "Electronic and Optical Properties of Noble Metal Oxides M₂O (M = Cu, Ag and Au): First-principles Study," *Journal of the Korean Physical Society* **55**, 1243–1249 (2009).

- [229] M. Meier and A. Wokaun, “Enhanced fields on large metal particles: dynamic depolarization.” *Optics letters* **8**, 581–583 (1983).
- [230] T. V. Raziman and O. J. F. Martin, “Polarisation charges and scattering behaviour of realistically rounded plasmonic nanostructures,” *Optics Express* **21**, 21500 (2013).
- [231] J. M. Romo-Herrera, A. L. González, L. Guerrini, F. R. Castiello, G. Alonso-Núñez, O. E. Contreras, and R. A. Alvarez-Puebla, “A study of the depth and size of concave cube Au nanoparticles as highly sensitive SERS probes,” *Nanoscale* **8**, 7326–7333 (2016).
- [232] L. J. Sherry, S.-H. Chang, G. C. Schatz, R. P. Van Duyne, B. J. Wiley, and Y. Xia, “Localized surface plasmon resonance spectroscopy of single silver nanocubes.” *Nano Letters* **5**, 2034–2038 (2005).
- [233] O. Nicoletti, F. de la Peña, R. K. Leary, D. J. Holland, C. Ducati, and P. A. Midgley, “Three-dimensional imaging of localized surface plasmon resonances of metal nanoparticles,” *Nature* **502**, 80–84 (2013).
- [234] X. Chen, Z. Zheng, X. Ke, E. Jaatinen, T. Xie, D. Wang, C. Guo, J. Zhao, and H. Zhu, “Supported silver nanoparticles as photocatalysts under ultraviolet and visible light irradiation,” *Green Chemistry* **12**, 414 (2010).
- [235] S. Shuang, R. Lv, Z. Xie, and Z. Zhang, “Surface Plasmon Enhanced Photocatalysis of Au/Pt-decorated TiO₂ Nanopillar Arrays,” *Scientific Reports* **6**, 26670 (2016).
- [236] A. R. Forouhi and I. Bloomer, “Optical properties of crystalline semiconductors and dielectrics,” *Physical Review B* **38**, 1865–1874 (1988).
- [237] U. Zywietz, M. K. Schmidt, A. B. Evlyukhin, C. Reinhardt, J. Aizpurua, and B. N. Chichkov, “Electromagnetic Resonances of Silicon Nanoparticle Dimers in the Visible,” *ACS Photonics* **2**, 913–920 (2015).
- [238] A. B. Evlyukhin, C. Reinhardt, A. Seidel, B. S. Luk’yanchuk, and B. N. Chichkov, “Optical response features of Si-nanoparticle arrays,” *Physical Review B* **82**, 045404 (2010).
- [239] S. Person, M. Jain, Z. Lapin, J. J. Sáenz, G. Wicks, and L. Novotny, “Demonstration of Zero Optical Backscattering from Single Nanoparticles,” *Nano Letters* **13**, 1806–1809 (2013).
- [240] Z. Ioffe, T. Shamai, A. Ophir, G. Noy, I. Yutsis, K. Kfir, O. Cheshnovsky, and Y. Selzer, “Detection of heating in current-carrying molecular junctions by Raman scattering,” *Nature Nanotechnology* **3**, 727–732 (2008).
- [241] D. R. Ward, D. A. Corley, J. M. Tour, and D. Natelson, “Vibrational and electronic heating in nanoscale junctions,” *Nature Nanotechnology* **6**, 33–38 (2011).

- [242] C. Torres-Torres, “Ablation and optical third-order nonlinearities in Ag nanoparticles,” *International Journal of Nanomedicine* p. 925 (2010).
- [243] A. Plech, V. Kotaidis, S. Grésillon, C. Dahmen, and G. Von Plessen, “Laser-induced heating and melting of gold nanoparticles studied by time-resolved x-ray scattering,” *Physical Review B - Condensed Matter and Materials Physics* **70**, 1–7 (2004).
- [244] M. D. King, S. Khadka, G. A. Craig, and M. D. Mason, “Effect of Local Heating on the SERS Efficiency of Optically Trapped Prismatic Nanoparticles,” *The Journal of Physical Chemistry C* **112**, 11751–11757 (2008).
- [245] Y. Gutiérrez, D. Ortiz, J. Saiz, F. González, H. Everitt, and F. Moreno, “The UV Plasmonic Behavior of Distorted Rhodium Nanocubes,” *Nanomaterials* **7**, 425 (2017).
- [246] T. Montini, M. Melchionna, M. Monai, and P. Fornasiero, “Fundamentals and Catalytic Applications of CeO₂-Based Materials,” *Chemical Reviews* **116**, 5987–6041 (2016).
- [247] G. Held, *Introduction to Light Emitting Diode Technology and Applications* (Auerbach Publications, 2008).
- [248] Y. Taniyasu, M. Kasu, and T. Makimoto, “An aluminium nitride light-emitting diode with a wavelength of 210 nanometres,” *Nature* **441**, 325–328 (2006).
- [249] V. N. Mochalin, O. Shenderova, D. Ho, and Y. Gogotsi, “The properties and applications of nanodiamonds,” *Nature Nanotechnology* **7**, 11–23 (2012).
- [250] A. O. Govorov and H. H. Richardson, “Generating heat with metal nanoparticles We describe recent studies on photothermal effects using colloidal,” *Review Literature And Arts Of The Americas* **2**, 30–38 (2007).
- [251] G. Baffou and R. Quidant, “Thermo-plasmonics: Using metallic nanostructures as nano-sources of heat,” *Laser and Photonics Reviews* **7**, 171–187 (2013).
- [252] Q. Wang, W. Cao, J. Kuang, and P. Jiang, “Spherical AlN particles synthesized by the carbothermal method: Effects of reaction parameters and growth mechanism,” *Ceramics International* **44**, 4829–4834 (2018).
- [253] X. Chen and S. S. Mao, “Titanium Dioxide Nanomaterials: Synthesis, Properties, Modifications, and Applications,” *Chemical Reviews* **107**, 2891–2959 (2007).
- [254] P. Tamizhdurai, S. Sakthinathan, S.-M. Chen, K. Shanthi, S. Sivasanker, and P. Sangeetha, “Environmentally friendly synthesis of CeO₂ nanoparticles for the catalytic oxidation of benzyl alcohol to benzaldehyde and selective detection of nitrite,” *Scientific Reports* **7**, 46372 (2017).
- [255] Á. I. Barreda, Y. Gutiérrez, J. M. Sanz, F. González, and F. Moreno, “Light guiding and switching using eccentric core-shell geometries,” *Scientific Reports* **7**, 11189 (2017).

- [256] P. Albella, T. Shibanuma, and S. A. Maier, “Switchable directional scattering of electromagnetic radiation with subwavelength asymmetric silicon dimers,” *Scientific Reports* **5**, 18322 (2015).
- [257] T. Shibanuma, P. Albella, and S. A. Maier, “Unidirectional light scattering with high efficiency at optical frequencies based on low-loss dielectric nanoantennas,” *Nanoscale* **8**, 14184–14192 (2016).
- [258] W. Rechberger, A. Hohenau, A. Leitner, J. R. Krenn, B. Lamprecht, and F. R. Aussenegg, “Optical properties of two interacting gold nanoparticles,” *Optics Communications* **220**, 137–141 (2003).
- [259] K. S. Novoselov, “Electric Field Effect in Atomically Thin Carbon Films,” *Science* **306**, 666–669 (2004).
- [260] V. Kochat, A. Samanta, Y. Zhang, S. Bhowmick, P. Manimunda, S. A. S. Asif, A. S. Stender, R. Vajtai, A. K. Singh, C. S. Tiwary, and P. M. Ajayan, “Atomically thin gallium layers from solid-melt exfoliation,” *Science Advances* **4**, 1–12 (2018).
- [261] D. Z. Metin, L. Hammerschmidt, and N. Gaston, “How robust is the metallicity of two dimensional gallium?” *Physical chemistry chemical physics : PCCP* pp. 27668–27674 (2018).
- [262] Q. Ji, C. Li, J. Wang, J. Niu, Y. Gong, Z. Zhang, Q. Fang, Y. Zhang, J. Shi, L. Liao, X. Wu, L. Gu, Z. Liu, and Y. Zhang, “Metallic vanadium disulfide nanosheets as a platform material for multifunctional electrode applications,” *Nano Letters* **17**, 4908–4916 (2017).
- [263] S. E. Collins, M. A. Baltanás, and A. L. Bonivardi, “Hydrogen chemisorption on gallium oxide polymorphs,” *Langmuir* **21**, 962–970 (2005).
- [264] F. G. Meng, J. Wang, M. H. Rong, L. B. Liu, and Z. P. Jin, “Thermodynamic assessment of Mg-Ga binary system,” *Transactions of Nonferrous Metals Society of China* **20**, 450–457 (2010).
- [265] L. Genzel, T. P. Martin, and U. Kreibig, “Dielectric function and plasma resonances of small metal particles,” *Z. Phys. B-Condens. Mat.* **21**, 339–346 (1975).
- [266] W. Kraus and G. C. Schatz, “Plasmon resonance broadening in small metal particles,” *J. Chem. Phys.* **79**, 6130–6139 (1983).
- [267] A. Manjavacas, J. G. Liu, V. Kulkarni, and P. Nordlander, “Plasmon-induced hot carriers in metallic nanoparticles,” *ACS Nano* **8**, 7630–7638 (2014).
- [268] M. Barbry, P. Koval, F. Marchesin, R. Esteban, A. G. Borisov, J. Aizpurua, and D. Sánchez-Portal, “Atomistic near-field nanoplasmonics: Reaching atomic-scale resolution in nanooptics,” *Nano Letters* **15**, 3410–3419 (2015).
- [269] P. García-Fernández, J. C. Wojdeł, J. Íñiguez, and J. Junquera, “Second-principles method for materials simulations including electron and lattice degrees of freedom,” *Physical Review B* **93**, 21–23 (2016).